Ludwig-Maximilians-Universität München

Love and Rayleigh Waves in the Microseismic Noise Field

Carina Charlotte Juretzek

Dissertation
zur Erlangung des Doktorgrades
an der Fakultät für Geowissenschaften
der Ludwig-Maximilians-Universität München

vorgelegt von

Carina Charlotte Juretzek
aus Hamburg

München, den 29.12.2020

1. Gutachter: Prof. Dr. Heiner Igel
2. Gutachterin: Prof. Dr. Céline Hadziioannou
Tag der mündlichen Prüfung: 12.05.2021

Abstract

Ocean surface wave generated seismic noise has become an important signal ressource for seismic noise applications, such as tomography and monitoring purposes. This motivates the investigations regarding common and different origins of Love and Rayleigh waves observed in the microseismic noise field presented in this thesis. In particular, the temporal and spatial variation of the wave type ratio was studied for the purpose of constraining source locations and source mechanisms of Love waves.

The content of this thesis is (1) a detailed systematic and large scale observational study of the Rayleigh and Love wave composition in the ocean wave generated wave field across Europe, (2) a study which links the observed Love to Rayleigh wave ratio in the primary microseismic noise band with ocean wave parameters in order to distinguish regions which correspond to especially efficient source areas, (3) a comparison between observed and modeled primary microseismic noise including an attempt to further minimize the misfit between model and observation, and (4) an analysis of reoccuring microseismic noise observations from confined source areas in small ocean basins based on a statistical analysis of instantaneous phase coherences.

In particular, the composition of the ocean surface wave generated microseismic noise field as observed with 3-component seismic data is analyzed in this thesis. A focus is laid on the characteristics of both seismic surface waves and on the inclusion of horizontal component seismic data in order to further understand the generation of Love waves in the microseismic noise bands.

Inhaltsangabe

Seismisches Rauschen, welches durch Wellen an der Meeresoberfläche erzeugt wird, ist zu einer wichtigen Signalquelle für verschieden seismische Anwendungen geworden, wie beispielsweise für Tomographien und für Monitoring. Dies stellt die Motivation der in dieser Arbeit vorgestellten Untersuchungen zu gemeinsamen und unterschiedlichen Ursprüngen von Love- und Rayleigh-Wellen, die im mikroseismischen Rauschfeld beobachtet werden. Insbesondere wurde die zeitliche und räumliche Variation des Wellentypverhältnisses untersucht, um Quellorte und Quellmechanismen von Love-Wellen einzugrenzen.

Der Inhalt dieser Arbeit ist (1) eine detaillierte systematische und großräumige Beobachtungsstudie der Zusammensetzung von Rayleigh- und Love-Wellen im ozeanwellengenerierten Wellenfeld über Europa, (2) eine Studie, die das beobachtete Verhältnis von Love- zu Rayleigh-Wellen im primären mikroseismischen Rauschband mit Ozeanwellenparametern verknüpft, um Regionen zu unterscheiden, die besonders effizienten Quellgebieten entsprechen, (3) ein Vergleich zwischen beobachtetem und modelliertem primären mikroseismischen Rauschen mit dem Versuch, eventuelle Abweichungen zwischen Modell und Beobachtung weiter zu minimieren, und (4) eine Analyse von wiederkehrenden mikroseismischen Rauschereignissen aus begrenzten Quellgebieten in kleinen Ozeanbecken auf der Basis einer statistischen Analyse von instantanen Phasenkohärenzen.

Insbesondere wird in dieser Arbeit die Zusammensetzung des durch Ozeanoberflächenwellen erzeugten mikroseismischen Rauschfeldes, wie mit seismischen 3-Komponenten-Daten beobachtbar, analysiert. Ein Schwerpunkt liegt dabei auf den Eigenschaften der beiden seismischen Oberflächenwellen und auf der Einbeziehung von seismischen Horizontalkomponenten, um die Erzeugung von Love-Wellen in den mikroseismischen Rauschbändern besser zu verstehen.

Contents

Summary **I**

Zusammenfassung **II**

1 Introduction **1**
1.1 Overview 1
1.2 Exploring Earth with Seismic Data 2
1.3 A Link between Earth's Ground, Ocean and Atmosphere Dynamics . . . 3
1.4 Ambient Seismic Noise Applications 5
1.5 Human's Attempt to Tame Microseisms 6
1.6 Research Objectives and Thesis Structure 9

2 Theory and methods **11**
2.1 Introduction to the theoretical background of primary and secondary microseismic noise generation 11
2.1.1 The Earth's elastic waves 11
2.1.2 Primary microseismic noise generation 14
2.1.3 Secondary microseismic noise 17
2.1.4 Estimation of vertical component microseismic noise 19
2.2 Outline of analysis methods used in this thesis 20
2.2.1 1-component and 3-component beamforming 21
2.2.2 Rank correlation coefficient 27
2.2.3 Coherence statistics using the instantaneous phase 28

3 Where do ocean microseisms come from? A study of Love-to-Rayleigh wave ratios **31**
3.1 Publication 1 33
3.2 Supplementary material 55

4 Linking source region and ocean wave parameters with the observed primary microseismic noise **57**
4.1 Publication 2 59
4.2 Supplementary material 87

5 Predicting primary microseimic noise, modeling the directional characteristics of the noise field observed from both sides of the earth **89**
5.1 Local variations in slope factor - a northern hemisphere perspective . . 92
5.2 Local variations in slope factor - a southern hemisphere perspective . . . 104
5.3 Summary 116

6 A phase coherence based analysis of microseisms in marginal seas **119**
6.1 Publication 3 121

7 Conclusion and Outlook **151**

List of Figures **155**

References **159**

1

Introduction

1.1 Overview

The classification of measurements of any physical quantity, including Earth's ground vibrations shown in Fig.1.1, into either of the two groups 'signal' and 'noise' is in first place a question of the available knowledge about making use of the data. Since humans are determined to proceed in discovering their environment, they are motivated to extend their data and competence basis to do so steadily. As soon as new promising ressources of potential knowledge gain are within reach, scientists will try to make use of them. What was once disregarded as a useless or even a disturbing measurement, may turn out to be a most usefull ressource for various scientific objectives and application purposes.

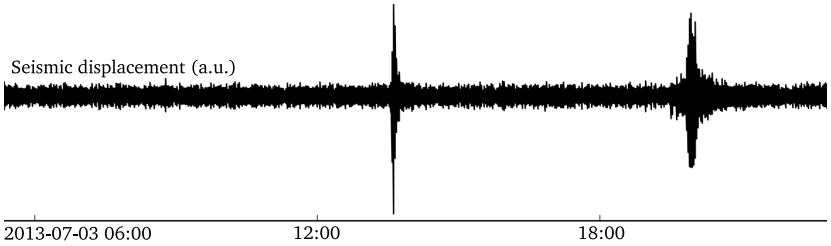

Figure 1.1: Example of a time series of vertical seismic ground displacement, including either two signals or a thousand signals, depending on one's research objectives.

The research focus of this thesis lies on a class of relatively tiny but persistent and omnipresent seismic background vibrations within a characteristic narrow frequency band. They have been recognized as part of ambient seismic noise in recordings of global seismometers for more than a century: *the ocean wave generated microseisms.* In the early 2000s, the potential of using this type of noise in order to investigate Earth's

properties was demonstrated in a number of studies. Since then, a variety of methods and application scenarios have evolved and interest in further understanding the origin, and predicting the properties of this noisy signal experienced a resurgence. The regained interest is especially motivated due to the fact that our knowledge about the origin of certain wave types present in the microseismic noise field is still limited, including the understanding of common and different origins of Love waves and Rayleigh waves. An improved understanding is however necessary in order to further encourage the usage of all different wave types contained in the microseisms and to enhance the accuracy of corresponding noise field applications. This chapter provides an introduction to the research objective of this thesis, and to the approach taken in order to adress them.

1.2 Exploring Earth with Seismic Data

In order to infer an understanding about the deeper internal structure of our planet, humans must be satisfied with observations from the exterior. Important hints to the composition of the Earth were provided by the gravitational, the electrical and the magnetic fields. However, like no other data ressource has the analysis of seismic waves excited by earthquakes provided insight into Earth' structure, from the uppermost sediment layers to the inner core.

Passive seismology considers the analysis of naturally generated seismic waves, which include two important groups of elastic waves, surface waves and body waves, with their propagation regimes along the surface or through the entire body of Earth, respectively. For each group, different wave types exist. Importantly, these wave types differ with respect to the characteristics of their periodic oscillations of ground particles, but also by their propagation velocity. Seismic waves propagate through Earth with phase velocities of up to several kilometers per second. Due to these high propagation velocities, seismic waves rapidly transport information, and the recorded seismic signals may be used to monitor temporal variations of earth properties in near real-time.

On their propagation through Earth, seismic waves cross regions with different material properties, such as in density or in elastic parameters, which alter the propagation velocity. Further, the layered material structure of Earth on large scales, with e.g. the core and the crust, but also on short scales, with e.g. sediments on top of ocean basalts, causes reflection, refraction and transmission and conversion of different seismic wave types at such material boundaries. In order to study Earth's structure along the propagation path of a seismic signal from the source to a receiver, properties such as its travel time or its amplitude may be analyzed. Seismic waves occur over a broad range

of frequencies and wavelengths. Depending on the seismic wave type and on the seismic wavelength considered, the resolution capability for analyzing material properties in the Earth significantly varies in lateral and radial extent. At the lower end of the frequency range, the interference of very long surface waves excites standing waves or free harmonic oscillations which correspond to the deformation of the Earth's entire body with a minimum eigenfrequency of 0.3 mHz.

Classical passive seismology concerns the analysis of Earth's natural seismic motions. However, seismic waves may be caused by a variety of sources. This includes anthropogenic sources, such as nuclear detonations or traffic, and natural sources, such as earthquakes in Earth's brittle upper layers, different processes in volcanoes, but also by the interaction of the solid Earth with the overlying fluid and atmospheric layer. Some of the more intense motions of the Earth's body, such as those caused by large earthquakes, have been recorded by man made seismometers for several hundreds of years by now. Nowadays, seismic vibrations are measured by means of highly sensitive recorders which are able to respond to very tiny amplitudes of displacement, velocity or acceleration of Earth's crust at or near the surface. These instruments enable the exploitation of faint seismic background motions known as ambient seismic noise.

The term ambient noise generally relates to background oscillations of a physical quantity, such as the pressure in the earth, ocean and atmosphere, or the ground displacement. The mechanisms causing the ambient noise background may however be very different for different frequency ranges. For a certain spectral band, the origin of ambient noise in the oceans, the atmosphere and the solid earth may theoretically be linked via a common origin. Today, ambient seismic noise is a widely used signal type for seismic tomography, monitoring purposes and climate research, providing more continuous data sets than other natural seismic sources. Hence improving the understanding of this ambient seismic signal, including the composition regarding different wave types, its temporal varibility and its origin, plays an important role regarding potential bias estimations for different noise applications.

1.3 A Link between Earth's Ground, Ocean and Atmosphere Dynamics

A continuous redistribution of energy and mass occurs constantly within Earth's system on very different time scales, including the atmosphere, the oceans and also the fluid and solid parts of Earth's interiour. For humans, these dynamic processes are most prominently evident in the form of e.g. wind, waves and tides, volcanic activity, the

magnetic field and earthquakes. An important and continuous role for redistributing energy is played by atmospheric turbulences in the form of wind and storms. These atmospheric motions are the source of wind-forced surface waves in the ocean. As a consequence, atmospheric processes are closely related to the wave climate in the hydrosphere. In presence of underlying solid layers, ocean surface waves may further act as source of seismic waves, known as the ocean wave generated microseisms. This term describes the continuous and omnipresent background of seismic motion recorded globally on inland seismometers in the frequency range between roughly $1 - 30\,s$. The corresponding global background noise field is known to be built from the superposition of propagating seismic waves, which are commonly understood to be generated by ocean surface waves in deep and shallow regions of the ocean.

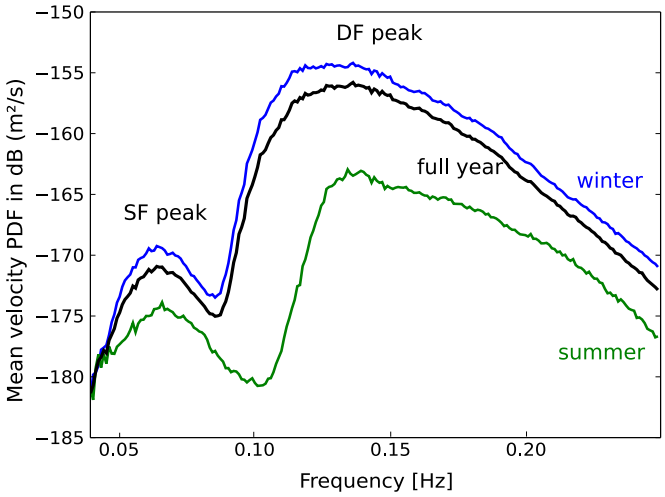

Figure 1.2: Example of a the mean power spectral density of seismic velocity over the microseismic noise bands observed with a seismic array on the northern hemisphere (Germany), evaluated for the full year, the summer half-year (April-September) and winter half-year period in 2013. Labels indicate the single frequency (SF) and the double frequency (DF) microseismic peaks as explained below in this chapter.

The sensitivity of modern seismic instruments allows to distinguish even further between two distinct peaks within the microseismic noise spectral band. Primary microseismic noise, also known as single frequency (SF) microseisms, refers to the seismic background motion which manifests itself as a moderate spectral peak within the 0.05-0.1 Hz frequency band of the power spectral density of ground velocity depicted in Figure 1.3. The fact that this spectral peak in seismic recordings agrees with a corresponding peak in spectral energy observed for ocean surface waves strongly hints

towards a causal link between the primary microseisms and the ocean waves [Haubrich et al., 1963].

The origin of primary microseisms can be understood theoretically by a mechanism, which transfers energy from the ocean surface waves with frequency and wavenumber f_w and k_w to seismic waves with the same frequency $f_{s1} = f_w$ but different wavenumber $k_{s1} \lll k_w$. Secondary microseismic noise, also known as double frequency (DF) microseisms, refers to the more energetic background motion corresponding to the stronger spectral peak found at twice the single frequency peak in the 0.1-0.5 Hz frequency band (cf. Fig. 1.3). This fixed relationship between the SF and DF spectral peaks provides evidence for a distinct generation mechanisms, which transfers ocean wave energy nonlinearly from ocean surface waves with frequency and wavenumber f_w and k_w to seismic waves of the secondary microseismic noise with frequency of $f_{s2} = 2f_w$ and wavenumber $k_{s2} \lll k_w$.

Many of the processes in the atmosphere and oceans display apparent periodic patterns driven by the Earth's interaction with the Sun and other solar system bodies. This includes seasonal patterns in e.g. meteorological processes or diurnal patterns in e.g. the tides. Likewise, microseismic noise shows seasonal and geographic variations in correlation with the changes in ocean wave heights and in their spectral energy distribution. In particular for geographic latitudes with a clear seasonal variation in wheather, and therefore wind conditions, the difference between the observed seismic background during summer and winter is apparent (cf. Fig. 1.3).

1.4 Ambient Seismic Noise Applications

Nowadays, ocean generated microseismic noise is an important and widely used signal ressource for different seismological applications. After it could be shown that the impulse response (Green's function) between two seismometer locations may be extracted from the cross-correlation of random wavefields [e.g., Derode et al., 2003; Lobkis and Weaver, 2001; Snieder, 2004], ambient seismic noise fields have become an alternative to the classical ressource of earthquakes generated seismic waves. In its characteristic frequency range, microseismic noise provides the dominant contribution to the ambient seismic noise field (cf. Fig. 1.3). Hence, it is important to further understand this signal type. Meanwhile, the geophysical community strongly relies on ambient seismic noise applications, including microseisms, for different purposes such as seismic tomography [Sabra et al., 2005; Shapiro and Campillo, 2004], passive monitoring of e.g. volcanoes or fault sites [Brenguier et al., 2008; Sens-Schönfelder and Wegler, 2006] or crustal seismology [Shapiro and Campillo, 2004]. Its key advantage is that it

provides more continuous and omnipresent data set in comparison to other sporadic seismic sources. The eqivalence between the cross-correlations and the Green's functions is theoretically obtained in the ideal case of isotropy of the wave energy. However, the ambient microseismic noise field commonly shows a strong azimuthal heterogeneity and temporal variability in dependence on the location of sources. These variations are known to potentially introduce biases in different noise applications and are therefore an important research topic for estimating the accuracy of such approaches [e.g., Tsai, 2009; Weaver et al., 2009; Zhan et al., 2013]. Temporal averaging can be used in order to retrieve more stable Green's functions for structural imaging. However, a demand for higher temporal resolution in earth property monitoring applications does not always allow for sufficient temporal avering durations. Another important application of microseisms is the monitoring of storms and hurricanes [Davy et al., 2014; Deacon, 1947; Iyer, 1958], which is enabled by the theoretical knowledge about the causal link between the ocean surface wave conditions and the microseisms noise [Ardhuin et al., 2012]. Furthermore, research on ocean wave generated seismic unrest provides a possibility for reconstructing historic wave conditions [Bernard, 1990] when seimometers were available but remote sensing of the ocean was not common, and even for monitoring climate change [Stutzmann et al., 2009]. Hence, a better understanding of the noise field characteristics paves the way for reducing biases in seismic noise applications and further encourages the usage of all wave types present in the microseisms. This applies in particular to knowledge about the temporal, spectral and spatial variation of the ambient seismic noise field on vertical and horizontal seismometer components, including the contributions from Love waves and Rayleigh waves.

1.5 Human's Attempt to Tame Microseisms

Already at the beginning of the 20th century Wiechert [1904] hypothetized the link between the ocean gravity wave periodicity observed at the shores of Scandinavia and those of the persistent vibrations recorded by seimometers in Germany. These ground motions had been described by researchers worldwide since the 19th century [e.g., Omori, 1899] and were referred to as microseisms, since these characteristic signals were found to be in the order of a micro-meter. Due to their large amplitudes recorded by seismometers, surface waves have traditionally been identified as a major contribution to the microseismic noise field [Zoeppritz, 1908]. In the first half of the 20th century, global observations further provided evidence for the causal link between microseisms and atmospheric disturbances over the oceans [e.g., Banerji, 1929; Klotz, 1910]. Further, observations showed that microseismic noise amplitudes decreased with distance to the

shore [Gutenberg, 1931] and indicated a 2 to 1 relationship between the periods of the energy peak of microseisms and of the ocean surface waves [Bernard, 1941; Deacon, 1947].

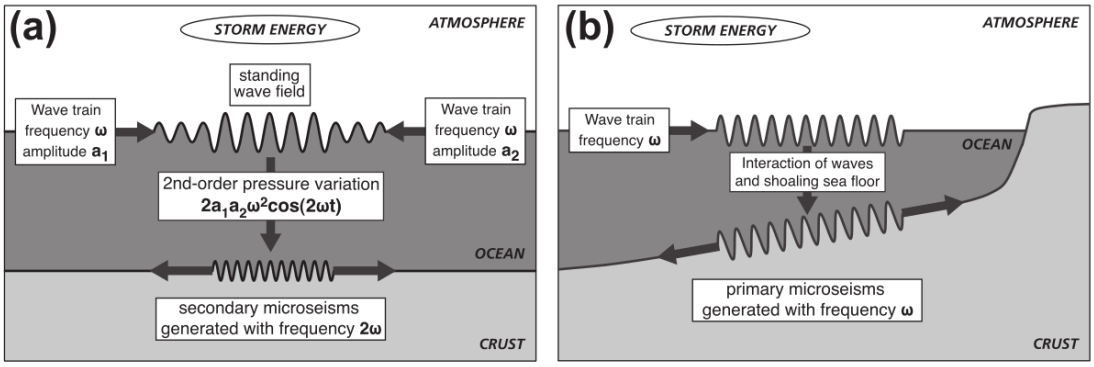

Figure 1.3: Reprint of Figure 1.7 from Ebeling [2012] shows a schematic of microseismic noise generation mechanisms: (a) for secondary microseisms in the case of interacting ocean wave trains of the same frequency traveling in opposite directions as formulated by Longuet-Higgins [1950]. A depth-independent second-order pressure variation, with an amplitude proportional to the product of the interacting wave amplitudes and with a frequency of twice that of the ocean waves, acts as source of microseisms, and (b) for primary microseisms in shallow water due to a coupling of ocean wave energy into the seafloor e.g. in the presence of constant sea-floor slopes as formulated by Hasselmann [1963].

Evolving physical explanations identified pressure oscillations as the possible sources of microseims [Miche, 1944]. A theoretical framework for the generation mechanism of the energetic double-frequency peak was initially formulated by Longuet-Higgins [1950], who identified the source of these seismic vibrations at the sea surface in the form of pressure oscillations caused by the non-linear interaction of oppositly travelling ocean surface gravity waves of similar period. This mechanism, termed secondary microseismic noise mechanism, explains how a non-linear coupling of ocean gravity wave energy into seismic energy at the twice the frequency of the ocean waves in deep water causes the more energetic peak. Further studies on microseisms found the presence of an additional weaker spectral peak [Banerji, 1930] corresponding directly to typical ocean surface wave frequencies [Haubrich et al., 1963].

The period ranges and amplitude differences between both microseismic noise peaks could be understood theoretically by two different generation mechanisms. A comprehensive theory for the generation of the single frequency peak, centered at a period of 12-15 s, was initially proposed by Hasselmann [1963], which explains this microseismic

noise peak due to an ocscillating pressure field caused by a direct interaction between ocean gravity waves with the seafloor in shallow water. This mechanism, termed primary microseismic noise mechanism, explains how a coupling of ocean wave energy into seismic energy at the same frequency of the ocean waves causes the weaker peak.

While early studies commonly found a particular type of seismic surface wave in the microseisms (Rayleigh waves) including the fundamental and higher modes, some found evidence for the additional presence of a second type of surface wave (Love waves) [e.g., Blaik and Donn, 1954; Darbyshire and Iyer, 1958; Haubrich and McCamy, 1969; Iyer, 1958; Rind and Donn, 1979] with a dependency on the geographic location and on the geology between source and receiver. Some studies attributed the presence of Love waves to conversion processes from Rayleigh waves during wave propagation [e.g., Toksöz and Lacoss, 1968]. But also P waves associated with storm events could be observed as early as the 1960s [e.g., Haubrich and McCamy, 1969; Toksöz and Lacoss, 1968]. In an ideal radially symmetric earth model with horizontal layering, the pressure oscillations identified theoretically as sources of microseisms excite wave types which include vertical particle motions. This includes seismic surface waves, i.e. Rayleigh waves and seismic body waves such as P waves. These theories did not provide an explanation for a direct generation of purely horizontally polarized wave types in the source area, such as Love waves.

After the emergence of ambient seismic noise applications in the 21st century, their focus remained on the usage of vertical component seismic data over two decades, considering Rayleigh waves and P waves. Significant P wave contributions to the secondary microseismic noise field generated especially under Hurricanes and storms at periods below 5 s proved suitable for global seismology [e.g., Gerstoft et al., 2006, 2008; Gualtieri et al., 2014; Koper et al., 2010; Landès et al., 2010; Retailleau et al., 2020; Zhang et al., 2010]. Further studies detailed how an ocscillating pressure field at the sea surface, namely its components which propagate with the appropriate phase velocities, simultaneously acts as a source of propagating acoustic noise in the atmosphere and ocean on one hand, and of propagating seismic noise in the solid earth on the other [Ardhuin and Herbers, 2013]. However, a knowledge gap remained concerning the origin of Love waves in microseisms. If generated directly by ocean surface waves, a source mechanism requires the involvement of horizontal forces. If generated along the propagation path due to a conversion from other wave types [Gregersen, 1978; Kennett and Mykkeltveit, 1984] or due to scattering [e.g., Kennett, 1972], the crustal properties require a sufficient heterogeneity.

1.6 Research Objectives and Thesis Structure

The fact that a considerable amount of Love waves are observed in the microseismic noise field, with a simultaneous lack of theoretical explanation of their origin, provokes the question of how and where this wave type is generated. A number of recent studies had confirmed previous discoveries of considerable amounts of Love wave in the microseismic noise field, but differed in their findings regarding the Love to Rayleigh wave ratio [e.g., Friedrich et al., 1998; Lin et al., 2008; Nishida et al., 2008; Tanimoto, 2013]. A clear picture of the wave field composition and its origin was further complicated due to regionally differing observations regarding the directions of propagation of both wave types, with indications for similar source directions but also for different source directions in the primary and secondary microseism band [Behr et al., 2013; Haubrich and McCamy, 1969; Nishida et al., 2008].

The aim of this thesis is to contribute to a better understanding of differently polarized surface wave types present in the microseismic noise field by analyzing their generation in different source regions and corresponding spatial and temporal variations in comparison to ocean wave parameters. This thesis further aims at constraining possible common or different generation mechanisms of Love and Rayleigh waves.

1. A brief summary of the theoretical background regarding microseismic noise and the analysis methods used in this thesis is presented in chapter 2.

2. Chapter 3 provides a systematic comparison of Rayleigh and Love wave characteristics in the ocean wave generated primary and secondary microseismic noise bands across Europe. The directional, seasonal and spectral variation in Love to Rayleigh wave amplitude ratio and kinetic energy ratio are detailed for one year of data from several arrays across Europe. Clearly lower wavetype ratios in the secondary microseism range among other characteristics indicated a difference in relevant source mechanisms compared to the primary microseism band. The content of this chapter was published in the Journal of Geophysical Research: Solid Earth [Juretzek and Hadziioannou, 2016]. The significant amount of Love waves in the primary microseisms, along with clear seasonal and directional variations in the wave type ratio, motivated an analysis on the origin of this variability, as adressed in the next chapter.

3. The influence of different earth and ocean wave properties in the source region on observed Love and Rayleigh wave noise amplitudes in the primary microseisms is discussed in chapter 4. The relative Love and Rayleigh wave noise generation effectivity in different source regions around Europe is analyzed by means of

beamforming and correlation of seismic noise amplitudes with output from a recent ocean wave model. One focus is on distinguishing between the influence of structural heterogeneity along the propagation path versus varying earth and ocean properties in the source region. The content of this chapter was published in the Geophysical Journal International [Juretzek and Hadziioannou, 2017].

4. The dependency of Rayleigh and Love wave proportions on source region properties found in the previous chapter, raised the questions if a state-of-the-art primary microseismic noise modelling for Rayleigh waves was able to reproduce this part of the wave field. Chapter 5 presents a comparison between theoretical predictions and observations of vertical component primary microseismic noise. The focus is on deriving local variations in an apparent seismic noise scaling factor, combining theoretical scaling effects due source site bathymetry and other effects due to propagation path structure, suitable for improving the agreement between modeled and observed noise. A part of the content of this chapter was published by Gualtieri et al. [2019] in the Geophysical Journal International.

5. Results from a phase coherence based approach, used for detecting and quantifying redundant and persistent signals in the microseismic noise field observed from the North Sea and the Mediterranean Sea, are described in chapter 6. Reoccurring efficient microseismic noise generation observed from specific source areas in these small ocean basins, provide an opportunity to further study the generation of Rayleigh and Love waves. Source locations of primary and secondary microseismic noise were estimated based on the analysis of phase coherences in comparison with beamforming. The content of this chapter was submitted to the Journal of Geophysical Research: Solid Earth.

6. Chapter 7 jointly summarizes the findings.

2

Theory and methods

In this chapter, the theoretical concepts for the understanding of the microseismic noise field and of corresponding generation mechanisms for the primary and secondary microseismic noise are summarized in section 2.1. For a more complete overview the reader may refer to the literature, e.g. Aki et al. [2002]; Ardhuin [2019]; Stein and Wysession [2003]. Further, an overview of the analysis methods, which were used in this thesis in order to quantify microseismic noise field properties on the basis of observations, is provided in section 2.2.

2.1 Introduction to the theoretical background of primary and secondary microseismic noise generation

2.1.1 The Earth's elastic waves

Considering the idealized case of an elastic earth model, seismic waves are oscillating physical disturbances corresponding to deformations of the material or to variations of pressure which propagate through the media. Body waves propagate inside the medium and correspond to compressional waves, with a particle motion parallel to the direction of wave propagation and to shear waves, with a particle motion perpendicular to the direction of wave propagation. The propagation velocity or phase velocity $c = \omega/k$ of these wave types differs, with the compressional wave velocity α exceeding the shear wave velocity β, since they similarly depend on the density of the Earth but differently on two elastic moduli, the bulk modulus and the shear modulus. In the presence of a free surface, additional elastic surface waves arise. The amplitude of their particle movement decays with depth. Two distinct types of surface waves arising in the Earth, Rayleigh waves and Love waves, differ in their particle motion. In a Cartesian

coordinate system, the particle motion for Rayleigh waves is constrained to the plane spanned by the vertical axis and the wave vector. For Love waves it is constrained to an horizontal motion perpendicular to the propagation direction of Love waves, i.e. in a plane perpendicular to the Rayleigh wave particle motion. The particle motion of the surface waves can be understood as the interference of multiple reflected body waves in a layered Earth structure, involving compressional and shear waves in the vertical plane for Rayleigh waves and horizontally polarized shear waves for Love waves. Hence, the propagation velocity of both surface waves differs and depends on the compressional and shear wave velocities of the surface layers of the Earth. While body waves are non dispersive, i.e. their phase velocity does not depend on their wave length, both surface wave types are dispersive in a layered Earth structure i.e. $c(k) = \omega(k)/k$. This is easily comprehensible by considering their representation by reflected body waves of different frequencies and hence wavelengths in a layered system, which will contructively interfer for different reflection angles and therefore different horizontal phase velocities. Hence, depending on their wavelength and particle motion characteristic, seismic waves help to study different properties of the Earth's body on different vertical and horizontal scales.

Seismic waves are excited due to a variety of source mechanisms in the Earth. These sources are commonly described by a set of different forces acting onto an area of the Earth. The seismic particle displacement $u_i(x)$ along the i-axis at a particular location of the Earth in response to a specific single point force $f_j(x_0)$ in j-direction at a source location, is related by the Green's function (impulse response) $G_i^j(x, x_0)$. Due to the conservation of momentum, the simple source representation by such a single point force is valid only for sources on the surface of the Earth. For internal sources, a superposition of force couples with different direction and amplitude can be considered for a representation of physical source pocesses. Without a priori knowledge on the source mechanism, a representation of the source may be given by a set of forces which theoretically excite the different seismic wave types observed, e.g. for an analysis of the rupture processes of earthquakes. Since the ocean surface waves interact with the surface of the Earth, the sources of microseismic noise may be represented by point forces along the surface. The theoretical maximum displacement amplitude along the vertical, radial and transversal components for a set of concentrically arranged seismometers around a central vertical and a central horizontal single point force at the surface of a horizontally layered Earth model are depicted in Figure 2.1. Only vertical and radial, but no tranversal component particle motions are excited due to the rotationally symmetric vertical point force. In contrast, the horizontal point force excites directionally variable proportions of particle motion on vertical, radial and tranversal

seismometer components. Hence, source mechanisms which may solely be represented by vertical point forces, do not provide an explanation for the direct generation of wave types with transversal particle motions, such as Love waves. Hence, different proportions of the different seismic wave types are generated in dependence on the physical characteristics of a specific underlying source mechanisms.

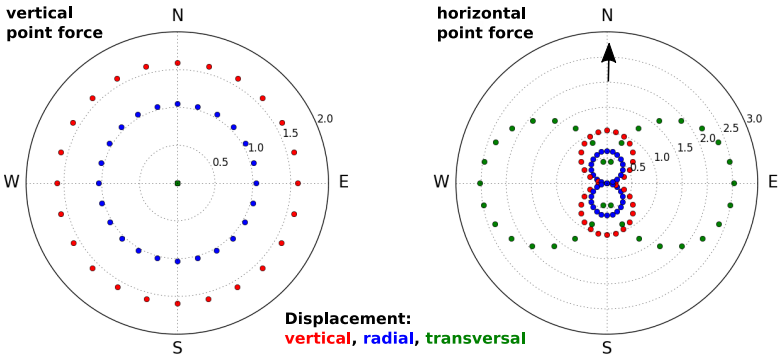

Figure 2.1: Theoretical maximum displacement amplitude along the vertical, radial and transversal seismometer components as modeled for a set of seismometers arranged in a circle in equidistance in response to a central vertical (left) and a central horizontal (right) single point force at the surface of a horizontally layered Earth model using Instaseis [van Driel et al., 2015]. The arrow indicates the direction of the horizontal point force.

How do the seismic wave fields generated by earthquakes and by the coupling between the ocean surface wave energy into the solid earth compare with each other? While large magnitude earthquakes may generate maximum displacements in the order of meters, the maximum amplitudes of the microseimic noise remain in the order of micrometers. While we find a general omnipresence of persistent microseimic noise, we find transient seismic signals with very distinct temporal onsets for most earthquakes. While we observe spatially strictly confined source regions for earthquake abundance, e.g. along plate boundaries, the source region of microseimic noise generation are the oceans, corresponding to about 70% of the Earth's surface area. While the sources of earthquakes are inside the solid part of the Earth, the microseismic noise sources are located in the ocean layer, which causes resonance effects amplifying the excited seismic waves of certain wave length in dependence on the water depth.

Thus, from an analytical point of view, earthquakes challenge us because of their sparcity, especially of those with larger magnitudes. In order to obtain statistical properties of the seismic noise fields generated by earthquakes, long time spans have to be considered in order to build a sufficient sample size. We may however represent single events in detail as the response of the Earth to a discrete source, i.e. as the impulse

response to point forces. On the other hand, the microseismic noise field challenges us since we are neither able to clearly separate a single discrete event, nor an individual source, which is not affected by other simultaneous sources. But since we are provided with a permanent time series of observations, we may determine statistical properties of the microseimic noise field in order to understand the nature of the sources.

As summarized in the following sections, the continuous microseismic noise field may be represented as the response to a continuous, ocean wave induced random forcing field at the Earth's surface. Since a stationary random forcing field within a surface source area acting as the source of microseisms may also be represented by a time varying central point force [Gualtieri et al., 2013; Hasselmann, 1963], the concept of forces is applicable for the analysis of microseismic noise, and may help to understand the generated wave types.

2.1.2 Primary microseismic noise generation

Propagating surface gravity waves in deep water, in most circumstances, are well described by the linear wave theory and their wavelength can be approximated by $\lambda_\infty = gT^2/2\pi$, where g is the gravitational acceleration and T is the wave period. These ocean surface waves display disturbances of the water layer in the form of pressure oscillations and particle motions, which are confined to the uppermost layer of the ocean and decay with distance to the free surface. If the water depth D decreases to less than approximately half of their wavelength, a propagating ocean surface wave causes particle motions within the whole water column and begins to directly interact with the seafloor. A theoretical source mechanism for single frequency microseisms in shallow water was initially described by Hasselmann [1963] and explains the generation of microseismic noise due to an oscillating pressure field arising from the coupling between ocean surface waves and the sea-floor topography. The amplitude of the bottom pressure oscillations due to the passing waves varies with the norm of the wavenumber vector $k = |\mathbf{k}|$ and the water depth D as $1/\cosh(kD)$. Hence, a shallow water depth in comparison to the wavenumber of ocean surface waves is an important criteria for the efficient generation of microseismic noise according to these theoretical explanations of the generation mechanisms of primary microseismic noise. With focus on the scope of the present thesis, key components of the theoretical concepts for primary microseismic noise generation mechanisms according to Hasselmann [1963],Ardhuin et al. [2015] and Ardhuin [2018] will be briefly outlined in the following.

Hasselmann [1963] demonstrated theoretically how the coupling between ocean surface waves and sea-floor topography in shallow water produces an ocean-wave induced

oscillating pressure field, which may be interpreted as an equivalent source term for vertical component primary microseismic noise. For a simplified approximation of microseismic noise generation over a small sea-floor inclination, he could show that the resulting ocean-wave induced pressure field power spectral density (PSD) $F_{p,1}$ scales linearly with the constant seafloor slope s.

The ocean-wave induced pressure field PSD as the source of primary microseismic noise $F_{p,1}$ was formulated by Ardhuin et al. [2015] in the form of a practical representation as

$$F_{p,1}(\mathbf{k} \approx 0, f) = s_{\text{eff}} \frac{\rho_{\text{w}}^2 g^4 (E_{\text{A}}(f, \theta_n) + E_{\text{A}}(f, \theta_n + \pi))}{k_{\text{A}} (2\pi f)^4 3200 L_x}, \tag{2.1.1}$$

which allows to make use of state-of-the-art ocean wave models for the quantitative estimation of the sources. $F_{p,1}$ has the SI units $\text{Pa}^2\text{m}^2\text{s}$. Here $\mathbf{k} = (k_x, k_y)$ where k_x, k_y and f correspond to the cross-shore and along-shore wave number vector and the frequency of the ocean surface gravity waves, respectively. Further, ρ_{w} is the density of water, g the earth gravity acceleration, θ is the azimuth of the ocean wave propagation direction and L_x is the distance normal to the coastline over which the seismic source is evaluated. $E_{\text{A}}(f, \theta)$ is the frequeny-direction dependent ocean wave energy spectral density in a water depth D_{A} for ocean waves propagating in directions normal to coasts θ_n and $\theta_n + \pi$. The subscript A denotes a normalization of the ocean wave field using a reference ocean wave amplitude in a water depth of $D_{\text{A}} = 4000\,\text{m}$ with corresponding ocean wave wavenumber k_{A} and frequency f, which are related by the linear wave dispersion relation

$$(2\pi f)^2 = g k_{\text{A}} \tanh(k_{\text{A}} D_{\text{A}}). \tag{2.1.2}$$

For the seismic noise generation, pressure variations at scales of seismic wavelength are relevant, which are significantly larger than those of ocean gravity waves at the same frequency. Hence, the equivalent pressure field PSD $F_{p,1}$ as source of the primary microseims is evaluated at near zero wavenumbers of the ocean gravity wave spectrum $k_x \approx 0, k_y \approx 0$. By adapting the simplified approximation of constant slopes to a slowly varying sea-floor topography, Ardhuin et al. [2015] introduced an effective seafloor slopes s_{eff} in Eq. 2.1.1, which determines the seismic source strength due to a realistic sea-floor topography profile in comparison to the source strength due to a constant seafloor slope of $s = 1\%$. In this formulation, along-shore variations in sea-floor topography are not taken into account. The ocean-wave propagation directions relevant for interacting with the sea-floor inclination is therefore confined to waves travelling perpendicular to and from shore-lines. Since detailed variations in bathymetry are

not accounted for in this theoretical framework, in a practical application of Eq. 2.1.1 the non-dimensional scaling factor s_{eff} accounts for additional unknown effects such as local bathymetry variations and is expected to vary globally along coasts. A more detailed discussion is provided by Ardhuin et al. [2015]. In order to estimate globally distributed locations and amplitudes of primary microseismic noise sources according to this mechanism, modeled output of the pressure PSD $F_{p,1}$ (Eq. 2.1.1) and the $E(f)$ directional-integrated ocean wave energy spectral density were used in this thesis. For this purpose, publicly available output for these quantities from a numerical ocean wave model WAVEWATCH III implementation [Ardhuin et al., 2014a] was retrieved from ftp://ftp.ifremer.fr/ifremer/ww3/HINDCAST with a temporal resolution of three hours.

When considering realistic seafloor slopes in coastal shallow waters of a few per cent, this mechanism does not readily reproduce the amplitudes of Rayleigh waves observed in the primary microseismic noise [Ardhuin et al., 2015; Gualtieri et al., 2019]. Moreover, it does not explain the observed portion of purely horizontally polarized seismic waves in this microseismic noise band, as detailed in chapters 3 and 4. More recently Ardhuin [2018] formulated theoretical source terms for the primary microseismic noise, which explain how ocean surface waves propagating over sea-floor variations of similar wavelengths may generate large scale horizontal and vertical forces of comparable magnitude. In comparison to the theoretical explanation by Hasselmann [1963], generating mainly Rayleigh waves, this framework also predicts horizontal forces, directly exciting Rayleigh and Love waves simultaneously. Importantly, the ratio between resulting large-scale vertical forces and large-scale horizontal forces was found to vary with water depth as

$$\alpha(k_0 D_0) = \frac{k_0 D_0 - \cosh(k_0 D_0)\sinh^3(k_0 D_0)}{(k_0 D_0 + \sinh(k_0 D_0)\cosh(k_0 D_0))^2}, \tag{2.1.3}$$

where the product $k_0 D_0$ corresponds to the nondimensional water depth as used in Ardhuin [2018]; Ardhuin et al. [2015]. Due to a depth dependent dominance of vertical or horizontal forces, this mechanism provides a possible explanation for a source site specific wave-type ratio generation and agrees with observations of regionally and direction dependent variations in Rayleigh to Love waves ratios as described in publication 1 [Juretzek and Hadziioannou, 2016], enclosed in chapter 3 of this thesis. Further, a phase shift between the horizontal and vertical force for shoreward propagating ocean waves was found to yield the same retrograd rotation sense as the particle motion of shoreward propagating Rayleigh waves in comparison to seaward propagating Rayleigh waves. This suggests a direction dependent amplification of Rayleigh waves by the

large scale forces when propagating towards the shore, which could explain indications of non-symmetrical effective Rayleigh waves radiation as described in publication 2 [Juretzek and Hadziioannou, 2017], enclosed in chapter 4 of this thesis.

2.1.3 Secondary microseismic noise

A theoretical description for the secondary microseism noise generation in deep water was initially provided by Longuet-Higgins [1950], who demonstrated how the second-order interactions between two oppositly traveling ocean-gravity wave trains of the same period produce standing waves of pressure oscillations. These pressure oscillations correspond to compressible waves propagating vertically downwards through the water column and may couple as seismic waves into the seafloor. In practice, this nonlinear interaction of pairs of ocean waves with slightly different periods and nearly opposite propagation directions give rise to pressure field components which propagate at high horizontal phase velocities, capable of contributing to the generation of microseismic noise composed of different wave types, such as Rayleigh waves and P waves [Ardhuin and Herbers, 2013; Hasselmann, 1963]. Hence, the source of the ocean wave generated microseismic noise can be given by an equivalent pressure field acting at the sea surface of a fluid-solid layered system.

In order to describe a source of seismic noise due to ocean gravity waves in deep water, the fluid motion in the ocean can be written as the expansion of the velocity potential into a pertubation series $\phi = \phi_1 + \phi_2$ [Hasselmann, 1963], where ϕ_1 corresponds to the first order water motion due to the incompressible ocean gravity waves and ϕ_2 which corresponds to a second order correction of the fluid motions, for which compressibility must be taken into account. Hasselmann [1963] showed how the solution of the second order term ϕ_2 can be obtained from the non-linear boundary conditions at the sea surface and may be written as the response of the ocean-solid system to the forcing from an equivalent pressure field p applied at the free surface of the ocean

$$(\frac{\mathrm{d}^2}{\mathrm{d}t^2} + g\frac{\mathrm{d}}{\mathrm{d}z})\phi_2 = -\frac{1}{\rho_w}\frac{\mathrm{d}p}{\mathrm{d}t}, \tag{2.1.4}$$

where ρ_w is the density of water and g is the gravitational accelleration.

The equivalent pressure field p in deep water ($k_w h \gg 1$) may be determined by the square of the velocity potential gradient and hence is proportional to the square of the orbital phase velocities at the sea surface [Hasselmann, 1963; Longuet-Higgins, 1950]

$$p = \rho_w(\boldsymbol{\nabla}\phi)^2 \tag{2.1.5}$$

According to e.g. Ardhuin et al. [2011], a practical representation of the power sprectral density of this equivalent pressure field F_{p2} at the sea surface evaluated at very small ocean wave wavenumbers $K \approx 0$, relevant for generating seismic waves, can be written in terms of the ocean surface displacement variance of the interacting wave trains $E(f)$ in m^2s as

$$F_{p2}(K \approx 0, f_s) = \rho_w^2 g^2 f_s E^2(f) \int_0^{\pi} M(f,\theta) M(f,\theta+\pi) \mathrm{d}\theta, \tag{2.1.6}$$

with the SI units Pa^2m^2s, where the seismic frequency f_s equals twice the frequency of the ocean waves $f_s = 2f$. $M(f,\theta)$ refers to the non-dimensional azimuth θ and frequency dependent energy distribution of the invonlved ocean wave pairs.

Owing to the fact, that the ocean surface gravity frequency-wavenumber spectrum shows a broad-band content, the superposition of pairs of ocean-wave trains produce second order interaction components, which have very different wave-length and phase velocities [Ardhuin and Herbers, 2013]. This range includes shorter wave length in comparison to the ocean gravity waves, capable of generating propagating acoustic waves in the ocean and in the atmosphere. But this also includes components with considerably larger wave-lengths and phase velocities than those of the involved ocean waves, being comparable to those of seismic waves, e.g. Rayleigh waves or P waves. Three important configurations provide the condition for a pronounced occurance of opposite wave trains are met for seismic noise generation due to this mechanism [Ardhuin et al., 2011], these are:

1. The interference of two different swell fields generated from e.g. two distant storms, which may occur anywhere in the ocean.

2. The interference of a swell field generated at a previous location along the trjectory of a rapidly travelling storm with the local wind sea produced under the same storm at a later instant in the storms life time, which may also occur anywhere in the ocean.

3. The interaction of incident ocean wave trains and their oppositely traveling reflections from the coast, which may occur near-shore.

However, this theoretical mechanism directly explains only the generation of those wave types, which may be excited by vertical point forces over a flat or slowly varying sea floor. The presence of transversally polarized waves, such as Love waves or SH waves, may only be explained for neglegible proportions of these wave types due to very tiny horizontal force components over realistic seafloor slopes, or for differing proportions

due to a secondary conversion of wave type energy of one type to another. Wave type energy conversion in the microseismic noise band has been speculated to occur along the propagation paths due to 3D structural effects such as scattering and mode conversions at continental margins [e.g., Gregersen, 1978; Kennett, 1972]. However, a significant structural heterogeneity must be assumed, if observed Love to Rayleigh wave type ratios are to be reproduced. For this reason, there is further need for in depth investigations of the microseimic noise type and its generation mechanisms.

2.1.4 Estimation of vertical component microseismic noise

The following paragraphs concern the estimation of the vertical displacement PSD of Rayleigh waves. In order to estimate vertical component microseismic noise at an arbritrary seismometer location, which is generated according to the primary or secondary microseismic noise mechanism described above, the equivalent pressure PSD F_p as source of the primary microseismic noise (F_{p1}) and as source of the secondary microseismic noise (F_{p2}) may be evaluated.

For a simplified earth model, consisting of a water layer overlying an elastic homogeneous half space, the vertical seismic displacement PSD $S(f_s)$ at a seismic frequency f_s contributed by a seismic source according to the primary or secondary mechanism can be written as a function of their ocean wave-induced equivalent pressure PSD $F_p(K \approx 0, f_s)$ as [Hasselmann, 1963; Longuet-Higgins, 1950]

$$S(f_s) = \frac{(2\pi)^2 f_s c_j^2 F_p}{\beta_c^5 \rho_c^2} \tag{2.1.7}$$

with SI units m/Hz. Here, the homogeneous half space at the source site is characterized by the crustal shear wave velocity β_c and the density ρ_c.

The seismic response to the forcing pressure PSD field as discussed in the previous paragraphs depends on the structural earth model at the source site. Regarding the source sites relevant for ocean wave generated seismic waves, the depth of the ocean layer over the solid earth in relation to the acoustic wave length determines the transfer function between the pressure PSD and the seismic displacement PSD for Rayleigh waves and P-waves as described in detail by Ardhuin and Herbers [2013]; Hasselmann [1963]. The non-dimensional coefficient c_j in Eq. 2.1.7 accounts for this water depth dependent amplification or transfer function between the surface pressure and the vertical ground displacement, which is distinct for each Rayleigh wave mode j. A detailed analysis of the amplification factor for the above mentioned two layer earth model is provided by e.g. Longuet-Higgins [1950], where c_j is given as a function of $f_s D_A/\alpha_w$, with the acoustic phase velocity α_w. For the modal excitation of Rayleigh waves in the

secondary microseismic noise band, the amplification coefficients significantly vary according to the spatial variation in water depth D_A throughout the ocean basins. For the Rayleigh wave excitation in the shallow water regime of the primary microseismic noise band, the amplification coefficients are approximately constant. Hence, for the primary microseismic noise modeling of fundamental mode Rayleigh wave displacement PSD in this thesis, c was taken as 0.2 according to the corresponding value for this shallow water limit obtained by Longuet-Higgins [1950].

For a radially symmetric earth model, the total vertical displacement PSD $u(f_s)$ of the microseismic noise at any geographic location may be calculated as superposition of the global distribution of either the primary or secondary microseism source contributions over the surface area of the Earth as [Hasselmann, 1963; Kanamori and Given, 1981]

$$u_p(f_s) = \int_0^{2\pi}\int_0^{\pi} S(\lambda,\phi,f_s)\frac{\exp^{-\omega R_E\Delta/(QU)}}{R_E\sin(\Delta)}R_E^2\sin(\phi)\mathrm{d}\lambda\mathrm{d}\phi. \tag{2.1.8}$$

Here, the spherical distance between the source and the receiver is given by Δ, the density of the crust by ρ_c, the S-wave velocity in the crust by β_c, the earth radius by R and the longitude and colatitude by λ and ϕ, respectively. Accordingly, for the modelling of primary microseismic noise for an arbitrary effective slope factor s_{eff} in this thesis, the total vertical displacement PSD $u(f_s)$ of primary microseismic noise using Eq.2.1.1 and 2.1.7 is estimated by

$$u_{p,1}(f_s) = s_{\mathrm{eff}}\int_0^{2\pi}\int_0^{\pi} \frac{(2\pi)^2 f_s c^2 F_{p,1}(\lambda,\phi,f_s)\exp^{-\omega R_E\Delta/(QU)}}{\beta_c^5\rho_c^2 R_E\sin(\Delta)}R_E^2\sin(\phi)\mathrm{d}\lambda\mathrm{d}\phi. \tag{2.1.9}$$

2.2 Outline of analysis methods used in this thesis

The joint analysis of the seismic wave field recorded with a group of recorders, e.g. with receiver arrays or receiver pairs, provides the possibility for an enhancement, selection or suppression of certain signals according to their characteristics. A mayor part of this thesis relies on array based analysis methods. In terms of the microseismic noise field, focus was laid on analyzing characteristics such as the phase coherence, temporal persistence and directional variation. Further, the joint analysis of multiple recorders allows for an improved resolution capability regarding the detection of different wavefield components. This is of vital importance for the analysis of such weak signal amplitudes associated with the microseismic noise wave field. In this section, the most

important multiple station methods used here are summarized. In practise, Python and in particular the ObsPy Toolbox [ObsPy, 2016] was used for implementing the methods.

2.2.1 1-component and 3-component beamforming

Seismic arrays are configurations of multiple seismometers. Corresponding seismic recordings may be analyzed jointly using various specifically tailored array methods, which commonly allow for improved signal detection in comparison to single station data [Rost and Thomas, 2002]. One of the important established and powerful array methods applied in the context of this thesis is beamforming. This method allows for an effective separation of coherent and incoherent portions of a given wave field and its performance regarding this capability generally scales with the number of associated seismometers, but also depends on other factors such as the specific array geometry or structural heterogeneities at the array site. Regarding the coherent parts of the wave field, the method provides the possibility to infer estimates for the propagation direction and phase velocity of passing seismic signals, but also more generally allow to analyze the spectral characteristics and the specific seismic wave-type composition of the wave field.

For the simple assumption of the incidence of a plane wave at an array, the basic concept of forming an array beam is the technique of diliberate time shifting of the individual seismic traces recorded at different array elements according to the theoretical arrival time differences Δt of an assumed wave front, propagating across the array from a given direction. The time shifted individual seismic traces may then be summed in order to form a so called array sum-trace or array beam. For coherent signals, the constructive interference of the seismic traces causes a larger beam amplitude. For a plane-wavefront beamformer, one common way of parameterizing a signal's incident wavefront is in terms of its backazimuth θ, as direction of arrival measured clockwise from north, and of its horizontal slowness $u_h = \sin(i)/v = 1/v_{app}$ as inverse of the apparent horizontal phase velocity v_{app} at the array site. Here, i is the incidence angle of a seismic ray measured relative to the vertical axis (z-axis), v is the phase velocity and the horizontal slowness vector in the direction of wave propagation is given by

$$\mathbf{u}_\mathrm{h} = [u_x, u_y, u_z] = u_h[\sin(\theta), \cos(\theta), 1/\tan(i)]. \tag{2.2.1}$$

Theoretical differential arrival times Δt between array elements and a reference location, usually given by a central array station or the center of gravity of the array, may be calculated for an impinging plane wave signal. With the location vector $\mathbf{r}_i$ from

the reference point to the location of an individual array element i in the horizontal plane, the time difference $\Delta t_i = \mathbf{r}_i \mathbf{u}_\mathrm{h}$ then correspond to the travel time offset to be corrected for regarding this array element, before forming a beam.

Considering recorded wave forms for a signal model described by a coherently propagating plane wave signal $a(t)$ and additional uncorrelated local noise $n(t)$ at $i = [1, ..., N]$ array elements $x_i(t) = a(t - \mathbf{r}_i \mathbf{u_h})) + n_i(t)$, a one component time domain array beam $b(t)$ can be formed by applying theoretical time shift corrections according to the incident wavefront properties $\mathbf{u}_\mathrm{h}$ and θ. If $\mathbf{u}_\mathrm{h}$ and θ are known, the differential arrival times Δt can be applied to $x(t)$, and $b(t)$ is then given by [Rost and Thomas, 2002]

$$b(t) = \frac{1}{N} \sum_{i=1}^{N} (a(t) + n_i(t + \mathbf{r}_i \mathbf{u_h})) = a(t) + \frac{1}{N} \sum_{i=1}^{N} n_i(t + \mathbf{r}_i \mathbf{u_h}). \tag{2.2.2}$$

The beam $b(t)$ then yields the coherent signal $a(t)$ plus an reduced amount of incoherent noise $n(t)$. In this ideal case, the improvement of the signal-to-noise ratio for an N-station array $\mathrm{SNR_N}$ as compared to the single seismic recording $\mathrm{SNR_S}$ was quantified according to Harjes and Henger [1973] as

$$\frac{\mathrm{SNR_N}}{\mathrm{SNR_S}} \approx \sqrt{N}. \tag{2.2.3}$$

In practice, neither $\mathbf{u}_\mathrm{h}$ nor θ are known a priori in order to steer the beam according to a true incident signal. A grid search through the parameter space is commonly applied in oder to identify parameter sets, which maximize the beam amplitude, indicating the presence of a coherent incident signal. The assumption of an incoming plane wave is often violated in practice, e.g. for signals which originate from nearby sources. Further, an incident wave field at array sites suffers from coherence losses and wavefront distortions due to the heterogeneity of the Earth's crust, which decreases the resolution and introduces biased beamformer results. In order to take a significant curvature of wave fronts into account, a curved wavefront beamformer can be defined, which includes the source-array distance as additional parameter. Here, the source location can be understood as the focal point of the theoretical incident curved wavefront across the array. Using a homogeneous velocity model, the theoretical phase delays corresponding to an assumed curved wavefront propagating across the array can be easily determined by the differential travel time between sensors in reference to the source location distance. Using a two-dimensional spatially heterogeneous velocity model, detailed in chapter 4 instead of a homogeneous model, theoretical phase delays were additionally determined from the differential travel times between sensors according to the wavefronts according to the isochrons of an impinging signal determined by means of ray-tracing.

Considering the signal model of a plane wavefront in the frequency-wavenumber domain, the Fourier transformed data recorded at the vertical components of the array elements may be written as [Esmersoy et al., 1985]

$$\mathbf{X}(\omega) = \mathbf{e}(\omega)A(\omega), \tag{2.2.4}$$

where the complex value $A(\omega)$ describes the amplitude and phase of the impinging signal and the phase delays due to wave propagation from the source to the array elements relative to an array reference location are captured by the steering vector

$$\mathbf{e}(\mathbf{u}_\mathrm{h}, \omega) = [e^{i\omega\mathbf{u}_\mathrm{h}(\mathbf{r}_1-\mathbf{r}_0)}, e^{i\omega\mathbf{u}_\mathrm{h}(\mathbf{r}_2-\mathbf{r}_0)}, ..., e^{i\omega\mathbf{u}_\mathrm{h}(\mathbf{r}_N-\mathbf{r}_0)}]^T. \tag{2.2.5}$$

The cross-spectral density matrix $\mathbf{R}$ between the Fourier transformed recordings $\mathbf{X}$ is given by the expectation value $E\{.\}$ of $\mathbf{R}(\omega) = E\{\mathbf{X}(\omega)\mathbf{X}^H(\omega)\}$ and contains the auto-power spectral density at each receiver in the diagonal, and the cross-power spectral densities and the phase relations between all array elements corresponding to an impinging true signal in the remainder. Here, H denotes the Hermitian transpose.

In order to estimate the signal power by means of a phase delay corrected summation process, the Bartlett or FK beam power may then be written as the linear stack over the weighted recordings at all array elements as [Esmersoy et al., 1985]

$$P_\mathrm{FK}(\mathbf{u}_\mathrm{h}, \omega) = E|y^2| = E|\mathbf{e}_\mathrm{w}^H(\mathbf{u}_\mathrm{h}, \omega)\mathbf{X}(\omega)|^2 = \mathbf{e}_\mathrm{w}^H(\mathbf{u}_\mathrm{h}, \omega)\mathbf{R}(\omega)\mathbf{e}_\mathrm{w}(\mathbf{u}_\mathrm{h}, \omega), \tag{2.2.6}$$

with the array output y. By means of a grid search over the possible parameter space of impinging plane wavefronts, the output power $\mathbf{e}_\mathrm{w}^H(\mathbf{u}_\mathrm{h}, \omega)\mathbf{R}(\omega)\mathbf{e}_\mathrm{w}(\mathbf{u}_\mathrm{h}, \omega)$ is maximized where the phase delays in the data $\mathbf{R}(\omega)$ are accurately corrected for by the corresponding weight $\mathbf{e}_\mathrm{w}(\mathbf{u}_\mathrm{h}, \omega)$. Under the constraint of $|\mathbf{e}_\mathrm{w}| = 1$, the theoretical phase delay corrections between the $n = 1, ..., N$ seismometer locations $\mathbf{r}_i$ and the reference location $\mathbf{r}_0$ maximizing the beam power are given by the FK beamformer weight vector $\mathbf{e}_\mathrm{w}$

$$\mathbf{e}_\mathrm{w}(\mathbf{u}_\mathrm{h}, \omega) = \frac{1}{\sqrt{N}}[e^{i\omega\mathbf{u}_\mathrm{h}(\mathbf{r}_1-\mathbf{r}_0)}, e^{i\omega\mathbf{u}_\mathrm{h}(\mathbf{r}_2-\mathbf{r}_0)}, ..., e^{i\omega\mathbf{u}_\mathrm{h}(\mathbf{r}_N-\mathbf{r}_0)}]^T = \frac{\mathbf{e}(\mathbf{u}_\mathrm{h}, \omega)}{\sqrt{N}}. \tag{2.2.7}$$

The beam power estimate depends on the recorded data represented by $\mathbf{R}(\omega)$. However, since an array consists of a discrete number of elements only, the retrievement of the signal power for a specific impinging plane wave front depends on the resolution capability of the specific array geometry. This resolution capability may be described by

the array response function given by the power output of the array over the parameter space in response to a plane wave signal of infinite phase velocity, i.e. a signal which is received exactly simultaneously at all array sensors and therefore implies zero phase delays between the array elements, corresponding to a vector of ones for $\mathbf{X}(\omega)$. With $\mathbf{k} = \omega \cdot \mathbf{u}$ the array response function may be written in the form of [Rost and Thomas, 2002]

$$\mathrm{ARF} = \left| \frac{1}{N} \sum_{n=1}^{N} e^{2\pi i(\mathbf{k}-\mathbf{k}_0)(\mathbf{r}_n-\mathbf{r}_0)} \right|^2 . \tag{2.2.8}$$

Figure 2.2 shows examples of the array transfer functions for three European arrays of different size and geometry. Here, the self normalized beam power is depicted as a function of the slowness u_h and the propagation direction backazimuth $\theta = \tan^{-1}(u_{hx}/u_{hy})$ of theoretically impinging plane wave signals calculated over the parameter space of $\theta = [0,\ 2\pi]$ and $u_h = [0,\ 0.5]$.

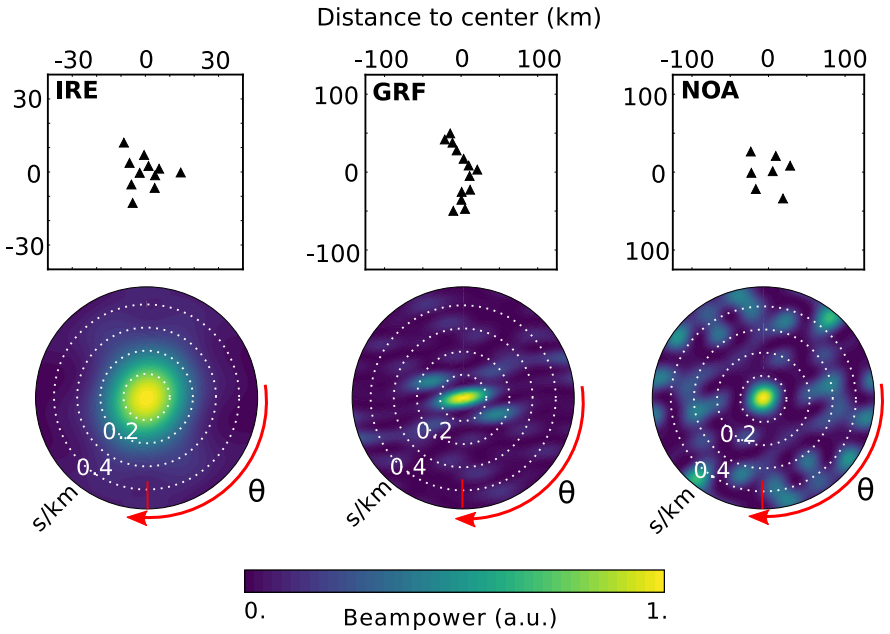

Figure 2.2: Example of three different array geometries for an array in Ireland (IRE), in Germany (Gräfenberg array, GRF) and in Norway (Norsar array, NOA) and their corresponding array response functions as a function of the horizontal slowness u_h and the backazimuth θ measured relative to North at a frequency of 0.125 Hz.

While the shape of the array transfer functions in Fig. 2.2 differ between the arrays, all of them yield a main lobe at $u = 0$, corresponding to the plane wave recorded simultaneously at all array elements. The width of the so called main lobe in the center

indicates the maximum resolution achievable at the specific wave number $\omega = 2\pi f$. For the same array geometry, the resolution capability decreases with decreasing frequency. Accordingly, the larger the array aperture, the higher is the resolution capability at a certain frequency. The arrays GRF and NOA have a larger aperture compared to the IRE array and yield a significantly smaller main lobe. By further comparing the three array geometries, it is apparent that a higher symmetry of the arrays corresponds to a higher symmetry of the ARF. The GRF array has a larger extend in north-south direction than in east-west direction. For a wave field propagating across the array in north-south direction, the array elements will sample the wave field over several wave length, which causes a higher sensitivity in capturing small phase changes due to slowness or azimuth variations. Hence, the main lobe is narrower along the north-south axis than along the east-west axis. Due to the discrete number and positions of the array elements, so called side lobes appear in the ARF. Especially for arrays with very regular interstation distances, multiple solutions of the slowness correspond to theoretical phase delays which maximize the ARF. When analyzing an arbitrary impinging signal with $\theta = \theta_0$ and $u_h = u_{h0}$ at the array, the beam power output corresponds to the ARF shifted to these locations in the slowness vs. backazimuth space. Accordingly, in the presence of multiple signals with different propagation characteristics, the beam power output is composed of the superposition of the corresponding shifted ARF functions. Hence, artefacts in the beam power may be caused due to the presence and superposition of side lobes. Such potential biases must be taken into consideration for an analysis of complex wave fields. One way of improving the resolution capability of beamforming is to use alternative beam power estimators.

An important method, introduced by Capon [1969] for improving the resolution in comparison to the Bartlett beamformer is the Minimum Variance Distortionless Response (MVDR) beamformer, also known as Capon beamformer. The main principle of the Capon beamformer is that the optimum weights $\mathbf{e}_\mathrm{w}$ are adapted according to the sensor recordings such that the methods minimizes the total output power $\mathbf{e}_\mathrm{w}^H \mathbf{R}(\omega)\mathbf{e}_\mathrm{w}$ from all directions except for the looking direction to the impinging signal, for which the power output is maintained according to $\mathbf{e}_\mathrm{w}^H \mathbf{e}(\mathbf{u}_\mathrm{h}, \omega) = 1$. Consequently, the output power in looking direction should correspond to the unmodified signal power, while uncorrelated noise and interferences are minimized. The optimum weights for the MDVR beamformer $\mathbf{e}_\mathrm{w}$ are given by

$$\mathbf{e}_\mathrm{w} = \frac{\mathbf{R}^{-1}\mathbf{e}(\mathbf{u}_\mathrm{h}, \omega)}{\mathbf{e}^H(\mathbf{u}_\mathrm{h}, \omega)\mathbf{R}^{-1}\mathbf{e}(\mathbf{u}_\mathrm{h}, \omega)}, \tag{2.2.9}$$

and the MDVR beam power estimate is given by

$$P_{\mathrm{MDVR}}(\omega) = \mathbf{e}_{\mathrm{w}}^{H}(\mathbf{u}_{\mathrm{h}}, \omega)\mathbf{R}(\omega)\mathbf{e}_{\mathrm{w}}(\mathbf{u}_{\mathrm{h}}, \omega) = \frac{1}{\mathbf{e}^{H}(\mathbf{u}_{\mathrm{h}}, \omega)\mathbf{R}^{-1}(\omega)\mathbf{e}(\mathbf{u}_{\mathrm{h}}, \omega)}. \tag{2.2.10}$$

3-component beamforming

An advantage of using 3-components in comparison to vertical-component beamforming is given by the fact that the particle motion of the different wave types can be included as additional parameterization of coherent signals propagating across the array. Since this thesis concerns the characterization of the ambient noise wave field including the composition of different seismic wave types, a 3-component beamforming approach, based on the approach described in Esmersoy et al. [1985] and Riahi et al. [2013], was used here. It was implemented in the frequency-wavenumber domain, in order to characterize the spectral characteristics of the primary and secondary microseismic noise bands.

The signal model for the 3-component case may be given by a combination of (a) the 1-component signal model describing the phase delays between array elements due to wave propagation, and of (b) the particle motion model describing the phase and amplitude relations between the three components of each array sensor corresponding to a specific seismic wave type polarization ρ [Esmersoy et al., 1985]. Considering the on 3-component signal model of a plane wavefront including the particle motion, the Fourier transformed data recorded at the three components $\mathbf{X}_1(\omega) = [X_{x1}, X_{y1}, X_{z1}]$ of the first array element may be written as

$$\mathbf{X}_1(\omega) = e_1(\omega)\mathbf{c}(\rho)_{\mathrm{xyz}}A(\omega), \tag{2.2.11}$$

Analogue to the 1-component case, $A(\omega)$ describes the amplitude and phase of the impinging signal and $e_1(\omega)$ describes the phase delay of the first array element due to wave propagation. The complex polarization state [Samson, 1983] at the sensor is described by $c(\rho)_{\mathrm{xyz}} = [c_x(\rho), c_y(\rho), c_z(\rho)]^T$.

Thus considering a 3-component array, the data vector $\mathbf{X}_{3\mathrm{C}}$ can be written as

$$\mathbf{X}_{3\mathrm{C}} = [X_{x1}, \ldots, X_{xN}; X_{y1}, \ldots, X_{yN}; X_{z1}, \ldots, X_{zN}]^T, \tag{2.2.12}$$

which is of length 3N. The cross spectral density matrix $\mathbf{R}_{3\mathrm{C}}(\omega)$ of the 3-component Fourier transformed recordings is then given by the expectation value

$$\mathbf{R}_{3N}(\omega) = E\{\mathbf{X}_{3\mathrm{C}}(\omega)\mathbf{X}_{3\mathrm{C}}^{H}(\omega)\}. \tag{2.2.13}$$

Now, the 3-component weight vector $\mathbf{w}_{3C}$ can be written as the Kronecker product $\otimes$ of the steering vector of theoretical phase delays due to a wave propagation $\mathbf{e}(\mathbf{u}_h, \omega)$ and the polarization state vector $\mathbf{c}(\rho)_{xyz}$ as

$$\mathbf{w}_{3C}(\mathbf{u}_h, \omega, \rho) = \mathbf{c}(\rho)_{xyz} \otimes \mathbf{e}(\mathbf{u}_h, \omega) = [c_x e_1, \ldots, c_x e_N; c_y e_1, \ldots, c_y e_N; c_z e_1, \ldots, c_z e_N]^T. \tag{2.2.14}$$

Hence, for a seismic array composed of N 3-component stations, the plane wave beam power output $P(\mathbf{u}_h, \omega, \rho)$ can be written as a function of the frequency f, the horizontal slowness $\mathbf{u}_h$ and the polarization ρ of an incident coherent signal as

$$P(\mathbf{u}_h, \omega, \rho) = \mathbf{w}_{3C}^H(\mathbf{u}_h, \omega, \rho)\mathbf{R}_{3C}(\omega)\mathbf{w}_{3C}(\mathbf{u}_h, \omega, \rho). \tag{2.2.15}$$

Analogue to the 1-componemt beamformer, $\mathbf{w}_{3C}$ depends on the specific choice of the beamformer. With the backazimuth $\theta = [0,\ 2\pi]$ and the ellipticity angle $\nu = \tan^{-1}(H/V) = [0,\ \pi/2]$ defined by the ratio between the horizontal H and vertical V Rayleigh waves amplitude, the ideal 3-component polarization state of a retrograde elliptically polarized fundamental mode Rayleigh waves is given by

$$\mathbf{c}(\rho_R) = [-i\sin(\nu)\cos(\theta), -i\sin(\nu)\sin(\theta), \cos(\nu)]^T, \tag{2.2.16}$$

while for a horizontally transversal polarized Love wave or SH-wave the polarization state is

$$\mathbf{c}(\rho_L) = [-\sin(\theta), \cos(\theta), 0]^T. \tag{2.2.17}$$

2.2.2 Rank correlation coefficient

Kendall's tau-b [Kendall, 1945] is a non-parametric correlation coefficient, which estimates the joint monotonous variation of two time series $x(t)$ and $y(t)$ as

$$\tau_b = (C - D)/\sqrt{(C + D + T_x) \cdot (C + D + T_y)}, \tag{2.2.18}$$

with the number of concordant C (e.g. $x_i > x_k$ and $y_i > y_k$) and discordant D ($x_i > x_k$ and $y_i < y_k$) pairs of the time series, respectively. T_x and T_y are the number of ties of either ($x_i = x_k$) or ($y_i > y_k$). A τ_b value of -1 indicates perfect anti-correlation and a value of 1, perfect correlation. Kendall's Tau was used in chapter 4 and 5 for estimating the joint variation between time series of microseismic noise and ocean wave parameters, since it is robust against outliers and does not assume a linear relation between the two variables.

2.2.3 Coherence statistics using the instantaneous phase

Phase coherence methods have proven their value for the analysis of weak amplitudes signal with respect to amplitude driven methods. The potential to use the instantaneous phase [Bracewell, 1986] $\Phi(t)$ of an analytic signal $S(t) = A(t)e^{i\Phi(t)}$ with amplitude $A(t)$ in order to evaluate the phase-coherence of $j = 1, ..., N$ seismic traces $s_j(t)$ was explored by Schimmel and Paulssen [1997] by the formulation of the phase stack

$$\mathrm{PS}(t) = \left| \frac{1}{N} \sum_{j=1}^{N} e^{i\Phi_j(t)} \right|^{\nu} \tag{2.2.19}$$

as an amplitude unbiased measure of signal coherence, ranging between the values 1 for perfectly phase aligned traces and 0 for destructive interference. This measure is widely used in form of the further developed phase weighted stack (PWS) for the purpose of efficient incoherent noise reduction but also as a method to detect weak but coherent signals. The PWS(t) was formulated as linear stack over N traces $s_j(t)$, each weighted by PS(t) according to

$$\mathrm{PWS}(t) = \frac{1}{N} \sum_{j=1}^{N} s_j(t)\mathrm{PS}(t). \tag{2.2.20}$$

The PWS efficiently downweighs the amplitude of the summed traces at time samples where the wave forms are not in phase, and provides the unmodified stack amplitude where the wave forms are in phase. Extending the PWS further for comparing the phase coherence between a pair of seismic traces $s_j(t)$ and $s_k(t)$ on a sample by sample basis in the manner of a cross-correlation considering a temporal lag τ between the traces, the phase coherence correlation (PCC) was introduced by Schimmel [1999], which can be written as

$$C_{\mathrm{pcc}}(t) = \frac{1}{N} \sum_{\tau=\tau_0}^{\tau_0+T} \left| \cos\left(\frac{\Phi_j(t+\tau) - \Phi_j(\tau)}{2} \right) \right| - \left| \sin\left(\frac{\Phi_j(t+\tau) - \Phi_j(\tau)}{2} \right) \right|. \tag{2.2.21}$$

This definition provides a metric for phase coherence, indicating perfectly coherent or non-coherent data on a practical range between 1 and -1, e.g. between a pair of seismic traces separated in time or space. By omitting the temporal shift, i.e. considering zero lag only, a measure of the phase-coherence at each time sample between any pairs of seismic traces $s_j(t)$ and $s_k(t)$ may be obtained according to

$$C_{jk}(t) = \left| \cos\left(\frac{\Phi_j(t) - \Phi_k(t)}{2} \right) \right| - \left| \sin\left(\frac{\Phi_j(t) - \Phi_k(t)}{2} \right) \right|. \tag{2.2.22}$$

For a set of N temporal subwindows, C_{jk} spans a matrix of N by N elements for each time sample, with zeros on the diagonal. A statistical approach using the phase coherence metric (Eq. 6.1.1) was introduced by Gaudot et al. [2015], which focuses on the analysis of the first and second moment (mean, variance) of the distribution of pairwise phase coherence comparisons C_{jk} between a number N of different traces. By defining μ_j as mean phase coherence between an individual trace j with all other N traces, the overall mean phase coherence $\bar{\mu}(t)$ over all possible N trace combinations was introduced according to

$$\bar{\mu}(t) = \frac{1}{N}\sum_{j=1}^{N}\mu_j(t) \text{ with } \mu_j = \frac{1}{N-1}\sum_{k=1}^{N}(1-\delta_{jk})C_{jk}(t). \tag{2.2.23}$$

δ denotes the Kronecker delta. Due to the symmetry of the pair-wise phase coherence $C_{jk}(t)$ (cf. Eq. 6.1.1) the evaluation of all valid pairs of phase coherence comparisons can be given by $C_i = (C_{jk} + C_{kj})/2$. With $p = n(n-1)/2$, the overall mean coherence can be written as

$$\bar{\mu}(t) = \frac{1}{p}\sum_{i=1}^{p}C_i(t), \tag{2.2.24}$$

and the corresponding variance as

$$\bar{\sigma}^2(t) = \frac{1}{p}\sum_{i=1}^{p}(C_i(t) - \bar{\mu}(t))^2. \tag{2.2.25}$$

For the detection and localization of persistent coherent sources in the ambient seismic noise field in this thesis, the phase coherence comparison (Eq. 6.1.1) was performed on a sample by sample basis between pairs of inter-station cross-correlation functions $\mathrm{CC}_j(t)$ and $\mathrm{CC}_k(t)$ as described in chapter 6.

3

Where do ocean microseisms come from? A study of Love-to-Rayleigh wave ratios

In this chapter, a study of Love to Rayleigh wave ratios in the ocean generated primary and secondary microseismic noise bands across Europe is presented.

Due to the global prevalence of persistent microseismic energy at frequencies between approximately 0.05 and 0.5 Hz caused by the ocean-earth interaction, ambient seismic noise studies had become a popular and widely spread application. Although a majority of studies still focused on vertical component seismic data, observations had proven that a considerable amount of horizontally polarized seismic signals could be found on horizontal component data. However, the theory of source mechanisms for ocean generated microseismic noise had been established for Rayleigh waves and P waves, but was not comparably developed for Love waves, especially regarding the secondary microseismic noise band.

For a better understanding of the composition of the microseismic noise wave field and eventually of their generation mechanisms, the ratio of Love to Rayleigh waves was studied here. For this purpose, a 3-component beamforming method was used, allowing for a separation of Love and Rayleigh wave polarized signals across both microseismic noise bands. For a characterization of the wave-field composition, the directional, seasonal and spectral variation of Love to Rayleigh wave ratios were analyzed.

Previous studies had observed a varying amount of Love waves in dependence on the geographical location and direction of propagation. Previously, the wavetype ratio of surface waves in the primary and secondary microseismic noise bands had been sparsely

studied jointly, especially across regional scales. This study added a systematic large scale analysis of the wave type ratio in both microseismic noise bands in Europe with special focus on the variability across seasonal and regional scales.

Love waves were found to dominate the primary microseismic noise band on average, with kinetic Love-to-Rayleigh energy ratios ranging from 0.6 to 2.0. The relative high Love-wave content and a pronounced directional dependence of the wavetype ratio hinted to the presence of a source mechanism, which directly causes significant horizontal forces. For the secondary microseism clearly lower Love-wave proportions were found with L/R ratios between 0.4 and 1.2, yielding a more directionally homogeneous wave-type ratio, except for locations far from the coast. An influence of the propagation path on the wave-type ratio seems likely.

Section 3.1 includes the content of the manuscript as published and section 3.2 presents supplementary material to the publication.

3.1

Publication 1

Where do ocean microseisms come from? A study of Love-to-Rayleigh wave ratios

Carina Juretzek[1] and Celine Hadziioannou
1: Department of Earth and Environmental Sciences, Ludwig-Maximilians-University, Munich, Germany.

Status:
Published in Journal of Geophysical Research: Solid Earth, 2016
DOI: https://doi.org/10.1002/2016JB013017]

The following text resembles the original manuscript as submitted to the journal. Figure, equation and reference numbers were adapted to match the consecutive labeling of this thesis. All cited sources can be found at the end of this thesis in the bibliography.

Abstract

Our knowledge of the origin of Love waves in the ambient seismic noise is extremely limited. This applies in particular to constraints on source locations and source mechanisms for Love waves in the secondary microseism. Here, 3-component beamforming is used to distinguish between the differently polarized wave types in the primary and secondary microseismic noise field, recorded at several arrays across Europe. We compare characteristics of Love and Rayleigh wave noise, such as source directions and frequency content, measure Love to Rayleigh wave ratios for different backazimuths, and look at the seasonal behavior of our measurements by using a full year of data in 2013. The beamforming results confirm previous observations that backazimuths for Rayleigh and Love waves in both microseismic bands mainly coincide. However, we observe differences in relative directional noise strength between both wavetypes for the primary microseism. At those frequencies, Love waves dominate on average, with kinetic Love-to-Rayleigh energy ratios ranging from 0.6 to 2.0. In the secondary microseism, the ratios are lower, between 0.4 and 1.2. The wavetype ratio is directionally homogeneous, except for locations far from the coast. In the primary microseism, our results support the existence of different generation mechanisms. The contribution of a shear traction type source mechanism is likely.

Introduction

Ocean microseisms are the continuous seismic background oscillations, which result from the interaction between the atmosphere, the ocean waves and the solid Earth. Two distinct peaks are globally observed in the microseism spectra, which differ in frequency and amplitude. The weaker single frequency peak, centered around 14 seconds, is known as primary microseism peak and results from a direct interaction between ocean gravity waves with the seafloor in shallow water [Hasselmann, 1963]. The more energetic secondary microseism peak, which appears at about twice the primary microseism frequency (7 seconds), arises from pressure oscillations at the sea surface caused by interaction of opposing gravity waves [e.g., Hasselmann, 1963; Longuet-Higgins, 1950].

Already at the beginning of the 20th century, interest in the origin of microseismic noise resulted in a significant number of studies [e.g., Gutenberg, 1911; Wiechert, 1904]. After the causal link of microseisms to ocean wave conditions had been established, the potential of monitoring e.g. storm systems was realized immediately and was continuously pursued by many authors [e.g., Davy et al., 2014; Deacon, 1947; Iyer,

1958]. For an extensive overview of the history of microseismic noise studies, we refer to [Ebeling, 2012].

Through the use of ambient noise correlations, this microseismic noise has become an important signal source for tomography [e.g., Sabra et al., 2005; Shapiro and Campillo, 2004] and monitoring purposes [e.g., Brenguier et al., 2008; Sens-Schönfelder and Wegler, 2006]. Most studies that cross-correlate ambient noise aim to obtain signals similar to the Green's function. In order for the equivalence to hold, one must start from the assumption that the ambient noise field is azimuthally isotropic and stable over time [e.g., Sanchez-Sesma and Campillo, 2006]. In practice however, many studies use the noise in the primary and secondary ocean-generated microseismic frequency bands. Oceanic noise sources are localized and not uniformly distributed, which in some cases can lead to a bias in measurements based on ambient noise correlations [e.g., Tsai, 2009; Weaver et al., 2009]. Therefore, a better understanding of the microseism noise field characteristics is desirable to further improve ambient noise applications.

The ocean generated microseisms consists mostly of surface waves, as well as a smaller amount of body waves [e.g., Gerstoft et al., 2008; Gualtieri et al., 2014; Koper et al., 2010; Toksöz and Lacoss, 1968]. Fundamental mode Rayleigh waves are found to dominate microseismic noise in most places. However, the excitation of different modes is dependent on water depths [Gualtieri et al., 2013; Longuet-Higgins, 1950] and higher mode surface waves have been observed onshore in some regions [e.g., Brooks et al., 2009; Kimman et al., 2012]. Nevertheless, considerable amounts of Love waves were already reported early on in microseism noise research [e.g., Darbyshire and Iyer, 1958; Haubrich and McCamy, 1969; Rind and Donn, 1979]. Since then, the interest in using and studying them has decreased. Hence, our knowledge about common and different origins of Love and Rayleigh waves in the microseism band is still limited. This applies in particular to constraints on source locations and generation mechanisms of Love waves, especially in the secondary microseism band.

Many recent studies concentrate on Rayleigh waves and P waves by focusing on the vertical component of noise. The generation mechanism of the Rayleigh and body waves in the secondary microseism band is well described by the theory of [Longuet-Higgins, 1950] and later [Hasselmann, 1963]. And their theory has since been confirmed in several studies by observations [e.g., Kedar et al., 2008] and simulations [e.g., Ardhuin et al., 2011; Gualtieri et al., 2013]. For the secondary microseisms, no direct generation mechanism of Love waves from ocean waves is presently known. Indirect generation has been proposed, such as conversion from Rayleigh waves on the propagation path between source region and the point of observation [e.g., Toksöz and Lacoss, 1968]. In the case of the primary microseisms, pressure forces over inclined bathymetry

during shoaling [Ardhuin et al., 2011; Hasselmann, 1963] and shear traction [Friedrich et al., 1998; Fukao et al., 2010; Nishida et al., 2008; Saito, 2010] were found to be the most plausible mechanism to generate Love wave simultaneously with Rayleigh waves in shallow water. Already in early noise studies, the observation was made that the amount of Love wave noise found can vary considerably depending on the geographical location and direction of propagation [Rind and Donn, 1979]. In several studies, Love waves in the primary and secondary microseism band were observed to propagate mainly from similar directions as Rayleigh waves [Haubrich and McCamy, 1969; Nishida et al., 2008] and with a comparable frequency content [Haubrich and McCamy, 1969]. However, studying the noise wavefield around New Zealand, Behr et al. [2013] observed similar source directions in the secondary but different source directions in the primary microseism band. Considering the ratio of Love to Rayleigh waves present in ambient seismic noise is one way to quantify the relative content of both surface wave types. Such a measurement simultaneously carries information about the initially generated wavetype content by the source mechanism, as well as any modifications due to propagation effects. For example, Rind and Donn [1979] state that geologic heterogeneities along the propagation path likely affect the observed Love to Rayleigh wave ratio, by altering amplitudes of Love waves differently than those of Rayleigh waves. However, the relative amount of the wavetypes generated directly by a noise source will also strongly affect the observed Love to Rayleigh wave ratio. Recent studies have aimed to quantify the Love wave content more precisely by considering the energy ratio of Love and Rayleigh waves present. They found a significant contribution of Love wave noise exceeding the Rayleigh wave content in the primary but not in the secondary microseism band [e.g., Friedrich et al., 1998; Nishida et al., 2008] although Tanimoto [2013] found comparable levels of both wavetypes.

Here, we study the directional, seasonal and spectral dependence of the Love wave noise content in the primary and secondary microseism band across Europe in detail and compare these observations to Rayleigh waves. We further measure Love to Rayleigh amplitude and kinetic energy ratios, and report on their dependence on direction and time. In this study, we use several arrays to be able to observe also potential local variations of these properties.

Data and Array Processing

In order to analyze the Rayleigh and Love wave content in the primary and secondary microseism band, we used available seismic data from eight seismic station sets distributed around Europe during the year of 2013. The array locations and geometries

are displayed in figure 3.1. Data from the permanent 3-component arrays Gräfenberg (GRF) and Norsar (NOA), as well as from four station sets of suitable geometries from the European network (CH, IT, NICE and THU) were retrieved from public data centers. Additionally, two non-public arrays were used, the Donegal array (IRE, from the Dublin Institute for Advanced Studies, DIAS) and the Morocco Münster array (MM, described by Spieker et al. [2014]). Due to the array dimensions, the IRE network is mainly suitable for the shorter period range of this study. For the MM network, data in 2013 was available from January to the beginning of April. The dimensions of this array suit the longer period range better.

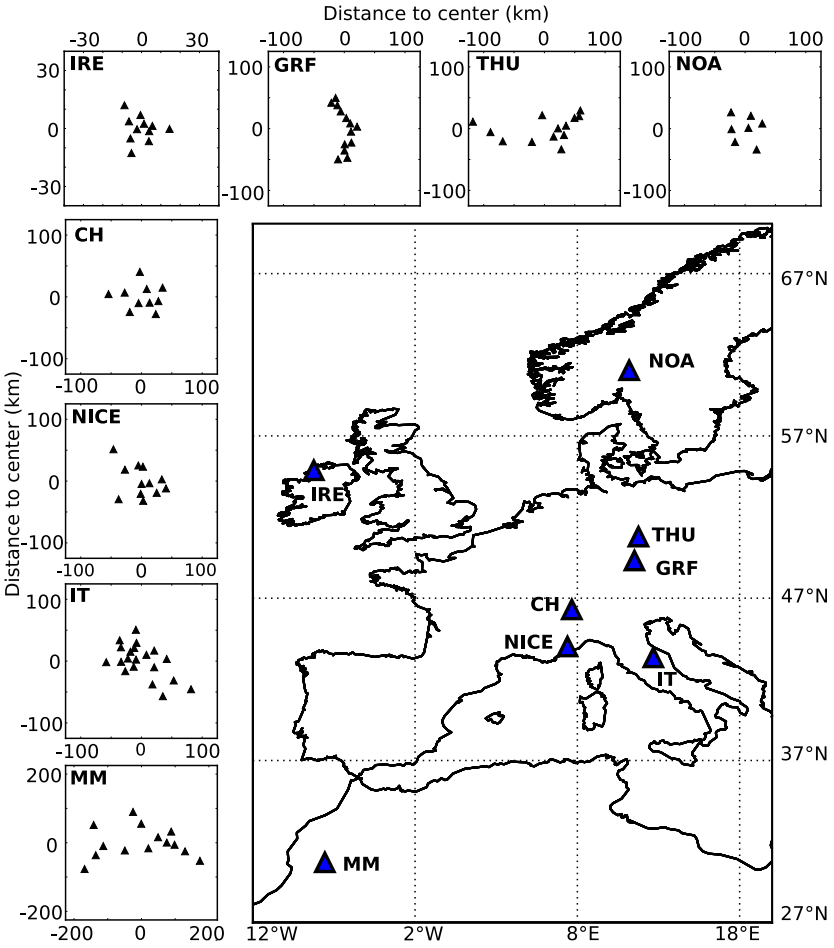

Figure 3.1: Center locations (triangles in map) and geometries of arrays used in this study.

For the analysis of microseisms in 2013, the data was corrected for instrument response, bandpass filtered between 0.25 Hz and 0.04 Hz and down sampled to 1 Hz.

3. WHERE DO OCEAN MICROSEISMS COME FROM? A STUDY OF LOVE-TO-RAYLEIGH WAVE RATIOS

The 3-component velocity seismograms were split into non-overlapping time segments of 1024 seconds using a Tukey window. The influence of earthquakes was reduced by the applications of an Short Time Average over Long Time Average (STA/LTA) filter, discarding time segments for which the vertical component data had a higher average power than twice the day average. For these processing steps we made use of the ObsPy toolbox [Beyreuther et al., 2010]. We use a 3-component beamforming method [Esmersoy et al., 1985] in the frequency domain to distinguish differently polarized waves, and to obtain estimates of the beampower, backazimuth and slowness of incoming coherent signals in the ambient noise field. The 3-component formulation was described in detail by Riahi et al. [2013] and is analogous to single component beamforming. The beamforming approach is briefly summarized here.

For a N-station array, the 3-component, classical plane wave frequency wavenumber beampower estimate as a function of polarization ρ, frequency f, backazimuth θ and slowness u can be written as:

$$P(f,\theta,u,\rho) = \frac{1}{N^2}\mathbf{w}_{3N}^{*}(f,\theta,u,\rho)\mathbf{R}_{3N}(f)\mathbf{w}_{3N}(f,\theta,u,\rho), \tag{3.1.1}$$

where $\mathbf{R}_{3N}(f)$ represents the temporally averaged cross-covariance matrix of the 3-component data Fourier transforms, here $*$ indicates the conjugate transpose operator. The weight vector is given by

$$\mathbf{w}_{3N} = [p_x e_1, \ldots, p_x e_N; p_y e_1, \ldots, p_y e_N; p_z e_1, \ldots, p_z e_N]^T. \tag{3.1.2}$$

It contains the phase delays for each sensor due to wave propagation in the N-component vector $\mathbf{e}_N$ and the amplitude factors and phase delays for each component due to the polarization in the 3-component vector $\mathbf{p}_{xyz}$. The cross-covariance matrix is temporally averaged over four consecutive time windows, giving approximately hourly beampower estimates. Fundamental mode Rayleigh waves are assumed to be retrograde polarized, with varying ellipticity angle. Love waves are assumed to be purely transversally polarized. For both, Rayleigh and Love type polarization, we search through a parameter space of slowness in 0.02 s/km steps and backazimuth in 2 degree steps. For Rayleigh waves we additionally test for the ellipticity angle in steps of 10 degrees. The beamformer response represents the beampower estimate as $P(f,\theta,u,\rho_L)$ of the transversal component T^2 for Love waves and $P(f,\theta,u,\rho_R)$ of the vertical and radial component $R_z^2 + R_r^2$ for Rayleigh waves.

Method Performance and Resolution

Since the availability of individual stations varies throughout the measurement period (i.e. data gaps for certain stations), the array geometry changes accordingly over time. The array transfer function is dependent on the array geometry, hence it fluctuates with station number. Further, the array transfer function indicates the resolution capability of an array and potential risk of wrongly determined signal parameters due to side-lobes. To maintain both a stable array transfer function and a good temporal observation coverage, we defined a threshold number for each array, above which the beamforming result is included. A table, detailing the threshold, the maximum and the average station number per array is provided as supporting information S1.

For each array we analyzed the availability of individual stations throughout the year. The operational duration for each station configuration above the threshold number was determined. Figure 3.2(a) shows the array transfer functions for an incoming plane wave with zero slowness at a period of 8 seconds, using the array configurations with maximum operational duration in the analysis above, i.e. configurations which were most frequently available. In the usual case for microseisms, the presence of multiple signals, the propagation parameters and beampower of the signals were shown to be practically retrievable if the number of stations in an array is large enough and if the signals propagation parameters are not too closely related (for more details see [e.g., Poggi and Fäh, 2010]). Due to the different array geometries, the beamformer capability to separate co-existing signals varies with the arrays used here. We use a synthetic dataset to test the capability of the 3-component beamforming algorithm to distinguish between Love and Rayleigh waves for the different arrays used here. Moreover, we investigate to what extent the relative signal strength for each wavetype is recovered in the presence of additive unpolarized noise. The synthetic 3-component data consists of the superposition of a retrograde polarized Rayleigh wave, a transversally polarized Love wave and unpolarized additive noise in the time domain. We use single-period signals, and set the total data length to three times the synthetic signal period considered, (e.g. at a signal period of 8 seconds). The surface wave signals are plane waves of uniform amplitude. The phases between the wavetypes are uncorrelated. Two unpolarized noise signals with random values for slowness, direction and initial phase from a Gaussian distribution and a total amplitude of either 0.5 or 1.0 were equally distributed over the three components. For each test, 60 realizations of the synthetic dataset were calculated.

Figure 3.2(b) shows the performance test for the array geometries of GRF and IRE at a period of 8 seconds. For each wavetype, the mean of the 60 individual beam-

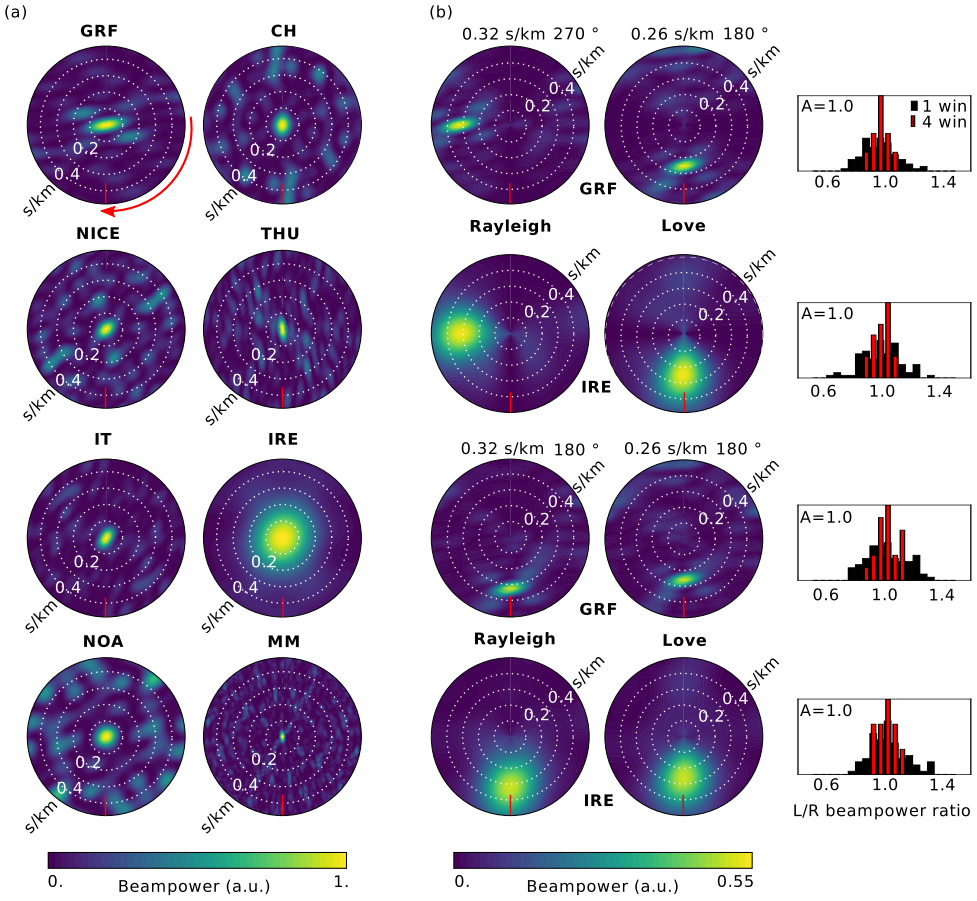

Figure 3.2: (a) Slowness vs. backazimuth (clockwise) representations of the response functions of the arrays used at a period of 8 s. (b) Beamformer performance test for the array geometry of GRF and IRE with a synthetic data set at 0.125 Hz. Data consists of one Love and one Rayleigh wave polarized plain wave of uniform amplitude from (top) different source directions and (bottom) same source direction and two additive uncorrelated noise signals with a total amplitude of $A = 1.0$. The polar graphs show the average beampower output for each wavetype. Labels above indicate backazimuth and slowness of synthetic signals. The histograms show the spread of the wavetype beampower ratio for single time windows (black thick bars) and for averaging over 4 consecutive time windows (red thin bars). A backazimuth of 180 degrees is marked by a red dash.

former outputs is plotted, along with the distributions of the Love to Rayleigh wave ratios. We consider two cases: when the Rayleigh and Love waves are coming from the same direction, and when the wavetypes' angles of approach are perpendicular to each other. For both additive noise level amplitudes, the correct backazimuth and slowness values are obtained. The wavetype ratios are distributed around the correct ratio of

1.0, but may be spread out considerably for the higher noise level case. Averaging the cross-covariance matrix over four time windows before beamforming, as applied in our data analysis, decreases the spread considerably. Since we are interested in average properties here, the 3-component beamforming analysis should recover a satisfactory approximation of the average wavetype ratio, when considering only the strongest signals observed. We further tested the wavetype ratio recovery in the synthetic test using the minimal number of station configurations. Also in this case, the expected ratio could still be retrieved on average (cf. Figure S2 in the supporting information).

In order to minimize the number of mis-detections, we discard beamforming results that do not match the expected surface wave phase velocity range. Therefore, we determine average local dispersion curves for Love and Rayleigh waves at each array by performing beamforming for a finer slowness spacing ($0.005\ \frac{s}{km}$) over a few months. Figure 3.3(a) shows examples of self-normalized yearly median beampower spectral density over backazimuth and slowness, determined at periods of 7 and 14 seconds. For the three arrays shown here, the directions of approach of Love waves correspond to distinct backazimuths which are often similar to those of Rayleigh waves. However, the relative wavetype strength varies for different source directions, which is especially obvious for the THU array at a period of 14 seconds and the GRF array at a period of 7 seconds. For each time window and each frequency, the slowness corresponding to the maximum of the beamformer power is selected. The slowness picks, summed over the course of up to three months are normalized and three examples are plotted in figure 3.3(b). We aim to restrict our analysis to fundamental mode surface waves. However, the dispersion plots for the GRF array and especially the Love wave result for the THU array indicate a frequent occurrence of signals of higher phase velocity than the emerging fundamental mode branch. Those were hence muted for the purpose of our analysis. The dispersion curves are then retrieved as a smoothed version of the mean slowness at each frequency $\overline{u}(f)$. We also determine the standard deviation $\sigma_u(f)$ of the slowness distribution at each frequency. In the remainder of this analysis, we reject beamformer results outside the slowness range $\overline{u}(f) \pm \sigma_u(f)$ to improve the separation between random and polarized noise and to confine our analysis to fundamental mode observations.

Signal Source Directionality

We use the outlined beamforming method to decompose the ambient noise field into Love and Rayleigh wave polarized signals. We are interested in spatial and directional

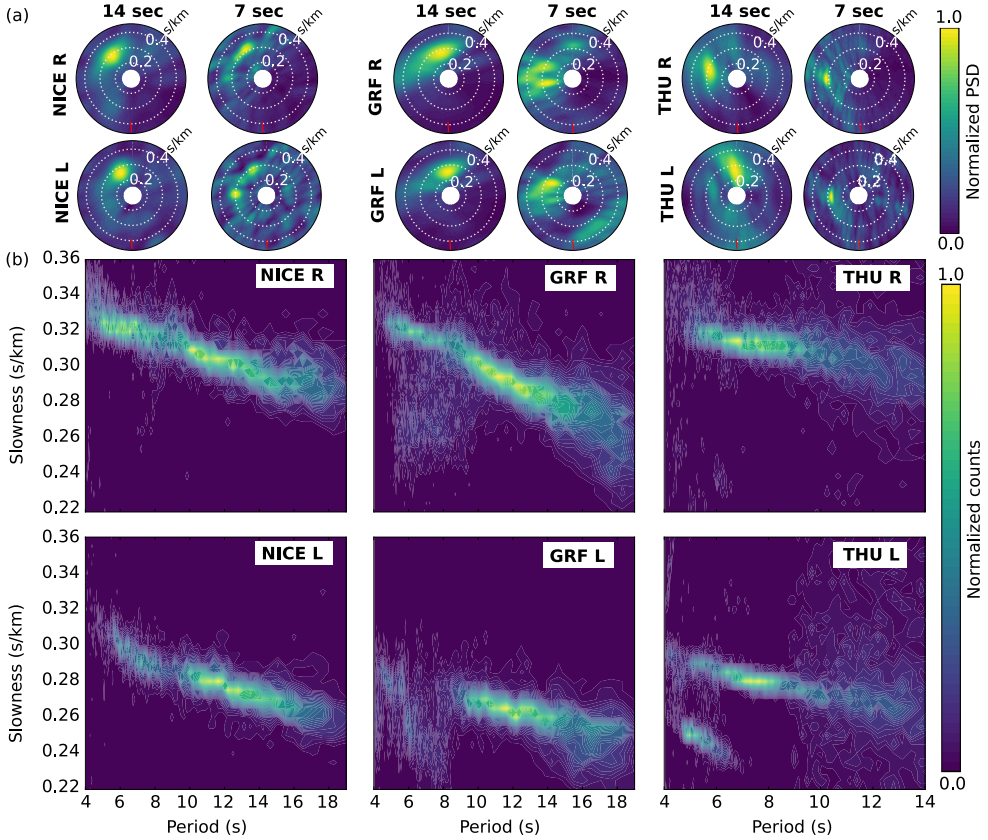

Figure 3.3: (a) Slowness vs. backazimuth representations of beamforming results for Rayleigh and Love waves at NICE, GRF, and THU. (b) Examples of frequency dependent slowness at the corresponding arrays.

characteristics of the surface wave noise composition. For each time segment and frequency bin we determine the backazimuth corresponding to the maximum beampower of Love and Rayleigh wave polarized signals, respectively, which fulfill the slowness range criteria. A number count histogram of the entire year results is collected with azimuthal bins of 6 degrees.

Figure 3.4 shows the radial histogram plot of the dominant surface wavetype observations over backazimuth for all array sites, averaged over the primary (13–15 seconds) (a) and the secondary (5–7 seconds) (b) microseism peak. The radial axis shows normalized counts per direction within backazimuth bins of 6 degrees.

The primary microseism Rayleigh wave noise in Europe most frequently originates from northern and north-western backazimuths, pointing towards the coast of Norway and the British Isles. Both these regions are are well known to be the origin of some of the stronger microseismic signals in Europe Friedrich et al. [e.g., 1998]. This correlates

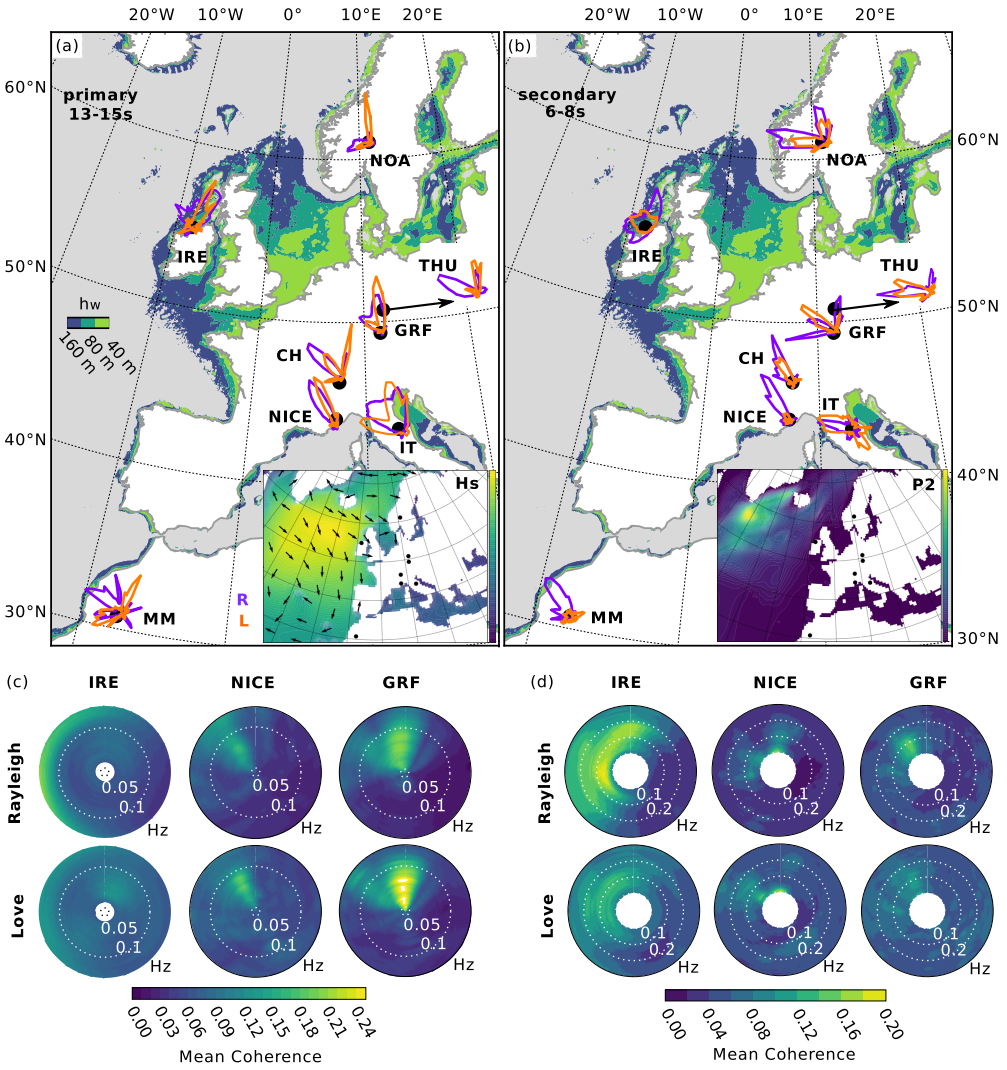

Figure 3.4: Yearly wavetype source direction counts in 2013 at different array sites around the primary (13–15 s) (a) and secondary (6–8 s) (b) microseism peak (per array, same scale for each wavetype). For the period range considered, intermediate water depths (h_w) are indicated by colored contour levels in the map. Yearly averaged wavetype coherence over backazimuth and frequency for the primary (c) and the secondary (d) microseism range in 2013. Insets (a): average significant wave height and most frequent mean ocean wave directions in 2013. The color scale ranges from 0 to 4 m. Inset (b): average wave-wave interaction induced surface pressure in 2013 as provided by ([Ardhuin et al., 2011]). The color scale ranges from 0 to 10^8 Pa^2m^2s.

well with average ocean wave parameters in 2013. As shown in the inset of figure 3.4 (a), the western European coasts are exposed to high average ocean wave heights.

In comparison to Rayleigh waves, dominant Love waves noise contributions from the north are even more frequent. Towards the southern array sites, contributions from the Atlantic coast and British Isles region more equally dominate for both wavetypes.

At the NOA array, which is located nearby the Norwegian source regions, preferred source directions of Love and Rayleigh waves differ clearly. The north African array MM shows a comparable pronounced difference between both wavetypes. Rayleigh waves are mainly observed from the coast directly to the north-west, while Love waves originate from more northern and south-western backazimuths. Generally, the directional spread in the Love wave backazimuths is smaller than for Rayleigh waves.

In the secondary microseism band, Rayleigh wave observations outnumber the occurrence of coherent Love wave observations. The most frequent dominant noise contribution for Rayleigh waves corresponds to backazimuths pointing towards the North Atlantic, the British Isles region and offshore Norway. This is in agreement with observations by [e.g., Essen et al., 2003; Friedrich et al., 1998; Kedar et al., 2008; Kimman et al., 2012], who find strong microseismic Rayleigh waves from the same regions. Furthermore, these observations correlate with the locations of high average wave-wave interaction induced secondary surface pressure in 2013 (inset of figure 3.4 (b)).

The directions of approach of dominant Love waves correspond to distinct backazimuths, which are similar to those of Rayleigh waves. However, at central European sites the relative occurrence frequency for particular source directions differs between Love and Rayleigh waves. At GRF, THU, CH and NICE, most frequent dominant Love wave contributions are commonly observed from north-western backazimuths, in the direction of the British Isles and the North Atlantic, while contributions from the remaining backazimuths are weaker on average. The occurrence of Love waves seems to always be accompanied by Rayleigh waves from similar directions. On the other hand, backazimuths exist from which Rayleigh wave occurrence dominates. Which means that the observation of Love wave signals, unambiguously meeting our detection criteria, is less frequent, i.e. if present they are obscured by background noise for our beamformer. For Love waves, the range of source directions is generally broader compared to Rayleigh waves. Since average ocean wave periods in the Mediterranean sea are relatively short, in addition to the secondary microseism, we expect to also observe microseisms generated by primary source mechanisms for periods of 5–8 seconds at e.g. the Italian array (IT).

For a comparison between source directions of both wavetypes across the whole frequency range of interest we look at the temporally averaged wavetype coherence within the expected surface wave velocity range in dependence on backazimuth and frequency as depicted for the arrays IRE, GRF and NICE in figure 3.4(c) and (d).

Here, the coherence for Love waves is given by the ratio between the beampower and the horizontal component power (X^2+Y^2) averaged over all array stations, respectively for Rayleigh waves as ratio between beampower and 3-component power ($X^2+Y^2+Z^2$) averaged over all array stations. In both microseism bands the source directions of persistent wavetype signals agree well across the whole frequency range analyzed.

A more detailed comparison of the time-dependent behavior of Love and Rayleigh waves is given in figure 3.5, which shows the frequency dependent dominant signal backazimuths (color scale) of each wavetype over a period of two months, from February to March 2013. Shown are the observations for the arrays in Ireland (IRE) and in central Europe (GRF). White gaps indicate periods of rejected or missing data. When visually comparing the two plots in figure 3.5(a), we find a high similarity of temporal and spectral variations between Rayleigh and Love wave source directions in the primary microseism range at GRF (approximately 8–20 s). Frequently, both wavetypes are jointly observed from northern (red colors) and western to north-western backazimuths (blue and pink colors).

In the secondary microseism range (below approximately 8 s) dominant signal backazimuths for both wavetypes at IRE show strong similarities (cf. figure 3.5(b)). At the GRF array, which is located further away from strong secondary noise sources, differences in dominant source directions are visible. For instance, during coherent Rayleigh wave noise observations from northern backazimuths, the Love wave noise is rarely dominated by signals from corresponding directions (areas in plot indicated by black rectangles in figure 3.5(a)).

Wavetype Ratio Directionality

The differences in source directionality between dominant signals of both wavetypes indicates that the Love to Rayleigh wave ratio must also be directionally heterogeneous. In order to investigate the directional dependence of the Love to Rayleigh wave ratio in detail, we determine beampower ratios for specific source directions. We select directions for which the strongest signal of both wavetypes is observed simultaneously (time segment of approximately 1 hour) from a common source backazimuth range of 20 degrees. For signals meeting those criteria, we calculate the wavetype ratio using the maximum beampower of both wavetypes and allocate it to the mean backazimuth of both. Possible propagation path deviations and travel time differences from the source are assumed to be accounted for by the chosen time and backazimuth range.

Since the beampower ratio corresponds to a measure of surface amplitudes, the ratio determined in this way is affected by the local subsurface structure. Since the

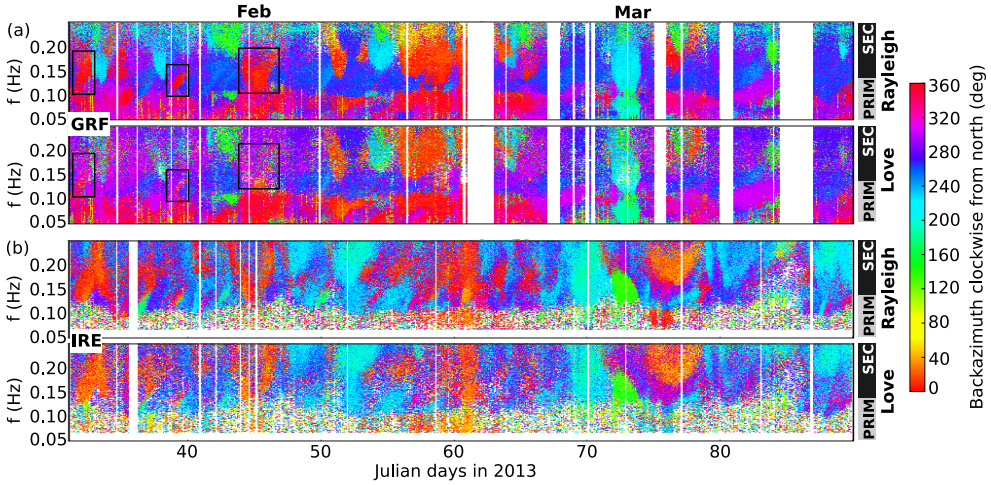

Figure 3.5: Frequency dependent signal backazimuths (color scale) of both wavetypes from February to March 2013, comparison of measurements at the arrays GRF (a) and IRE (b). White areas correspond to periods of missing or rejected data. Black rectangles indicate the observation discussed in section 3.1.

subsurface structure varies from array to array, a direct comparison between beampower ratios at the different sites is inaccurate. In a second step, we therefore estimate the ratio between Love wave and Rayleigh wave kinetic energy density (E_L, E_R respectively) [e.g., Harkrider and Anderson, 1966] under consideration of the local structure at the array sites.

Here, at each frequency the kinetic energy density ratio is given by

$$E_L/E_R = \int_0^{z'} \rho T(z)^2 dz \left(\int_0^{z'} \rho (R_z(z)^2 + R_r(z)^2) dz \right)^{-1} . \tag{3.1.3}$$

The eigenfunctions for the local velocity structure are denoted by $T(z)$ for Love waves and $R_z(z), R_r(z)$ for vertical and radial Rayleigh wave displacement respectively and were calculated with the software package by Herrmann [2013]. They are scaled such that their ratio at the surface corresponds to the measured wavetype ratio.

A comparison of our dispersion curve measurements and theoretical dispersion curves from the reference velocity model CRUST1.0 [Laske et al., 2013] at grid points near our array centers show deviations that are not negligible especially for periods below 10 seconds. We retain the P-wave velocity profile, the density profile and the layer geometry from the CRUST1.0 model. For Rayleigh and Love waves separately, we use our corresponding fundamental mode dispersion curve measurements to invert for the anisotropic S-wave velocity in the shallow crust using *geopsy* [Wathelet, 2008].

Since the kinetic energy density ratios are sensitive to variations in the assumed velocity structure, we analyze the changes in the velocity profiles due to changes in the dispersion curve measurements. Therefore, we also determined the S-wave velocity profiles at both uncertainty limits of the considered dispersion curve slowness range $\overline{u} \pm \sigma_u$.

Figure 3.6 shows the resulting direction dependent kinetic energy density ratios and their uncertainty ranges in gray, smoothed with a moving backazimuth window of 30 degrees for the primary (13-15 s) (a) and secondary (6-8 s) microseism peaks.

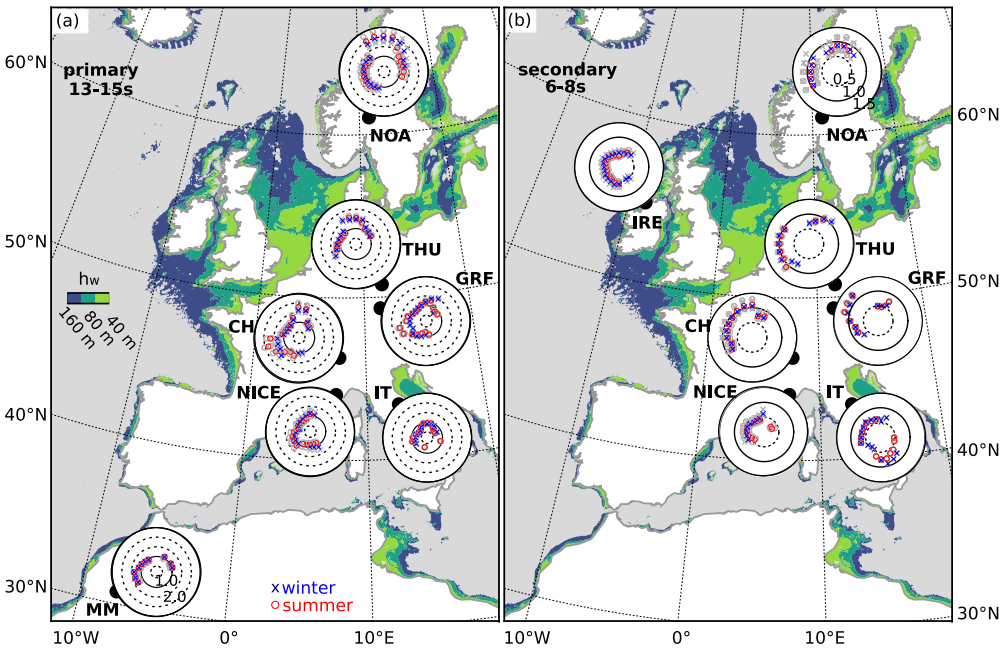

Figure 3.6: Direction dependent average summer (Apr – Sep, circles) and winter (Oct – Mar, crosses) Love/Rayleigh wave kinetic energy density ratios for (a) the primary (13–15 s) and (b) the secondary (6–8 s) microseism peak. The gray symbols show ratio uncertainty ranges corresponding to velocity structure deviations according to the dispersion curve standard deviation range.

In the primary microseism band, most arrays show a pronounced directional variation of the wavetype ratio. For the central European arrays (CH, GRF, IT, NICE, and THU), the largest ratios are commonly found for northern and south western backazimuths. At NOA, the azimuthal heterogeneity is most prominent. In almost all cases, Love waves dominate with ratios larger than one on average.

Secondary microseism ratios show less directional dependence at most array sites. However, at central European arrays (THU, GRF, CH) the ratio peaks towards northwestern backazimuths, corresponding to the directions of highest noise occurrence in

figure 3.4(b). Kinetic energy ratios in the secondary microseism vary with array site and direction between about 0.4 and 1.2. At both microseism peaks, the wavetype ratio direction pattern remains considerably stable between the summer and winter period.

Seasonality

Figure 3.7(a) shows a full year spectrogram of the vertical component seismograms averaged over the array GRF. The higher amplitudes in the secondary and lower amplitudes in the primary microseism are apparent. Moreover, the well known seasonal variations in noise amplitudes in both microseism bands are clearly present [Stutzmann et al., 2009]. In comparison, figure 3.7(b) and 3.7(c) show the spectrograms of the ratio between array averaged horizontal to vertical component seismograms (H/V) and of the ratio between maximum Love to Rayleigh wave beampower (L/R) at GRF, respectively. White lines in (a)–(c) mark discarded periods either due to the minimum number of station criterion as explained in section 3.1 or due to the STA/LTA rejection criterion as explained in section 3.1. In (c) white gaps further correspond to frequencies at which beamforming result were rejected due to the slowness range criterion as given in section 3.1.

On a seasonal scale, we observe a decrease of the H/V ratio (b: darker colors) in the secondary microseism band during Northern Hemisphere summer months. This decrease in H/V ratio does most likely not correspond to a seasonal variation in ratio of coherent Love and Rayleigh wave noise as we do not observe a significant simultaneous alteration in (c). By analyzing the P-wave beamform results (see Figure S3 provided in the supporting information), we notice an increase in P-wave noise levels arriving from southern backazimuths during summer, contributing to the vertical power spectrum. Such P-waves could be likely attributed to strong distant storms, as observed by Gerstoft et al. [e.g., 2008]; Zhang et al. [e.g., 2010]. The observation would also be in agreement with the expected dominance of P-wave noise over Rayleigh wave noise with increasing distance due to lower attenuation at secondary microseism frequencies, as observed by Landès et al. [2010] and expected from modeling results [Ardhuin and Herbers, 2013]. Therefore, we attribute the variation in figure 3.7(b) to the relative increase in P-wave noise compared to Rayleigh wave noise. However, Tanimoto et al. [2006] also showed the possible relation between seasonal H/V ratio variations and differences in the modal content connected to seasonally changing source regions depths. As our analysis is limited to coherent signal observations of the fundamental mode surface waves, a potential relative variation in modal content or incoherent (weak) signal ratio can not be resolved.

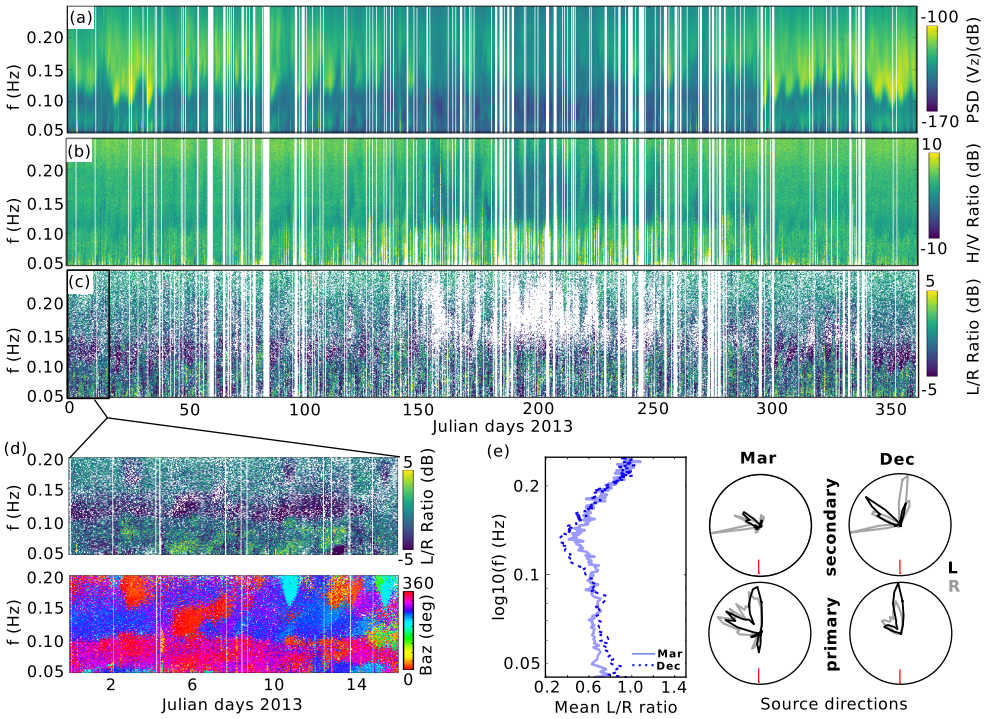

Figure 3.7: Seasonal variation at GRF of the array averaged vertical component power spectral density (a), array averaged horizontal/vertical components power spectral density ratio (b), and Love/Rayleigh wave beampower spectral density ratio (c). Short term comparison (d) of Love/Rayleigh wave beampower spectral density ratio (top) and corresponding source directions of Rayleigh waves (bottom). Directionally averaged beampower spectral density ratio variation for different months, corresponding to different source directions being active (polar plots, right hand panel) (e).

As the zoom into the wavetype ratio shows (d), a variation in ratio on short time scales (hours/days) is clearly visible and correlates well with noise arrivals from varying backazimuths. When considering directionally averaged wavetype ratios of simultaneously observed wavetypes, as in figure 3.7(e) for one months periods in spring and autumn, we observe a variation in wavetype ratio with time. We also plot the corresponding source direction occurrence of both wavetypes during the same time periods. We notice a clear temporal variations in relative contributions from different source areas in both microseism bands. As we observed a temporally stable azimuthal wavetype ratio pattern in figure 3.6, the directionally averaged wavetype ratio variations can be attributed to a varying contribution of source areas with time.

The most pronounced spectral attribute in figure 3.7(c) and 3.7(e) is the distinct step in ratio between the primary to secondary microseism frequencies around 0.1 Hz.

This was also observed by others [Friedrich et al., 1998; Nishida et al., 2008] and clearly hints at different capabilities of the source mechanisms to generate Love waves in the primary and secondary microseism band.

Discussion

Primary Microseisms

The analysis of the average properties of surface waves in the microseismic noise field once more showed the different proportions of Love waves in the primary and secondary microseism band. For the primary microseism band, the main findings can be summarized as such:

1. Love waves were found to dominate the coherent noise field on average.
2. Further, common noise source directions were observed on average for both wavetypes, but with clearly different relative occurrence frequency (fig. 3.4(a)).
3. The difference in directivity of the wavetype strength is also supported by the observed directional dependence of Love to Rayleigh wave ratios (fig. 3.6(a)).
4. The directional pattern of the wavetype ratio exhibited low seasonal variations.

While local crustal heterogeneity and anisotropy could also cause directional ratio variations, the stability of the directional pattern across Europe and the magnitude of the ratio variability makes a dominance of these contributions unlikely. Therefore, the cause of the directional ratio pattern is likely related to the source mechanism.

The primary microseism is commonly believed to be generated in shallow water at water depths (h_w) of much less than the ocean wave wavelength (λ_w), e.g. $2\pi h_w/\lambda_w \ll 1$ [Hasselmann, 1963]. At the primary peak, this would mainly correspond to the region within the shallowest depth contour in fig. 3.4 and fig. 3.6.

Two source mechanism types are proposed to explain horizontal component seismic noise generation. Ocean gravity waves in shallow water could generate shear tractions either

1. directly, due to friction between the ocean wave particle motion and the seafloor [Friedrich et al., 1998] or as the water propagates over sea-floor topography as described in [Fukao et al., 2010; Saito, 2010], or

2. indirectly, as the water propagates over inclined topography, pressure sources generated during shoaling also lead to a horizontal force component proportional to the sea-floor slope Ardhuin and Herbers [e.g., 2013]; Hasselmann [e.g., 1963].

This mechanism was shown to be capable of describing observed noise levels of the vertical hum [Ardhuin et al., 2015].

Individually occurring, these source mechanisms would generate both Rayleigh and Love waves at approximately the same location. We would therefore expect to observe both wavetypes from similar directions in general. However, the relative amount of Love or Rayleigh waves generated would be different for each mechanism: the first type would be expected to generate more Love waves than the second. This means that the observed wavetype ratio could depend on source mechanism. Moreover, the radiation pattern of each wavetype will be different: given water waves propagating perpendicularly towards the coast, Rayleigh waves radiate either symmetrically or most strongly towards onshore, while Love waves radiate along shore [e.g., Ardhuin et al., 2015; Friedrich et al., 1998]. Therefore the wavetype ratio observed at a certain position also depends on the respective radiation pattern, and an observation of high amplitude Love waves noise is more dependent on an appropriate array position.

In general, at all array locations, we observe high portions of Love waves, with similar average source directions as the Rayleigh waves. This strongly supports the hypothesis of a significant contribution by excitation mechanisms that primarily induce a horizontal force, e.g. a shear traction source type. Mainly coinciding source directions, and a dominance of Love waves were also observed for Japan by Nishida et al. [2008], who suggested a shear traction as the common source of primary microseisms.

Friedrich et al. [1998] stated that the primary microseisms are likely generated by multiple source mechanisms simultaneously, that dominate in slightly different areas. Hence, source directions can be expected to agree in general but deviate in detail. This is supported by our observations at several arrays, as well as by Friedrich et al. [1998], where the azimuthal range of incident noise directions appeared to be broader for Rayleigh waves than for Love waves (fig. 3.4(a)). In a different study, Matsuzawa et al. [2012] observed moderately differing source directions for both wavetypes when tracking a strong storm near the Norwegian coast. The authors conclude that the wavetypes are generated by different source mechanisms, at similar, but not identical locations. Pronounced differences in most frequent source directions for both wavetypes were reported for New Zealand by Behr et al. [2013], who also suggested different generation areas for the wavetypes. However, concerning the differences in source directions in all studies, this observation could also partly reflect the effect of the different radiation patterns, as described above.

When looking at directionally averaged wavetype ratios of the strongest noise signals, we observed a temporal variation, which could be attributed to varying importance of different source areas due to seasonal variations in swell (fig. 3.7). The strongest seasonal ratio variations were observed at CH and GRF for south western directions (fig. 3.6(a)). During spring, ocean swell frequently propagated southwards onto the north coast of Spain, causing a large number of high Love to Rayleigh wave ratio observations at these arrays. The generally seasonally stable azimuthal ratio pattern suggests that the proportions of the wavetypes are largely independent of the seasonally varying wave height levels.

A more quantitative estimation of theoretical wavetype ratios would be needed to resolve the relative importance of each individual source mechanism. One must keep in mind that a simultaneous acting of several generation mechanisms and the influence of the propagation path should be taken into account.

Secondary Microseisms

For the secondary microseism band, the main findings can be summarized as such:

1. Rayleigh waves were found to dominate the coherent noise field on average.
2. The wavetype ratio shows little directional dependence.
3. The directional pattern of the wavetype ratio exhibited low seasonal variations.
4. An increase in Love to Rayleigh wave ratio was found for specific source directions in central Europe.

The seismic velocity models used for kinetic energy density calculations are less well constrained at shallow depths. Therefore, the uncertainty on the exact ratio levels is higher at secondary microseism periods than for the primary microseism range. At most sites, wavetype ratios generally show little azimuthal dependence, with the exception of array sites in central Europe (fig. 3.6(b)). These arrays exhibit an increase in Love to Rayleigh wave ratio for backazimuths that coincide with directions of noise observations which often have higher phase velocities than the fundamental mode.

Dispersion curve results for the central European array THU indicate the presence of a higher Love wave mode in the noise field (see fig. 3.3). Resulting velocities fit well to values of the first higher mode from our local velocity structure estimation, which was retrieved from the fundamental mode dispersion curve only. Fig. 3.3 does not necessarily show higher modes of Rayleigh waves. Moreover, an examination of dispersion curves from vertical and radial component beamformer results (not shown

here) did not give a clear indication of their presence. While higher phase velocities were measured at GRF (fig. 3.3), they appear to be scattered and generally remained below the expected value of higher modes of either wavetype.

The presence of higher mode surface waves in the microseismic noise field has been observed previously. For instance, Kimman et al. [2012] used an array in the Netherlands to detect fundamental and first higher mode Rayleigh waves in the secondary microseisms, with source directions pointing towards the north-west (British Isles).

Although an effort was made here to measure the ratio properties of the fundamental modes only, a possible mixture of modes or different signals with similar propagation parameters in the beamforming can not be fully excluded here.

Despite these uncertainties, coherent Rayleigh wave observations can be measured at all the array sites. In some cases, the main Rayleigh wave directions are only weakly accompanied by coherent Love waves (fig. 3.5). Whenever coherent Love wave source directions were detected, they were found to generally coincide with those of Rayleigh waves (fig. 3.4(b)). Still, in the secondary microseism band, the coherent noise field is dominated by Rayleigh waves on average. The amount of coherent Love wave measurements is clearly lower, yet considerable, with wavetype energy ratios ranging from about 0.4 to 1.2 (fig. 3.6(b)) within the range of uncertainty.

The clearly lower wavetype ratios in the secondary microseism range, along with the lack of directional dependence in wavetype ratio, especially observed near coasts, reflects the difference in relevant source mechanisms compared to the primary microseism band. The dominance of Rayleigh waves in the coherent secondary microseismic noise field was also obtained by Friedrich et al. [1998] and Nishida et al. [2008]. Moreover, it is in agreement with the commonly accepted pressure type source mechanism of opposing ocean waves in deep water ($2\pi h_w/\lambda_w \gg 1$), even if this mechanism does not explain any direct excitation of Love or SH waves [e.g., Ardhuin and Herbers, 2013; Hasselmann, 1963; Longuet-Higgins, 1950]. Since the noise field measured in central Europe has propagated across changing continental crust, an alternative explanation for the azimuthal Love to Rayleigh ratio variations could be wavetype conversion along the propagation path, e.g. at the continental margin [Gregersen and Alsop, 1976]. The structural properties along the path can also influence the Love to Rayleigh wave ratio significantly, by altering the amplitudes of Love waves differently than those of Rayleigh waves or even inhibiting Love wave propagation [e.g. Rind and Donn, 1979]. Similar to the primary microseism band, the azimuthal wavetype ratio pattern does not exhibit much seasonal variation (fig. 3.6), even for the central European arrays with azimuthal ratio variations. Since source regions are not necessarily stationary throughout the year, this would suggest that the coherent wavetype ratio does not primarily depend

on the location of the source, but rather on permanent conditions between sources and receivers. Another possibility would be that we are unable to measure ratio variations due to source location changes since nearby source areas might dominate our results throughout the year.

Conclusion

We systematically compared Rayleigh and Love wave characteristics for one year of ocean microseisms across Europe. We found relatively stable azimuthal patterns of the Love to Rayleigh wave ratio. The directional dependence of the wavetype ratio is stronger in the primary microseism band, where Love to Rayleigh wave ratios vary between 0.6 and 2.0. The strong directional dependence is likely caused by the different radiation patterns of the wavetypes. The high relative Love wave content hints to the presence of source mechanisms that generate strong horizontal forces.

For the secondary microseism band we find that the source directions for both wavetypes mainly coincide. We observe little azimuthal dependence of the wavetype ratio, with the exception of Central European sites, where it varies between 0.4 and 1.2. Temporal variations of the directionally averaged wavetype ratio are observed, and correlate with changing contributions from different source areas.

A better knowledge of the source regions and corresponding wavetype ratios is desirable, in order to understand the spatial and physical origin of Love waves.

Acknowledgments

The data for all other arrays used here (GRF, IT, NICE, NOA, THU), can be freely accessed through the GEOFON data center at http://geofon.gfz-potsdam.de.
We thank Chris Bean for access to the Science Foundation Ireland (SFI) funded WaveObs array data from NW Ireland and Christine Thomas (University Münster for access to the Morocco Münster array data.) We also thank the group of Fabrice Ardhuin (Ifremer, Brest) for making their modeled ocean wave parameter data available. We are grateful to Kiwamu Nishida and Toshiro Tanimoto for useful discussions and comments. We wish to thank Oner Sufri and an anonymous reviewer for their support in improving this manuscript. This work was funded by the Emmy Noether program (HA7019/1-1) of the German Research Foundation (DFG).

End of original manuscript

3.2 Supplementary material

Introduction

For the arrays CH, GRF, IT, NICE, and THU the number of available seismic station varied over the time span analyzed in this study. The supporting information table S1 lists further information regarding the array configuration for these arrays. For arrays named in Table S1, the results of the Love to Rayleigh wave ratio recovery test, that was explained in section 3, were summarized in Figure S2 (a) and (b). The comparison between the test cases for N_{min} and N_{max} shows, that the allowed variation in array station configuration does not alter the performance in wavetype ratio recovery significantly. The seasonal variation of seismic noise signal characteristics in the primary and secondary microseism band was discussed in section 6. Figure S3 (a) shows the temporal and spectral variation of the strongest P-wave noise signal backazimuths for the full year 2013. In the 0.1–0.25 Hz frequency band we notice an increase in P-wave noise signal observations from southern backazimuths during summer. These noise observations correspond to high coherence values, which was calculated as the ratio between beampower and 3-component power ($X^2 + Y^2 + Z^2$) averaged over all array stations.

Table 3.1: S1: Summary of array configuration parameters: the maximum number of array stations available at any time N_{max}, the defined minimal number of stations N_{min} for the station threshold criterion, and the average number of available stations N_{av}. For all arrays not listed here, only the full array configuration was used.

Array	$\mathbf{N_{max}}$	$\mathbf{N_{min}}$	$\mathbf{N_{av}}$
CH	10	9	10
GRF	13	11	12
IT	19	13	15
NICE	11	8	9
THU	13	9	11

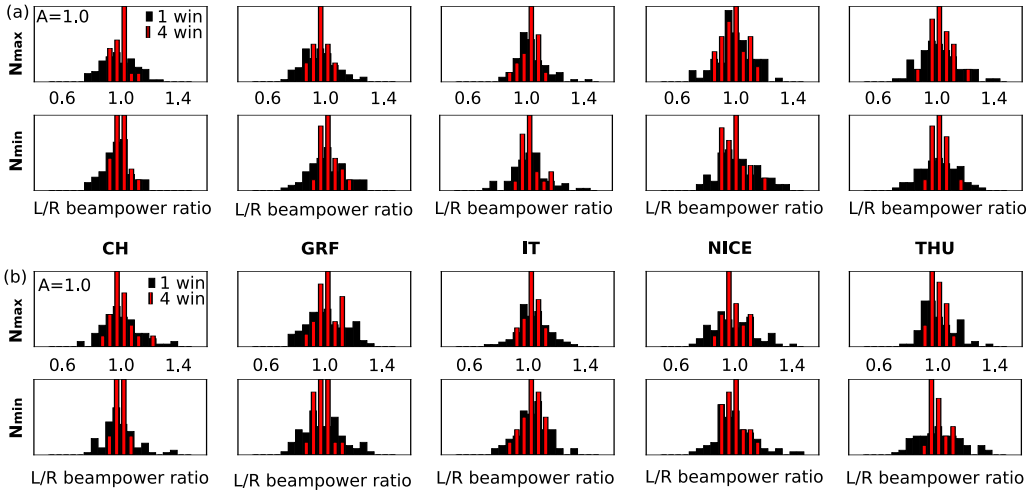

Figure 3.8: S2: Wavetype ratio histograms from the synthetic test for arrays with varying station configuration throughout the study: (a) with Love and Rayleigh waves propagating from different backazimuths as in fig. 2 (b) top; and with Love and Rayleigh waves propagating from the same backazimuth as in fig. 2 (b) bottom. N_{max} denotes the maximum number of array stations and N_{min} the minimum number of array stations accepted. In both cases the expected L/R ratio is one. Please note that the average number of available stations is generally better than the worst case scenario illustrated here (N_{min}).

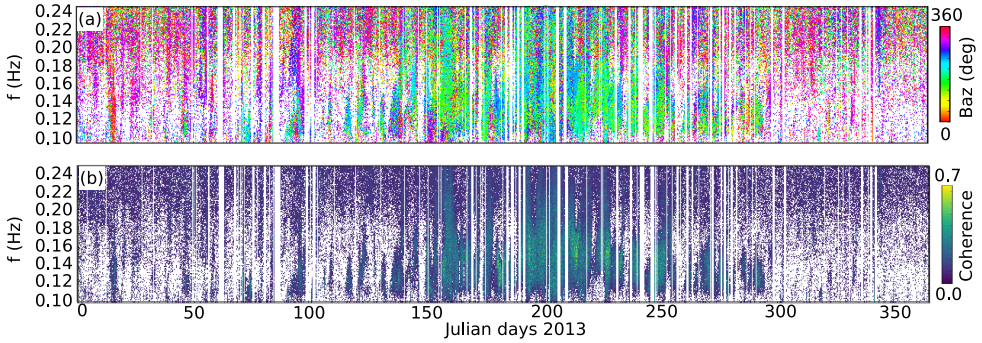

Figure 3.9: S3: Seasonal variation in 2013 at GRF of source directions for dominant P-wave noise signals (a) and of the corresponding P-wave signal coherence (b) given by the ratio between beampower and 3-component power ($X^2 + Y^2 + Z^2$) averaged over all array stations.

4

Linking source region and ocean wave parameters with the observed primary microseismic noise

In this chapter, primary microseismic noise characteristics are linked to relevant ocean wave parameters in the source region.

The theoretical framework of primary microseismic noise excitation from pressure variations generated by ocean surface waves propagating in shallow water covered the efficient excitation of mainly vertical component seismic displacement at the time of this study. Existing theoretical explanations for horizontal component microseismic excitation included the presence of bathymetry variations in shallow water.

However, seismic studies had indicated a comparable or even larger contribution of Love waves to the primary micoseismic noise field than that of Rayleigh waves. Analyses of primary microseimic noise as in chapter 3 had further shown that both wave types could be observed from similar source propagation directions but with varying Love to Rayleigh wave ratio at a variety of geographic locations.

In order to investigate the origin of such wave type ratio variations, the dependence of primary microseimsic noise on structural heterogeneity along the propagation path versus varying earth and ocean properties in the source region was studied here. Primary microseismic noise levels are known to correlate well with ocean wave heights at nearby shores, agreeing to a linear coupling of ocean gravity wave energy into seismic wave energy at the same period as predicted by theory [Haubrich and McCamy, 1969].

Therefore, a correlation study between noise amplitudes with ocean wave heights was performed here in order to study how primary microseismic noise source areas of Love and Rayleigh waves compare with each other. Beamforming was used to obtain the direction dependent ambient noise amplitudes in an initial step.

For the purpose of investigating the generation mechanisms of different wave types in the primary microseimic noise field, the relation between ocean wave height and seismic noise amplitude of both wave types was studied as a measure of noise generation effectivity in different regions. Moreover, the dependence of relative Love and Rayleigh wave noise generation effectivity on ocean gravity wave propagation direction and bathymetry was analyzed. These observations were complemented by synthetic tests on the possible influence of wave type dependent noise excitation and source radiation.

In this study, information carried by Love to Rayleigh wave ratios is exploited for evaluating the the reproducibility of observations with different primary microseismic noise source mechanism expectations. Results show a similar dependence of Rayleigh and Love wave noise amplitudes on ocean wave heights, hinting at a joint or coupled source mechanism for both wave types. Further, observed azimuthal variations in the wave-type ratio in this analysis suggest a regionally varying influence of different possible generation mechanisms, with a likely dependence on bathymetric conditions.

Section 4.1 includes the content of the manuscript as published and section 4.2 presents supplementary material to the publication.

4.1

Publication 2

Linking source region and ocean wave parameters with the observed primary microseismic noise

Carina Juretzek[1] and Céline Hadziioannou
1: Department of Earth and Environmental Sciences, Ludwig-Maximilians-University, Munich, Germany.

Status:
Published in Geophysical Journal International, 2017
DOI: https://doi.org/10.1093/gji/ggx388]

The following text resembles the original manuscript as submitted to the journal. Figure, equation and reference numbers were adapted to match the consecutive labeling of this thesis. All cited sources can be found at the end of this thesis in the bibliography.

Abstract

In previous studies, the contribution of Love waves to the primary micoseismic noise field was found to be comparable to those of Rayleigh waves. However, so far only few studies analyzed both wave types present in this microseismic noise band, which is known to be generated in shallow water and the theoretical understanding has mainly evolved for Rayleigh waves only. Here, we study the relevance of different source region parameters on the observed primary microseismic noise levels of Love and Rayleigh waves simultaneously. By means of beamforming and correlation of seismic noise amplitudes with ocean wave heights in the period band between 12 and 15 s, we analyzed how source areas of both wave types compare with each other around Europe. The generation effectivity in different source regions was compared to ocean wave heights, peak ocean gravity wave propagation direction and bathymetry. Observed Love wave noise amplitudes correlate comparably well with near coastal ocean wave parameters as Rayleigh waves. Some coastal regions serve as especially effective sources for one or the other wave type. These coincide not only with locations of high wave heights but also with complex bathymetry. Further, Rayleigh and Love wave noise amplitudes seem to depend equally on the local ocean wave heights, which is an indication for a coupled variation with swell height during the generation of both wave types. However, the wave-type ratio varies directionally. This observations likely hints towards a spatially varying importance of different source mechanisms or structural influences. Further, the wave-type ratio is modulated depending on peak ocean wave propagation directions which could indicate a variation of different source mechanism strengths but also hint towards an imprint of an effective source radiation pattern. This emphasizes that the inclusion of both wave types may provide more constraints for the understanding of acting generation mechanisms.

Introduction

Primary microseismic noise is known to be generated in shallow water by linear coupling of ocean gravity wave energy into seismic wave energy at the same period [Haubrich and McCamy, 1969]. Due to this direct coupling, noise levels are known to correlate well with ocean wave heights at nearby shores [e.g., Barruol et al., 2006; Bromirski, 2001] and are affected by the presence of sea-ice [Stutzmann et al., 2009] and tidal sea-level variations in the shallow coast regions [Beucler et al., 2015; Young et al., 2013]. Various authors investigated the possibilities to deduce short term local swell heights as well as long term variations of climate related ocean wave weather from seismic noise

amplitudes [e.g., Aster R.C. et al., 2008; Bromirski, Peter D. and Flick, Reinhard E. and Graham, Nicholas, 1999; Ebeling, 2012; Ferretti et al., 2013; Grevemeyer et al., 2000]. Recently, Ardhuin et al. [2015] made a detailed quantitative estimate of seismic noise levels due to pressure variations generated by ocean gravity waves propagating in shallow water in the presence of seafloor slopes, as proposed by Hasselmann [1963]. They found a good agreement between theoretical expectations and measurements of vertical component noise levels due to this mechanism in the primary micoseismic and the hum frequency bands.

A theoretical framework has mainly evolved for Rayleigh waves only. However, in previous studies, the contribution of Love waves to the primary micoseismic noise field was found to be comparable to or even larger than those of Rayleigh waves [e.g., Friedrich et al., 1998; Lin et al., 2008; Nishida et al., 2008]. Observations of the primary microseimic noise field showed that both wave types are generally observed from similar directions but with different azimuthal amplitude distributions at a variety of geographic locations [Behr et al., 2013; Juretzek and Hadziioannou, 2016; Poli et al., 2013]. This poses the question whether the directional wave type ratio variations arise due to structural influence along the propagation path or emerge in the source region. Since crustal heterogeneities become increasingly important for surface wave propagation towards higher frequencies, wave type conversions at e.g. continental margins [Gregersen, 1978] or along the propagation path [Kennett and Mykkeltveit, 1984], and scattering of Rayleigh waves at structural features with length scales of the order of the surface wave wavelength [e.g., Kennett, 1972] could be a possible explanation for the presence of Love waves in the microseimic noise bands. However, suggestions how Rayleigh and Love waves could be excited simultaneously by source mechanisms were made by [e.g., Friedrich et al., 1998; Fukao et al., 2010]. While the theoretical frameworks by Hasselmann [1963] and Fukao et al. [2010] focus on sources with effective isotropic seismic wave radiation, Saito [2010] and Friedrich et al. [1998] described how the presence of bathymetry structure could cause directive sources with different effective radiation patterns for both wave types, which can be dependent on ocean gravity wave propagation direction.

For the purpose of understanding the relevance of different parameters on the observed surface wave noise levels, we test the influence of different earth and ocean properties in the source region on the Love and Rayleigh wave noise strength. In this study we

1. resolve primary microseismic source areas of Love waves in comparison to Rayleigh waves by correlating seismic noise with ocean surface elevation and by array based

localizations,

2. measure the relation between ocean wave height and seismic noise amplitude of both wave types as a measure of noise generation effectivity at different locations,

3. compare the relative Love and Rayleigh wave noise generation effectivity in different source regions with different parameters such as ocean surface elevation, ocean gravity wave propagation direction and bathymetry.

Data and Seismic observations of primary microseismic noise

In order to investigate azimuthal variation in primary microseimic noise strength of both wave types, and to resolve source regions of Love and Rayleigh waves by noise observations at multiple locations, we use seismic array data and apply a frequency domain 3-component Capon beamforming based on Esmersoy et al. [1985] and explained by Riahi et al. [2013] in more detail. Here, we analyze noise signals on vertical, radial and transversal components. Our data set includes publicly available 3-component seismic data of permanent stations from the Norwegian Seismic Array (NOA), and from selected stations CH of the Swiss Seismological Service (SED; https://doi.org/10.12686/sed/networks/ch) over a time span of a full year in 2013 to capture effects of seasonal variations in noise generation. Additionally, we use data for the period from December 1, 2008 to February 28, 2009 from the temporary LAPNET/POLNET array [POLENET/LAPNET data set, 2012], in order to enhance the available azimuthal range of our observation locations with respect to the noise sources. From studies analyzing seismic noise properties during periods of several years, [e.g., Schimmel et al., 2011], we know that the average properties of microseismic noise are similar for the same season over different years. Therefore, we add this data set for a comparison between dominant source regions during e.g. Northern Hemisphere winter, when strong primary microseismic noise is generated in Northern Hemisphere oceans around Europe [e.g., Stutzmann et al., 2009]. Since there were many stations and the array covered a large area, we are able to divide the network into a northern and central sub-array, LAPN and LAPM respectively.

Using Obspy 1.0.2. [ObsPy, 2016] we apply standard processing steps, consisting of demeaning, linear detrending, bandpass filtering (4^{th} order Butterworth-Bandpass 0.04 – 0.25 Hz), resampling (1 Hz) and deconvolving the instrument response from the seismic data. The data was divided into windows of 512 s length with 50% overlap, and tapered with a Tukey window. We removed each time window which was dominated by highly energetic transients in the frequency range between 0.05 and 0.1 Hz, by defining

a STA/LTA variance ratio rejection threshold of 2 with a long-term average of one day. The cross-covariance matrix of the Fourier transformed velocity seismogramms is temporally averaged over 42 windows giving intervals of approximately 3 hours, which equals the sampling rate of the ocean wave parameter data used in this study. The number of data snapshots which form the average of the the cross-covariance matrix was large enough to obtain stable Capon beamforming solutions for the array configurations used.

For the purpose of gaining insight into primary microseimic Love wave generation, we want to analyze how source directions of the highest average noise amplitudes of Love and Rayleigh waves compare with each other, and how they relate to specific source regions. In Europe long periodic primary microseimic noise (e.g. periods ≥ 20 s) can be observed from large distances [e.g., Matsuzawa et al., 2012; Sadeghisorkhani et al., 2016; Yang and Ritzwoller, 2008]. Therefore, we restrict our analysis to the primary microseismic peak range (12–15 s), where the influence of attenuation suppresses very distant source regions. We additionally use the phase velocity as selection criterion between the two wave types. Phase velocities of fundamental mode Love and Rayleigh waves at the array sites were determined in a previous study [Juretzek and Hadziioannou, 2016]. We consider vertical, radial, and transversal component beamformer results and form the mean of each component over the total time span analyzed.

Figure 4.1 (a) shows slowness vs. backazimuth plots of the self-normalized mean beampower on the transversal component and the sum of the mean vertical and radial component results. The typically observed slowness range of signals on the different components is highlighted by white solid lines and agrees with our two target wave types. Love waves (transversal beamformer result) and Rayleigh waves (vertical+radial beamformer results) share similar backazimuth ranges corresponding to local beampower peaks. However, we observe primarily different source directions for the noise amplitude maxima between the wave types. This characteristic holds for window lengths between 128–512 s and covariance matrix averaging lengths between 1.5–3 hours as inferred from additional tests. Since the azimuthal noise distributions of the individual radial and vertical component results were found to be very similar, azimuthal ellipticity differences of Rayleigh waves do not seem to cause these differences. Primary microseimic wave type differences with azimuth were observed previously at different locations [Behr et al., 2013; Juretzek and Hadziioannou, 2016]. Although inhomogeneous structures beneath the array could cause such effects, the consistency between observations likely hints to common source or propagation path effects.

Pronounced seasonal variations in noise strength are a well known feature at mid and high latitudes [Stutzmann et al., 2009], and results in Fig. 4.1 (a) are likely dominated

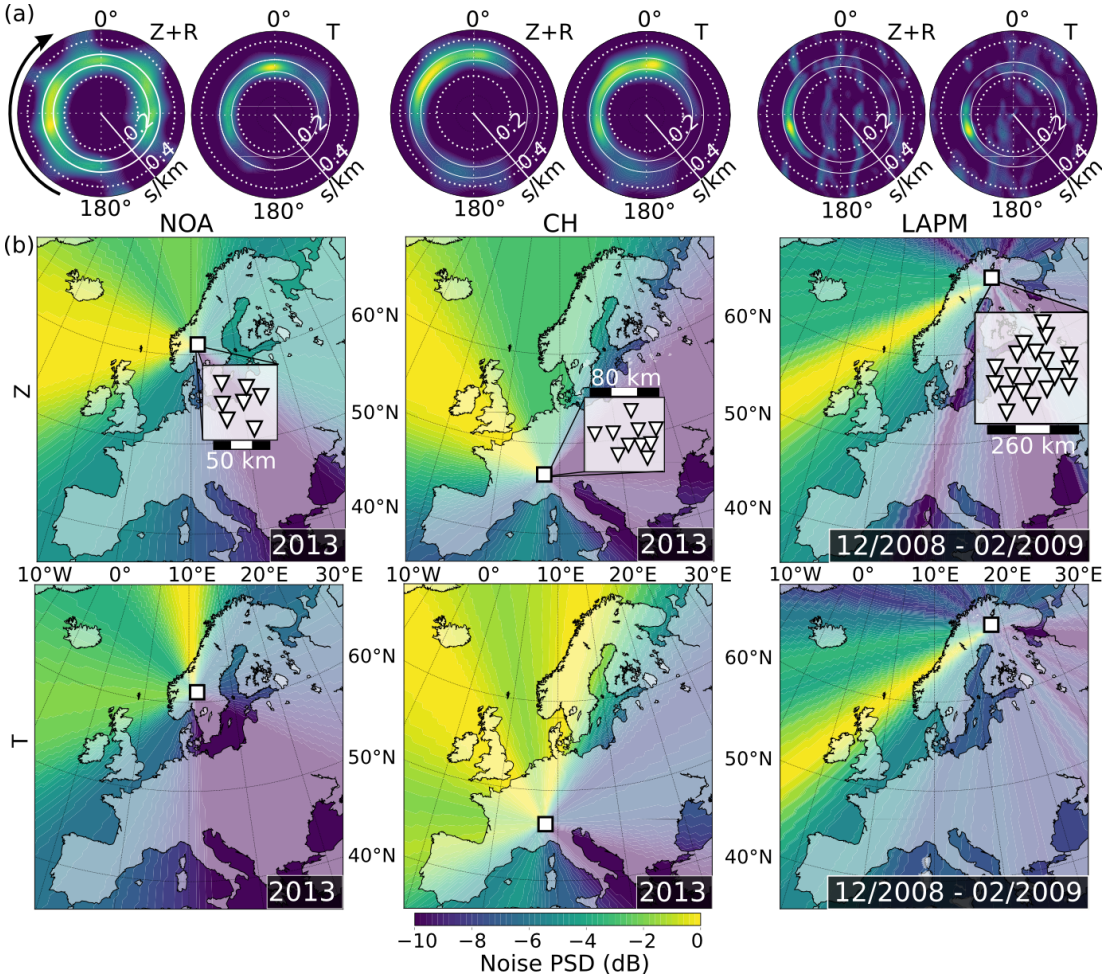

Figure 4.1: Self-normalized mean beampower PSD for vertical (Z), radial (R) and transversal (T) component noise observations in slowness vs. backazimuth representation (a), and self-normalized median beampower PSD as backprojection from the array centers according to great circle path propagation (b) at three different array sites (white squares show station geometry) and a period of 15.1 s. Labels in maps indicate the time span of the data averages for (a) and (b) and the same color scale is used for (a) and (b). The arrow indicates the backazimuth clockwise from North.

by the winter results. Since we are also interested in the most common azimuthal noise amplitude distribution at the arrays in this study we self-normalized each 3-hourly slowness vs. backazimuth beamform result and take their median over the total time span analyzed. For an illumination of the geographic regions which correspond to high relative beampower, the maximum amplitudes within the highlighted slowness range in Fig. 4.1 (a), is back-projected for each array according to great circle path propagation

as shown in Fig. 4.1 (b).

We constantly find an illumination of the western coasts of Norway and the British Isles, which agrees with other publications [e.g., Friedrich et al., 1998; Kimman et al., 2012; Möllhoff and Bean, 2016; Sadeghisorkhani et al., 2016]. Since simultaneous signals from similar directions of arrival below the resolution limits of an array cause distorted beampower and signal parameters as addressed by Gal et al. [2016], caution must be taken in the interpretation of results. The arrays used here, have different resolution capabilities, and azimuthal distributions with respect to the source areas. Still, wave type amplitude differences agree between the arrays, which indicates a sufficient resolution for the regional source areas.

For a better understanding of the time dependence of directional amplitude differences between the wave types found in Fig. 4.1 (a) and (b), we form daily means for beampower at the Norsar array and for corresponding wave heights near the Norwegian shore. Figure 4.1 shows these means for few days in December 2013. Although the beampower pattern of both wave types resemble each other, maximum Rayleigh wave amplitudes tend to follow the highest wave height locations. Love wave amplitudes from specific northern backazimuths remain on a higher level in addition to weaker varying amplitude maxima, which follow largest ocean wave heights. Azimuthal strength differences that were observed for the yearly results (Fig. 4.1) are reflected in these daily averages. This relatively stronger transversal component beampower peak indicates significant horizontally polarized ground motions that occur even for moderate near coastal wave heights north of the array, as estimated from WAVEWATCH III® modeled ocean wave parameters. Ocean wave model resources are described in section 4.1 in more detail. Such deviations between differently polarized seismic signals could likely arise due to locally different source processes and propagation effect in heterogeneous earth structure.

Structural effects

It is well known that crustal heterogeneities cause substantial refraction of surface waves at the microseimic period range and longer periods [e.g., Oliver, 1962]. Cotte et al. [2000] found up to 30° of azimuthal deviations for Rayleigh and Love waves at periods above 20 s in the French Alps. In a different study Paulssen et al. [1990] observed strong surface wave amplitude distortions and great circle path deviations in southern Spain for Rayleigh waves from teleseismic events and suggest scattering, defocusing and anelastic attenuation as possible causes. This is an obstacle for the process of source localization approaches, which rely on back-projection as applied in this study,

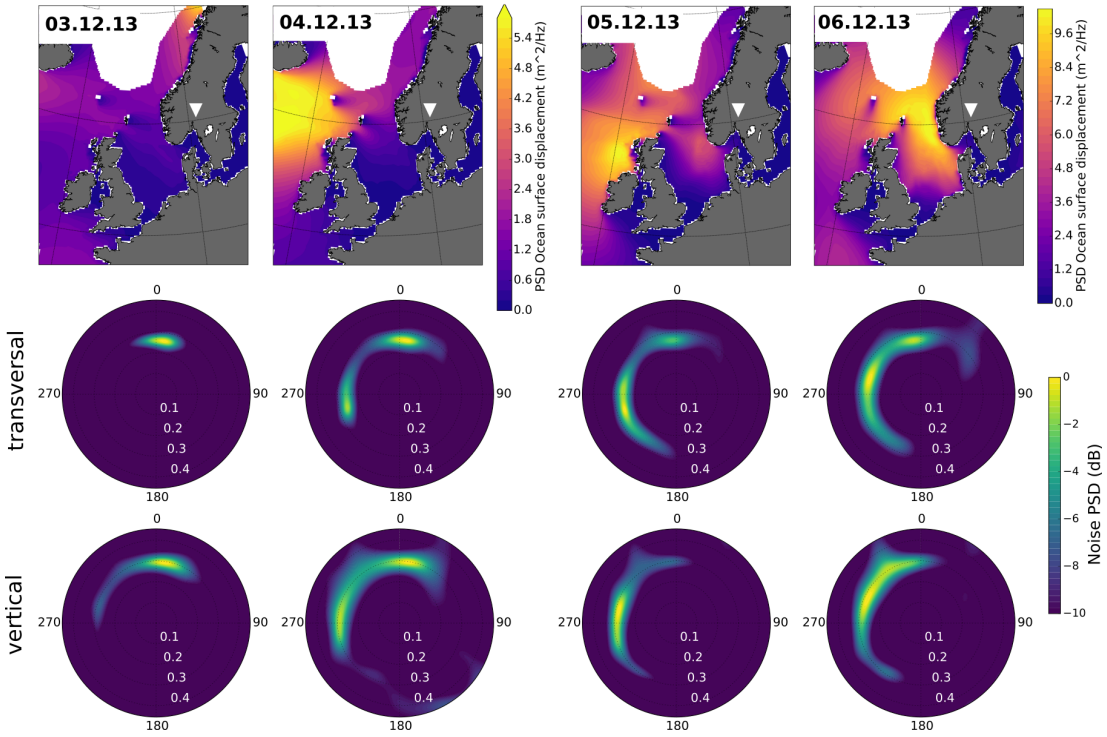

Figure 4.2: Sequence of 4 days in December 2013 showing daily averages of ocean wave height (top) and of vertical and transversal beampower spectral density as backazimuth versus slowness diagrams (bottom) for the Norsar array (triangle indicates array center)

.

especially when observing signals from far-field distances. Especially for the central European Swiss array (CH), great circle path deviations are likely not negligible, since wave propagation distances across complex structure are considerably large in this case. With focus on this array, we choose two approaches to obtain a best estimate of the structural influence on the surface wave propagation from the source. By measuring travel path deviations using a number of earthquakes mainly located near typical noise source regions on one hand, and by using ray tracing in a regional velocity model on the other.

In a first approach, we compare theoretical backazimuths of surface wave arrivals for a number of regional earthquakes, detailed in Table 1 in the supplementary material, to their backazimuths observed with beamforming at the Swiss array.

In a second approach, we test whether a seismic velocity model for the European region is able to reproduce observed travel path deviations at our frequency range of interest. We use the velocity model described in Afanasiev et al. [2016], which

was derived from a combination of available velocity models of multiple scales and therefore includes regional information wherever possible. Processing details for both approaches and a comparison between results from both approaches are detailed in the supplementary material. We conclude, that this velocity model is suitable to serve as an indicator of the propagation deviation strength.

Figure 4.3 shows the earthquakes derived great circle path deviations (labels) and direction dependent travel path deviations, estimated by ray tracing into different propagation directions from three array centers (lines). The estimated deviations to great circle path backazimuth are mainly within a range of few degrees in the distance range and azimuthal range of strong primary microseismic noise sources. However, deviations for surface waves propagating from the south-western most coasts of Europe are larger, which could be related to a lack of significant surface wave amplitudes from these azimuths. In most cases backazimuths for Rayleigh waves deviate more strongly from the great circle path assumption than for Love waves. Those deviations could explain moderate differences between Rayleigh and Love wave beamformer peak azimuths, e.g. observed at CH for the British Isles direction (cf. Fig. 4.1 (b)).

In summary, both approaches emphasized that propagation effects for more distant source regions within the reach of our study are not negligible. Additionally, for certain source azimuths, differences in relative azimuthal noise strength between the wave types could arise due to focusing effects, great circle path deviations and changes in polarization, caused by the crustal structure.

Further knowledge of the small scale structure, suitable for short period surface wave simulations, would be needed to overcome this bias. Here, as a consequence we chose to apply azimuthal binning for our following analyses. The bin size reflects the average accuracy of the propagation direction retrieved from beamforming.

Correlation between primary microseismic noise and ocean wave height

In order to constrain the source locations of our noise observations, we compare ocean wave heights with the beamforming results. We obtained open access ocean-wave parameters from resources detailed in [Ardhuin et al., 2011] which were modeled with WAVEWATCH III® [Ardhuin et al., 2010; Tolman, 1991]. In particular, we use the directionally integrated ocean surface elevation power spectral density $E(f)$, gridded at 3 hours time intervals and at 0.5° Latitude and Longitude increments. The Earth's surface around each array center was discretized symmetrically into bins of 100 km

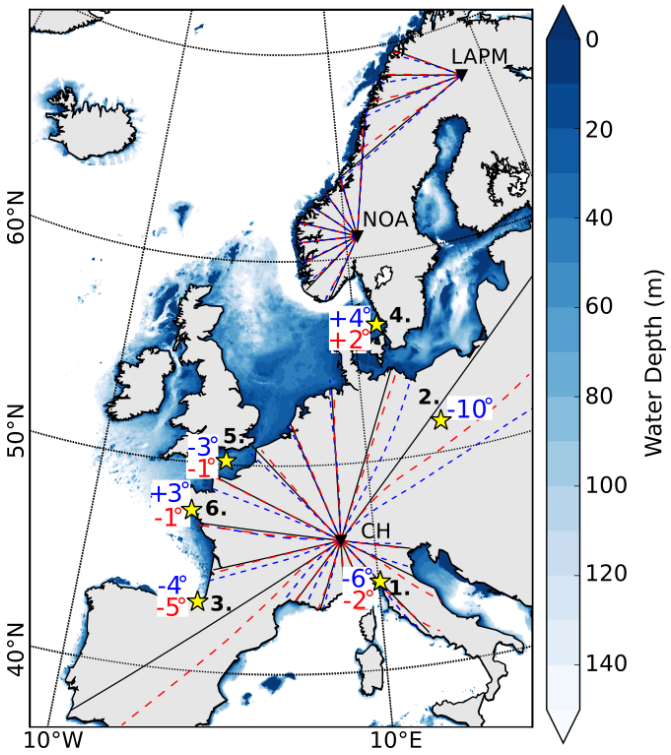

Figure 4.3: With respect to the CH array center, differences between event backazimuth as estimated from the great circle path and from beamforming in degrees (positive sign for clockwise deviation) (red: Love wave; blue: Rayleigh wave). Black labels indicate event numbers (see Table 1 in the supplementary material) and yellow stars mark event locations. The water depth (blue color range: ETOPO1.0 [Amante and Eakins, 2009]), with a maximum depth corresponding to approximately 1/2 of the wavelength for deep water ocean gravity waves at a period of 14 s, indicates regions of intermediate and shallow water. For azimuth increments of 20 degrees from the array center, great circle paths are indicated by black solid lines, and fundamental mode ray paths, using the velocity model of section 4.1 at a period of 14 s are, are indicated by red (Love wave) and blue (Rayleigh wave) dashed lines.

distance and 8° of azimuthal width overlapping by 25%. For each bin, the spatial mean of $E(f)$ over all included grid points is collected in a time series at period bins around approximately 12.5, 13.8, and 15.1 s averaged over 6 hours. Using smaller temporal increments of 3 hours, did not change our results.

Likewise, we form time series of the maximum direction dependent polarized noise PSD $P(f,\theta)_{max}$ from beamforming, within each azimuthal bin and for the slowness range indicated in Fig. 4.1 (a) at corresponding period bins. Here, the azimuthal binning is performed to account for travel path deviations, such as estimated in the pre-

vious section, but also for array mis-localizations e.g. due to inhomogeneous structure beneath the array.

For each noise-source direction and earth-surface bin combination, the corresponding time series are self-normalized and correlated with each other. Testing the common Pearson correlation coefficient generally indicates a good agreement between the two parameters in coastal regions. However, we use Kendall's Tau [Kendall, 1938], for testing the joint monotonous variation of both parameters in this study. The importance of using non-parametric techniques in the context of noise-ocean parameter correlation was recently emphasized by Craig et al. [2016]. Unlike the Pearson correlation coefficient, Kendall's Tau correlation is robust against outliers and does not assume a linear relation between the two variables. In the presence of multiple sources, as it is usually the case for ocean generated noise, the beampower estimate can be biased unpredictably, which also requires a more robust measure of correlation than comparing actual amplitudes. We estimate the correlation of the two time series $\mathbf{x}$ and $\mathbf{y}$ by Kendall's $\tau_b = (C - D)/\sqrt{(C + D + T_x) * (C + D + T_y)}$, where C and D are the number of concordant (e.g. $x_i > x_k$ and $y_i > y_k$) and discordant ($x_i > x_k$ and $y_i < y_k$) pairs of the time series, respectively. T_x and T_y are the number of ties of either ($x_i = x_k$) or ($y_i > y_k$). Hence, τ_b ranges between -1 and 1, indicating perfect anti-correlation and perfect correlation, respectively.

Results for the different period ranges tested are very similar to each other, hence Figure 4.4 shows these correlation maps for a period of 14 s for the arrays NOA, CH and LAPM. We interpret highest correlation coefficients as indication of especially clean source regions, where ocean state and noise state variations at the arrays are closely linked throughout the year. As expected from theory and in agreement with Fig. 4.1, best correlation coefficients are found in near coastal areas, which correspond to backazimuths of peaks in the azimuthal noise strength distribution. Regions including strong local maxima of the correlation coefficient are marked by boxes in Fig. 4.4. The geographical distribution of high correlation coefficients for Love and Rayleigh waves are more similar to each other, than the azimuthal beampower backprojections in Fig. 4.1. Likely, because propagation path effects are of less importance in the binned correlation approach.

The extent of the regions showing high correlation coefficients is mostly larger than areas of shallow water we would like to resolve. Partly because less resolution is achieved along the back-projection direction. But also due the spatial correlation of ocean wave parameters, which increases the width of a point source to a larger area in the correlation maps. Craig et al. [2016] suggested to consider autocorrelation maps to obtain an estimate of the spatial correlation of the model parameter. Therefore, we calculate

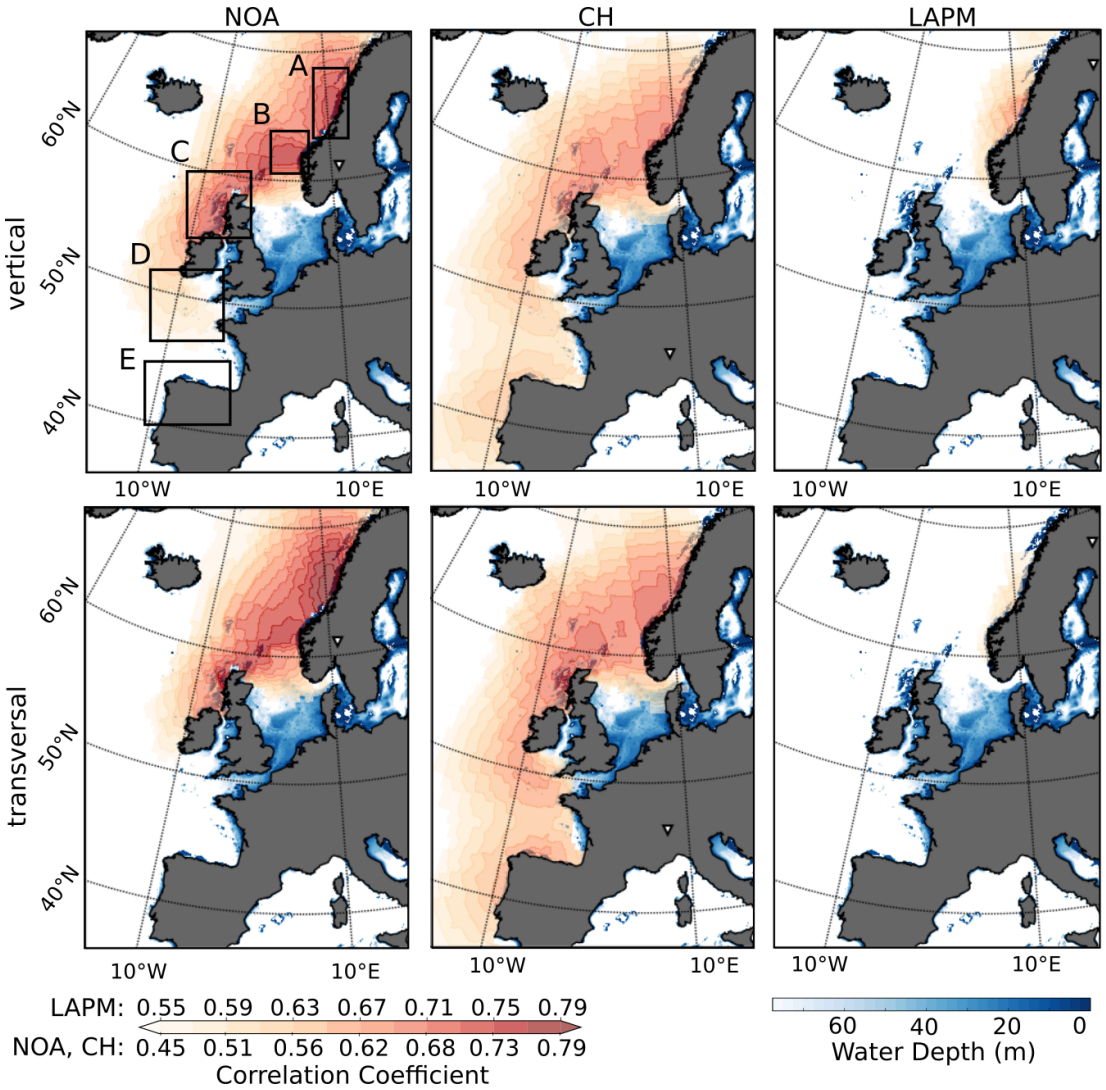

Figure 4.4: Correlation coefficients (red color range) between noise and ocean surface elevation at different array sites (triangle: array center) and a period of 14 s for vertical and transversal component noise observations; and water depth in the background (blue color range). Boxes (A–E) mark different regions mentioned in this study.

the mean Kendall's Tau correlation coefficient between the yearly ocean wave elevation time series of a data grid point and its surrounding grid points within different distance radii, increasing in 100 km increments. As consequence, we obtain the distance range at each location, for which ocean parameter data is well correlated in space (Kendall's Tau mean above 0.8). This is performed for all center points on a grid with Longitude and Latitude increments of 2°. Figure 4.5 (a) and (b) show a comparison between map

views of autocorrelation ranges and of mean yearly ocean surface elevations at a period of approximately 14 s, respectively. The correlation ranges in Fig. 4.5 (a) are relatively large near Norway and Spain, i.e. more than 500 km, but smaller near the British Isles and in regions where Islands scatter the ocean waves (compare with Fig. 4.5 (b)). The spatial correlation of ocean wave parameters seems to be an major limitation for noise source localization as shown in Figure 4.4 with this approach. However, the spatial resolution estimate in most coastal areas suggests reliable localizations of source areas which contribute most to the noise levels of the two different wave types.

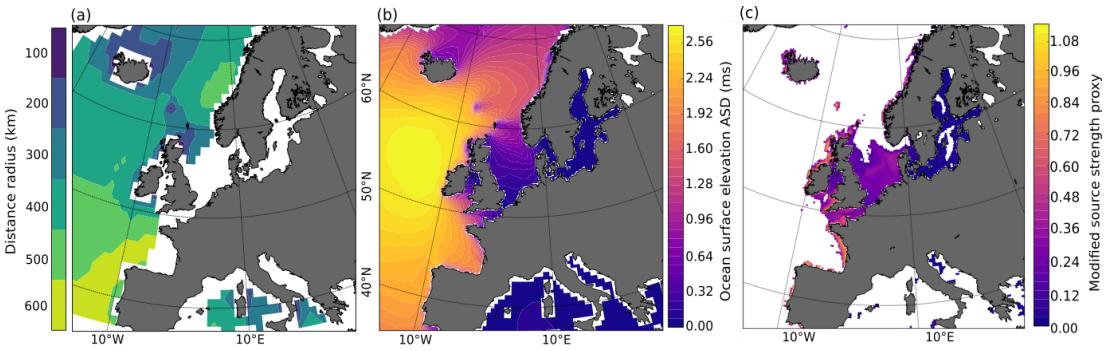

Figure 4.5: (a) Map view of the distance range at each location within which the model data has an average CC above 0.8. (b) Average ocean surface displacement PSD at a period of approximately 14 s in 2013. (c) Average seismic source proxy of wave height scaled by water depths.

Highest correlation coefficients in Fig. 4.4 do, on average, not only correspond to coastal sections with the largest ocean wave heights. The shallow water regime is an important condition for primary microseismic noise generation ($kh \ll 1$), with the water depth h from the ETOPO01.0 data set [Amante and Eakins, 2009] and the wave number of ocean gravity waves k [Hasselmann, 1963]. Therefore, taking the water depth into account provides a better source strength proxy. We scale the mean of $E(f)$ from Fig. 4.5 (b) with $1/\cosh(kh)$, which was referred to as hydrodynamic filtering factor by Fukao et al. [2010]. The local ocean gravity wave number k was calculated via the Airy wave theory dispersion relation $\omega^2 = g\,k\,\tanh(kh)$, with the angular frequency of ocean gravity waves ω and the gravitational acceleration $g = 9.81$ m/s^2. Most important source areas in 2013, as marked in Fig. 4.4, are in accordance with this modified source proxy in Fig. 4.5 (c). We will study one of them, the Norwegian source regions, in more detail in the next section and focus on differences between Love and Rayleigh waves observed from these locations.

Array based localization

We exploit the vicinity of the Norsar and the Lapnet array to the Norwegian coastal source regions in order to constrain their location more accurately. Due to low ratios between source distance and array aperture, the plane wave assumption is often violated for these source regions. Therefore, we are able to use a curved wavefront approach to estimate the source distance in addition to direction by beampower maximization. We test whether the velocity model of section 4.1 is accurate enough to estimate traveltime differences for surface waves in the period range of interest, using the larger Lapnet array, which spans over a few grid points of the velocity model. Figure 4.6 (a) shows wavefronts corresponding to the fundamental modes of both wave types at a period of 14 s using the velocity model with respect to a test source location (star). Comparing resulting beampowers of this approach, to one which uses a homogeneous velocity model, shows no improvement. Therefore, beamforming phase shifts are applied according to assumed regular wavefront curves corresponding to a homogeneous velocity model, with origin distance increments of 50 km. We do not attempt to locate surface wave signals from more distant locations than the Norwegian coast and disregard such time windows for this analysis. Since the resolution capability of the localization decreases with source area size and superpositions of sources, we disregard extended sources by excluding beamformer maxima which are smeared out in azimuth and distance. We consider source positions which were localized at least twice during the given winter month periods.

Detailed localization results for a sequence of individual time windows during few days in February 2009 can be found in the supplementary material. Here, we show a localization stack for the total time span analyzed. Figure 4.6 (a) and (b) shows source localizations of the strongest Rayleigh wave (vertical component) and Love wave (transversal component) noise signals, respectively, along the Norwegian coast. The color of the markers represents results of the corresponding array and its time spans (Norsar: Nov–Dec 2013; Lapnet: Dec 08–Feb 09).

An interesting observation is that, independent of the highest swell distribution, specific locations are responsible for the most frequent strongest noise generation. During both time spans, we locate a dominant source region near 65° N and 11° E (in region A) for both wave types. Although primary micoseismic noise is also generated directly to the west of the Norsar array (region B), region A produces higher noise amplitudes for Love wave signals observed at this array. Both arrays indicate a slight difference in source position near 65° N and 11° E. Considering the velocity model at hand, this difference could be explained by propagation path effects for the Lapnet

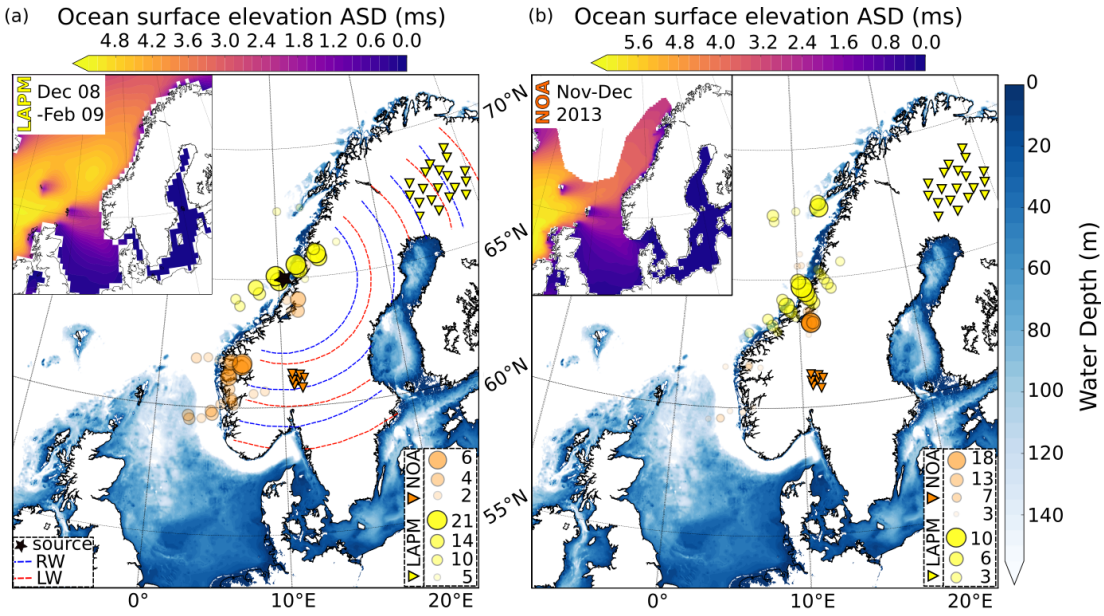

Figure 4.6: Map view of number counts of source positions (circle size) for vertical component (a) and transversal component (b) noise observations from the curved wavefront beamforming localization with the Norsar array (orange) and the LAPM sub-array (yellow). Insets: Ocean surface elevation spectral density at a period of approximately 14 s averaged over the indicated time spans, corresponding to the LAPM data period in inset (a) and the Norsar data period in inset (b). In (a), dashed lines indicate wavefronts of the fundamental modes of both wave types from raytracing with the velocity model of section 4.1, originating from the location marked by the star.

array (cf. Fig. 4.3 and 4.6 (a)). For the Norsar array the observed deviation is minor and also propagation path effects were estimated to be small.

Using a German array, Matsuzawa et al. [2012] tracked microseismic noise generated by a storm, propagating along the Norwegian coast, at a period of 20 s. They found that Love waves originated from a more confined and more eastern azimuthal range compared to Rayleigh waves. Via ray tracing the authors refuted propagation path effects as explanation for the wave-type difference. They instead interpreted them as indication of different source locations. In our analysis, with arrays near the Norwegian coast, we do not find independent source locations, but observe spatial differences in source localization rate for each wave type with more spatial variability for Rayleigh waves. The observations in this section suggest a difference in the efficiency with which each wave type is generated in different regions or observed from these regions.

Local noise generation efficiency for different locations

We analyze the spatial dependence of the relation between local ocean wave heights and microseismic noise amplitudes of both wave types. Therefore, we compare the time series of azimuth dependent noise amplitude spectral density $\sqrt{P(f,\theta)_{max}}$ from beamforming and vertical ocean surface displacement spectral density $\sqrt{E(f)}$ from the ocean model. Both time series are averaged over 6 hours. Since the data is analyzed in a narrow period band at approximately 14 s, we take $\sqrt{P(f,\theta)_{max}}/i\omega$ for comparison between vertical displacements. The microseismic noise amplitudes are obtained from azimuthal bins θ_m with high relative beampowers at the Norsar array. Ocean wave heights are taken from the nearest ocean data bin in the corresponding directions. Figure 4.7 (a) and (b) shows the relation between both time series for two ocean bin locations as indicated in the map in Fig. 4.7 (c).

Depending on the sea-floor topography some directional parts of the ocean wave spectra could contribute more to seismic noise generation than others. Since we used the directionally integrated parameter E_f we neglected this directional information here, which likely contributes to the spread in the parameter relation. However, in the observed range, the relation between ocean surface elevation and seismic-noise amplitude spectral density is of approximately linear character for both wave types. This agrees with the theoretical understanding of Rayleigh wave generation, as detailed by Hasselmann [1963] and by Ardhuin et al. [2015], and with several previous observations at sufficient distance from the source area [e.g., Barruol et al., 2006; Young et al., 2012].

By a least square approach we fit linear functions ($\sqrt{P(f)} = L + T\sqrt{E(f)}$) to the parameter relations, corresponding to all regions with Kendall's Tau coefficient above 0.55. As additional measure of source quality and of linear curve approximation validity, we use the mean relative residuals, and set an upper reliability threshold of it to 0.25. We relate the slope T (or transfer factor) with the efficiency of generated microseismic noise strength, observable at an array, due to a given ocean wave height within a source location bin. L is interpreted as random background noise level at the array. Map views of the resulting transfer factors T for both wave types, and corresponding mean normalized residuals are shown in Fig. 5.

As expected, areas with low residuals (dark colors), which are approximated best by the linear curve, coincide with highest correlation coefficients (Fig. 4.4) and with relative noise strength peaks (Fig. 4.1). For some backazimuths with respect to an array, several different coastal regions are located along the same great circle path direction. If the distance difference is small, the further source is not eliminated by attenuation, and source mixing likely decreases the correlation coefficient and linear character of

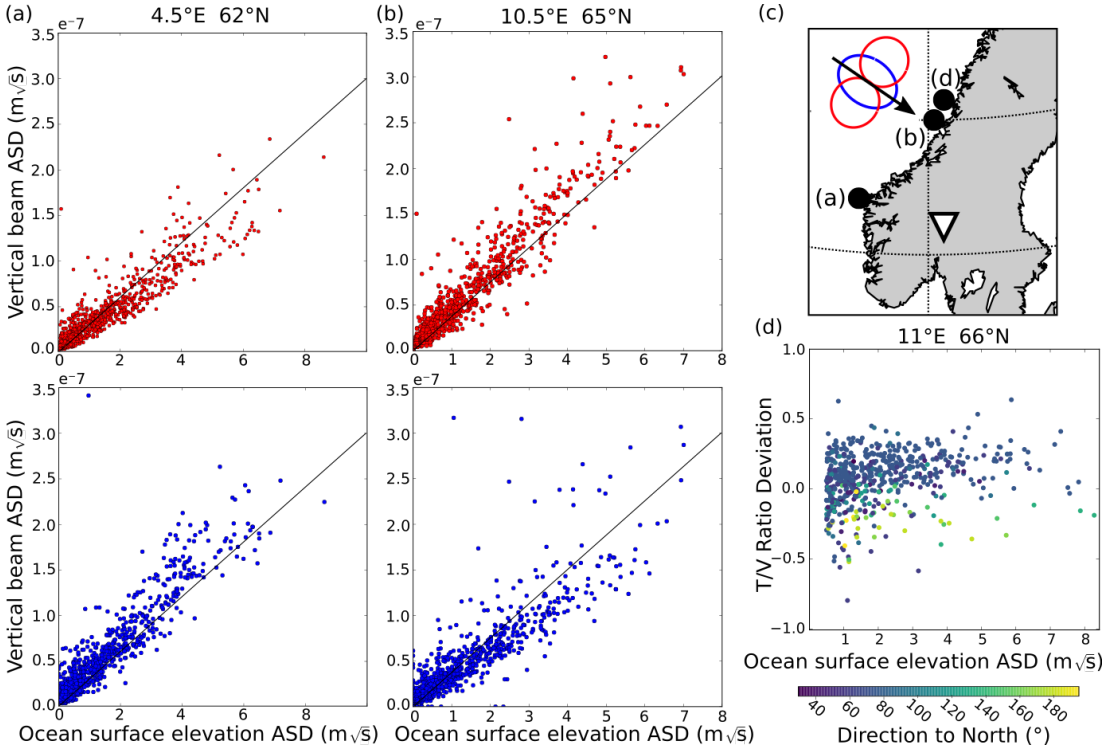

Figure 4.7: (a), (b) Relation between seismic noise and ocean surface elevation ASD for two locations of high correlation coefficient using Norsar array measurements. (c) Map indicating ocean parameter data locations for subplots (a), (b), and (d) of this figure. Schematic illustration of the radiation pattern of Love waves (red) and Rayleigh waves (blue) due to a superposition of a vertical and a horizontal single force (black arrow). (d) Relation between transversal/vertical noise ratio vs. ocean surface elevation ASD. Color range: Ocean gravity wave propagation direction with respect to north (clockwise).

the relation. This is especially obvious in the case of CH results for distant coasts. Nevertheless, for directions with a single possible source region nearby, we expect it to dominate the noise observation from that specific direction. For these regions, we can identify a close link between the ocean state and noise state variations.

The highest values for efficiency T are obtained for specific coastal sections and do generally correspond to low mean normalized residuals. Parts of the surface bins used include more shallow water area, where ocean surface elevations are on average lower than in deeper water. The efficiency could be biased in these cases. Nonetheless, despite the possible overestimation, low relative residuals distinguish these regions as especially bright sources. Further, attenuation is expected to decrease T with distance to the source. Remembering these limitations, we concentrate on the relative compar-

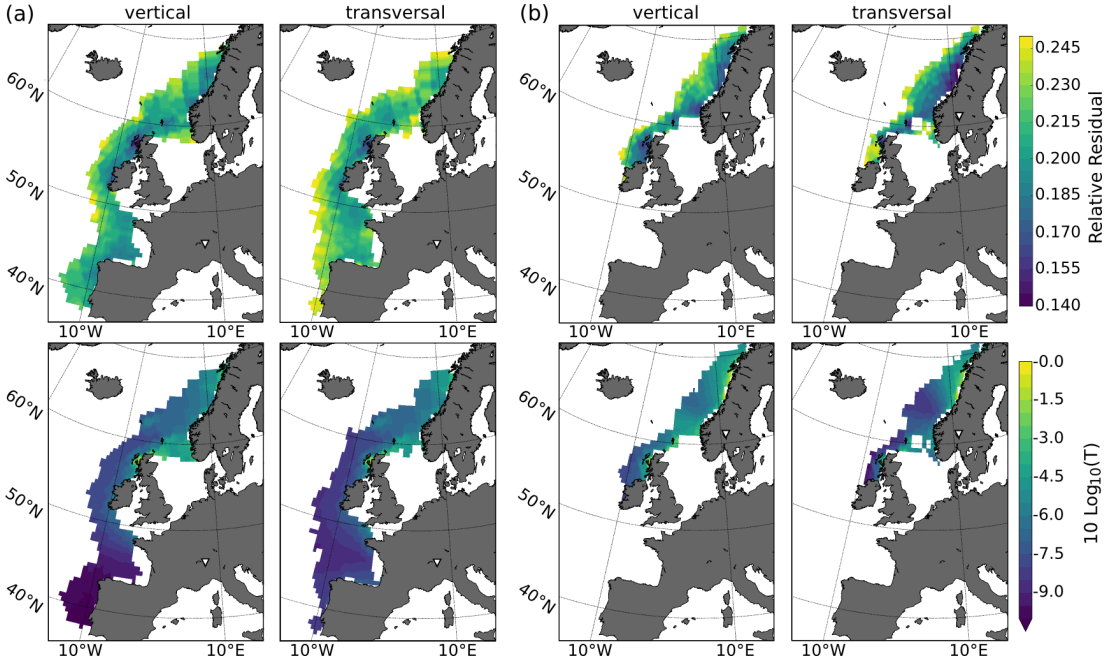

Figure 4.8: Map view of mean relative residuals (top; color range) and corresponding relative values of T from linear function fits (bottom; color range) for vertical and transversal beamformer results observed at the Swiss array (a) and at the Norsar array (b).

ison between the wave types. For both, we note that the transfer factor T and the linearity depend strongly on location. The most clean and efficient noise generating regions are found at coasts near Norway and the northern part of the British Isles (regions A, B, C). However, for Love wave measured at NOA from regions B and C we find lower efficiencies than for Rayleigh waves. On the other hand, the Norwegian coast area (region A), which was found to be a frequent source area with the array based localizations, shows a cleaner source signature and efficiency for Love waves than for Rayleigh waves. Similar to higher relative noise amplitudes, the relative source brightness for Love waves observed with CH is higher at coasts near Spain and France. These differences between the wave types could be imposed by earth structure but also by generation conditions in the source area. In the following section we will study the influence of properties in the source region, especially the so far neglected effect of swell direction.

Dependence on source region parameters

The ability to explain observed amounts of seismic motion for transversal and vertical/radial polarizations is a requirement for understanding the process of primary micoseismic generation entirely. Previously, different authors discussed primary microseism source processes in addition to pressure type sources [Hasselmann, 1963], that feature horizontal tractions, capable of generating both wave types simultaneously.

On one hand, such a generation of both wave types was suggested for certain conditions, with different radiation patterns for Love and Rayleigh waves [Friedrich et al., 1998; Saito, 2010]. E.g. ocean gravity waves propagating across the shallow surf zone at shores or across regular topography patterns, likely cause directed shear tractions. These could excite most energetic Rayleigh wave radiation either symmetrically or dominantly parallel with respect to the ocean wave propagation direction or with respect to sea-floor gradients, while Love waves can be expected to radiate strongest towards perpendicular directions [e.g., Ardhuin et al., 2015; Friedrich et al., 1998; Saito, 2010]. A corresponding wave type radiation pattern for this scenario is illustrated in Fig. 4.7 (c).

On the other hand, the relative strength of multiple source mechanisms (pressure vs. shear sources) could vary differently in dependence on the swell direction. For both of these cases, a variation of the wave-type ratio, observed at a fixed location, could be expected for varying ocean-wave propagation directions. Hence, the polarization type noise ratio can hold information about generation processes. We test the dependence of observed Love to Rayleigh wave noise ratios on ocean wave parameters.

Ocean wave propagation direction

For selected locations around Europe, at the 300 meter depth contour, modeled full ocean wave directional spectra are available from open data resources described in Ardhuin et al. [2011] and Ardhuin et al. [2015]. Additionally, model output at several buoy locations was available. Both datasets were obtained for locations of interest. A time series of ocean wave propagation direction relative to North corresponding to the spectral peak at a desired frequency, discretized in steps of 15°, is extracted with 6 hourly increments similar to the parameters in section 4.1. The time series of this peak direction is linked with the wave-type ratio. Fig. 4.7 (d) shows the demeaned transversal/vertical component noise amplitude spectral density ratio using Norsar array observations versus ocean surface elevation spectral density at an exemple position as marked in Fig. 4.7 (c). The color range of the data points indicates peak propagation direction. Here, measurements corresponding to wave heights lower than 0.5 m were excluded, since microseimic noise levels did not significantly rise above the background

level at the array. We observe a separation of wave-type ratio with the peak direction (darker and lighter color). The wave-type ratio for similar peak directions remains relatively stable over the observed ocean wave height range. The characteristics shown here, are representative for the majority of test locations along the coasts.

For a detailed analysis of the wave-type ratio modulation in Fig. 4.7(d), we directly plot ratio versus ocean wave direction Fig. 4.9 (a) and (b) show the demeaned transversal/vertical component PSD ratio at the arrays NOA and CH versus peak ocean wave propagation direction at the near-coastal locations which show high correlation coefficients and linear relation approximation. For each given location, the ratio varies with ocean wave propagation direction in a harmonic manner. In order to find the peak propagation directions corresponding to the extrema of the data, we fit a sine (red dashed line) to the mean ratio data points (red dots). Figure 4.9 (c) and (d) show map views of the ocean wave directions corresponding to the minimum (blue) and maximum (red) transversal/vertical component noise ratio, as determined by the fitted function. We observe a difference of approximately 90° between the extrema. Transversal/vertical component ratio minima occur mainly for peak ocean wave propagation directions towards the observation point and maxima occur for ocean wave directions perpendicular to it. This would agree with an imprint of a source mechanism that depends on swell direction. The insets for each array in Fig. 4.9 (c) and (d) show histograms of the fit function period from all locations. For noise measurements at both arrays, the period shows a peak around 190°. We note that using peak ocean wave direction is a simplification since the shape of the full ocean wave directional spectrum is not accounted for. Additionally, ocean wave directions in the shallow water area ($h \leq 40\ m$) and in 300 m of water depth likely differ to some extent. Despite this, results for different locations show consistency and the periodicity distribution peaks agree with the average angular difference between the ratio extrema of 90°.

From the point of view of a single array it is difficult to determine whether the wave type ratio modulation depends on swell propagation direction with respect to the coastline. Since different authors discussed the possibility of primary microseismic source mechanisms that feature specific radiation characteristics for Love and Rayleigh wave energy [e.g., Friedrich et al., 1998; Saito, 2010], we test our wave type ratio data against an imprint of these source radiation models. In order to evaluate the possibility of such a dependence we test the symmetry orientation of the wave type ratio variation. We use Norsar array measurements of the wave-type ratio in different azimuthal bins and compare them to peak ocean wave propagation directions at locations marked by circles in Fig. 4.10 (c). We form ratio medians for corresponding ocean propagation

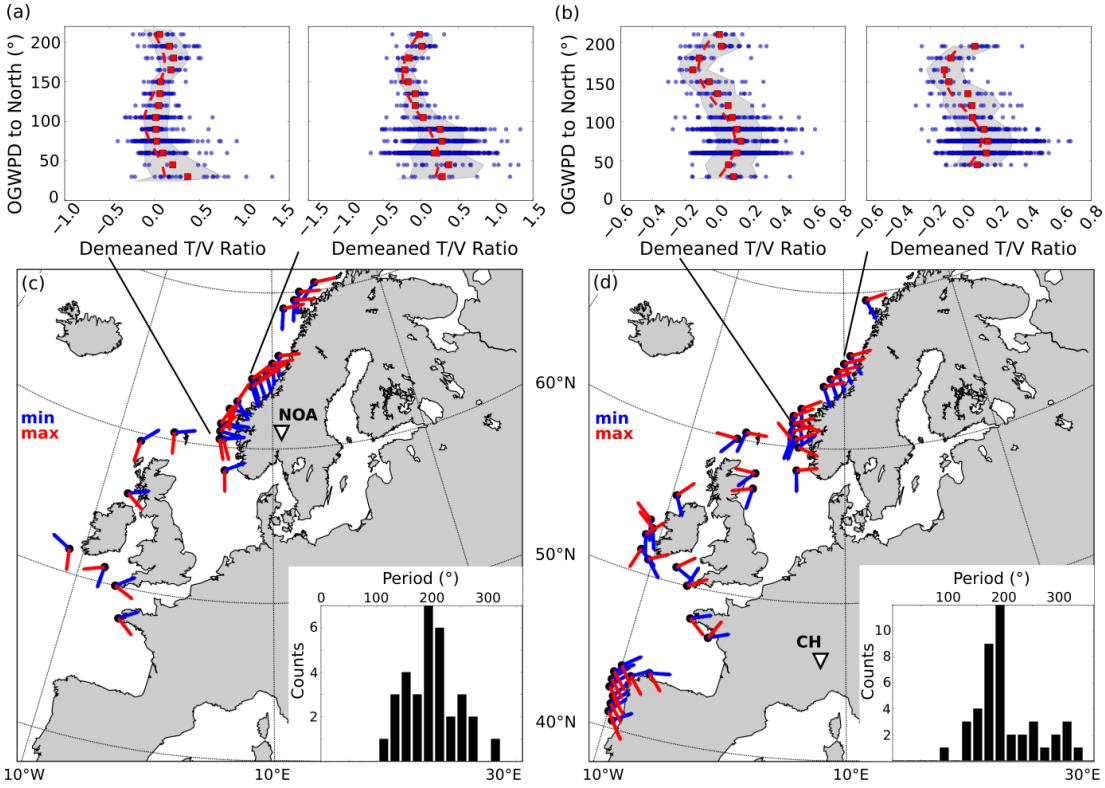

Figure 4.9: (a), (b) blue dots: Demeaned transversal/vertical component noise ratio at two arrays (NOA for (a), CH for (b)) vs. ocean gravity wave propagation direction (OGWPD) at indicated locations (lines) at a period of 14 s; red dots: data means; gray area: 1σ range; red dashed line: fitted sine. (c), (d) Map views of OGWPD corresponding to minimum (blue) and maximum (red) transversal/vertical noise ratios. Insets: Histograms of fit function periods at a periods 14 s.

directions within relative angular increments of 15° for two different symmetry orientations (a) relative to the great circle path direction to the array and (b) relative to the coast normal. Results are shown in Figure 4.10 (a) and (b), respectively.

We evaluate the degree of correlation between both parameters, with the non-parametric Kendall's Tau coefficient, and transfer the result to gray scales indicating perfect correlation (1: black) and no correlation (0: white). Fig. 4.10 c) shows these values as color range filling the marker symbols. We find a higher degree of correlation for symmetry orientation (a). Lower Love to Rayleigh wave ratios could be expected when most energetic ocean waves propagate directly onto coastal slopes. In that case, the shoaling mechanism for Rayleigh wave excitation proposed by Hasselmann [1963] likely increases relative to possible other generation mechanisms. However, our obser-

vations indicate a more direct dependence of the wave-type ratio modulation on peak ocean wave propagation directions than their propagation relative to the coast.

We find that the average wave-type ratio level differs for coastal sections in Fig. 4.10 (marked sections I., II., and III.). This hints to additional constraints for the generated proportions of the different wave types. One likely cause for this observation are bathymetric conditions that differ for the corresponding locations causing difference in importance of potential multiple mechanisms. Another possibility would be the character of the coast. For instance in the case of a straight coastline (e.g. region A and E), where sources are aligned along a large portion of the coast, the ratio pattern of the wave type radiation would translate into the observations, but average out for a random source orientation at a chaotic coast line (e.g. region C).

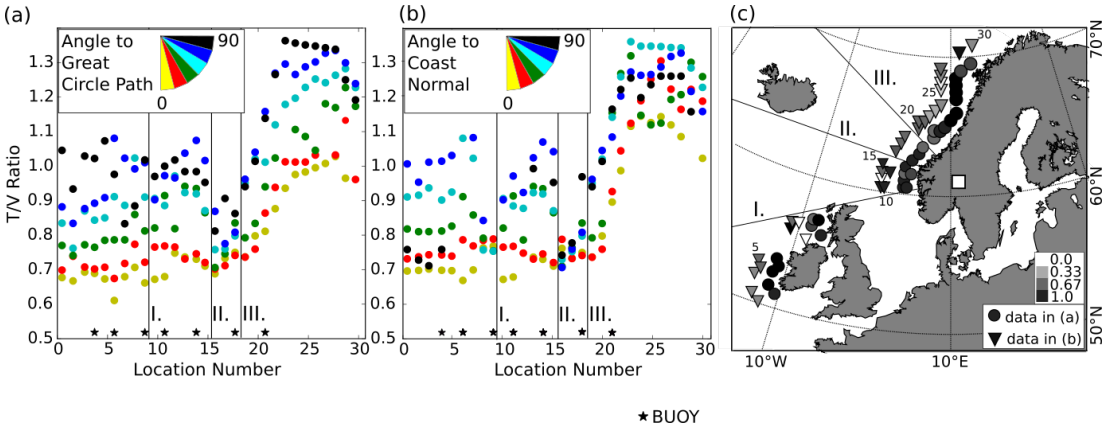

Figure 4.10: Relation between transversal/vertical noise ratio vs. ocean gravity wave propagation direction at different locations from the Wavewatch model output located at the 300 m depth contour and at buoy locations (black stars) with respect to the great circle path direction (a) and to the local coast normal (b). (c) Corresponding locations (circles) with correlation coefficient between noise ratio and ocean propagation direction increments in gray scale, indicating Kendall's Tau values from 1 (black) to 0 (white) for case (a) and (b). Triangle symbols for case (b) were shifted from their original location for visibility.

Bathymetry

For a period of 14 s the deep water ocean gravity wave length λ is approximately 300 meters according to the Airy wave theory dispersion relation. In the period range considered here, the shallow water regime corresponds to depths h of a few tens of meters and less. Hence, efficient primary microseism generation should occur within a narrow region of coastal shallow water, Fig. 4.5 (c). By analyzing which regions correspond

to the highest relative beamformer amplitudes Fig. 4.1, correlation coefficients (dark colors in Fig. 4.4), and efficiency factors (light colors in Fig. 5), we find the following characteristics: (1) the most important noise contributions from the Norwegian coast (region A, B) as well as from the Scottish coast (region C) originate from regions with extended shallow water areas including several small islands and fjords. (2) clearly lower correlation coefficients are obtained for the Celtic sea south of Ireland (region D), a region of average deeper water, which includes sea-mount topography raising below few tens of meters in water depths. (3) From the Spanish coast (region E), comparably high Love waves levels are observed, compared to Rayleigh waves. This coastal region includes both, shallow water as well as steep sections. An array near this area would be desirable for a confinement of source regions there. On the other hand, relatively high Love to Rayleigh wave signal ratios observed from regions A and E, and might be an indication for favorable bathymetry conditions for shear tractions in these regions. In summary, these observations agree with studies, which suggest a strong influence of topography on noise generation effectivity [e.g., Ardhuin et al., 2015; Fukao et al., 2010; Saito, 2010].

Testing the source imprint

Wave propagation in complex earth structure influences the relative content of different surface waves in the microseismic noise field. However, high Love to Rayleigh wave energy ratios, and similar azimuthal modulation of wave-type ratio at different European array sites [Juretzek and Hadziioannou, 2016] suggests an additional imprint of source processes onto observations. Since primary microseimic noise is possibly generated by multiple mechanisms [Friedrich et al., 1998], the relative strength of individual mechanisms could differ with region e.g. due to bathymetric conditions. Still, our observations in section 4.1 cannot easily be explained by such static causes alone. They likely hint towards a dynamic effect, e.g. a mechanism ratio that is ocean swell direction dependent or towards an imprint of directive wave-type radiation.

In order to estimate if such effects qualitatively fit our observations, we use Instaseis [van Driel et al., 2015] with the radial symmetric 1D anisotropic PREM model. We calculate vertical and transversal component seismic displacement RMS amplitudes at the centers of the Norsar and Swiss array in response to different force field distributions. To be able to separate the differently polarized wave types simply by radial and transversal components, we separately calculate the seismic response to sources within azimuthal windows of 8° width. Since detailed information on shallow water bathymetry would be required for a quantitative evaluation of the source terms, we

apply general proportionality assumptions for magnitudes of shear traction and pressure type sources. Following Gualtieri et al. [2013] we use single forces representing extended shear traction or pressure source fields within spatial grid cells near coastal regions ($h \leq 100m$). We apply a distribution of horizontal and vertical forces which are proportional to local wave heights. Additionally we take force strengths to scale inversely proportional with water depth, specifically with $1/\cosh(kh)$ [e.g., Fukao et al., 2010]. Since the PREM model does not provide realistic attenuation properties at our frequencies of interest, we use the correlation coefficients between microseismic noise and ocean wave heights, determined in section 4.1, to empirically approximate the maximum distance of source sensitivity for an array. Therefore, we disregard source locations outside regions with a correlation coefficient ≥ 0.4.

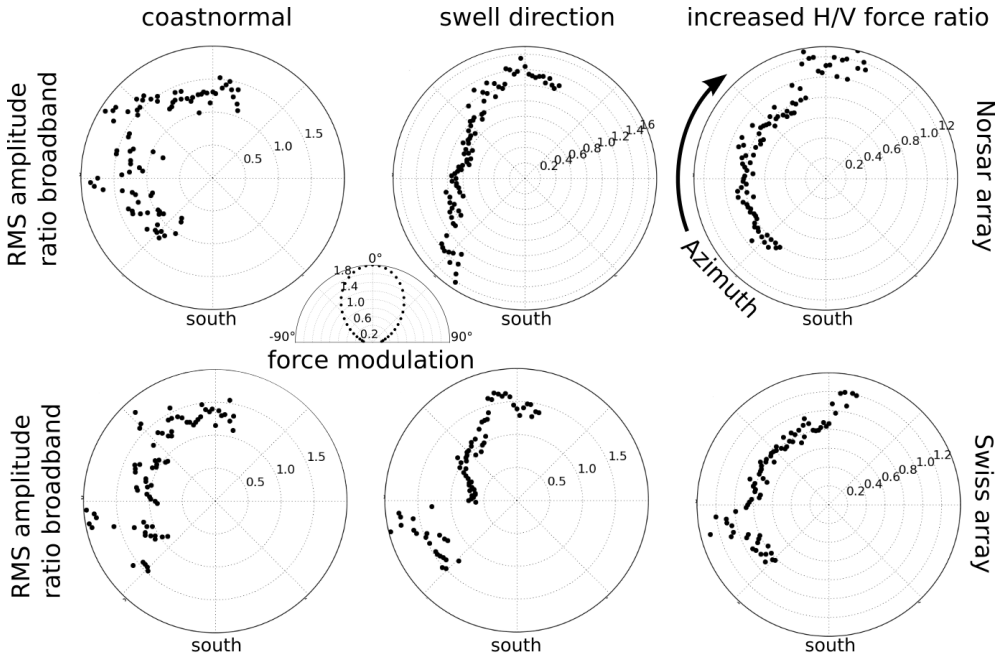

Figure 4.11: Modeled transversal/vertical component RMS displacement amplitude ratios (radial axis) vs. source azimuth observed from the array centers for three different test cases. The direction dependent horizontal force modulation around a test orientation is shown in the inset.

We use the yearly mean of modeled wave heights in 2013 at a period of 14 s as mean source strength distribution proxy and interpolate the data onto the same grid which is used for scaling with water depth. We estimate the azimuthal pattern of wave-type ratio generated by the spatial distribution of co-located vertical and horizontal forces with H/V force ratio of 1.1. We choose three different settings for horizontal force

orientations: (1) normal to the smoothed European continental coastline, (2) aligned with most frequent peak ocean wave propagation direction near coasts during 2013, and (3) purely random orientations. In case (1) and (2) we use a half sided cosine with 180° periodicity for an angular force modulation of 80% around the main force orientation (see inset in Figure 4.11). In case (3) we increase the H/V force ratio within region A and E to 1.4. Figure 4.11 shows the transversal/vertical amplitude ratios at both array centers for the 3 test settings. By comparing our estimated azimuthal wave-type ratios to observations in Fig. 4.1, we find that the swell direction dependent force orientation as well as a regional increase in H/V force ratio reproduce azimuthal wave-type dominance qualitatively. An imprint of directed horizontal forces normal to coasts does not fit our observations. Additionally, for an inclusion of detailed coastline roughness for this case, we envision an effective randomization of the force orientation and less agreement with direction dependent ratio observations.

Discussion

In this study we observed that primary microseimic noise of both Love and Rayleigh waves, correlates well with modeled ocean wave heights in near coastal areas. This meets with expectations from the theoretical understanding of primary microseismic noise generation and is in accordance with previous observations [e.g., Ardhuin et al., 2015; Barruol et al., 2006; Bromirski, Peter D. and Flick, Reinhard E. and Graham, Nicholas, 1999]. Regions of highest correlation coefficient coincide between the wave types (cf. Fig. 4.4), which agrees with our observations that Rayleigh and Love waves mainly propagate from similar directions as shown in Fig. 4.1.

Our measurements showed a linear relation between noise and vertical ocean surface displacement spectral density in near coastal areas. This enabled the localization of regions which act as especially bright source areas for the different arrays. Most efficient source regions (e.g. the Norwegian coast and the British Isles) found here, agree with locations which were identified as strong primary micoseismic sources for Rayleigh waves in previous studies [e.g., Friedrich et al., 1998; Möllhoff and Bean, 2016; Sadeghisorkhani et al., 2016]. However, we also found that noise generation efficiency is location dependent (Figure 5), in agreement with observations by Barruol et al. [2006], and appears to differ for Love and Rayleigh wave type noise from several areas. This agrees with azimuthal variations in the wave-type ratio, which were observed previously [Juretzek and Hadziioannou, 2016]. Both coinciding source azimuths between the wavetypes and a stable wave-type ratio with ocean wave height variations

(Fig. 4.7 (d)) argue against entirely independent generation mechanisms and source regions of Love and Rayleigh wave primary mircroseimic noise.

Structural effects (e.g. focusing, waveguide interruption, change in polarization etc.) likely influence observations of primary micoseismic noise signals. Estimates of propagation path deviations within paths to nearby source regions in this study, propose that theoretical and observed backazimuths can deviate up to the order of tens of degrees from each other, in agreement with previous studies. Hence structure should be considered in more detail in future studies in complex or far inland terrain. An estimate of potential secondary generation of Love waves through conversions from Rayleigh waves, especially occurring near or in the source region, is not within the scope of this study. This option and the influence of sedimentary layers and crustal heterogeneities at the ocean-continent transition on surface wave amplitudes [e.g., McGarr, 1969] is not considered in many studies and remains to be evaluated. However, observations from arrays at different geographic locations suggest that local source region properties seem important for noise generation efficiency differences and for wave-type ratio differences. One likely important factor for both the source efficiency differences and for the wave-type ratio, is the local bathymetry present in the source areas. The effect of the shallow surf zone on noise generation strength was also estimated to be significant by Hasselmann [1963] earlier. This bathymetry influence was also supported by the work of Fukao et al. [2010], who showed how ocean gravity waves in deep water could generate Love and Rayleigh waves simultaneously in the hum frequency band when seafloor topography is present. We can not confine source regions accurately enough to clearly evaluate particular bathymetry types. However, the regions for which we obtain peaks for the correlation coefficient as well as for the efficiency, often correspond to areas of extended shallow water depths with topography and islands.

Love wave generation may be possible through horizontal tractions due to ocean wave movement [Ardhuin et al., 2015; Friedrich et al., 1998; Saito, 2010]. Here, we found a correlation between the transversal/vertical component noise ratio and peak ocean wave propagation direction. This rather hints towards generation of both wave types in the source region and towards time dependent conditions for the excitations efficiency of each wave type. Our observations of a link between wave-type ratio and peak ocean wave propagation direction (Fig. 4.9) is an indicator for this possibility. One likely important cause for efficiency differences and ratio differences is an effective wave-type radiation pattern from the source area, for at least one of the wavetypes. Another possibility would be a varying importance of different source mechanisms in dependence on swell direction.

An anisotropic wave type radiation and a time dependent wave type excitation strength could be enabled by bathymetric filtering conditions and by a link between shear traction strength and ocean wave propagation conditions [Ardhuin et al., 2015; Saito, 2010]. Considering high resolution topography characteristics on the scale of ocean gravity wave lengths will be required in order to answer these questions.

Conclusion

By means of beamforming and correlation of noise amplitudes with ocean surface elevation we studied how primary microseismic noise source areas of Love and Rayleigh waves compare with each other. We found that beamformer results as well as correlation with ocean surface elevation showed differences between noise strengths of the wave types emitted from the same coastal sections. Further, some parts of the coast serve as especially bright sources of Love waves, meaning that the relation between ocean parameters and noise strength is especially close and that they seem relatively more effective at horizontally polarized noise generation. For Northern and Central Europe most energetic microseimic noise of both wave types is measured from sources along the coasts of Scotland and Norway.

We find that both Rayleigh and Love wave noise amplitudes depend similarly on the ocean wave heights, which hints at a joint or coupled source mechanism for the wave types. We observe a correlation between the wave-type ratio and the peak ocean wave propagation direction. This hints towards a dependence of wave type excitation efficiency on swell direction or an effective source radiation pattern. One possible reason for this could be horizontal tractions which are directive in orientation relative to ocean wave propagation.

Observed azimuthal variations in wave type ratio suggest regional differences in the importance of different possible generation mechanisms. This could arise due to different excitation of the wave types dependent on bathymetric conditions but could also be explained by directive wave type radiation. These options is supported by a good qualitative agreement between our synthetic tests and observations. Synthetic tests do not support a dominant imprint of shear forces which are oriented perpendicular to coastlines. Overall, we conclude that the Love to Rayleigh wave ratios carry supplementary information about the primary microseism excitation mechanism.

Acknowledgments

We wish to thank F. Ardhuin, M. Gal, L. Krischer, S. Mader, H. Sadeghisorkhani, T. Tanimoto, J.-N. Tödt, and D. Ziane for helpful discussions and suggestions for the improvement of this material. We thank M. Afanasiev and A. Fichtner for providing their velocity model. We thank the editor and two anonymous reviewers for comments which helped improve the manuscript. We acknowledge support from and discussions within TIDES COST Action ES1401. This work was funded by the Emmy Noether program (HA7019/1-1) of the German Research Foundation (DFG).

End of original manuscript

4.2 Supplementary material

(1) For the first approach in section 3, we use a moving time segment of one minute for this purpose, and focus on the part of the waveform, corresponding to the most energetic surface-wave arrivals filtered around 14 s within the typical wave type velocity ranges at the array sites.

For the second approach we use model parameters discretized at 0.5° Latitude and Longitude and 1 km depth increments. Phase-velocity maps for the fundamental modes of both wave types at a period of 14 s were created with the software package Geopsy (Wathelet 2008). We apply a flat earth transformation to the phase velocities (Jobert Jobert, 1983), linearly interpolate in the horizontal direction and perform standard 2D kinematic ray tracing.

In comparison to the earthquake observations with CH, the velocity model reproduces near great circle path propagation towards the events 5, and 6 for Love waves. For the events 1, 2, and 4 the rotation sense of the deviations was reproduced, but not for event 3. By the use of this model, measurements for Rayleigh waves are less well reproduced. With a different set of earthquakes Essen et al. (2003) estimated azimuthal deviation of microseismic Rayleigh waves for the Grnberg array in Germany. Our results for the Swiss array agree with their observations of small deviation for north-western events. Further, they found more important positive rotation deviation (about 13°) from locations near the western Norwegian coast. This agrees with our estimated ray paths deviation direction for north-south propagation across Scandinavia and Germany.

(2) For a sequence of 3 hourly snapshots on 24th and 25th of February 2009, ocean surface elevation ASD at a period of approximately 14 s is shown in Figure 4.12, for a region including the North East Atlantic. During these hours, zones of higher ocean surface elevations propagate along the Norwegean coast. For corresponding time

Table 4.1: Regional earthquakes used for great circle path deviation estimates.

Index	M_w	*Date*	*Lon*	*Lat*
1	5.30	21/06/13	10.11	44.19
2	4.70	19/03/13	16.06	51.51
3	4.39	23/03/13	-1.97	43.3
4	4.36	06/08/12	12.00	56.63
5	4.31	14/07/11	-0.66	50.17
6	4.29	21/11/13	-2.92	47.67

windows, the DOA and distance estimates of the strongest arrival from beamforming, are marked in the maps by crosses, using transversal (a) and vertical (b) component results. Except for the first time windows, during which swell is especially high at the coast near 70° N, the strongest noise amplitudes are often observed from a region near 65° N. This sequence is also included as a snapshot video in the supplementary material.

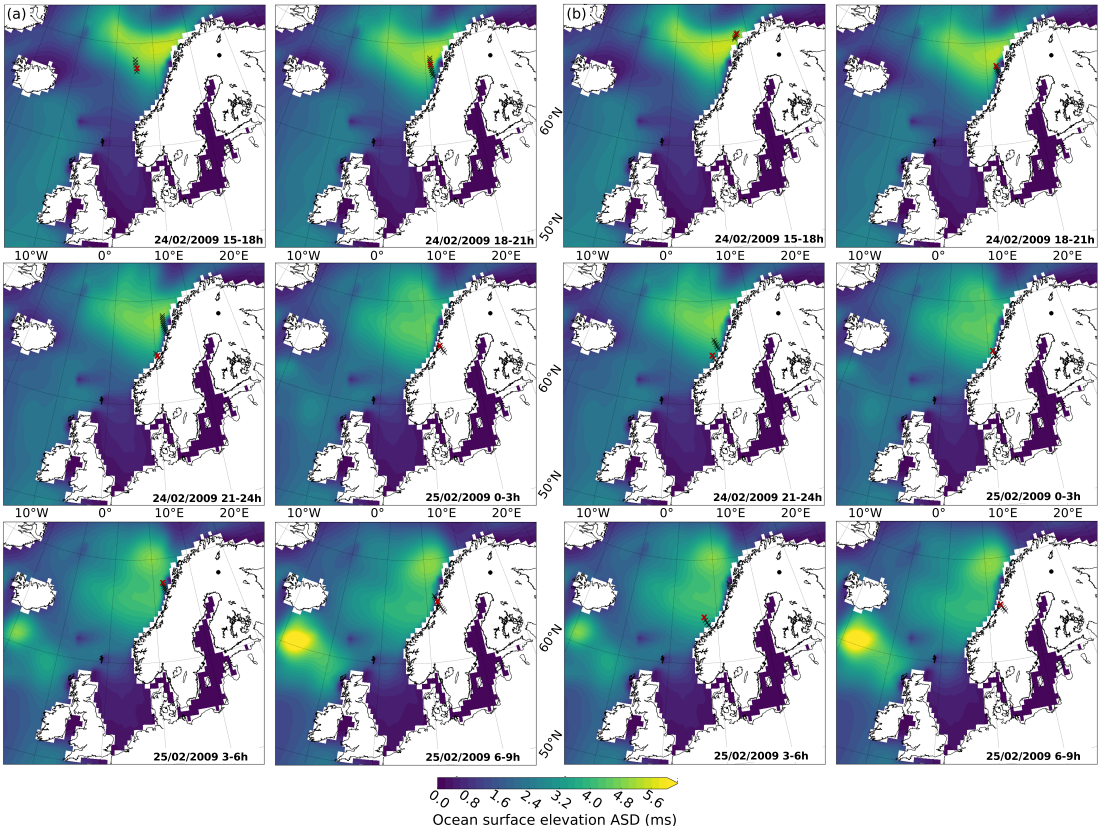

Figure 4.12: Sequence of ocean surface elevation PSD (color range) from Feb 24 and 25, 2009 and array based localization of noise sources for transversal (a) and vertical (b) beamforming results at a period of 14 s (black crosses: more than 75% of maximum beampower; red cross: beampower maximum). Time labels indicate averaging period for beamform results.

5

Predicting primary microseimic noise, modeling the directional characteristics of the noise field observed from both sides of the earth

The theoretical description of a source mechanism in shallow water proposed by Hasselmann [1963] states that primary microseismic noise can be generated by an oscillating pressure field at the sea bottom arising from the coupling between ocean surface waves and the solid earth in presence of a seafloor inclination, presenting a generation mechanism which causes seismic noise at the same frequency as the involved ocean waves. In the case of a simplified approximation of the bathymetry variation by a constant slope as formulated by Hasselmann [1963], the arising ocean-wave induced pressure PSD $F_{p,1}$, acting as the source equivalent of microseismic noise, was found to scale linearly with the seafloor slope s. Ardhuin et al. [2015] adapted this approximation to a slowly varying seafloor topography, where the ocean-wave induced pressure PSD $F_{p,1}$ scales linearly with a parameter introduced as effective seafloor slope s_{eff}, as described in chapter 2. s_{eff} was defined such that it provides a factor for the source strength due to a particular topography variation profile in comparison to the source strength due to a constant seafloor slope of $s = 1\%$.

Accounting for the source effect due to realistic topographic depth profiles, vertical displacement PSD according to this primary mechanism was previously modeled us-

ing a recent numerical ocean wave model and compared to observations from several geographic locations by [Ardhuin et al., 2015], presenting a first attempt for a global verification of this theoretical description over the period range of the hum and the primary microseismic noise peak. Ardhuin et al. [2015] achieved a best quantitative agreement between data and model in the hum and primary microseimic noise frequency bands by assuming a globally homogeneous effective seafloor slope s_{eff} of 6 %. Their estimate of such a globally constant factor was based on the analysis of realistic bathymetry profiles corresponding to large scale topography variations, such as continental margins. However, the seafloor topography shows variations at different length scales, including small scale variations in the order of the wave length of ocean surface waves at frequencies above 0.05 Hz. Hence, regional variations in the bottom topography might cause a spatial variation of s_{eff}. Additionally, spatially varying contributions from additional microseismic noise source terms, as those suggested by Ardhuin [2018], might be of importance for the observed vertical and horizontal component seismic noise field. To date, a limited knowledge of this small scale bathymetry at different geographic locations prevents an accurate estimation of s_{eff} for the primary microseimsic noise band and an evaluation of potentially different source term contributions across regional and global scales.

This chapter presents an analysis on how accurately time series of observed vertical component primary microseimic noise in the frequency range between f=0.05 − 0.08 Hz from several geographic locations may be reproduced by modeled primary microseismic noise using either a regionally homogeneous or heterogeneous s_{eff}. For the theoretical estimation of the global distribution of primary microseismic noise sources in shallow water, model results of the equivalent pressure field PSD $F_{p,1}$ were used, as calculated by [Ardhuin et al., 2015] based on output from a numerical ocean wave model (at the time of writing accessible at ftp://ftp.ifremer.fr/ifremer/ww3/HINDCAST). Using vertical component displacement data from seismic stations on both hemispheres, the deviation between observed and modeled displacement PSD using a homogeneous s_{eff} was quantified. Source regions, which contribute strongly to the mismatch, were identified. Aiming at improving the agreement between observations and model predictions for these identified source regions, the assumption of a fixed, globally homogeneous effective slope factor s_{eff} was adapted in this chapter to a regionally heterogeneous effective slope factor $s_{\text{eff}}(\mathbf{x})$.

For the purpose of analyzing the imprint of regional sources, we focus on (i) the high frequency limit of the primary microseiminc noise range, (ii) on the most dominant recorded noise amplitudes attributable to specific regional source regions and (iii) the inclusion of near coastal seimic stations, where possible. Results for $s_{\text{eff}}(\mathbf{x})$ are

eventually discussed in the context of possible local bathymetry variations but also in regard of additional influencing factors.

On one hand, direction dependent microseismic noise amplitudes were analyzed by means of beamforming using European seismic arrays. An estimate of effective slope factors required for an improved angreement between model and data was obtained as azimuth θ dependent factors $s_{\text{eff}}(\theta)$ using beamforming results in combination with a harmony search fitting approach as presented in section 5.1. The array based analysis of spatially heterogeneous $s_{\text{eff}}(\mathbf{x})$ in this section considers relative effective azimuth dependent variations around a mean effective slope factor.

On the other hand, non-directional vertical component displacement amplitudes from single stations were compared with modeled data in order to obtain a best fitting estimate of local effective slope factor variations $s_{\text{eff}}(\mathbf{x})$ based on a simmulated annealing approach. Corresponding results are presented in section 5.2 concerning the Australian region. With s_{eff} referred to as effective fitting parameter γ, findings of section 5.2 were published as contribution to **Global scale analysis and modelling of primary microseisms** by [Gualtieri, Stutzmann, Juretzek, Hadziioannou, and Ardhuin, 2019].

5.1 Local variations in slope factor - a northern hemisphere perspective

In this section, the modeled vertical displacement time series were compared to observations derived from beamforming using two seismic arrays in Europe. For the analysis, a whole year of data in 2013 was used. The estimattion of theoretical seismic sources according to the primary mechanism was based on the output of a current ocean wave model. The analysis focuses on the question how accurately primary microseismic noise observations may be reproduced at both array locations, using either a homogeneous s_{eff} or heterogeneous $s_{\text{eff}}(\mathbf{x})$, which varies with the geographic location $\mathbf{x} = [x_1, x_2, \ldots, x_n]^T$ of the theoretical sources.

For the analysis of observed primary micsoseimic noise, a beamforming approach as detailed in chapter 2 and chapter 4 was applied to the vertical component seismic data from the Norsar array and a Swiss station network subset. A detailed decription of both arrays is provided in chapter 3. Similar to the processing steps in chapter 4, beampower maps in the azimuth-slowness domain were formed for both seismic arrays and the full year of seismic data in 2013. For this purpose, seismic data was downloaded, demeaned, detrended, corrected for the instrument response and the resulting seismic displacement data was filtered between 0.04 Hz and 0.25 Hz using a fourth order Butterworth-Bandpass filter and downsampled to 1 Hz. Beampower maps were calculated within temporal windows of three hours in accordance with the available temporal resolution of the modeled ocean-wave induced primary microseimic noise sources. Following the approach detailed in chapter 4 the beampower maps were calculated as temporal average of the Fourier transformed windowed displacement seismogramms using Welch's method with by 50% overlapping time windows of 1024 s length. Since the vertical component displacement of generated primary microseismic noise is typically dominated by Rayleigh waves, the target of the beamformer analysis was a set to a narrow slowness range corresponding to Rayleigh wave phase velocities as obtained from the analysis in chapter 3. An examination of the azimuth-slowness domain beampower results confirmed that the largest amplitude peaks were located within this slowness range of Rayleigh waves. Time series of observed azimuth dependent vertical displacement PSD $u_{\text{obs}}(f_s, \theta)$ were then evaluated within azimuth bins of 2°.

For the modeling of primary microseimic noise displacement PSD observable at the geographic locations of the arrays, the notation described in chapter 2 was used. The theoretical shallow water seismic sources (Eq. 2.1.7) distributed along coasts derived by [Ardhuin et al., 2015] on the basis of a numerical ocean wave model implementation of WAVEWATCH III [Ardhuin et al., 2014a] was used in order to calculate time series

of theoretical displacement PSD $u_{p,1}(f_s)$ (Eq. 2.1.9) expected at each of the arrays. Theoretical individual source contributions to the total displacement PSD as received at the array centers were integrated according to the Eq. 2.1.9. A homogeneous effective seafloor slope factor of $s_{\text{eff}} = 1\%$, a group velocity of $U = 2.6\,\text{km/s}$ and a quality factor of $Q = 260$ was used for the initial modeling for both arrays. The output of the ocean wave model provides estimates of the ocean-wave spectrum as forced by wind within time steps of three hours. This temporal resolution determined the time steps at which the the ocean-wave induced pressure PSD F_{p1} (Eq. 2.1.1) was available from Ardhuin et al. [2014b].

Correlation with individual theoretical sources

In order to evaluate the temporal accordance between observed displacement PSD and modeled displacement PSD contributions of individual sources, the azimuth dependent time series at a frequency of approx. 0.07 Hz, as observed with beamforming at the array $u_{\text{obs}}(f_s, \theta)$, were correlated with corresponding modeled time series of received displacement PSD from individual source locations $u_{p,1}(f_s)$ within the corresponding azimuthal bin of 2°using the Pearson correlation coefficients C_p. Figure 5.1 shows the resulting C_p mapped to the location markers (dots) of the individual contributing sources. Source locations with $C_p < 0.05$ are not shown here. For certain source regions (parts of the Norwegian Coast, Scottish Coast and French Coast) C_p yields values of more than 0.8 indicating that observed direction dependent PSD time series correlate well with estimates based on the primary mechanism model used here.

These results agree with findings detailed in chapter 4, obtained from a correlation study between directional beamforming results and ocean surface wave parameters. Comparing Fig. 5.1 with Fig. 4.4 of chapter 4 yields an agreement between the most well correlated source regions (especially regions A-C in Fig. 4.4). Results from the Swiss array indicate an additional region of high correlation coefficients at the French coast (marked by the box in Fig. 5.1) which was not evidend from the analysis in chapter 4. For this particular near-coastal region, ocean wave height data was not available and could therefore not be used in chapter 4. The water depth dependent primary microseimic noise amplification factor as shown in Fig. 4.5 (c) indicates geographic locations of potentially efficient primary mechanism noise generation. Considering this water depths dependence, an efficient primary mechanism generation along the French coast is in agreement with the high values of C_p obtained here.

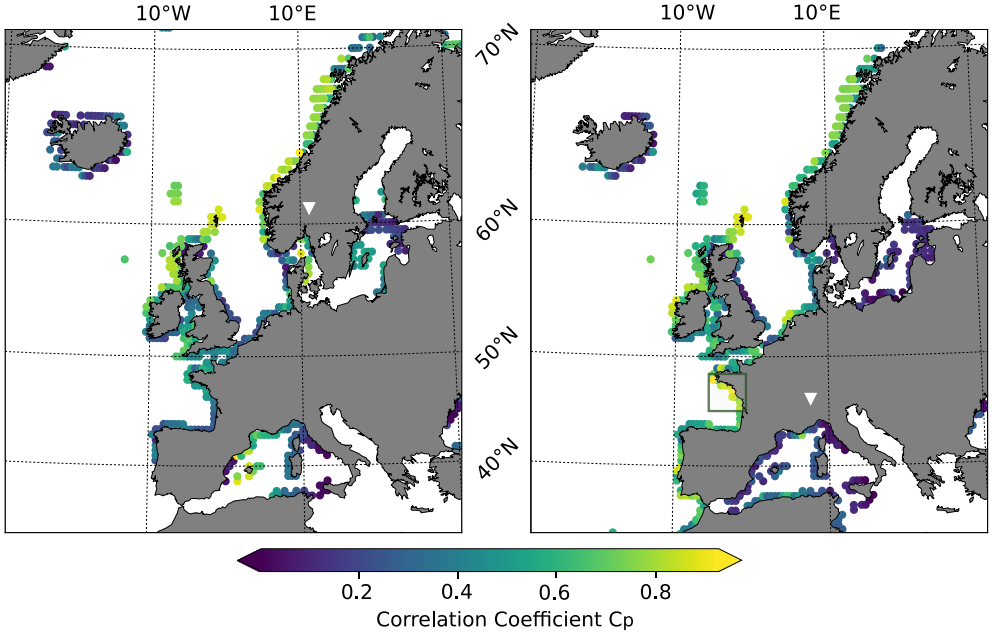

Figure 5.1: Correlation coefficient (color range) between the individual theoretical noise source contributions as received at the array and the observed displacement PSD at both arrays (white triangles). Dots indicate the individual source positions.

Azimuth dependent agreement between model and observations

In order to model the azimuth dependent vertical component displacement PSD $u_{p,1}(f_s, \theta)$ observable at the arrays, the quantity was calculated as direction dependent superposition of those contributions from global coastal primary mechanism sources $S_{p1}(\lambda, \phi, f_s)$ (Eq. 2.1.7) which are located within a defined azimuthal segment. For each azimuthal step of 2°, an angle range of ±5 °was used in order to integrate over modeled source contributions for a direction dependent estimate of the observable displacement PSD. The finite angle was chosen in order to capture propagation path deviations as observed in chapter 4 and structural heterogeneities underneath the array, which may cause biases in the apparent direction of arrival. The modeled source contributions in each azimuth bin were then superposed to form azimuth dependent vertical component displacement PSD according to Eq. 2.1.9 providing $u_{p,1}(f_s, \theta)$ within temporal windows of three hours. As in the previous section, a homogeneous effective seafloor slope factor of $s_{\text{eff}} = 1\%$ and a group velocity of $U = 2.6\text{km/s}$ and a quality factor of $Q = 260$ was used for the initial modeling for both arrays. Here, the integration was performed for an angular propagation distance of $\Delta = \pi$ along the great circle

paths within a given azimuthal segment. Due to the rapid decline in amplitude at the frequency range considered here, the contribution of sources in larger distances than half an orbit around the earth were neglected for estimating the received displacement PSD from a particular azimuth.

For an overview of the average agreement between the theoretical estimate and the beamforming results, monthly means of observed and modeled azimuth dependent vertical displacement PSD were calculated. The mean azimuth dependent displacement PSD was self normalized and the projected on a geographic map using a logarithmic scale. Figure 5.2 shows an example of a monthly mean of the azimuth dependent vertical component displacement PSD (color range) for the Norsar array and the Swiss array obtained from beamforming on one hand and as predicted for both of the array centers by the theoretical model on the other hand. Additionally, the geographic locations of theoretical sources used for the modelling are displayed as dots along the coastlines. In order to reduce the computational time in the following estimation of the locally adapted effective slope factor $s_{\text{eff}}(\mathbf{x})$, the number of source contributions was reduced by source aggregation into areal bins. Here, the total number of theoretical source contributions was reduced in the form of the summation of sources within coastal sections of 500 km length. The source locations are shown in a color range corresponding to the individual contributions of each source section to the received displacement PSD $u_{p,1}(f_s)$ at the array centers of the Norsar array (top) and the Swiss array (bottom) according to Eq. 2.1.9.

Concerning the monthly average shown here, the theoretical predictions reproduce observed direction dependent characteristics at the Norsar array, where azimuths corresponding to relative peaks in the mean monthly modeled displacement PSD are generally in accordance with observed peak azimuths. This suggests that on a monthly average, the theoretical predictions reproduce the most dominant relative azimuthal characteristics at the Norwegian array even without a spatial adaption of s_{eff}.

Modeled observed noise calculated for the Swiss station network center on the other hand deviates more clearly from observations for certain azimuths. In particular, the local source contribution modeled for parts of the Iberian Peninsula seem to be relatively overestimated in comparison to received microseismic noise as observed from corresponding source azimuths. A qualitative estimate of the structural imprint on observed noise levels at both arrays was performed in chapter 4. These results indicated that structural effects in this study region can not be neglected for the frequency range considered here. The determination of the quantitative impact on observed microseismic noise amplitudes due to a heterogeneous crustal structure between the source

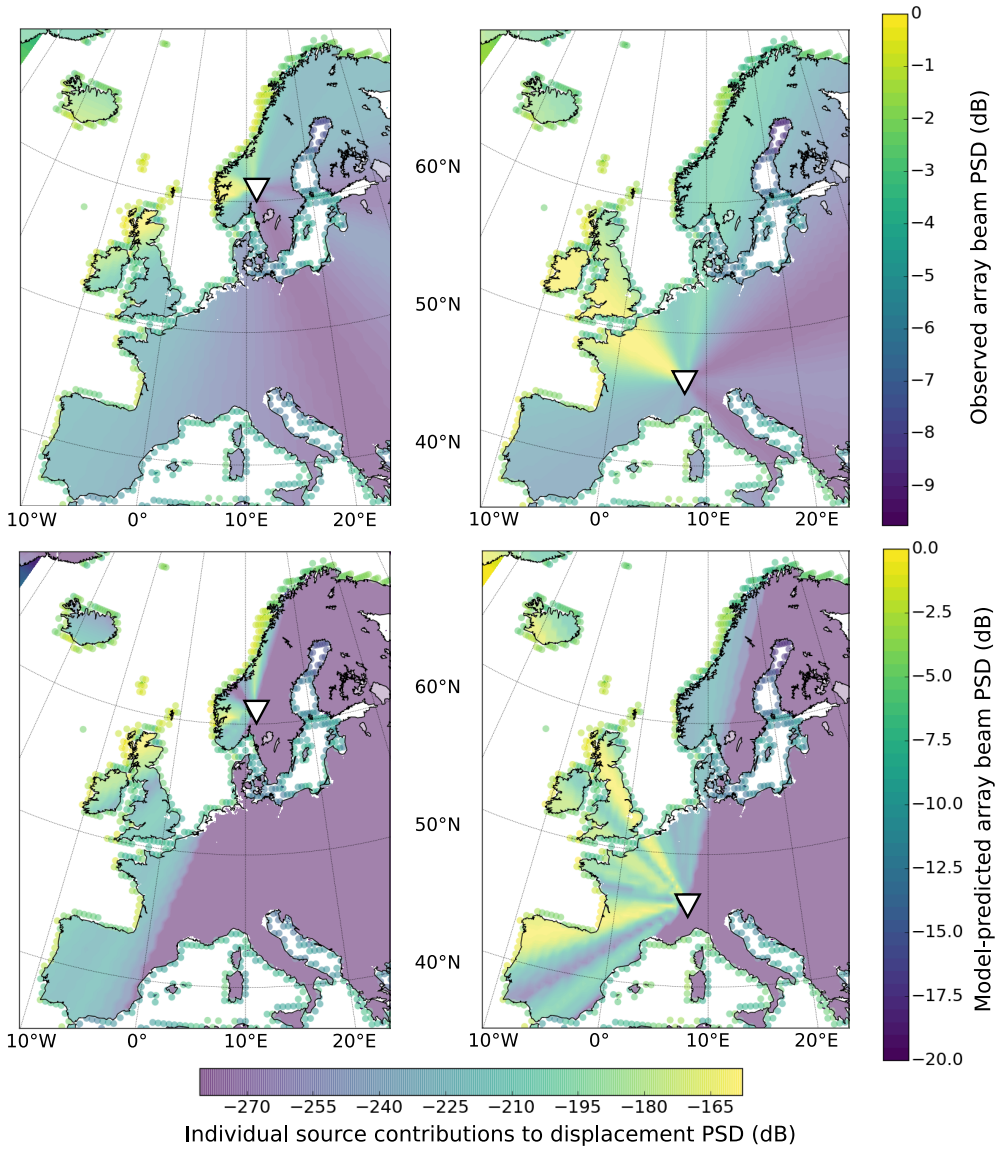

Figure 5.2: In the top row, a direction dependent back-projection of observed beam PSD at a seismic period of approx. 14 seconds in January the Norsar array (left) and the Swiss aray (right) is depicted by color contours. In the bottom row, the analog back-projection of modeled displacement PSD according to the theoretically modeled seismic sources (shown as colored dots) is depicted at both arrays. For comparison with the observation, the modeled seismic sources from the bottom row are also shown the the top row.

regions and the arrays is beyond the scope of this study. Hence, s_{eff} used in the following sections for improving the agreement between the modeled and observed data,

should be interpreted as a factor which captures source and structure effects.

The inclusion of directional information due to beamforming provides clear advantages in terms of the spatial localization of mismatches for the purpose of analyzing the primary mechanism model validity. Yet, a number of limitations have to be remembered concerning the usage of beamforming for this purpose. One limitation is that only the coherent part of the wave field is considered. Hence, due to the suppression of the incoherent part of the wave field as described in chapter 2, beamforming does not provide reliabe absolute amplitude estimates. Acknowledging this, the array based analysis of spatially heterogeneous $s_{\text{eff}}(\mathbf{x})$ in this section considers only relative effective azimuth dependent variations of the effective slope factor. Another drawback of non-ideal arrays is the presence of side lobes in the array transfer function (cf. chapter 2). Especially in the case of interferences between several simultaneous signals, side lobes in the array transfer function may cause biased beampower peaks. To alleviate the influence of these biases on the analysis, the azimuthal information on displacement PSD for both of the arrays used here is retricted to the more robust estimate of the source azimuth of the maximum beampower peak for each time increment and frequency bin. Hence, the amplitude information is neglected and solely the source azimuth of the relatively strongest coherent signal enters the analysis.

For each three hour long temporal window, the direction of arrival corresponding to the observed beampower peak in each sprectral bin is stored in a peak azimuth matrix as examplarily shown in Figure 5.3 (top) for the Norsar array. In a similar manner, a theoretical peak azimuth matrix is formed as predicted from the direction dependent modeled primary microseismic noise expected at the array center location. Modeled and observed maximum source azimuth as observable from an array center are then available for the same spectral and temporal resolution. Figure 5.3 (middle) shows the correspondig modeled peak azimuth matrix for the Norsar array using the initial assumption of a homogeneous s_{eff} in comparison.

For this geographic location, the assumption of a homogeneous s_{eff} (middle) reproduces several detailed sequences of observed (top) source azimuths of the maximum beampower within a frequency range between approx. 0.06 and 0.1 Hz. However, the modeled result overestimates the occurence of peak beampower arrivals from source azimuths between $200^\circ < \theta < 260^\circ$ (blue colors) and underestimates the occurence of peak noise amplitudes from source azimuths between $280^\circ < \theta < 320^\circ$ (purple colors).

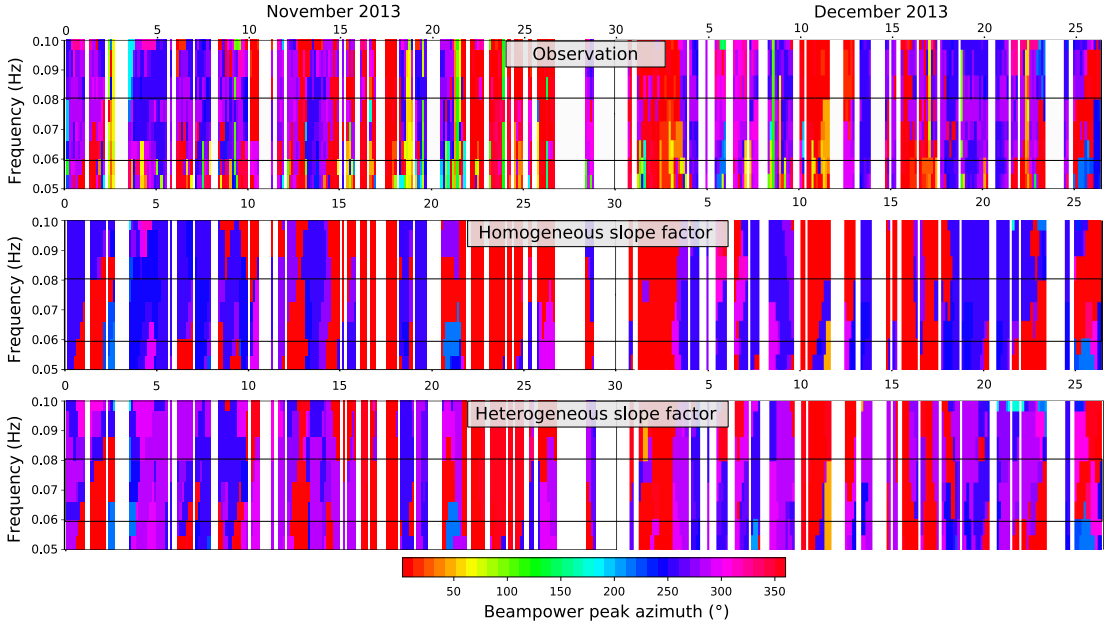

Figure 5.3: Observed (top) and modeled (middle) initial homogeneous s_{eff}, bottom: best optimized $s_{\text{eff}}(\mathbf{x})$) peak beampower signal azimuth of the peak beampower signal within given time and frequency bins at the Norsar array. The colorscale indicates the arrival azimuth clockwise from North. The black boxes indicate the frequency range, which is used for the evaluation of the misfit during the optimization process.

Estimating spatial heterogeneities in the effective slope factor - Europe

In this section, the time series of observed and modeled azimuth dependent vertical displacement PSD are used in order to test if a local heterogeneity of the effective slope factor $s_{\text{eff}}(\mathbf{x})$ may improve the agreement between the predictions and observations. Using both arrays, an optimum solution of $s_{\text{eff}}(\mathbf{x})$ is evaluated according to the azimuth dependent fit between model and observations. The resulting direction dependent deviation of $s_{\text{eff}}(\mathbf{x})$ in comparison to a constant s_{eff} for sources confined within a limited distance range of 3000 km is expected to highlight source regions for which the observed primary microseimic noise is not sufficiently reproduced by the constant s_{eff} and hence, where it might be necessary to extend the modelling approach further in terms of the earth model complexity or the source mechanism description.

Based on the theory of the generation mechanisms in the microseimsic noise band, secondary microseismic noise is expected to dominate observations up to a frequency of 0.1 Hz [Ardhuin et al., 2015]. Due to their higher amplitude in comparison to primary microseismic noise, observations at lower frequencies could still be influenced by sig-

nals generated by the secondary mechanism. Since the target of the analysis are seismic waves which are generated by the primary mechanism at regional scale, the fit optimization is confined to a narrow frequency range around the primary microseimic peak $0.06\,\mathrm{Hz} < f < 0.08\,\mathrm{Hz}$. For each month, a histogram of the number of peak azimuth occurances within this confined frequency range was calculated for the modeled and observed peak azimuth matrices, $N_{\mathrm{mod}}(\theta_i)$ and $N_{\mathrm{obs}}(\theta_i)$ respectively, with $i = 1, ..., 36$ using increments of $10\,°$. The difference vector $\Delta_N(\theta_i)$ between $N_{\mathrm{mod}}(\theta_i)$ and $N_{\mathrm{obs}}(\theta_i)$ indicates where the modeled data overestimates or underestimates the occurance of observed peak signal directions of arrival as shown in Figure 5.4 (a). The quality factor Q was estimated empirically by grid search over a range of Q=[100, 600] as the value which provides the lowest peak azimuth misfit between model and observation according to the L1 norm between the directional azimuth histograms given by

$$M_{l1} = \sum_{i=1}^{K} |N_{\mathrm{obs}}(\theta_i) - N_{\mathrm{mod}}(\theta_i)| \tag{5.1.1}$$

yielding $Q = 200$ at the Norsar array and $Q = 550$ at the Swiss array. However, the local Q is typically not well known at the given freuqency range. With keeping $U = 2600\,\mathrm{km/s}$ fixed, this approach displays a practical estimation of an effective combination of UQ, which is assumed to be constant over the very narrow frequency range consired here.

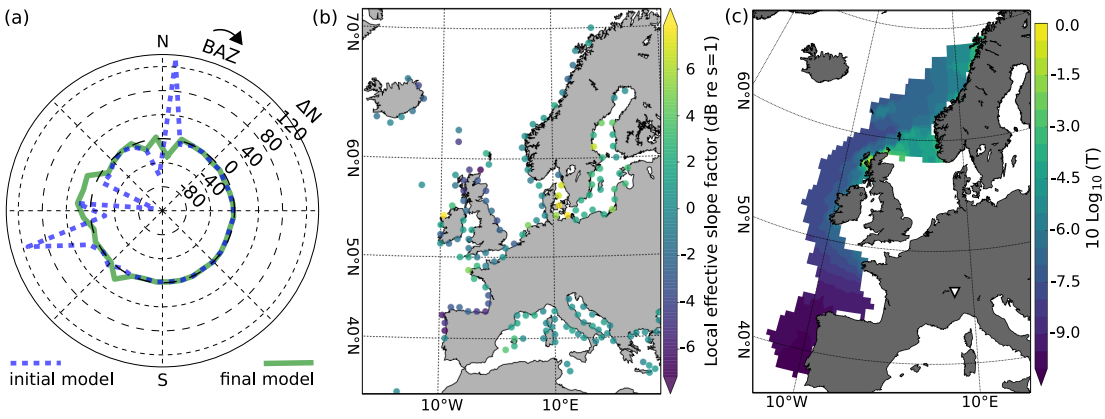

Figure 5.4: (a) Difference vector $\Delta_N(\theta_i)$ indicating where the modeled data overestimates or underestimates the occurance of observed peak signal directions of arrival. (b) Harmony search optimized solution for the effective slope factor variation in comparison to a homogeneous value of s=1 combining both arrays and all 12 month. (c) Transfer factor (ocean wave height to noise) from chapter 4.

5. PREDICTING PRIMARY MICROSEIMIC NOISE, MODELING THE DIRECTIONAL CHARACTERISTICS OF THE NOISE FIELD OBSERVED FROM BOTH SIDES OF THE EARTH

For the purpose of finding a global optimum of locally varying effective slope factors $s_{\text{eff}}(\mathbf{x})$ which minimize the misfit between the modeled and observed peak azimuths histograms as described above, a meta-heuristic optimization approach was chosen. The Harmony Search algorithm [Geem et al., 2001] was used for obtaining a best fitting model vector of $s_{\text{eff}}(\mathbf{x}) = [s_{\text{eff}}(x_1), s_{\text{eff}}(x_2), ..., s_{\text{eff}}(x_N)]$, based on the minimization of the M_{l1} of peak azimuth histograms (Eq. 5.1.1). The optimization of the aggregated source contribution elements in $s_{\text{eff}}(\mathbf{x})$ was confined to sources within a distance range of 3000 km from the array center.

A characteristic of the Harmony optimization approach is the iterative joint optimization of a set of $k = 1, 2, ..., K$ model vectors stored in a matrix, the Harmony memory, given by

$$\text{HM} = \begin{bmatrix} s_1 \\ s_2 \\ .. \\ s_{\text{K}} \end{bmatrix} = \begin{bmatrix} s_{\text{eff1}}(x_1), s_{\text{eff1}}(x_2), ..., s_{\text{eff1}}(x_N) \\ s_{\text{eff2}}(x_1), s_{\text{eff2}}(x_2), ..., s_{\text{eff2}}(x_N) \\ ... \\ s_{\text{effK}}(x_1), s_{\text{effK}}(x_2), ..., s_{\text{effK}}(x_N) \end{bmatrix} \tag{5.1.2}$$

Each model vector $[s_1, s_2, ..., s_{\text{K}}]$ in the Harmony memory is linked to the corresponding L1 norms in the misfit memory $\text{LM} = [M_{l11}, M_{l12}, ..., M_{l1\text{K}}]$. Importantly, new sets of model vectors are generated based on the existing models and new randomly generated models, which are included or disregarded based on method specific criteria detailed below. In order to make use of the directional information available from beamforming, the approach was adapted such that new solution vectors were either generated by a non-directed or by a directed modification of the existing solutions, based on the knowledge on the current over- and underestimation of directional peak occurances or by random choice. The method sprecific pitch adjustment rate P_{ad} was used in order to set the probability of a directed adaption of the elements $s_{\text{eff}}(\mathbf{x})$ corresponding to a specific azimuthal bin θ_i according to the result of $\Delta_N(\theta_i)$. The Harmony memory consideration rate, which is used to steer the probability of choosing random new elements of HM versus the non-directed or directed modification of previous elements, was set to HMCR = 0.9.

The optimum model vector set of $s_{\text{eff}}(\mathbf{x})$ in HM was then estimated by the iterative Harmony Search procedure outlined in the following:

1. the generation of a new element $s_{\text{k+1}}$ of HM, dependent on a randomly drawn number *Rand* from a uniform distribution [0,1]: if *Rand* > HMCR the new $s_{\text{k+1}}$ is a randomly created vector; if *Rand* <= HMCR the new $s_{\text{k+1}}$ is a directed modification using a randomly selected existing element of HM. The directed adaption of the selected elements is achieved according to their corresponding

azimuth bin (θ_i) by addition of a random adaption $mod(\theta_i)$ which sign depends on the corresponding difference vector $\Delta_N(\theta_i)$, enforcing $mod(\theta_i) < 0$ for $\Delta_N(\theta_i) > 0$ (overestimation) and an $mod(\theta_i) > 0$ for $\Delta_N(\theta_i) <= 0$ (underestimation),

2. the calculation of the L1 norm M_{l1k+1} for the new solution,

3. the new solution is either accepted and included in HM by replacing the least optimal existing solution if $M_{l1k+1} < min(LM)$ or is disregarded otherwise.

The iterative search was stoped when either a maximum of 2500 iterations were reached or when the decrease rate of $Lnorm_{new}$ stagnated for at least 150 iterations.

The Harmony search approach was implemented in Python using the multiprocessing and functools packages in order perform the optimization for the full year in parallel processing.

In order to depict the optimization process we consider the month November at the Norsar array. Figure 5.4 (a) shows the initial and the final best result of $\Delta_N(\theta_i)$. The initial azimuthal overestimation and underestimation regarding the directional beampower peak occurences is significant and exceeds more than 100 occurences per month for certain azimuths. This mismatch corresponds to predicted abundances of azimuths near $\theta \approx 250\,^\circ$ (blue colors) and $\theta \approx 300\,^\circ$ (purple colors) in Fig. 5.3 (middle). During the optimization approach the azimuthal mismatch decreased to less than 40 overestimations and underestimation per month with a relatively even distribution in azimuth (cf. Fig. 5.4 (a)). Likewise, the improvement between observations and optimized result is visible by examining the bottom plot of Figure 5.3.

Here, the twelve optimized sets of HM in 2013 according to the Harmony search approach were estimated from jointly minimizing $\Delta_{N_{NOR}} + \Delta_{N_{SW}}$ at both arrays for each month. The best model vector of $s_{\text{eff}}(\mathbf{x})$ was then considered as the mean $s_{\text{eff}}(\mathbf{x})$ over the twelve optimized sets of HM in 2013. This approach aims at a reduction of the incluence of path effects and site effects on the resulting $s_{\text{eff}}(\mathbf{x})$. In practice, primary microseimic noise observed at the arrays is determined by the seismic source term, which scales with s_{eff} according to the theory, but also by e.g. structural effects. The unknown influence of structural heterogeneities, but also of the subsurface underneath an array, is assumed to remain constant over the analyzed time span. On the other hand, the regional distribution of seismic source amplitudes is expected to vary over time. Hence, the optimization approach taken here is expected to mainly respond to the seismic source term dependent misfit between model and observations.

Figure 5.4 (b) shows the annual combined result of $s_{\text{eff}}(\mathbf{x})$ that optimizes the fit between model and data at both arrays. The effective slope factors are shown at the

corresponding individual source locations according to the color range relative to a mean s_{eff} of 1%. A noteworthy decrease in s_{eff} is found for a major part of the Iberian Peninsula.

The result of s_{eff} obtained in this section may be compared to results from chapter 4, where observed primary microseismic noise at the same seismic arrays was compared to the ocean surface displacement variance $E(f)$ in Eq. 2.1.1.

Results of the relative spatial increase and decrease in $s_{\text{eff}}(\mathbf{x})$ are in agreement with results of noise generation transfer factors T for the vertical component, which were obtained in chapter 4 and reprinted in Figure 5 bottom row. A high transfer factor in chapter 4 indicated a region of efficient noise generation i.e. high primary microseismic noise amplitudes for given ocean wave heights in the source region.

High transfer factors were found in chapter 4 for the Norwegian coast and the British Isles, which agrees with a local relative increase of the resulting slope factors $s_{\text{eff}}(\mathbf{x})$ in this chapter. A more pronounced shallow water topography in these areas could be one reason for a local increase in the effective slope factor. Likewise, the low transfer factor values in chapter 4 around Portugal and Spain are in accordance with a relative decrease of effective slope factors in this chapter. The relatively high quality factor $Q = 550$ obtained in this chapter for the Swiss array could be partly influenced by the overestimation of source azimuth occurances from south-western directions according to the model. Observations confirm significantly less time windows during which the peak coherent noise PSD arrives from these azimuths. The transfer factors T in chapter 4 may be interpreted as estimate of an effective source term scaling factor T, based on the assumed linear seismic source term dependence on ocean wave height. While this chapter provides a more comprehensive estimate of an effective source term scaling factor s_{eff} based on the theoretically modeled primary mechanism source distribution. Hence, results obtained in both chapters indicate that either the true seismic source contributions are overestimated by the model or that microseisms generated in these regions are significantly attenuated on their propagation path to central Europe.

Complementing single station analysis

In order to further investigate whether the slope factor variations around the Iberian Peninsula reflect source region effects or structural effects along the propagation path, a complementary analysis of vertical component data from individual seismic stations was performed. Two of the seismic stations used for this purpose were located near to the northern coast of the Iberian Peninsula. Another station on the british Isles was used for comparison. Due to the limited source-receiver distances here, the effects of

attenuation and structural heterogeneities are assumed to be nelegible in comparison to the source term effects.

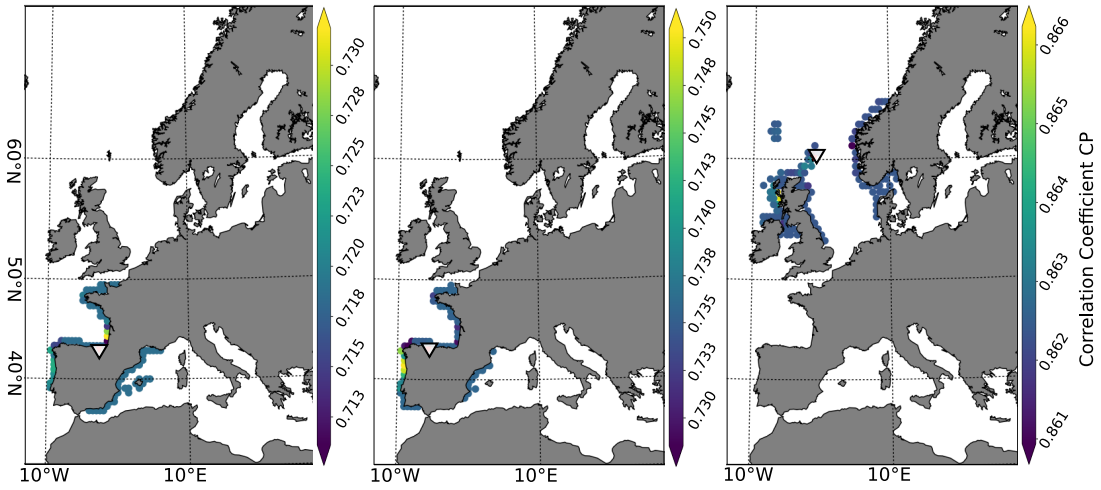

Figure 5.5: Jackknife test showing the Pearson correlation coefficient (color range) between the observed and modeled time series of displacement PSD at three seismic stations (marked by a triangle) obtained when disregarding each individual source contribution as indicated by dots. The source dots show the correlation coefficient resulting from their omission.

As detailed in the previous section, observed and modeled time series of vertical component displacement PSD at the different seismic station locations were calculated for the full year of 2013. In order to test the impact of individual source contributions on the temporal correlation between the model and the observation, a Jackknife test was performed. Therefore, individual source contributions were subsequently disregarded in the calculation of the modeled displacement PSD time series. The effect on the fit between model and data is evaluated based on the C_p correlation coefficient between both RMS displacement time series. Figure 5.5 (a) shows the result of the Jackknife test for the source locations displayed as colored dots. For both stations at the north coast of Spain the results of the Jackknife test show an increase in C_p when certain source contributions along local coasts were disregarded. These locations correspond to an extended region for which a decrease in $s_{\mathrm{eff}}(\mathbf{x})$ lead to an optimized fit between the modeled and observed time series in the array analysis. This agreement hints towards a possible local overestimation in modeled source terms, which is apparent at seismic stations in near and far distance. In contrast, no significant variation in C_p was found for a station north of Great Britain (cf. the color scale limits). Likewise, only a

moderate heterogeneity of $s_{\text{eff}}(\mathbf{x})$ was found from the arrays analysis, indicating that the model was capable of more accurately predicting the locally received microseismic noise in Great Britain.

Conclusion

In this section, primary microseismic noise displacement PSD were modeled and compared to observations at different array locations in Europe. In summary, results obtained here show that the modeled primary microseimic noise assuming a constant effective slope factor and a radially symmetric earth model may reproduce the dominant characteristics of observations. However, the modeled results for both arrays used here, differ in their agreement with observations. Regarding the validity of the constant slope factor assumption, a direction dependence of the qualitative agreement between model and observations hints to a spatial heterogeneous influence given by e.g. structual effects or source effects. Results from a complementing single station analysis indicate, that certain local effective slope factor adaptions in southern Europe are more likely caused by source region effects, since the single station results near the source region support a corresponding overestimation of individual source contribution in agreement with the array based analysis.

5.2 Local variations in slope factor - a southern hemisphere perspective

In this section, local effective slope factor variations $s_{\text{eff}}(\mathbf{x})$ were estimated based on a simmulated annealing approach using seismic data fom two single stations in the southern hemisphere. Parts of the content presented here, were published as section 3.4 in a global study [Gualtieri et al., 2019] on the validity of the theoretical model for predicting primary microseismic noise amplitudes described in Ardhuin et al. [2015].

The comparison between modeled and observed vertical-component displacement PSD at stations from the global Geoscope network yielded an overall high agreement as detailed in Gualtieri et al. [2019]. However, significant deviations at a frequency of $f = 0.05\,\text{Hz}$ were found for a seismic station in Australia (CAN). Interestingly, such a mismatch was not observed for other frequency ranges. In order to investigate whether the disagreement between model and observations at this particular frequency and location may be linked to the noise generation at specific source regions, a full year of seismic data in 2013 from two different stations around Australia was analyzed. Further, it was examined whether a small scale spatial variation of the effective slope

factor $s_{\text{eff}}(\mathbf{x})$ allows to improve the agreement between the model and the observations in this region.

Estimating spatial heterogeneities in the effective slope factor - Australia

For the regional analysis of local effective slope factor variations $s_{\text{eff}}(\mathbf{x})$ in the southern hemisphere around Australia, a full year of seismic data in 2013 recorded at two seismic stations of the Geoscope network, CAN and NOUC, was used. Similar to the processing steps in section 5.1, time series of seismic displacement PSD $u_{\text{obs}}(f)$ were formed for both seismic stations for temporal subwindows of three hours according to the available temporal resolution of the ocean wave generated primary microseimic noise source terms as described by Ardhuin et al. [2015]. For this purpose, data from BHZ channels of both stations was downloaded, corrected for the instrument response, filtered between 0.04 and 0.25 Hz using a fourth order Butterworth-Bandpass filter and downsampled to a sampling rate of 1 Hz. The displacement PSD $u_{\text{obs}}(f)$ in each time step of three hours was calculated using Welch's method averaging the Fourier transformed windowed displacement seismogramms using by 50% overlapping time windows of 1024 s length. In order to align with the processing approach described by Gualtieri et al. [2019], vertical component seismic displacement PSD time series from the LHZ channel of both stations processed according to the description by Gualtieri et al. [2019] were considered additionally. A comparison between resulting displacement PSD time series of both channels yielded approximately identical results, hence the BHZ channel data was used in this analysis. Finally, the time series of displacement PSD $u_{\text{obs}}(f)$ and RMS displacement $u_{\text{obs},RMS}$ were then formed by considering the respective minimum amplitude within each non-overlapping temporal windows of 24 hours. The frequency range of interest was constraint to a range between $f_1 = 0.05$ Hz and $f_2 = 0.08$ Hz.

Corresponding modeled time series were formed according to Eq. 2.1.9 by integrating over all global source contributions to the total seismic displacement PSD theoretically received at the target station. Here, a quality factor of $Q = 249.9$ and a Rayleigh wave group velocity of $U_R = 3.322$ km/s were used in Eq. 2.1.9 corresponding to the values from Gualtieri et al. [2019]. Similar to the treatment of the observations, time series of modeled displacement PSD $u_{mod}(f)$ and RMS displacement $u_{\text{obs},RMS}$ were then obtained as the minimum within each temporal window of 24 hours.

Since we aim at reproducing the true displacement amplitudes observed at both seismic stations, the modeled individual source terms may be scaled to a first order fit by means of an overall global effective slope factor s_{eff}. An overall value of $s_{\text{eff}} = 8$

at station CAN and of $s_{\text{eff}} = 15$ at station NOUC was used, representing the value of s_{eff} which minimized the L1-norm misfit between the 24h sampled minimum displacement times series of model and observations at the corresponding station as detailed in Gualtieri et al. [2019]. Figure 5.6 (a) and (b) show the resulting RMS minimum displacement time series corresponding to the observation and the model at $f_1 = 0.05\,\text{Hz}$ and for the higher frequency range of $[0.067, 0.08]\,\text{Hz}$, respectively. The model closely reproduces the observed primary microseismic noise RMS minimum displacement at the higher frequency range $[0.067, 0.08]\,\text{Hz}$ except for an high amplitude peak in the observations. Contrasting this, the mismatch at $f_1 = 0.05\,\text{Hz}$ is striking. At this frequency, the modeled time series (red) shows a significant overestimation of RMS minimum displacement amplitudes for the station location of CAN. In particular, regarding the extreme amplitude peaks, which do not exist in the observations. Nevertheless, the overall slope factor of $s_{\text{eff}} = 8$ enables the reproduction of the mean baseline of the observed time series.

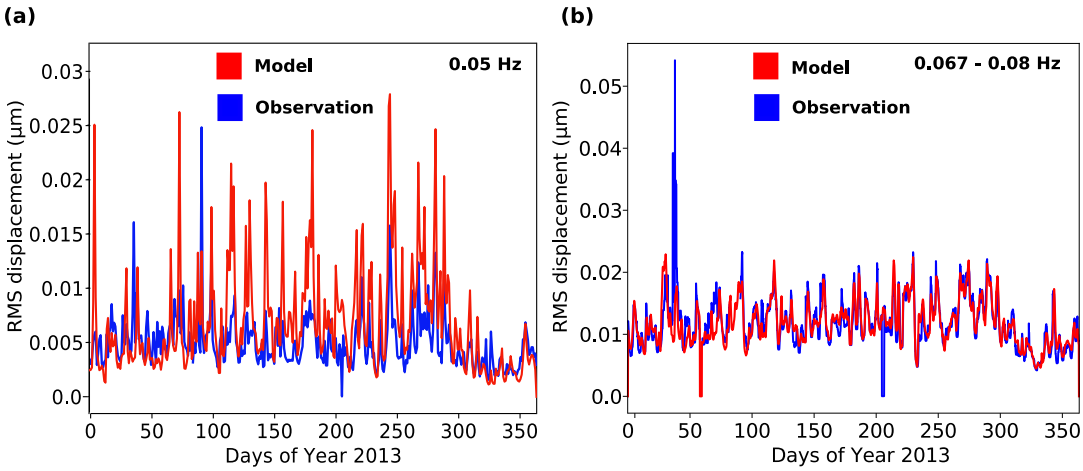

Figure 5.6: Time series of vertical displacement amplitudes from data and model at station CAN, using an overall slope factor of 8 at (a) 0.05 Hz and (b) $[0.067, 0.08]\,\text{Hz}$.

This striking deviation between model and observations for high amplitude peaks at 0.05 Hz might be related to the source on one hand e.g. by (1) a mismatch between modeled and true source terms at particular geographic locations, or by (2) an overall regional overstimation by the model at larger wave heights. On the other hand it might be related to (3) propagation path effects, which diminish the generated microseismic noise amplitudes more than expected from the homogeneous structural model assumed here.

For the estimation of local slope factor variations, the total number of modeled source contributions was reduced by an aggregation of theoretical source contributions within coastal bins of 500 km. In order to examine the geographic origin of the spectral particularity regarding the agreement between model and data, the time series of observed minimum displacement PSD were correlated with corresponding modeled time series contributed by each individual aggregated source bin. Despite a significant misfit between modeled and observed time series was found in amplitude, the temporal agreement of amplitude variations might still hold. Here, the Kendall Tau rank correlation coefficient τ_b (Eq.2.2.18) was used. Figure 5.7 shows the corresponding rank correlation coefficient for both frequency bands analyzed. The maximum τ_b is found for the southern coast of Australia at both frequencies, indicating that these regions produce an important contribution to the recorded temporal pattern in the displacement time series relative to other locations.

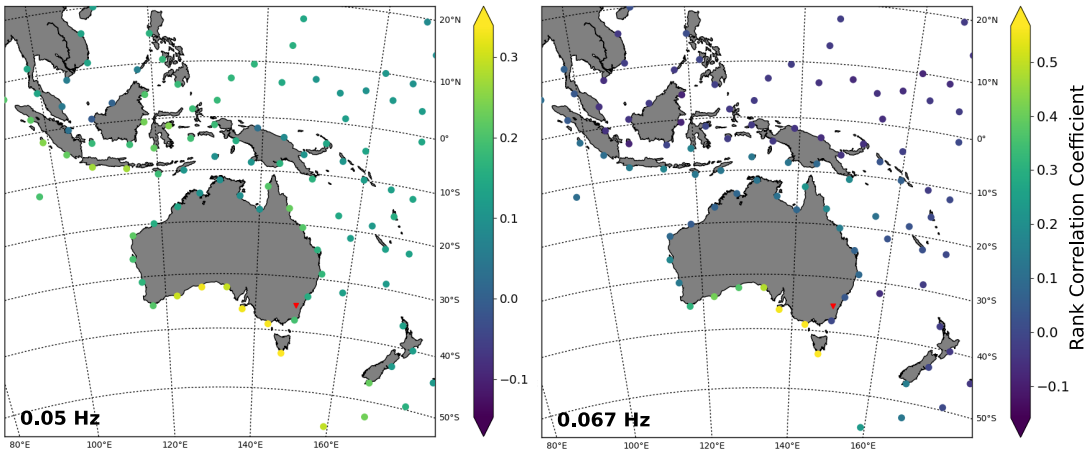

Figure 5.7: Rank correlation coefficient τ_b (color range) between the time series of the individual modeled noise source contributions and the observation for station CAN at 0.05 Hz and 0.067 Hz. Dots indicate the aggregated contributing sources.

Further, the decrease of τ_b with distance to station CAN is more pronounced at 0.067 Hz than at 0.05 Hz. This agrees with the general finding in [Gualtieri et al., 2019], that observed primary microseimic noise at around f=0.05 Hz is determined by source contributions on a hemispherical scale, while the recorded microseisms at around f=0.08 Hz are mainly determined by regional source contributions. Interestingly, maximum values of τ_b obtained for $0.067\,Hz$ exceed the resulting τ_b values for $0.05\,Hz$, which yield $\tau_b \leq 0.33$, even for the southern Australian coasts.

5. PREDICTING PRIMARY MICROSEIMIC NOISE, MODELING THE DIRECTIONAL CHARACTERISTICS OF THE NOISE FIELD OBSERVED FROM BOTH SIDES OF THE EARTH

For the further analysis of the peculiar disagreement between model and observations, we perform a Jackknife test by subsequently disregarding each individual source contributions around Australia during the calculation of the modeled displacement PSD time series. In order to analyze the impact of the neglection of a given coastal sections, the L1-norm misfit between modeled and observed time series at $f_1 = 0.05\,\mathrm{Hz}$ is considered. The Jackknife test was performed for individual source contributions on two different spatial resolutions, for the aggregated sources and for the total number of theoretical sources derived by Ardhuin et al. [2015] within a limited sections of southern Autralia. Figure 5.8 (a) shows the result of the Jackknife test for the aggregated source contributions as colored dots represented by a central position in each coastal source bin. Additionally, the inset shows results of the Jackknife test using the non-aggreagated sources along the south coast of Autralia. Interestingly, relatively lower misfits according to the L1-norm are obtained when source contributions from the southern Australian coast are disregarded in the modeled data for both cases. The non-aggregated result further highlights that the L1-norm misfit decreases over a continuous section of the southern Australian coast and Tasmania. Nevertheless, the exclusion of one particular source contribution at the Tasmanian coast is responsible for a clear maximum in misfit decrease. Still, the southern coastal mismatch appears to be caused by an extended coastal section and is not caused by single outliers. This hints towards a specific geographic region at the southern Australian coast, for which observed primary microseimic noise amplitudes are not well represented by the modeled noise contributions at this frequency.

The ocean-wave induced pressure PSD of the primary mechanism $F_{p,1}$ scales linearly with the primary microsseismic noise source term (cf. Eq. 2.1.7). The significant mismatch at $f_1 = 0.05\,\mathrm{Hz}$ appears to be influenced by the high peak amplitudes predicted by the model for southern Australia. Since $F_{p,1}$ varies over several orders of magnitude according to the known variability of the oceans wave state over space and time, in practice only the strongest source contributions yield a relevant individual impact on the misfit regarding the peak amplitudes. In contrast, the weaker and more distant regional and global sources mainly contribute to the amplitude baseline level. The overall value of $s_{\mathrm{eff}} = 8$ was evaluated based on the L1-norm rearding the displacement PSD over the frequency range $[0.05, 0.08]\,\mathrm{Hz}$ as described in detail by Gualtieri et al. [2019]. It therefore accounts for the fit of the amplitude baseline and peaks to a similar degree as well as for the whole spectral bandwidth.

In practice, an effective slope factor as high as $s_{\mathrm{eff}} = 8$ does generally exceed realistic seafloor slopes in water depths relevant for the primary microseismic noise band, as already discussed by Ardhuin et al. [2015]. Moreover, the effective seafloor

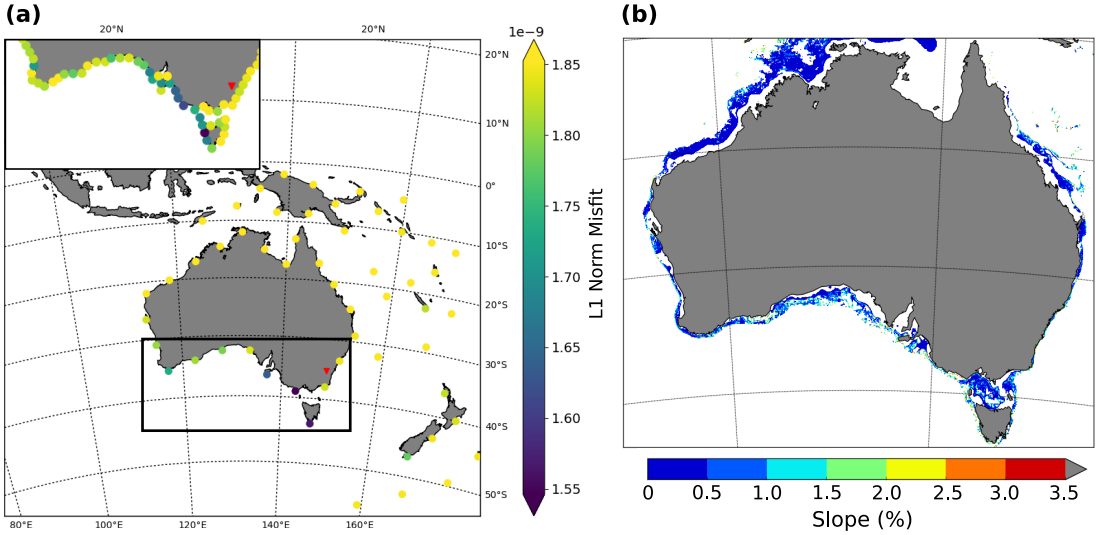

Figure 5.8: (a) Result of the Jackknife test showing the L1-norm misfit between the modeled and observed time series obtained when disregarding individual theoretical aggregated source contributions indicated by colored dots. The inset shows detailed results using the non-aggreagated sources. The source dots show the correlation coefficient resulting from their omission. (b) Large scale seafloor inclination calculated for Etopo1 bathymetry data.

roughness and the effective seafloor slope depend on the length scale considered. Due to the lack of high resolution bathymetry data with length scales, relevant for primary microseismic noise generation, a realistic estimate of these properties is beyond the scope of this study. For an indicative estimate of the variation of the large scale nearcoastal seafloor slope around Australia, the gradient of the Etopo1.0 bathymetry dataset [Amante and Eakins, 2009] was calculated as shown in Figure 5.6 (a), yielding values which do not exceed 4 %. Hence, the high overall effective slope factor of 8 likely reflects the presence of additional small scale bathymetry variations which effectively contribute to the ocean-wave induced pressure PSD (Eq. 2.1.1) Ardhuin et al. [2015]. Keeping in mind, that the bathymetry resolution is not sufficient for the frequency range considered, the present gradient estimate did not provide an evidence for a specific deviation of s_{eff} for southern Australia.

For the estimation of local effective slope factor adaptions for the aggregated areal bins $s_{\text{eff}}(A_i)$, which further minimize the misfit between the model and the data, a simulated annealing approach is applied, which is a metaheuristic method introduced by Kirkpatrick et al. [1983] suited for multivariate optimization. The most striking deviations between data and model at a frequency of $0.05\,Hz$ were found to be significantly

determined by the disagreement of the amplitude peaks in the RMS displacement time series (cf. Fig. 5.6). The misfit in the simulated annealing approach is evaluated based on the RMS error,

$$M_{RMS} = \sqrt{\frac{1}{N}\sum_{i=1}^{N} |\{a_{\mathrm{obs}}(t_i) - a_{\mathrm{mod}}(t_i)|^2\})} \tag{5.2.1}$$

aiming at a high sensitivity to necessary adaptions in $s_{\mathrm{eff}}(A_i)$ at geographic locations which cause a severe model-data mismatch at peak amplitudes.

In order to prevent the inclusion of source contributions in the optimization process, which are not sufficiently resolved by observations, the adaption of $s_{\mathrm{eff}}(A_i)$ was regionally confined. The sensitivity of the misfit regarding a modification of each individual aggregated source bin A_i was estimated. For this purpose, each aggregated source was scaled by $10^{0.2}$ and $10^{-0.2}$. The corresponding difference in misfit δM_{RMS} for each aggregated source bin was normalized by the regional median on a logarithmic scale. Source bins for which this sensitivity measure did not exceed -20 dB relative to the regional median, were not considered for the estimation of local effective slope factor $s_{\mathrm{eff}}(A_i)$ adaptions. $s_{\mathrm{eff}}(A_i)$ was then estimated by the simmulated annealing procedure described below, while minimizing the initial misfit $M_{\mathrm{RMS}i}$ between the observed and modeled minimum RMS displacement annual time series. The estimate of $s_{\mathrm{eff}}(A_i)$ is performed with the following iteration procedure with $k = [1, ..., N]$:

1. the generation of a model of $s_{\mathrm{eff}}(A_i)$ where the slope factor adaption in each iteration is randomly drawn from a uniform distribution in the range [-0.3,0.3],

2. the calculation of the misfit $M_{\mathrm{RMS},k+1}$ for the new model,

3. the acceptance of slope factor adaptions: if $M_{\mathrm{RMS},k+1} < M_{\mathrm{RMS}k}$ the new model is accepted with probability $P = 1$; else the new model is accepted with a probability of $P = e^{-(M_{\mathrm{RMS},k+1} - M_{\mathrm{RMS}k})K/T}$.

The simulated annealing approach was implemented as iterative procedure, where the individual elements of $s_{\mathrm{eff}}(A_i)$ were updated consecutively in order. This approach was chosen, since it provided a more rapid convergence of slope adaptions for the most dominant source contributions than a joint adaptions of all points simultaneously. The probability P of the acceptance of slope factor adaptions follows a modified Metropolis criterion (Metropolis et al. 1953) described in the iterative procedure above. The annealing temperature T varies with iteration number according to the annealing schedule. The annealing schedule was set as an annealing temperature decrease after 25 full cycles through all source region bins according to $T = T_0 0.8^{k/25}$, with the initial temperatur

T_0. The scaling factor defined as $K = \frac{10}{M} \sum_{m=1}^{M} |a_{obs}(t_m)|$ allows the further steering of the model acceptance slowdown. For the generation of new models, the accepted range of $s_{\text{eff}}(A_i)$ was bounded within a symmetric range of 1 and 16 around the overall mean of $s_{\text{eff}} = 8$ for station CAN and of 1 and 30 around the overall mean of $s_{\text{eff}} = 15$ for station NOUC.

Figure 5.9 shows the resulting $s_{\text{eff}}(A_i)$ which minimize the misfit between observations and model according to the simmulated annealing process. The iteration process was stopped when the decrease rate of the misfit stagnated for at least 150 iterations Fig. 5.9 (c). Homogeneously coloured dots correspond to the initial, unmodified s_{eff}, which cover partly different geographic areas for CAN and NOUC, according to the set of sensitive source bins included in the adaption. For both stations, the optimized $s_{\text{eff}}(A_i)$ which minimized the misfit between modeled and observed RMS amplitude time series, shows a significant downweighting of source contributions from the southern Australian coast on one hand. On the other hand, source contributions in the vicinity of station NOUC and of New Zealand's coasts show a similar downweighting (cf. Fig. 5.9 (a)). In contrast to this, a consistent increase of $s_{\text{eff}}(A_i)$ is found for the east Australian coast, while a non-consistent increase is found for sources located within the area indicated by a red square in the maps of Fig. 5.9 (a).

Figure 5.9 (b) shows time series of observed displacement RMS amplitudes for both stations at $f = 0.5\,\text{Hz}$ in comparison with the modeled results using the initial s_{eff} and the final optimized $s_{\text{eff}}(A_i)$ corresponding to the reduced misfit shown in panel (c). An overestimation of peak amplitudes by the initial homogeneous s_{eff} occurs for both stations here. However, peak amplitudes are overestimated to a lesser degree for station NOUC with the initial homogeneous value of $s_{\text{eff}} = 15$. Hence, an optimized solution of $s_{\text{eff}}(A_i)$ must ensure an improved agreement between peak amplitudes in modeled and observed time series. The resulting optimum $s_{\text{eff}}(A_i)$ shown in Fig. 5.9 (a) yields that a misfit reduction regarding these peak displacement amplitudes could only be achieved by a severe downweighting of the peak RMS displacement contributions generated at the southern Australian coast, i.e. by very low values of $s_{\text{eff}}(A_i)$ in this region for both stations considered. The effective slope factor for southern Australian sources which minimizes the misfit corresponds to the minimum of the allowed range during the simmulated annealing, with a value of $s_{\text{eff}}(A_i) = 1$. At the same time, the agreement regarding the overall mean amplitude level of the modeled and observed minimum time series could be retained for station CAN and even be improved for station NOUC. The downscaling of southern Australian coast sources, but also the upscaling for the east coast, display a robust result which was also found in a number of additional test

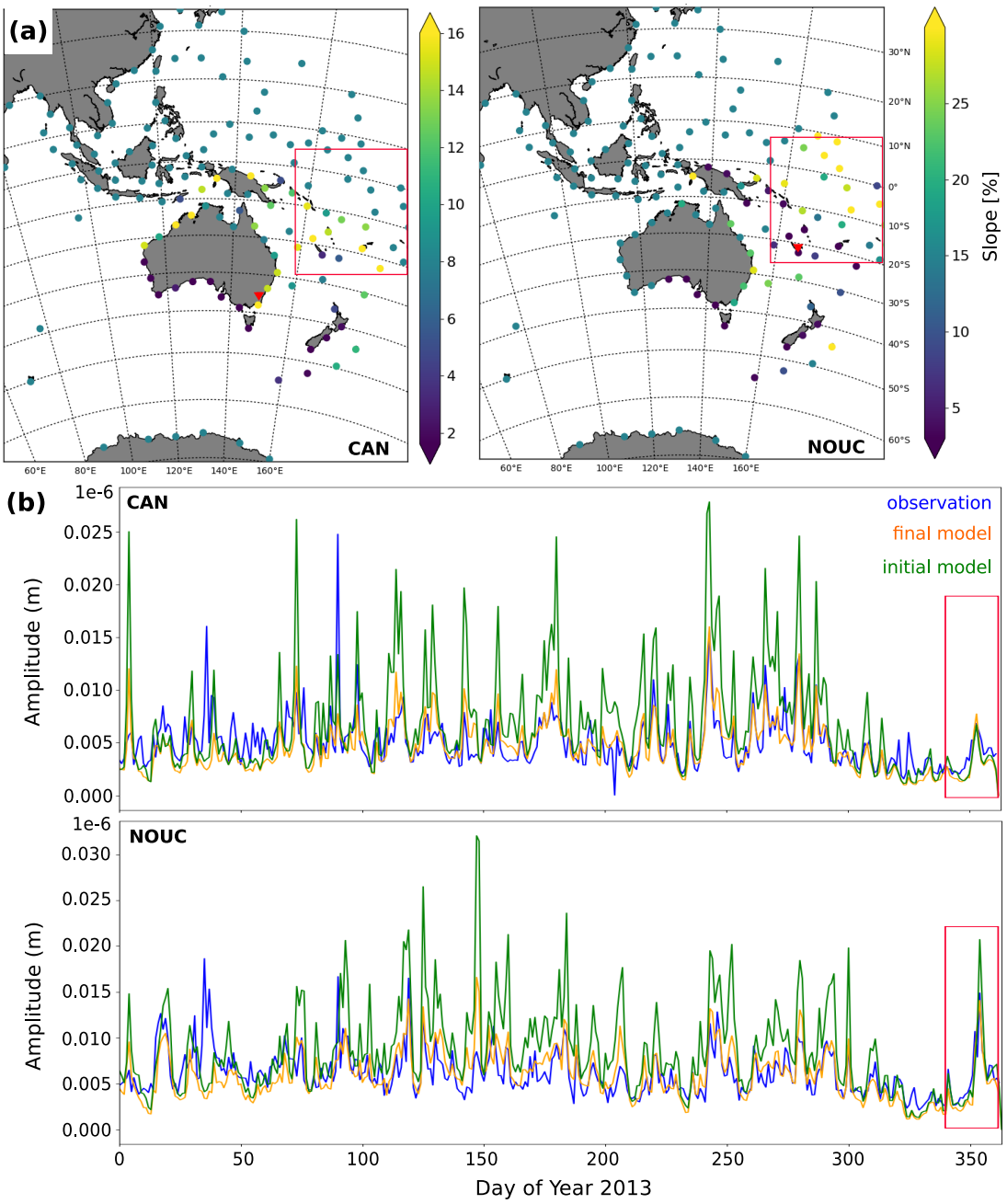

Figure 5.9: (a) Map view of the final $s_{\text{eff}}(A_i)$ (color range) for station CAN and NOUC at $f = 0.5\,\text{Hz}$. (b) Time series of modeled displacement RMS amplitudes for both stations in comparison to observations; with the initial $s_{\text{eff}} = 8$ and the final optimized $s_{\text{eff}}(A_i)$.

runs of the optimization process using different configurations, such as a different areal aggregation of sources and a higher time sampling (12 hours instead of 24 hours). The increase of $s_{\text{eff}}(A_i)$ at other geographical locations however, partly differed between both stations and for different test settings. This includes the downscaling of sources in the vicinity of station NOUC.

An noteworthy amplitude peak during December of 2013 appears in the time series of both stations as highlighted by the red boxes in Fig. 5.9 (b). Interestingly, no overestimation of this particular peak amplitude occured with the initial model at station CAN and a only moderate initial overestimation occured at station NOUC. In contrast to most other extreme amplitude peaks, the source region responsible for this peak is likely not located along the southern Australian coasts, since the modeled peak amplitude between the initial and the optimized $s_{(A_i)}$ did not significantly differ for station CAN. This microseismic noise burst more likely originates from a region, which is near station NOUC, concluded from the large relative amplitude of the peak in comparison to the overall mean level. Furthermore, the due to the stability in peak amplitude between initial and optimized time series, the potential source area likely corresponds to an area for which $s_{\text{eff}}(A_i)$ was not significantly adapted for station CAN and only moderately adapted for station NOUC during the simmulated annealing. A region which likely includes the source area of this peak is highlighted by the red box in the map views of panel (a). Hence, the accuracy of modeled source contributions obtained from the homogeneous s_{eff} approach seem to differ between certain subareas in the Australian region.

In order to further analyze the spatial accuracy of the model representation, 9 different subareas were considered. Figure 5.10 (a) shows an analysis of all 9 coastal sections (as indicated by colored regions in the map inset) with respect to their influence on the modeled time series for station CAN in comparison to the observation at a frequency of $f = 0.05\,\text{Hz}$. The southernmost Australian and Tasmanian coast (section 4) corresponds to low values of s_{eff}. The correponding modeled time series in (a) and (b) highlight the presence of very strong amplitude peaks which stand out from the overall minimum level. In contrast, section 5 corresponds to a region of increased values of s_{eff}. For this region, the modeled source contributions do not show as extreme variatons in modeled amplitudes as source contributions of section 4. Modeled sources in section 1, a region which includes the station NOUC, indeed contribute significantly to the amplitude peak observed during December in Fig. 5.9 (b). Although the local coasts of Australia were found to contribute most of the displacement PSD observed at CAN (cf. [Gualtieri et al., 2019]) at all frequencies, this observation indicates, that primary microseismic noise generated near the Pacific islands may still contributes to the RMS

displacement time series at $f = 0.05\,\mathrm{Hz}$ observed at CAN. In particular, the Pacific Island souces should be taken into account for a correct model prediction during time spans, when local source contributions from the Australian coast are at their minimum.

Conclusion

In this section, observed time series of vertical component displacement in the primary microseismic noise band were quantitatively compared with modeled time series according to the primary mechanism theory Ardhuin et al. [2015]; Hasselmann [1963] for two seismic stations in the Australian region. An observed mismatch between the modeled expectations and the observations arising at a frequency of $f = 0.05\,\mathrm{Hz}$ could be significantly improved by the adaption of the homogeneous effective slope factor s_{eff} to a local varying effective slope factor $s_{\mathrm{eff}}(A_i)$.

The improved fit between modeled and observed displacement time series at $f = 0.05\,\mathrm{Hz}$ could be achieved by a decrease in $s_{\mathrm{eff}}(A_i)$ along the southern Australian coast and an increase along the eastern Australian coast and the Pacific island sources. Interestingly, the modeled peak amplitudes from source contributions along the southernmost Australian coast seem to significantly overestimate the observations. A reduction of $s_{\mathrm{eff}}(A_i)$ to the minimum allowed value was able to optimize the fit between model and observations. At the same time, the observed RMS displacement time series was found to be comparably well correlated in time with modeled source contributions from southern Australia as with source contributions from other locations (cf. Fig. 5.7). On one hand, this decrease in $s_{\mathrm{eff}}(A_i)$ might hint towards a possible overestimation of the source term in this geographic region. However, this would require a bias, which only influences the specific frequency $f = 0.05\,Hz$. The estimate of the ocean-wave induced pressure PSD as source of the primary microseismic noise could be affected by a possible bias in the ocean wave model results. The analysis of this possibility is beyond the scope of this study. On the other hand, structural effects could lead to a significant decrease of generated primary microseismic noise amplitudes from certain geographic areas. However, results for both stations analyzed here yield the severe downweighting of $s_{\mathrm{eff}}(A_i)$ at the southern Australian coast. Since the propagation path towards the two stations includes only a short common section, any possible structural influence would have to be localized near the source site.

As mentioned in Gualtieri et al. [2019] one possible explanation for the increase in $s_{\mathrm{eff}}(A_i)$ along the north-eastern Australian coast and at Pacific islands could be a ocean wave model underestimation regarding large ocean wave heights during the frequent storm activity in this part of the Pacific. Such a possible underestimation of regional

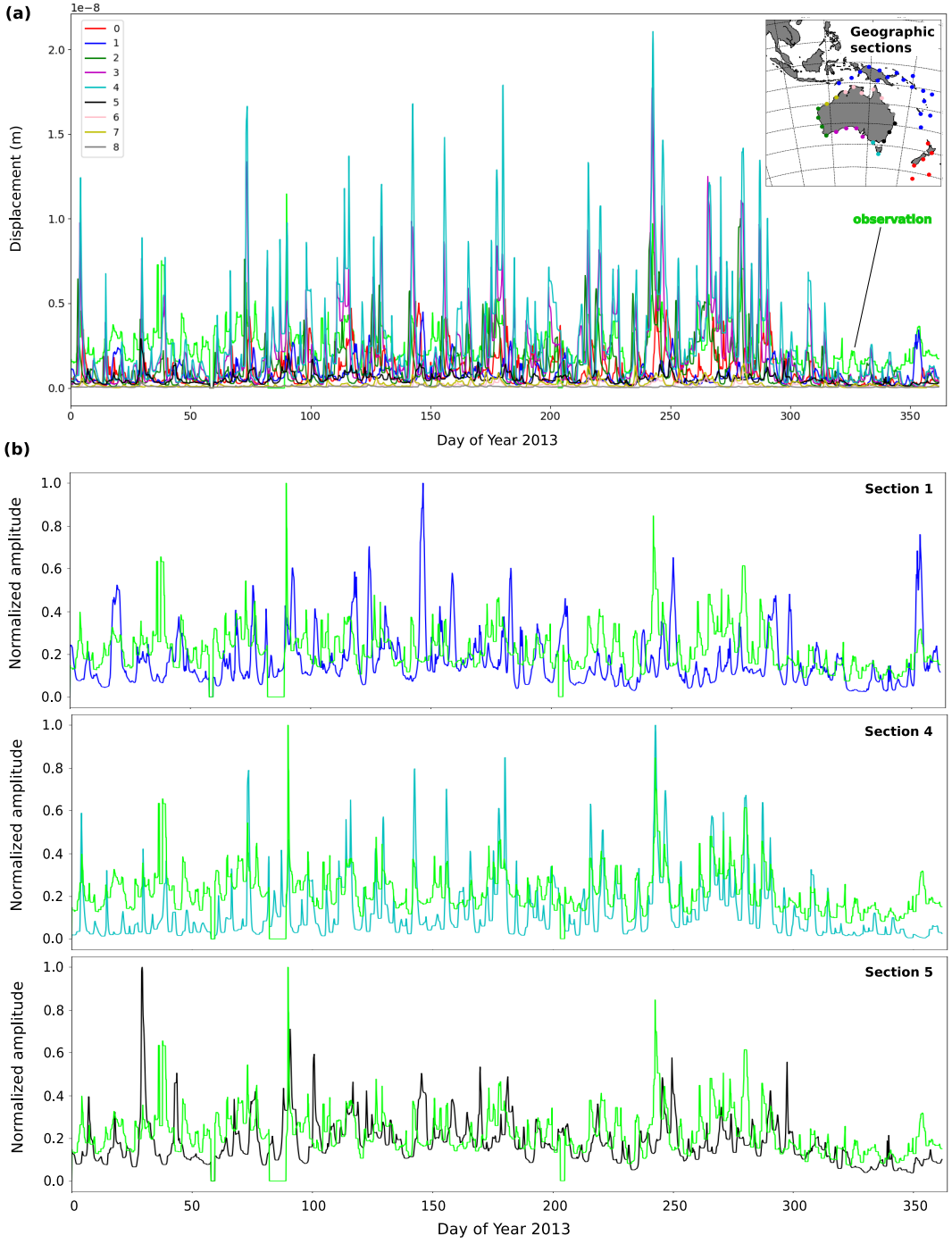

Figure 5.10: (a) Individual modeled time series for 9 seperate areal sections according to the labels and colored regions depicted in the map view inset in comparison to the observed time seris at station CAN. (b) Separate graphs depicting the self normalized time series for sections 1, 4 and 5 in comparison to the observation.

source contributions from these locations could likely transfer into an underestimation of the mean minimum noise level at both stations. Hence, modeled amplitude peaks from other regions, such as the southern Australian coast, would no longer be masked by the background, but appear as overestimated amplitude peaks. Additionally, a possible mis-estimation of regional source contributions from specific locations could arise due to the neglection of additional noise generation mechanisms, as such described by Ardhuin [2018].

In conclusion, the analysis detailed in this chapter confirms that several charateristics of the observed vertical displacement time series can be reproduced well with the theoretical and practical modeling framework applied here. Yet, local adaptions of $s_{\text{eff}}(A_i)$ may further improve the agreement between the model and the observations. The interpretation of $s_{\text{eff}}(A_i)$ hints towards geographic locations, for which the modeling approach applied is not yet sufficient. The resulting effective slope factor adaptions can be interpreted as indication for required model improvements, especially regarding the knowledge on small scale topography in the source area, the consideration of the detailed structural model and the input parameters from the ocean wave model.

5.3 Summary

In summary, this chapter provides an analysis on the reproducability of observed vertical component primary microseismic noise by means of theoretical predictions based on the primary mechanism. Modeled vertical component displacement seismograms were compared to observed time series using seismic data from both hemispheres. Results obtained in this chapter indicate that the average vertical component microseismic noise field can be estimated based on the known average characteristics of the ocean wave field with the approach used here. Further, the modeling approach was able to reproduce several temporal and spectral primary microseismic noise characteristics in 2013 at the seismic stations considered here. However, non-negligible deviations between the modeled and the observed data remained, but could be compensated for due to the estimation of local effective slope factor adaptions. Using different optimization approaches, local estimates of $s_{\text{eff}}(A_i)$ were derived. Using the resulting $s_{\text{eff}}(A_i)$ allowed to improve the agreement between modeled and observed data in (a) the case of an initial misfit found with an array analysis for certain source azimuths in Europe but also (b) for an initial misfit found at a certain frequency as observed in the Australian region. Hence, a spatial heterogeneity of the slope factor $s_{\text{eff}}(\theta)$ improved the fit between modeled primary microseismic noise predictions and observations.

In practice, the agreement between modeled estimates of primary microseimic noise levels and observations further depends on a number of parameters, which are not captured by the model approach taken here. These include the detailed subsurface at the seismometer site, the structural heterogeneity along the propagation path but also the accuracy of the ocean wave model used for calculating the seismic source term. Therefore, the estimation of $s_{\text{eff}}(\mathbf{x})$ in this chapter is interpreted as an approach for a fit optimization which inevitably responds to a combination of the source term and the above mentioned influencing parameters. Hence, $s_{\text{eff}}(\mathbf{x})$ depends on all potential effect along the entire propagation path from the noise source to the receiver.

Since seimic wave amplitudes dacay with propagation distance dependent on the wave frequency, long periodic primary microseimic noise may reflect the wave climate on a larger geographic scale while short periodic seismic waves attenuate rapidly across limited distances. Therefore, the seismic displacement at any geographic location is mainly defined by effectively contributing sources within a frequency dependent distance range. At the lower limit of primary microseimic noise frequencies (around f=0.05 Hz), effective source contributions arise from sources on a hemispherical or even global scale [Gualtieri et al., 2019]. Towards the higher frequency end of the primary microseimic noise band (around f=0.08 Hz), a higher attenuation results in a more regional confinement of effectively contributing sources as also described in chapter 4. Especially for seimometers located near the coast, the seismic noise generated at local nearby source regions dominates the recorded data and leads to the well known high correlation coefficients of microseimic noise amplitudes and ocean wave heights at nearby shores e.g. [Bromirski, 2001].

The consideration of heterogeneous effective slope factors displays one possible way to represent source and structure dependent deviations to the modeled estimate, which may be taken into account for further predictions of the expected primary microseismic noise field. This could be exploited in the context of e.g. microseimic noise applications, for which the propoperties of the wavefield, such as the contributing directions of propagation, are of importance. The resulting locally adapted s_{eff} may further help to improve the accuracy in estimating the absolut displacement PSD, valuable e.g. for an improved accuracy of estimating detection capabilities of signals (e.g. earthquakes) at specific seismometer locations. State of the art ocean wave models may provide a very valuable contribution for the prediction of seismic noise characteristics. On the other hand, the accuracy of ocean wave models can be probed by seismic noise observations. Results obtained in this chapter further contribute to the ongoing improvement of ocean wave model based predictions of primary microseismic noise.

5. PREDICTING PRIMARY MICROSEIMIC NOISE, MODELING THE DIRECTIONAL CHARACTERISTICS OF THE NOISE FIELD OBSERVED FROM BOTH SIDES OF THE EARTH

6

A phase coherence based analysis of microseisms in marginal seas

A statistical phase coherence analysis is applied for detecting and localizing persistent microseismic noise sources in two small scale ocean basins, the North Sea and the Mediterranean Sea, as presented in this chapter.

The analysis of instantaneous phase information instead of amplitude information plays an important role for the analysis of weak amplitude signals. A statistical approach regarding the phase coherence between a pair of seismic traces was used here for detecting and quantifying redundant and persistent signals in the microseismic noise field.

In this chapter, an evaluation on the applicability of a statistical redundancy of instantaneous phase (SRIP) analysis is presented. Within the context of two different case studies, the ocean wave generated noise field in the primary and in the secondary microseismic noise bands are studied by means of SRIP in comparison with beamforming.

For both, the primary and secondary microseismic noise bands, it is demonstrated that the SRIP analysis is applicable to the detection and localization of persistent and reoccurring microseismic noise sources. A reoccurring source region for short periodic primary microseismic noise is localized in the southern part of the North Sea. Further, frequent occurrences of secondary microseismic noise sources, which dominate the microseisms observed at seismometers in southern Europe, are analyzed and localized here. In comparison to beamforming, a comparable or better source localization was obtained with the SRIP analysis, especially with respect to the resolution of separated regional source areas in the Mediterranean Sea.

6. A PHASE COHERENCE BASED ANALYSIS OF MICROSEISMS IN MARGINAL SEAS

Findings support the direct and efficient joint generation of Love and Rayleigh waves in the primary microseismic noise field in shallow southern North Sea, where an undulating topography likely causes the effective excitation of both wave types according to primary mechanisms. An analog analysis regarding frequently reoccuring secondary microseismic noise from the Mediterranean Sea yields, that especially vertical component cross-correlations from seismometers in southern Europe may be influenced by spurious arrivals from caused by these source regions. A broader range of source azimuths observed in transversal component beamformer results, is not explained by theoretical coastal sources of secondary microseismic noise and hints to a possible influence of the propagation path.

Section 6.1 includes the content of the manuscript as submitted.

6.1

Publication 3

A phase coherence based analysis of microseisms in marginal seas

Carina Juretzek[1,2] and Céline Hadziioannou
1: Department of Earth and Environmental Sciences, Ludwig-Maximilians-University, Munich, Germany.
2: Institute of Geophysics, Center for Earth System Research and Sustainability (CEN), University of Hamburg, Hamburg, Germany.

Status:
Submitted to JGR: Solid Earth

The following text resembles the original manuscript as submitted to the journal. Figure, equation and reference numbers were adapted to match the consecutive labeling of this thesis. All cited sources can be found at the end of this thesis in the bibliography.

Abstract

During the last few years, substantial knowledge has been built regarding the further understanding of the microseismic noise field. In particular, studies including the horizontal seismometer components drew new attention to the complexity of the microseismic noise field and to the further need of theoretical considerations. Different methodologies have been used for analyzing and localizing sources of microseisms, including beamforming. But also phase coherence methods have proven their value for the analysis of weak amplitudes signal with respect to amplitude driven methods. Here, we use a statistical phase coherence analysis for detecting and localizing persistent microseismic noise sources in two small scale ocean basins, the North Sea and the Mediterranean Sea. Results from this approach and beamforming are compared. Due to the energetic ocean waves in large scale ocean basins, microseisms in Europe is often dominated by sources in the Atlantic ocean. ere, a reocurring source region in the southernmost part of the North Sea was found to efficiently generate primary microseisms, including Love and Rayleigh waves. Further, frequent Mediteranean Sea sources for the secondary microseismic noise band, which dominate the microseisms observed at seismometers in southern Europe, were localized. Small scale ocean basin microseism are interesting with for the analysis of generation mechanisms of microseismic noise. One one hand, the proximity of several seismic recorders generally improves the accuracy of source localization. On the other hand, they may provide very specific characteristics regarding e.g. the water depth or bottom topography, relevant for the further understanding of generation processes.

Introduction

Scientific interest in understanding and exploiting the omnipresent ambient seismic noise field remains at a peak level. Within a certain frequency range, the ocean surface wave generated microseismic noise is one of the signal types used for monitoring different properties and processes of the Earth, providing a more continuous data set than other seismic signals.

Wind acting on the ocean surface drives the formation of ocean-surface waves, in the form of local wind sea but also of swell fields, which propagate over very large distances across the ocean basins. Upon their arrival at the shorelines, but also in interaction with each other in the open ocean, these ocean surface wave fields may generate microseismic noise with a typical spectrum which is characterized by two distinct peaks at about 7 and 14 s, referred to as the secondary and primary microseisms, respectively. Source

mechanisms for the generation of microseismic noise at both spectral peaks were initially described in theoretical studies by Hasselmann [1963]; Longuet-Higgins [1950]. For a review on microseismic noise, the reader is referred to [e.g., Ebeling, 2012]. Observations on the microseismic noise field highlighted the need for further investigation regarding potential other source mechanisms [Juretzek and Hadziioannou, 2016, 2017; Matsuzawa et al., 2012; Nishida et al., 2008; Tanimoto, 2013], and additional source processes were proposed more recently [Ardhuin, 2018; Fukao et al., 2010; Saito, 2010]

The temporal, spectral and spatial variation of the microseismic noise field plays an important role in potential bias estimation for different monitoring methods [Tsai, 2009; Weaver et al., 2009]. But also a heterogeneous source distribution, including dominant and persistent sources contributing to the background noise field, often disturbs cross-correlation functions by causing spurious arrivals [Kimman and Trampert, 2010]. However, single recurring coherent sources may not only pose a threat to tomography and other ambient noise field approaches. They may also be exploited, e.g. for improving the physical understanding of processes behind natural signals, such as the ocean wave generated microseismic noise, volcanic tremor, but also for identifying anthropogenic sources. Hence, spurious arrivals are being used increasingly as an explicit source of information about coherent and persistent background signals and their appearance in cross-correlation functions has been used for a source localization e.g. by Retailleau et al. [2017]; Shapiro et al. [2006].

Relying on instantaneous phase information instead of amplitude information for the analysis of low amplitude signals in a noisy background was a major motivation for the development of different methods for signal detection or signal filtering, such as e.g. the phase weighted stack [Schimmel and Paulssen, 1997] or the phase cross-correlation [Schimmel, 1999]. Gaudot et al. [2015] proposed a statistical approach regarding the phase coherence for detecting and quantifying redundant and persistent signals in the background noise field. Similar to other coherence based approaches, the analysis of the statistical redundancy of instantaneous phases (referred to as SRIP in the following) is especially helpful when target-signal amplitudes do not stand out from the background noise field. The analysis of SRIP provides a possibility to detect and localize multiple different coherent sources but also to quantify their persistence in the present wave field over time.

One potential application for a SRIP analysis is the detection and monitoring of persistent and dominant source regions in the microseismic noise field. This study aims at exploring the applicability of the statistical redundancy of instantaneous phases analysis to the ocean wave generated noise field in the primary and in the secondary microseismic noise bands. Within the context of two different case studies, we analyze

primary microseisms in the North Sea and secondary microseisms in the Mediterranean Sea by means of SRIP in combination with beamforming.

Considering the temporal variability of the ocean wave climate, and therefore of the microseismic noise field, we investigate the possibility to estimate persistent source locations with SRIP for the limited life times of such sources. Further, we include horizontal component data into our application of SRIP, which may help to better understand and interpret source mechanisms of observed microseismic noise signals.

Data and processing

Due to the application of an amplitude-unbiased approach, the common pre-processing steps which target an amplitude normalization, such as one-bit normalization or the removal of earthquakes, are superfluous here. Hence, the pre-processing of the raw seismic data may be limited to a minimum. Publicly available seismic data was downloaded, de-meaned, de-trended, pre-filtered and corrected for the instrument response in order to obtain seismic displacement. According to the different types of seismic signal targeted in the following case studies, the data was further bandpass filtered and down-sampled as needed. This pre-processing was then directly followed by the calculation of cross-correlation functions between pairs of seismic stations among each of the seismic networks used in the different case studies.

The SRIP approach applied here follows Gaudot et al. [2015] and focuses on the analysis of the first and second moment (mean, variance) of the distribution of pairwise phase coherence comparisons C_{jk} between pairs of seismic time series, e.g. corresponding to empirical cross-correlation functions, $s_j(t)$ and $s_k(t)$, where C_{jk} is given by

$$C_{jk}(t) = \left|\cos\left(\frac{\Phi_j(t) - \Phi_k(t)}{2}\right)\right| - \left|\sin\left(\frac{\Phi_j(t) - \Phi_k(t)}{2}\right)\right|, \tag{6.1.1}$$

and $\Phi(t)$ is the instantaneous phase [Bracewell, 1986] of their corresponding analytic signals $S(t) = A(t)e^{i\Phi(t)}$ with amplitude $A(t)$. By defining μ_j as mean phase coherence between any seismic trace j and a number N of other traces, the overall mean phase coherence $\bar{\mu}(t)$ over all possible trace combinations can be written as [Gaudot et al., 2015]

$$\bar{\mu}(t) = \frac{1}{N}\sum_{j=1}^{N}\mu_j(t) \text{ with } \mu_j = \frac{1}{N-1}\sum_{k=1}^{N}(1-\delta_{jk})C_{jk}(t). \tag{6.1.2}$$

δ denotes the Kronecker delta. Due to the symmetry of the pair-wise phase coherence $C_{jk}(t)$ the evaluation of all valid pairs of phase coherence comparisons can be

given by $C_i = (C_{jk} + C_{kj})/2$. With $p = n(n-1)/2$, the overall mean coherence can be written as

$$\bar{\mu}(t) = \frac{1}{p} \sum_{i=1}^{p} C_i(t), \tag{6.1.3}$$

and the corresponding variance as

$$\bar{\sigma}^2(t) = \frac{1}{p} \sum_{i=1}^{p} (C_i(t) - \bar{\mu}(t))^2. \tag{6.1.4}$$

For the detection and localization of persistent coherent sources in the ambient seismic noise field in this study, the phase coherence comparison (Eq. 6.1.1) was performed on a sample by sample basis between pairs of inter-station cross-correlation functions $\mathrm{CC}_j(t)$ and $\mathrm{CC}_k(t)$.

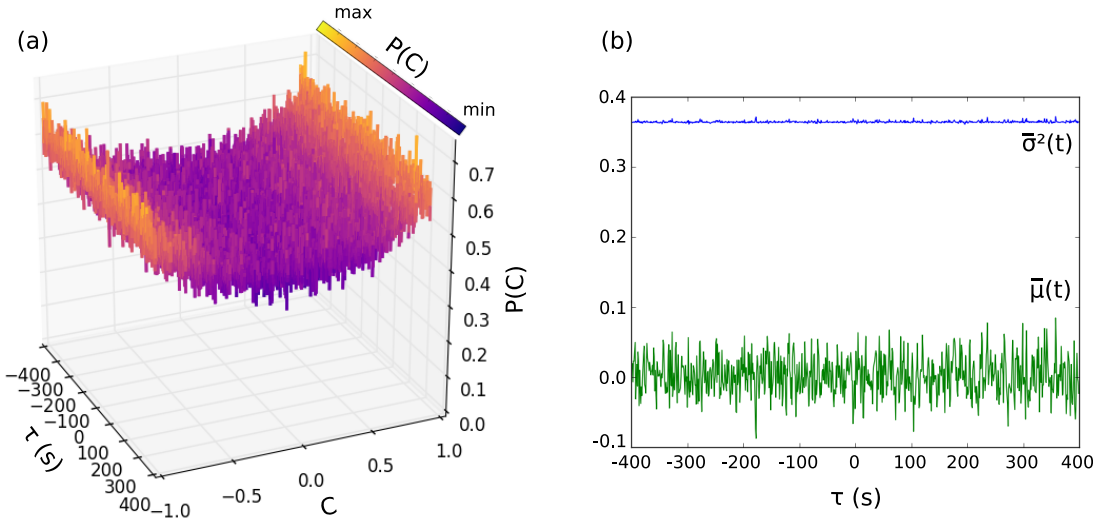

Figure 6.1: Distribution of pairwise phase-comparisons for a synthetic dataset of random noise (a), with lag time τ of the cross-correlation functions on the x-axis, the distribution of pair-wise phase coherences at each lag time on the y-axis and the empirical probability density of phase coherences on the z-axis. Corresponding overall coherence $\bar{\mu}$ (green) and variance $\bar{\sigma}^2$ (blue) (b).

The distribution of pairwise phase comparisons may be displayed in a 3D histogram plot as depicted in Figure 6.1 (a), with lag time τ of the cross-correlation functions on the x-axis (here $-400\,\mathrm{s} < \tau < 400\,\mathrm{s}$), the distribution of pair-wise phase coherences at each lag time on the y-axis, and the empirical probability density of phase coherences on the z-axis. As demonstrated by Gaudot et al. [2015], an absence of coherent signals

converges to a characteristic u-shape in the distribution of pairwise phase coherence comparisons C_{jk}, and to an expectation value of $\bar{\mu} = 0$ and $\bar{\sigma}^2 \approx 1-2/\pi$. For a synthetic time series of random noise amplitudes drawn from a Gaussian distribution with zero mean and $\sigma = 0.3$, these expected characteristics readily appear in a 3D histogram plot as depicted in Figure 6.1 (a) and in the corresponding overall mean coherence and variance depicted in Fig. 6.1 (b). Considering synthetic and real data examples Gaudot et al. [2015] further validated that deviations from these characteristic values indicate the presence of coherent signals in the data sample analyzed, which temporal persistence can be quantified. Hence, we will refer to $\bar{\mu}$ and $\bar{\sigma}^2$ as coherent signal indicators (CSI) in the following. In practice, the deviation of the CSI's indicate a modification of the bimodal u-shape distribution peaking at $C_{jk} \pm 1$ for perfectly random signals to an unimodal distribution peaking at $C_{jk} = 1$ for perfectly in-phase signals with a variance converging to $\bar{\sigma}^2 = 0$.

The CSI's describe average properties during the analyzed period. In practice, seismic signals of different origin, including the microseismic noise field, are known to vary significantly in coherence and amplitude over different time spans (from minutes, over hours and days to season). Additional complexity may arise due to signal interferences between interrupted or alternating multiple sources. Since we are interested in exploring rather short term application limits of SRIP (i.e. for time spans in the order of hours/days), the CSI based signal detection for such short time spans additionally relies on rather limited data samples. Moreover, the detection ability based on a the CSI suffers in practice e.g. for interrupted signals or in presence of incoherent local noise during a portion of the period studied.

Using a synthetic dataset, we depict the behavior of coherence ($\bar{\mu}$) and variance ($\bar{\sigma}^2$) for different cases, when a coherent signals exists only during a part of the analyzed time span. We form a set of 100 synthetic traces with random noise amplitudes drawn from the same Gaussian distribution as described above. At different lag times, the random noise in a fraction of the 100 time windows was replaced by 50 s of coherent signal given by a sine wave. For increasing lag times, the number of time windows containing the coherent signal increased (10, 32, 48, 63, 78, 86, 96). Fig. 6.2 shows the resulting $\bar{\mu}$ and $\bar{\sigma}^2$.

$\bar{\mu}$ increases linearly from 0 to 1 scaling with the proportion of time segments including the perfectly coherent signal versus the incoherent noise as expected. At the same time, $\bar{\sigma}^2$ initially increases for small proportions of coherent signal traces. This effect can be explained by the change between the dominance of the bimodal random noise distribution of C_{jk} to the dominance of the unimodal coherent signal distribution. The time series including the coherent signal with additional incoherent noise corresponds

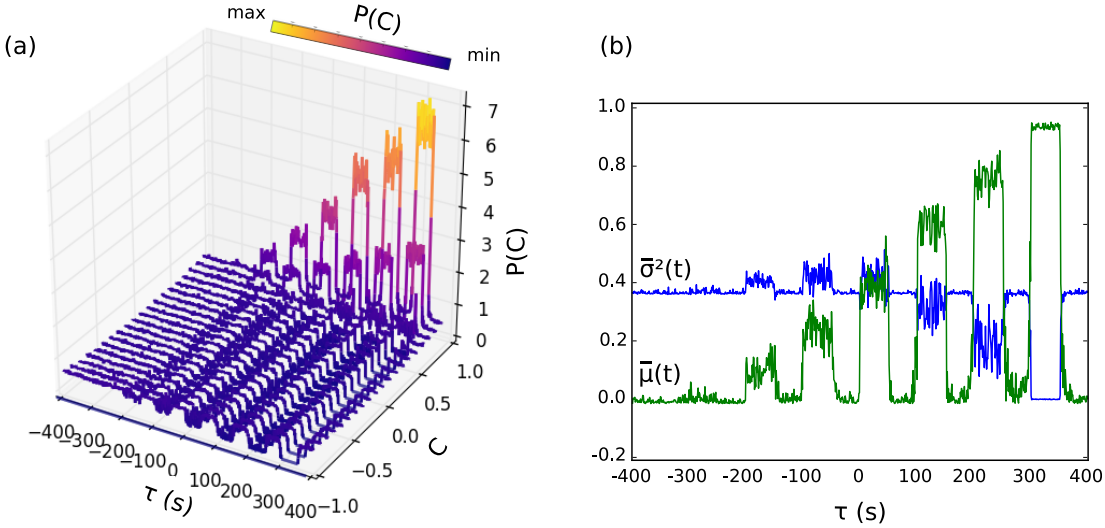

Figure 6.2: Distribution of pairwise phase-comparisons for a synthetic dataset of random noise with increasing proportions of a perfectly coherent signal as described in the text (a). Corresponding overall coherence (green) and variance (blue) (b).

to a superposition of the above mentioned types of characteristic distributions of C_{jk}. Whenever the random signal proportion is strong enough, the variance of pair wise phase coherences will not necessarily converge to zero.

Hence, $\bar{\mu}$ is found to be the more robust CSI in indicating a persistent source presence compared to $\bar{\sigma}^2$. E.g. interrupted sources may cause no decrease in variance although a peak in overall coherence is observed. In return, the presence of the simultaneous opposite deviation of $\bar{\mu}$ and $\bar{\sigma}^2$ is an even more robust indicator for a persistently coherent signal, especially for small sample sizes for which spurious high values of $\bar{\mu}$ might be obtained by pure chance.

In order to verify the applicability of the statistical CSI's of SRIP for the detection and quantification of coherent seismic signals in the microseismic frequency range, we consider cross-correlation functions of an exemplary station pair in the European seismic network. To illustrate the difference in SRIP CSI's between two distinct time spans analyzed, which correspond 1) to the absence and 2) to the presence of persistently coherent signals, we compare the resulting distribution of pairwise instantaneous phase comparisons, the corresponding overall mean coherence and the overall mean variance. Analog to the representation of these parameters in Fig. 6.1, Figure 6.3 (a) depicts the first case, which closely resembles the characteristics obtained for the synthetic random data test. Here, the distribution shows the characteristic u-shape as in Fig. 6.1 at all time-lags and deviation of $\bar{\mu}$ from zero remains below a value of 0.05. Contrasting this,

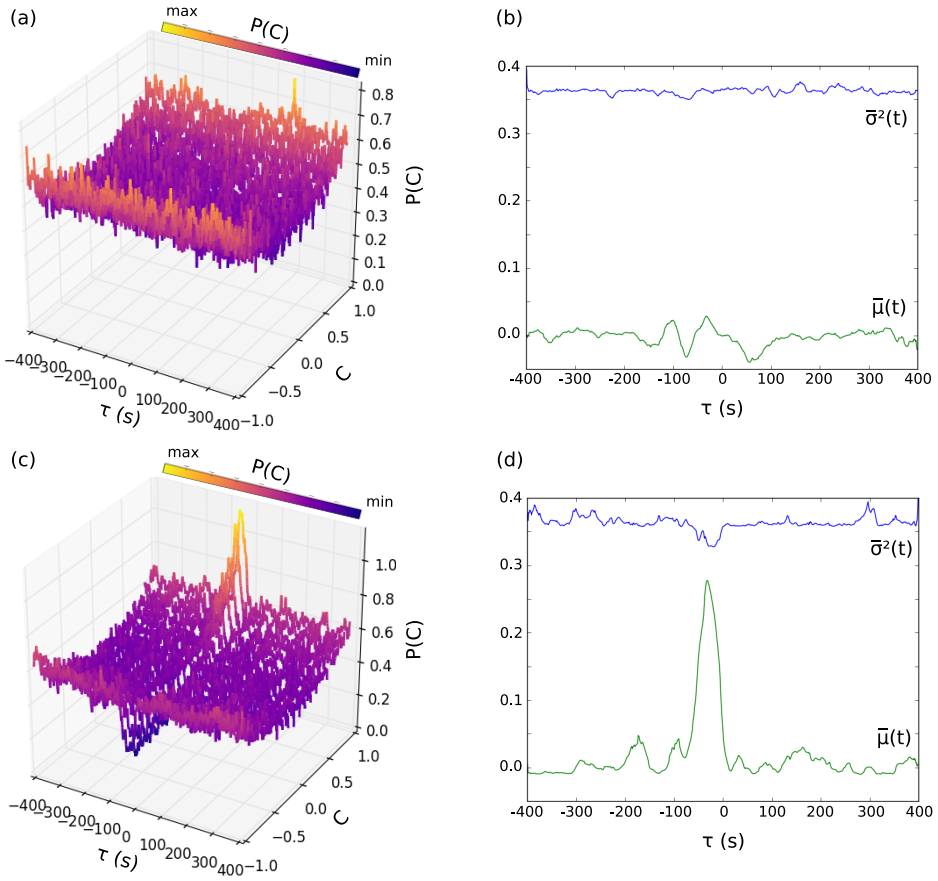

Figure 6.3: Distribution of pairwise phase-comparisons (left panels) and overall coherence (green) and variance (blue) (right panels) for data examples from the European seismic station network in the microseismic frequency range for a time span, during which either random noise (a,b) or the presence of a coherent signal (c,d) was detected.

$\bar{\mu}$ in Fig. 6.3 (c) clearly indicates the presence of a coherent signal centered around a time lag $\tau \approx -50\,\mathrm{s}$, while the remaining time axis yields similar CSI's as for Fig. 6.3 (a). As expected, the distribution of pairwise instantaneous phase comparisons yields a peak at $C \approx 1$, corresponding to an increase in the occurrences of in-phase comparisons ($C = 1$), and a simultaneous drop in the occurrence of anti-phase ($C = -1$) comparisons (cf. Eq. 6.1.1). The corresponding $\bar{\mu}$ and $\bar{\sigma}^2$ displayed in panel (b) and (d), respectively, show a clear increase in $\bar{\mu}$ which is accompanied by a weaker decrease in $\bar{\sigma}^2$.

The overall mean coherence over a given time span describes an average property. In practice, seismic signals of different origin, including the microseismic noise field, are known to vary significantly in coherence and amplitude over different time spans from

minutes to seasons. Additional complexity may arise due to signal interferences due to interrupted or alternating multiple sources. Since we are interested in exploring rather short term application limits of SRIP (i.e. for time spans in the order of hours/days), the CSI based signal detection for such short time spans relies on rather limited data samples. Hence, the detection ability based on a mean coherence likely suffers in practice e.g. for interrupted signals or in presence of incoherent local noise during a portion of the period studied.

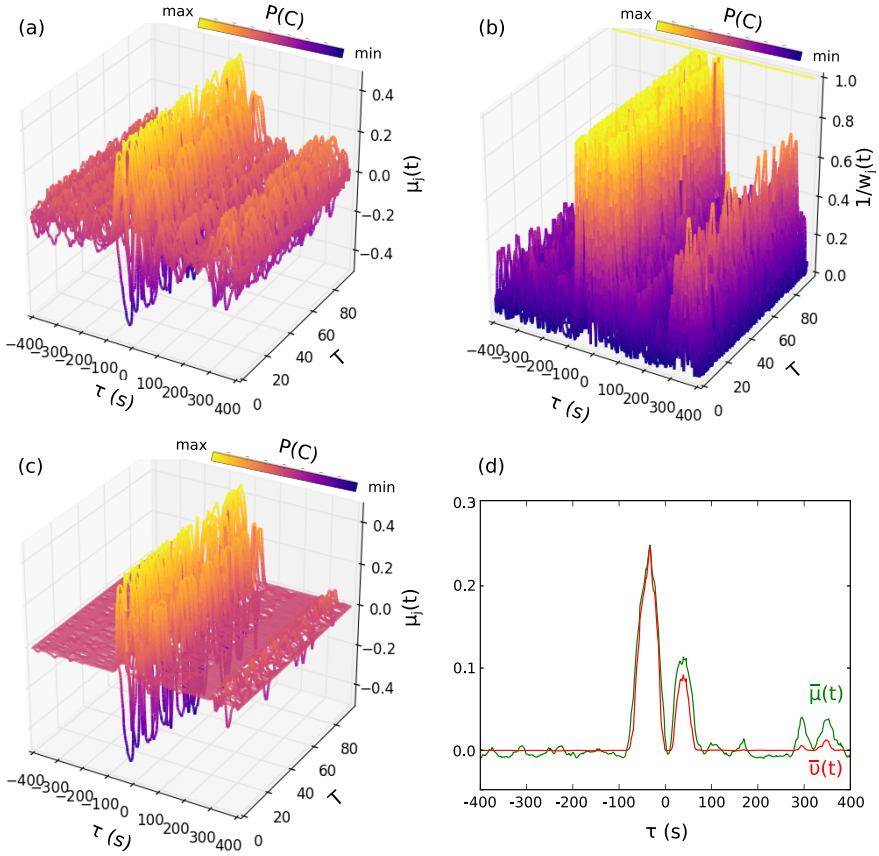

Figure 6.4: Temporal waterfall plots of the individual coherence traces, showing the unweighted $\mu_j(t)$ (a), the inverse variance weight $1/w_j(t)$ (b) and the variance weighted $\mu_j(t)$ (c) for one day of data from a station pair of the European network. Panel (d) shows a comparison between $\bar{\upsilon}(t)$ and $\bar{\mu}(t)$, the amplitude peak of $\bar{\mu}(t)$ is unmodified for stable coherent arrivals while non-persistent signals and random peaks are down-weighted.

For an improved coherent signal extraction, we exploit the fact, that variance and overall coherence should simultaneously indicate a coherent arrival by deviating from the random noise expectation values. Instead of forming the linear stack $\bar{\mu}(t)$, we form a variance-weighted stack $\bar{\upsilon}(t)$ of the individual coherence traces $\mu_j(t)$. Each time sample

of the individual phase coherence trace $\mu_j(t)$ in Eq. 6.1.2 (sum of phase coherence of trace j with all others) is therefore weighted by

$$w_j(t) = \left| \frac{1}{N-1} \sum_{k=1}^{N} \frac{\left(C_{jk}(t) - \mu_j(t)\right)^2}{\mu_j(t)} \right|, \tag{6.1.5}$$

and the variance-weighted stack $\bar{v}(t)$ is then given by

$$\bar{v}(t) = \begin{cases} \frac{1}{N} \sum\limits_{j=1}^{N} \frac{\mu_j(t)}{w_j(t)^2} & \text{for } w_j(t) > 1 \\ \frac{1}{N} \sum\limits_{j=1}^{N} \mu_j(t) & \text{for } w_j(t) \leq 1. \end{cases} . \tag{6.1.6}$$

Figure 6.4 shows an example of the variance weighted stacking using half-hourly cross-correlations functions between the stations LMK and CWF during one full day of data in March 2013. Panel (a)-(c) show a temporal waterfall plot of the individual coherence traces $\mu_j(t)$ corresponding to each of the half hourly time windows along the T axis. Panel (a) depicts the unmodified $\mu_j(t)$, panel (b) depicts the inverse of the variance weight $1/w_j(t)$ and panel (c) presents the variance-weighted $\mu_j(t)$. Since we only down-weight parts of the seismic traces, where the variance in instantaneous phase comparisons is comparable or larger than $\mu_j(t)$, the maximum overall mean coherence value $\bar{\mu}(t)$ is preserved. As shown in panel (d), the amplitude peak of $\bar{\mu}(t)$ is unmodified for stable coherent arrivals while non-persistent signals and random peaks are suppressed.

Case Studies

Primary microseismic noise: a North Sea source

Land bodies such as islands pose obstacles to the propagation of ocean surface waves and effectively cause a shadow zone of calmer water on their leeward side. Due to shielding by the British Isles, high swell propagating across the Atlantic ocean is effectively prevented from traveling into the southern North Sea. Still, microseismic noise could be generated directly in the North Sea due to local storms on one hand, but also due to occasionally entering swell from the Atlantic ocean.

The horizontal extent of an ocean basin over which the wind drives the ocean-wave field influences the peak frequency of the swell f_o, which translates into the peak frequency of the generated microseismic noise f_s with a relation of $f_o = f_s$ and $f_o = 2f_s$ for the primary mechanism and the secondary mechanism, respectively. The relation between the local water depth h_{w} and the wave number k of the ocean gravity waves

constrains the ocean regime in which either of the two source mechanism is able to efficiently generate seismic noise. While the theory on the primary mechanism explains the generation of seismic noise in a shallow water regime ($kh_w \ll 1$), the secondary mechanisms requires a deep water regime for efficient noise generation [Ardhuin and Herbers, 2013]. While the water depth h_w reaches significant depth towards the north, the southern North Sea is characterized by extended areas of shallow water h_w well below 50 m, limiting the possible efficient seismic noise generation mechanisms to those which may act in this regime. Hence, the North Sea is a promising region in order to study microseismic noise generation in a small and shallow ocean basin, due to a very high density of nearby permanent seismic stations including seismic arrays on one hand, and due to still higher average ocean wave heights than found for other shallow ocean basins such as the Baltic Sea or the Adriatic Sea.

Primary and secondary microseismic noise observed with 3-component seismometers across Europe were found to typically originate from the north Atlantic ocean e.g. [Cessaro, 1994; Essen et al., 2003; Kedar et al., 2008; Sergeant et al., 2013] and the northern North Sea near Norway in previous studies [Juretzek and Hadziioannou, 2017; Matsuzawa et al., 2012; Sadeghisorkhani et al., 2016]. In general, observations from European instruments document the presence of Rayleigh waves and Love waves in both microseismic noise bands with varying wave-type rations depending on source direction and possibly source region [Friedrich et al., 1998; Juretzek and Hadziioannou, 2016, 2017; Tanimoto et al., 2016].

In this study, we consider seismic data recorded by seismometers located around the North Sea. We use a 3-component beamforming approach in comparison to a SRIP analysis in order to investigate microseismic noise observations with a potential source region in the North Sea across both microseismic noise bands (i.e. from 0.2 to 0.06 Hz) during 2013. In particular, we analyze occurrences of temporally confined microseismic noise outbursts within a period range from 8 to 11 s, just in between the typically observed primary and secondary microseismic noise peak periods, which were observed at a number of seismic stations and arrays around the southern North Sea. The arrays and the beamforming approach used here, were described in detail in a previous study [Juretzek and Hadziioannou, 2016].

Figure 6.5 shows an example of beamforming results for March 23 2013 during which such a local 10 s microseismic noise event was observed in addition to the typical primary and secondary microseims at three different seismic arrays located in Ireland (IR), in Switzerland (CH) and in Germany (GRF). Their array center locations are shown in Figure 6.6. Vertical component beamforming results for the primary and secondary microseismic noise band, shown at the center period of about 15 s and 7 s

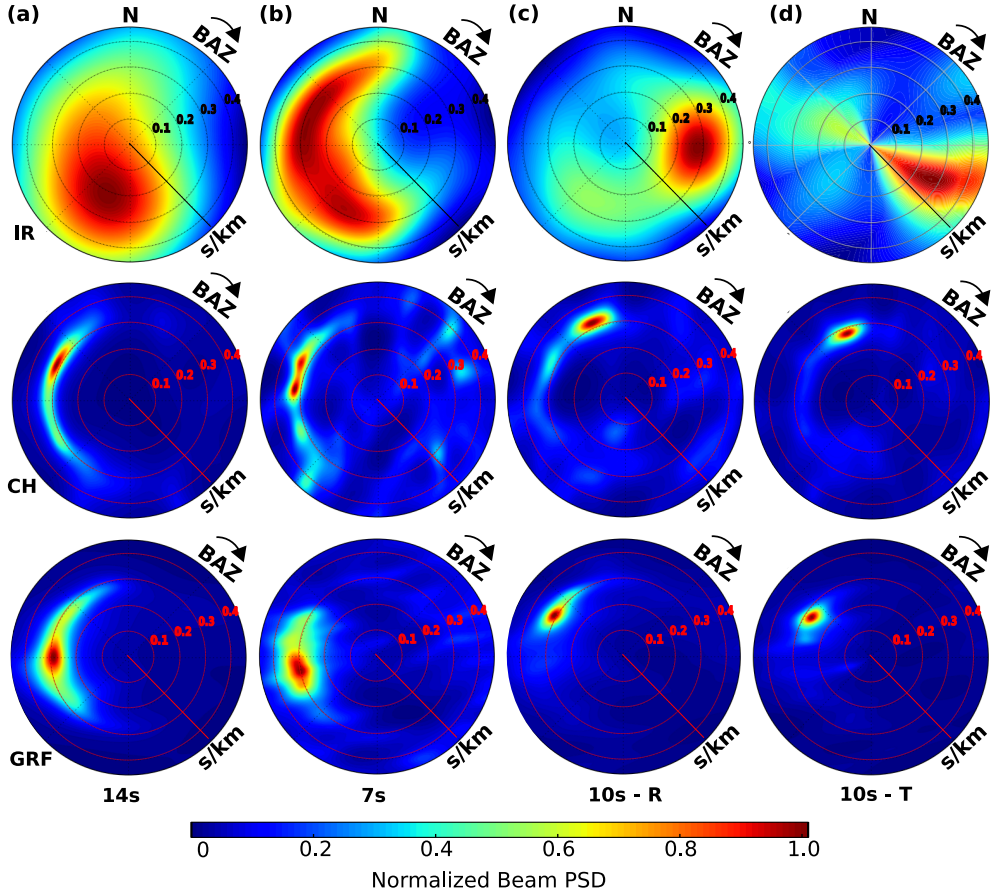

Figure 6.5: Normalized vertical component beampower at three different arrays (corresponding to the different rows and labels IR, CH and GRF) during a North Sea source outburst on 23 March 2013 at a period of 14 s (a), of 7 s (b) and 10 s (c), and normalized transversal (T) component beampower (d).

as daily mean beam PSD in panel (a) and (b) respectively, indicate source directions corresponding to the north Atlantic ocean at all three arrays (IR, CH and GRF). Since the corresponding transversal component beamformer results yield comparable source directions at all arrays, Fig. 6.5 shows results for the vertical component only.

In addition to the typically observed primary and secondary microseismic noise bands we observe an interesting signal corresponding to an intermediate period range of 8-11 s on the vertical and transversal component mean beam PSD results as shown in panel (c) and (d) respectively, at all arrays. Contrasting the source direction estimate according to beamforming from panel (a) and (b), the observed peak beam PSD at a center period of around 10 s show a clearly different source direction at all arrays. This is most apparent for results obtained at array IR (cf. panel (c) and (d)). The detection

of the corresponding beampower peak in the vertical and transversal component results hints towards the presence of Rayleigh and Love waves during periods of this 10 s source activity. Here, beamformer results are shown for both components in order to emphasize the agreement of directions of arrivals on both components and to confirm that the phase velocity of the beampower peak signal on both components is in agreement with expectations for either fundamental mode Rayleigh waves or Love waves. However, transversal component results for IR appear to be biased and serve as an indication of the signal presence but will not further be used in the analysis.

This particular noise event was also observed during the two follwing days, lasting in total from March 23 to 25 and during a number of other days during 2013. Figure 6.6 shows map views of the vertical component beampower back-projected from the center of each of the three different arrays, with results from the first and the last day of the event in panel (a) and (b), respectively. The red color range depicts the back-projected beampower of corresponding peaks identified in the beampower maps. For both days, results from all arrays indicate a beampower peak at backazimuths which are in agreement with a source region in the southern North Sea.

To complement the seismic observations with an estimate of the ocean wave state in the North Sea, we consider open access ocean wave model output. In particular, we obtained modeled local ocean wave height PSD $E(f)$ with a temporal resolution of three hours and a spatial resolution of 0.5° from resources available for download as described by Ardhuin et al. [2011]. The color range in the map background of Fig. 6.6 shows the daily mean of the modeled ocean wave height ASD $\sqrt{E_f}$ at a period of $\approx 9\,s$.

Indeed, the presence of the intermediate frequency signal coincides with a local increase in modeled ocean wave heights in the southern North Sea during both days. In this case, a swell field entered from the Atlantic ocean and propagated southwards into the southern North Sea. The ocean wave model predicts clearly lower ocean wave heights on March 25 compared to March 23, which agrees with a decrease in beam PSD over this time span found for all arrays. However, the source direction estimate according to the beam PSD for March 25 is comparably well constrained as for March 23 hinting to an ongoing source activity despite the decreased ocean wave heights predicted by the wave model. On March 23 the modeled mean wave height yields comparable levels in the north-east Atlantic ocean and the North Sea. According to the ocean wave model, the near-shore wave-heights in shallow water areas along the western shorelines of the British Isles and Norway remain below wave heights estimated for the North Sea on both days. Most likely, only these overall low ocean wave heights in the Atlantic ocean enable the detection of the North Sea source across Central Europe.

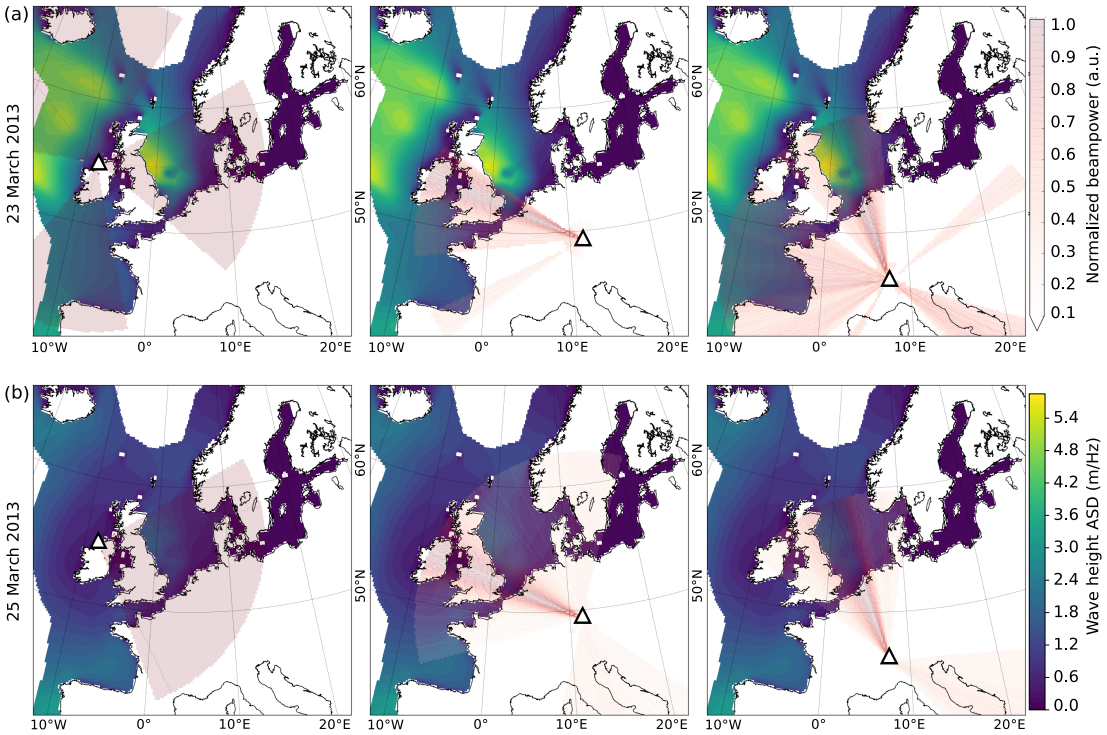

Figure 6.6: Back-projected array beampower for the 9-11 s band observed from 3 different array center locations (triangles) during March 23 (a) and March 25 (b) in 2013 (red color range) and corresponding mean daily ocean wave height ASD at a period of $\approx 9\,s$ (blue color range).

In order to constrain the corresponding source region, we focus on the March 23 signal in more detail by using the source directions obtained from beamforming on one hand and using a SRIP analysis on a small set of seismic stations around the North Sea on the other hand.

For the localization approach by means of beamforming, we use vertical component beamformer results obtained for 24 subwindows of one hour length during March 23 and apply a grid search in order to estimate the source location corresponding to a minimum triangulation misfit. For each of the three arrays $i = 1, 2, 3$, we therefore consider a mean source azimuth $\bar{\theta}_i$ over all direction of arrival estimates corresponding to peaks in the beam PSD maps within subwindows containing a signal detection from the North Sea region within the expected slowness range. The corresponding standard deviation of the direction of arrivals at each array is given by σ_i. Neglecting propagation path deviations, each potential source location $\mathbf{x}$ on a grid in longitude and latitude is represented by the theoretical backazimuth $\theta(\mathbf{x})$ relative to each array center location.

With the absolute angular deviation Δ_θ between the backazimuth to the test location $\theta(\mathbf{x})$ and $\bar{\theta}_i$, the most likely source location was estimated as the minimum of the triangulation misfit product TRI defined as

$$\min \text{TRI}(\mathbf{x}) = \prod_i \frac{\Delta_\theta}{\sigma_i^2}. \tag{6.1.7}$$

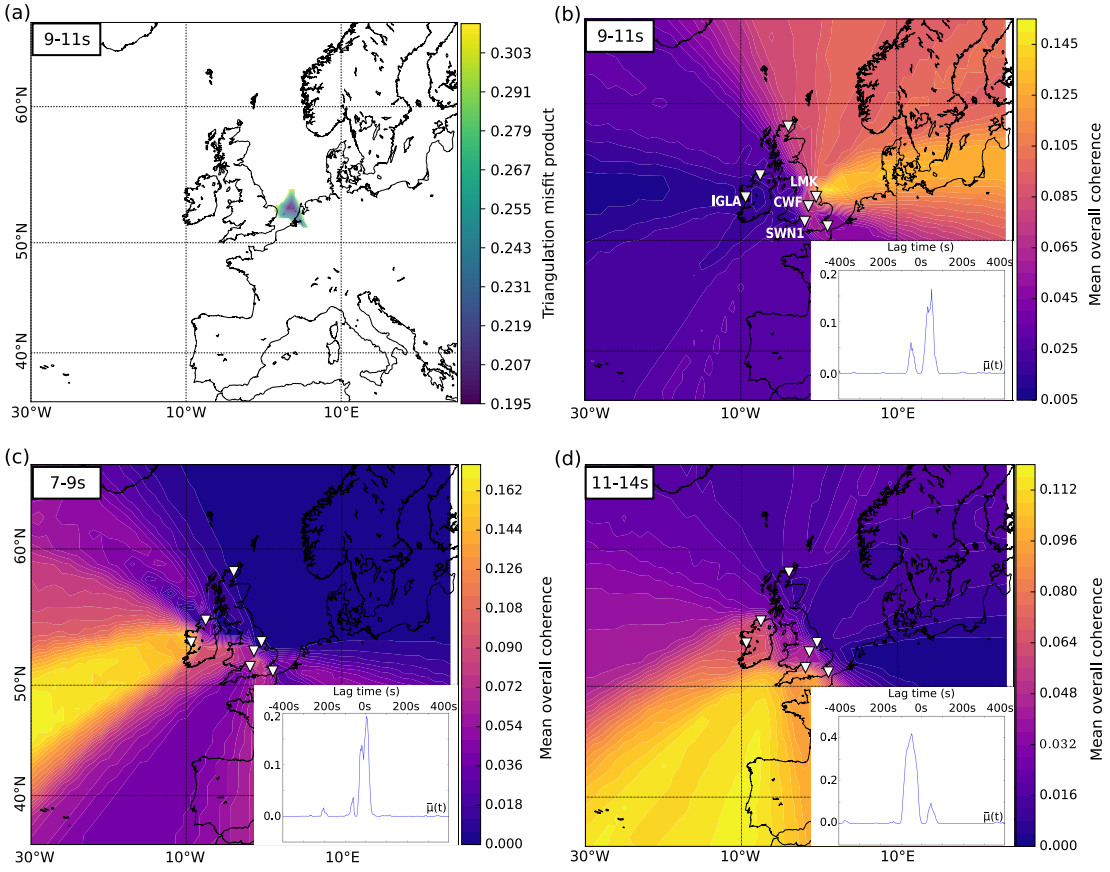

Figure 6.7: Map view of the most likely source region of the 23 March microseismic noise outburst in the 9-11 s period band estimated according to the triangulation misfit product TRI (a) and according to the mean overall coherence from SRIP (b). For comparison, panel (c) and (d) show the most likely source regions according to the mean overall coherence for observed microseismic noise within the surrounding period bands 7-9 s and 11-14 s, respectively.

Figure 6.7 (a) shows the most likely source region for the 23 March intermediate frequency band noise event according to the triangulation misfit product TRI, which yields a minimum at a distinct geographic region in the south-western North Sea. The

shallow local water depth in this particular region hints towards an area of efficient microseismic noise generation due to the primary mechanism.

For the localization approach by means of phase coherence statistics, we use vertical component displacement data from 7 seismic stations with locations shown in Figure 6.7 (b). We perform the SRIP processing on the cross-correlation functions between pairs of the station set. In agreement with the beamforming analysis, we consider seismic data bandpass-filtered for three distinct narrow frequency bands: (1) the North Sea microseismic noise event, (2) the secondary and (3) the primary microseismic noise peak, corresponding to period ranges of 9-11 s, 6-9 s and 11-14 s respectively. In order to estimate the source region of detected coherent signals present in the mean overall coherence according to SRIP, we use a straightforward grid search approach as described by Gaudot et al. [2015]. Assuming a constant phase velocity, the overall coherence at each lag time is back-projected to the theoretical source locations according to the corresponding travel time differences between a station pair. By forming a geographic map of the mean overall coherence corresponding to each geographic test location, the most likely source region is then given by the geographic maximum of this value.

Figure 6.7 (b) shows the most likely source region for the 23 March intermediate frequency band noise event derived by means of the SRIP analysis. The mean overall coherence yields a maximum in the south-western North Sea, in proximity to the most likely source region derived from the triangulation misfit product. The coherence based approach estimates the source region to be located slightly further north than obtained from beamforming results.

However, both methods used here hint towards a region of limited spatial extent which persists as efficient generation area for microseismic noise over the course of three days. Hence, localization estimates for this coherent microseismic noise signal observed with both, the IR array and the seismic station network, do not coincide with the region corresponding to the largest modeled ocean wave heights shown in Fig. 6.6 (a). Instead our results suggest that the observed seismic signals originate from a region further south.

In agreement with the beamforming derived source-directions shown in Fig. 6.5 for the typical primary and secondary microseismic noise reference bands, the most likely source region using the SRIP approach was localized in the Atlantic ocean as shown in Figure 6.7 (c) and (d) for the period bands 7-9 s and 11-14 s, respectively. For these spectral bands, the source regions can not be constrained as accurately as the North Sea source region. One possible reason for a less well constrained source region would be the presence of a more extended source or multiple sources generating the microseismic noise recorded in these frequency bands. Another explanation would be

the presence of a more distant source region which can not be constrained using the limited station network aperture given here. For the 11-14 s band results, the mean overall coherence yields higher values near the shore-line of Portugal, which agrees with locally elevated near-shore wave-heights in this region as predicted by the ocean-wave model-output shown in Fig. 6.6. For the 7-9 s band, the mean overall coherence increases with distance to the British Isles and likely indicates far-distant source regions in the north-east Atlantic ocean. The insets in Figure 6.7 (b)-(d) further depict the overall coherence for March 23 for the station pair SWN1-CWF within the three different frequency bands. The differences in lag-times, for which a peak in the CSI indicates the presence of a coherent signal in these three cases, clearly hints to different geographic origins of the corresponding microseismic noise.

While a peak in $\bar{\mu}$ for the 9-11 s band appears at approximately 0 s, we find two peaks with coinciding lag-times but differing relative peak amplitudes in the resulting $\bar{\mu}$ for both of the other period bands. This indicates a spectral overlap of the North Sea signal with the primary microseimic noise band, which transfers into the SRIP results for the vertical components.

For this station-pair, the maximum value obtained for $\bar{\mu}$ in the typical primary microseismic noise band (11-14 s) during March 23 yields 0.41 and clearly exceeds the corresponding maximum of 0.17 in the secondary microseismic noise band (9-11 s) and of 0.19 in the North Sea signal band (7-9 s). However, we find a clear dominance of one distinct source region for each of the spectral bands analyzed for March 23.

Figure 6.8 shows results of the SRIP analysis for three station pairs with names and locations depicted in Fig. 6.7 (b). Panels (a)-(c) show the resulting distributions of pairwise instantaneous phase comparisons and panels (d)-(f) show the corresponding overall mean coherence $\bar{\mu}$ and overall mean variance $\bar{\sigma}^2$ using vertical-vertical component cross-correlation functions. Since the North Sea event was clearly detected on both, the vertical and horizontal component beamformer results, the statistic of the instantaneous phase comparisons was additionally analyzed including horizontal components, in particular using cross-correlation functions between east-east-components and between vertical-east components. Fig. 6.8 shows the corresponding $\bar{\mu}$ and $\bar{\sigma}^2$ for the east-east component cross-correlation functions in panels (g)-(i) and for the vertical-east component cross-correlation functions in panels (j)-(l). Panels (m)-(o) show the distributions of pairwise instantaneous phase comparisons using the vertical-east component cross-correlation functions.

For all station pairs shown here, the phase distribution and the CSI's for the vertical component results indicate the presence of coherent signals with peaks centered around two distinct lag-times as marked by labeled vertical lines. By examining the

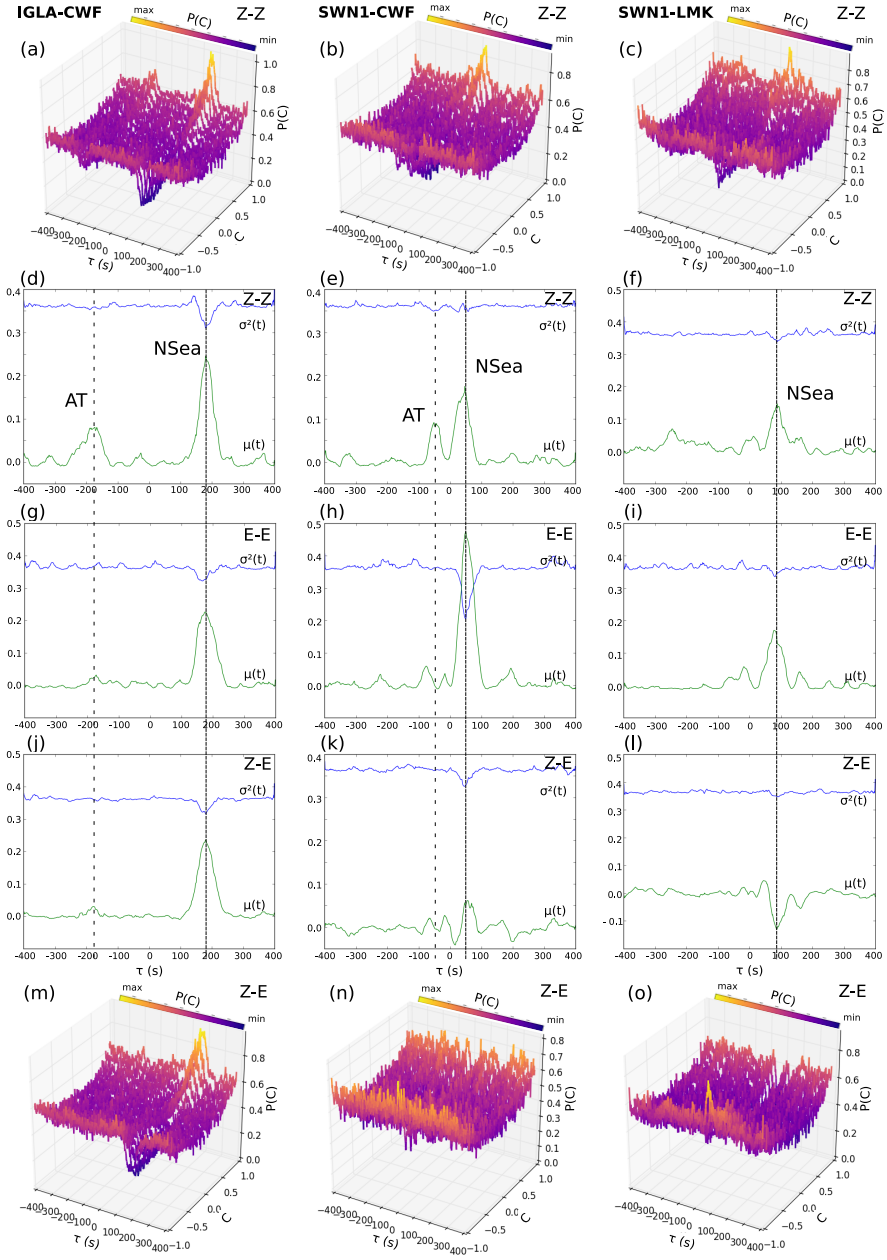

Figure 6.8: Distribution of pair-wise phase-comparisons using Z-Z correlation functions for different station pairs corresponding to the three collumns as labeled (a)-(c). Instantaneous phase coherence indicators analyzed for Z-Z (d)-(f), E-E (g)-(i) and Z-E (j)-(l) cross-component correlation functions. Vertical lines indicate lag-times corresponding to a source in the North Sea (NSea; dotted line) and in the Atlantic ocean (AT; dashed line). Distribution of pair-wise phase-comparisons using Z-E correlation functions (m)-(o).

corresponding lag-times, one of the peaks in overall coherence can be attributed to the location estimate in the North Sea region labeled with NSea, while the lag-time of the weaker peak labeled with AT agrees with a source region attributed to the location estimate for the 11-14 s band in the Atlantic ocean (cf. Fig. 6.6).

For all station pairs, results for the east-east component cross-correlation functions clearly indicate a deviation in the CSI's at similar lag-times as those attributed to the North Sea peak in the vertical-vertical component results. While $\bar{\mu}$ and $\bar{\sigma}^2$ for the vertical component results further indicated the coherent signal from the Atlantic ocean, this additional signal is absent in the east-east component results, except for a faint peak in $\bar{\mu}$ found for the station-pair IGLA-CWF.

Despite the larger inter-station distance of ≈ 550 km for station pair IGLA-CWF, the overall coherence for the North Sea signal yields clear peaks on all component combinations tested here. This observation agrees with the fact, that the North Sea signal could still be detected near the west-coast of Great Britain, using the vertical and horizontal component beamforming results of the IR array. Interestingly, the peaks in $\bar{\mu}$ attributed to the North Sea signal for the east component results yield equal or higher values in comparison to the vertical component results. The maximum overall coherence, with a value of $\bar{\mu} = 0.45$ (cf. panel (h)), was found for station-pair SWN1-CWF with an inter-station distance of ≈ 140 km.

Finally, the vertical-east cross-component results differ between station-pairs. As depicted in panels (j)-(o), neither $\bar{\mu}$ nor the distribution of pair-wise phase comparisons indicate an increased coherence of microseismic noise, except for station pair IGLA-CWF. Assuming that North Sea source microseisms most likely originate from the spatially constrained region as shown in Fig. 6.7 (a) and (b), the east components approximately correspond to a radial component for station pair IGLA-CWF. Hence, this case may be considered as representative SRIP analysis of vertical-radial component cross-correlations. Assuming a Rayleigh wave particle motion, the vertical-east component cross-correlation functions is expected to yield a stable in-phase relation persistent over time, in agreement with the observed CSI results for this station pair.

Contrasting this, an increase in pair-wise phase comparisons in anti-coherence ($C_{ik} = -1$) between the vertical and east components can be observed at lag-times attributed to the NSea source for the station pairs SWN1-CWF and SWN1-LMK. Furthermore, $\bar{\mu}$ even yields a decrease in overall coherence for station pair SWN1-LMK.

For both of these station pairs, the east component does neither correspond to a pure radial component nor to a pure transversal component. Assuming a mixture of Rayleigh and Love wave particle motions for the east component recordings, the cross-correlation functions between these components may not be expected to yield

a stable phase relation over time. The decrease of time dependent coherence for the east-vertical cross-component cross-correlation found here, agrees with the assumption of a distinct time dependent signal imprint for each of the components. The vertical component seismic traces are likely dominated by the temporal signature of Rayleigh waves generated in the North Sea source region, while the east component seismic traces contain a mixture of both, Rayleigh and Love waves.

However, the pair-wise phase comparisons and the CSI's between the east-vertical component cross-correlation functions may still indicate a deviation from a purely random wave field at certain lag-times. In particular, if the phase coherence comparison is made on components, which capture different seismic phases, leading to a predominance of anti-coherence between temporal windows.

Finally, we do not observe a deviation in coherence nor in variance at lag times corresponding to the AT source in the cross-component results. This agrees with a lack of the Atlantic source peak on the east component results as observed in panel (g)-(i), assuming a comparison between a coherent signal captured on the vertical components with a random wave field dominating on the east components. Assuming that the AT signal captured here, corresponds to primary microseismic noise leaking into this intermediate frequency range, the origin of these microseisms is likely located along the shore line of Portugal (cf. Fig. 6.7 (d)). One possible explanation for the lack of the Atlantic ocean signal on the horizontal component results in the intermediate period band could be a low transversal to vertical component amplitude ratio for the microseismic noise field recorded on the British Isles from this region. While previous studies largely agree on the observation that the primary microseismic noise wave field typically yields a relatively significant portion of seismic energy on the transversal components, the amplitude ratio for the intermediate period band is hardly studied. Local and remote microseisms are likely mixed in this band [Becker et al., 2020]. Another possible explanation could be a more temporally variable or spatially incoherent microseismic noise field recorded from the Atlantic source region on the horizontal components across our station set.

Secondary Microseismic Noise - a Mediterranean Sea source

The analysis of near shore and far shore source regions can be important for understanding the origin of horizontal transversally polarized signals observed in the secondary microseimic noise field. The different propagation path conditions from near versus far shore source regions, but also the seafloor topography at the source site has to be considered when studying potential generation hypothesis such as scattering, surface

wave mode conversions or wave-type conversions at the continental margin and direct excitation due to shear tractions [Fukao et al., 2010; Gregersen, 1978; Gualtieri et al., 2015; Ying et al., 2014; Ziane and Hadziioannou, 2019] Source locations of effective secondary microseimic noise generation are theoretically determined by the second order pressure variations due to ocean surface wave interactions but also by a water depth dependent amplification of the seismic noise excitation [Gualtieri et al., 2013, 2014; Longuet-Higgins, 1950]. Oppositely traveling ocean gravity waves may interact anywhere in the open ocean but also near shore-lines where coastal wave reflection is of importance. In this case study, we test the application of a SRIP analysis to secondary microseismic noise generated in the Mediterranean Sea. Again, we estimate the source region of microseismic noise events using SRIP and beamforming and compare these location estimates with modeled seismic sources according to the secondary mechanism as described by Ardhuin et al. [2011].

In 2012 a small scale temporary 3-component broadband seismic array in the Évora region was operating in Portugal within the context of the DOCTAR (Deep OCean Test ARray; FDSN code Y7) experiment, provided the opportunity of observing secondary microseismic noise in detail from the Iberian Peninsula. Using seismic data recorded during February of 2012, the secondary microseimic noise field was analyzed with the beamforming processing scheme as described above. Figure 6.9 (a) and (b) shows an example of the vertical and transversal component mean beam PSD during February 2012 at a period of approximately $T = 7\,\mathrm{s}$. For each array location, the mean beampower within discrete backazimuth increments and a narrow slowness range around the peak beam PSD was back-projected onto a geographic map. The figure insets show the corresponding beampower in the slowness versus azimuth domain. Here, the slowness range including the peak beampower is expected to correspond to the fundamental mode of Rayleigh and Love wave phase velocities at this period and was considered for the back-projection.

According to Fig. 6.9 (a) and (b), we find a similar but not identical azimuthal distribution of mean beampower for both, the vertical and transversal component results. Especially the North Atlantic ocean appears to provide relevant contributions to the observed secondary microseismic noise at the array location. Further, we find a significant mean contribution from the Mediterranean Sea (labeled by I. in Fig. 6.9). An overall weaker local mean beampower peak from a north-eastern direction (labeled as direction II.) is more clearly observed for the vertical component beampower result.

We examine the backazimuth of the beampower peak within each temporal and spectral bin in the frequency-wavenumber beamforming over the full frequency range and time span considered as shown in Fig. 6.9) (c). Indeed, the peak beampower in the

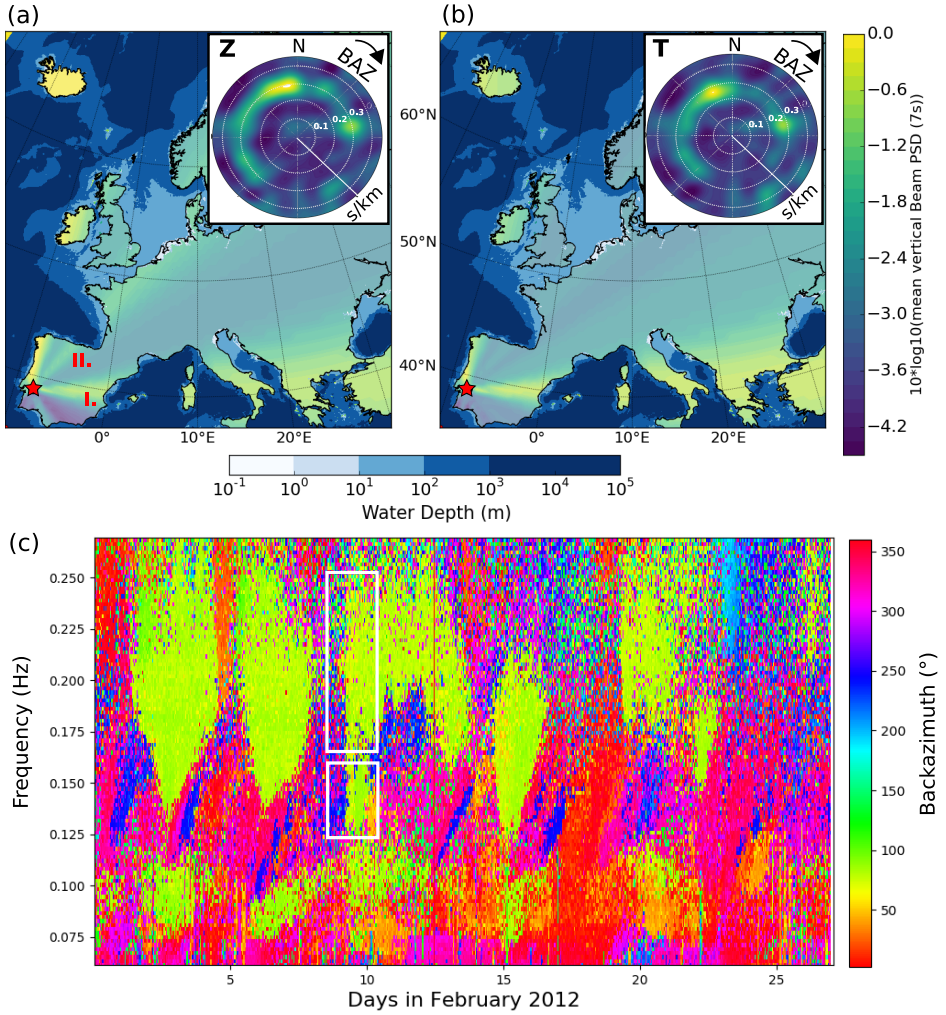

Figure 6.9: Map projection of mean beampower for one month of data in 2012 for the vertical (a) and transversal (b) components at a period of 7 s as observed with the Doctar array (indicated by red star). The insets show the beampower in the slowness vs. azimuth domain. Frequency vs. time representation of the backazimuth corresponding to the beampower peak within each spectral and temporal bin in the frequency-wavenumber beamforming (c). The two spectral peaks of the Mediterranean source outburst on Feb 10th are marked by white boxes.

short periodic secondary microseismic noise band is frequently observed from eastern backazimuths (green-yellow colors) corresponding to the central Mediterranean Sea. We focus on the analysis of two specific microseisms events. On February 10th, the Mediterranean source direction corresponds to the observed peak beampower in two distinct frequency ranges within the secondary microseismic noise band (as marked by

white boxes in Fig. 6.9 (c)) in addition to the primary microseismic noise at lower frequencies. On February 16th, relatively low frequent secondary microseismic noise is observed. In the following, we will further analyze the source location of these microseismic noise peaks during both days.

Using publicly available modeled ocean wave model output, providing the ocean surface pressure PSD as source of secondary microseismic noise as described by Ardhuin et al. [2011] (see download links provided therein), the distribution of theoretical seismic sources as observed at the array location during February was estimated. Here, we downloaded modeled ocean surface pressure PSD output on a grid of 0.5°resolution as calculated based ocean wave model output which considers wave-wave interactions in the open ocean and additionally due to coastal reflections. These two sets of modeled pressure PSD corresponds to an output where no coastal reflections are taken into account and an output which considers a reflection coefficient of 0.1 at the shorelines of continents and of 0.2 at small scale islands below the grid resolution. For visualizing the difference between both data sets, the median of the modeled seismic sources at a seismic period of 7 s for both cases were depicted corresponding to a hypothetical receiver location in central Europe.

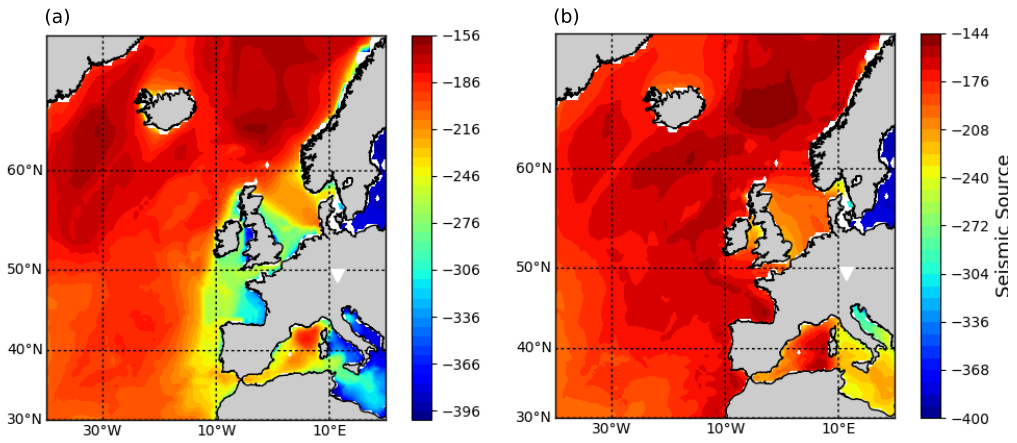

Figure 6.10: Difference between ocean surface pressure PSD as source of secondary microseismic noise without (a) and with (b) considering ocean wave reflection at the shore line estimated for February 10 in 2012.

The modeled median seismic source distribution at a period of 7 s shown in Figure 6.10 (a) and (b) indicates the presence of off-coastal secondary microseismic sources in the north Atlantic ocean. Additionally, a distributed source region is predicted for

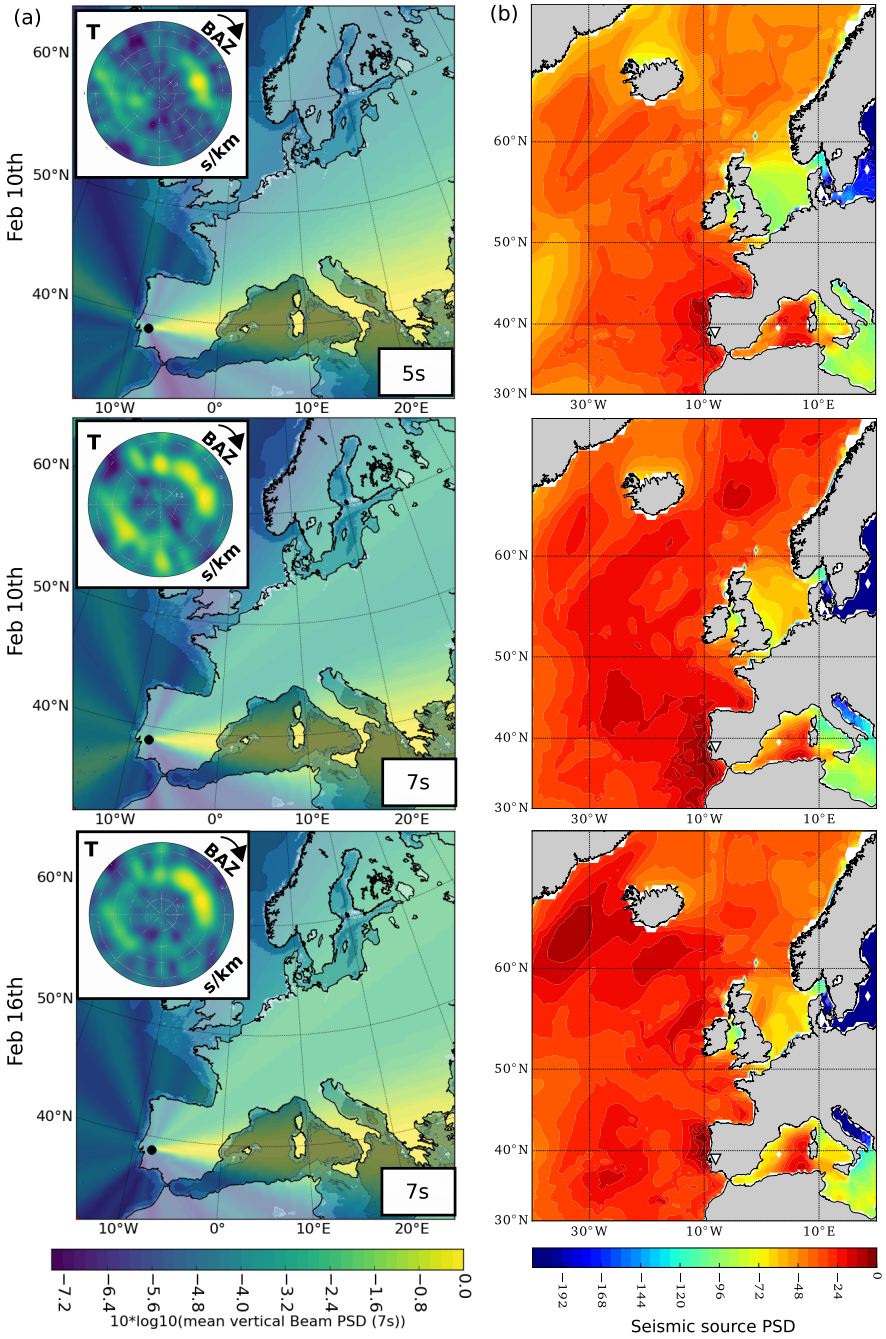

Figure 6.11: Analysis of data from February 10 and 16 (according to labels) showing vertical component beamforming derived source directions (a) and the modeled seismic source distribution (b). The insets in (a) show transversal component beampower maps.

the western Mediterranean Sea basin. While a single source area is predicted without coastal ocean wave reflections, two separate source patches are found from the data set which includes reflection, a northern and a southern coastal local maximum, roughly separated at a Latitude of 40°N. The southern local maximum arises only when coastal reflection is included. The local coastal reflection coefficient R is generally not well known and likely varies with frequency but also spatially within the geographic region considered here [Ardhuin et al., 2011]. For an estimate of the theoretical secondary microseismic noise sources on February 10, the output from both data sets were combined in order to obtain a reflection coefficients of 0.05 and 0.1 for shorelines of continents of small scale islands, respectively.

Figure 6.11 (a) shows the beamforming derived source directions during February 10th and 16th at a period of 5 and 7 s and the corresponding modeled seismic source distributions. During both days, the peak backazimuth of the mean vertical component beampower observed at a period of 5 and 7 s corresponds to a Mediterranean Sea source region as shown in Fig. 6.11 (b). The resolution of the Mediterranean Sea beampower peak does not allow for a distinction between a single or multiple source patches. Additionally, the transversal component beampower is depicted in the insets. At a period of 5 s a single beampower peak is found at the same Mediterranean Sea source azimuth observed in the vertical component results, while a broader azimuthal range yields multiple maxima of comparable amplitude from the Mediterranean Sea and the Atlantic ocean at a period of 7 s. The broader azimuthal range would agree with source locations along the northern shore-lines of the Mediterranean Sea. However, the modeled source distribution does not indicate a presence of additional coastal sources in these days. Further, comparable beam power is obtained for the transversal component results from source azimuth I. and II. as labeled in Fig. 6.9 on both days.

Figure 6.12 shows the SRIP derived source location estimate for using stations from the European network as shown in the map view. At both periods, two or three distinct source region are localized near the modeled source patches of secondary microseismic source estimated from the dataset with coastal wave reflection. Two of them are found at both periods shown here, of them is located near the west coast of Corsica. Another peak stretches over a wider area north of the coasts of Algeria. A third peak can be found at a period of 5 s near the Balearic Islands. Hence, beamforming and SRIP analysis results hint to coherent secondary microseismic noise from certain Mediterranean Sea source region. The observed dominance of these sources exceeds the expected relative amplitude in comparison to simultaneous Atlantic sources based on the modeled source estimates (cf. Fig. 6.11). However, the SRIP derived localization allows for a

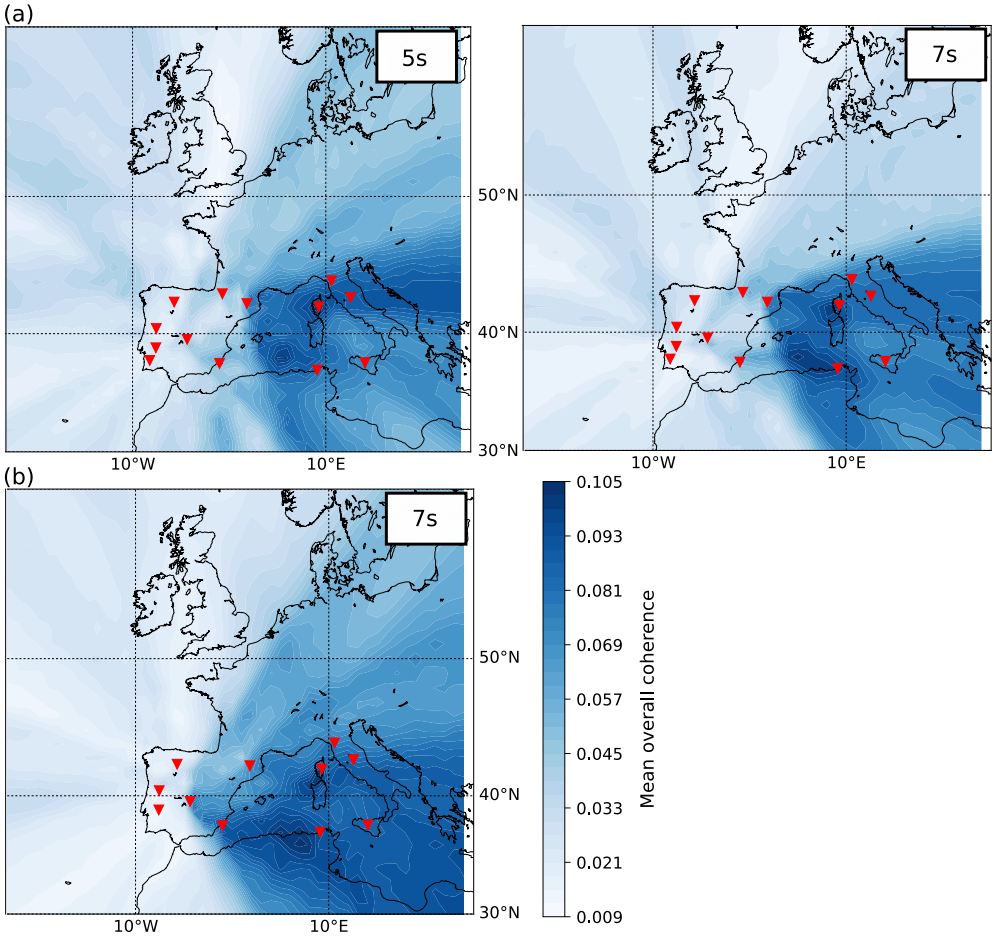

Figure 6.12: SRIP derived source localization for February 10 (a) and February 16 (b) at different periods as indicated by labels.

higher resolution in source localization and closely agrees with the theoretical prediction of the source areas.

Discussion

Regarding the analysis of the North Sea microseisms, both methods used here indicate that the most likely efficient generation area of primary microseismic noise in the North Sea is located further south than the area of the maximum modeled ocean wave heights shown in Fig. 6.7 (a). The southern North Sea is characterized by a varying sea-floor topography at different scales. Recently, Ardhuin [2018] described theoretically how ocean surface waves propagating over sea-floor variations in shallow water

may simultaneously generate horizontal and vertical forces of comparable amplitudes. In comparison to the theoretical explanation of vertical component microseismic noise by Hasselmann [1963], this framework also predicts horizontal forces, directly exciting Rayleigh and Love waves simultaneously. Importantly, the ratio of a resulting large-scale vertical force and a resulting large-scale horizontal force was found to vary with the water depth, in agreement with observations on site specific wave-type generation [Juretzek and Hadziioannou, 2017] but also with regionally and direction dependent variations in Rayleigh to Love waves ratios [Juretzek and Hadziioannou, 2016]. Further, the strength of the excitation of seismic waves was found to largely depend on the small scale bathymetry variations. Considering the regular undulating sea-floor patterns found in the shallow southern North Sea, these additional source terms provide a possible explanation for a locally efficient generation of Love and Rayleigh waves in presence of only moderate ocean wave heights.

The proximity of the North Sea source region and therefore short propagation paths to the receivers, agree with relative high overall coherences obtained for this signal, in comparison to those found for a simultaneous source in the Atlantic ocean. Additionally, the extent of the source region in the North Sea according to the source region estimates is spatially limited, while the extent of the source region for the Atlantic ocean generated signal is not comparably well resolved and a mixture of wave field components from different sub-regions remains possible. The three seismic arrays used here, cover an azimuthal range of approximately 180° around the source region, allowing for a well constrained source localization. The seismic station set used here is confined to the British Isles, but still provides a comparably well constrained source region estimate based on the SRIP analysis. Additionally, the CSI's further revealed the relative differences in overall coherence between the North Sea source and a simultaneously observed signal from the Atlantic ocean. The presence of both of these wave fields generated in different regions was not immediately obvious in the frequency-wavenumber beamforming results.

The characteristics of the seafloor topography at scales of few hundreds of meters would be required for a quantitative estimate of primary microseismic noise generation of vertically and horizontally polarized seismic waves as described recently [Ardhuin, 2018]. In comparison to the Atlantic ocean, only significantly lower ocean wave heights prevail in the southern North Sea. Nevertheless, persistent microseismic noise fields may still be observed from this region, possibly enabled by its specific sea-floor characteristics.

Regarding the analysis of the Mediterranean Sea microseisms, both approached used here indicate the reoccurring activity of certain source areas, which produce coherent

secondary microseisms. These source areas seem to dominate over simultaneous near coastal Atlantic sources at seismometers in southern Europe and at a temporary array in Portugal. For estimating the ocean-wave induced pressure PSD as source of secondary microseisms, the same constant reflection coefficient was used for the shorelines in the Mediterranean Sea and the Atlantic ocean. One possible explanation for the deviation between the modeled and observed relative source contributions from Atlantic ocean and Mediteranean Sea is a potential difference in wave reflection conditions at these different coasts, which was not taken into account here.

Chevrot et al. [2007] have also identified stable near coastal generation areas of secondary microseismic noise in the Mediteranean Sea by means of beamforming and polarization and amplitude analysis using single stations. They found localized reoccurring source areas near the western coast of Corsica and the northern coast of Menorca Island. Findings in this study support the persistance in source locations very near the localizations in their study and further show the agreement with theoretical estimates from modeled ocean wave induced pressure according to the secondary generation mechanism [Longuet-Higgins, 1950].

The broader azimuthal range of beampower at a period of 7 s observed in the transversal component beamformer results, is not explained by additional coastal sources along the northern shore-lines of the Mediterranean Sea according to the modeled source distribution. One possible explanation would be a conversion between the wave types in the northern part of this ocean basin. Transversal component beamformer results at a period of 5 s yield a narrow peak at a similar azimuth as observed for Rayleigh waves. However, coastal Love wave generation at this period could be masked by strong signal amplitudes from the central source direction.

While vertical component cross-correlations in southern Europe seem to be at risks of being influenced by spurious arrivals from Mediterannen Sea sources, less risk for bias seems to exist for the transversal component data sets at the main spectral peak of the secondary microseismic noise field due to a more homogenized wave field over different azimuths.

Conclusion

Within the scope of two case studies, we demonstrate that the phase coherence statistic analysis is applicable to the detection and localization of persistent and reoccurring microseismic noise sources in both, primary and secondary microseismic noise bands. The SRIP analysis is an interesting option for localizing sources, when arrays, suitable for the analysis of microseisms, are not accessible. The comparison between the SRIP

analysis, using a number of regionally distributed seismic stations, to beamforming, using one or three arrays, yields a comparable or better source localization. In particular the SRIP method was demonstrated to be able to detect two separate sources in the Mediterranean Sea, which were indistinguishable by means of beamforming.

In summary, results obtained from beamforming and from the SRIP analysis on cross-correlation functions between different seismic components confirm a microseismic noise source region in the southern North Sea, which efficiently generates Love and Rayleigh waves simultaneously. Considering theoretical source mechanisms, only the primary source mechanism would be in agreement with an efficient generation of Love and Rayleigh wave contributions to the microseismic noise field in the shallow water depth of the southern North Sea. Based on the observations made here, the southern North Sea serves as efficient source region for microseismic noise generation. Moreover, microseismic noise observed in the intermediate frequency range considered here, provides an opportunity to further study the generation of Rayleigh and Love waves due to the primary source mechanism in this region.

Secondary microseismic noise from the Mediterranean Sea was found to frequently dominate in vertical component seismic observations despite simultaneous sources in the Atlantic ocean. Similarly, Love waves were found to propagate from the Mediterranean Sea during these events, but their source directions often yield a broader azimuthal range than Rayleigh waves. Hence, such sources can be interesting in order to further study the origin of Love waves in the secondary microseismic noise field. Potential indirect sources of Love wave generation, such as scattering regions, corresponding to e.g. strong topography, continental slopes, and sediment basins, could possibly cause the transversal component signal source directions observed here. Such sources may be expected to contribute to the observed wave field and act as relatively persistent source regions, redistributing seismic energy. The coherence based method could further help to identify such weak amplitude source regions, if their signals remain coherent for a sufficient amount of time.

Acknowledgments

We acknowledge the GFZ Potsdam for providing the data of the temporary array in Portugal and Chris Bean for access to the Science Foundation Ireland (SFI) funded WaveObs array data from NW Ireland. The data for all other seismic stations used in this study is publicly accessible at the European data centers ORFEUS, GFZ (GeoForschungsZentrum), INGV (Istituto Nazionale di Geofisica e Vulcanologia) and IPGP

(Institut de Physique du Globe de Paris). Ocean wave model output and theoretical predictions of the ocean wave induced pressure PSD are publicly accessible from ftp://ftp.ifremer.fr/ifremer/ww3/HINDCAST. We thank the Obspy development team ObsPy [2016] for their seismic analysis toolbox. We wish to thank Martin Schimmel for fruitful discussions. We acknowledge funding by the TIDES program and by the Emmy Noether program (HA7019/1-1) of the German Research Foundation (DFG).

End of original manuscript

7

Conclusion and Outlook

The ambiguity in observations of the proportions and characteristics of Love waves and Rayleigh waves in the microseismic noise field, with a simultaneous lack of knowledge about the origin of the Love wave content, motivated the study of ocean-wave generated Love and Rayleigh waves as presented in this thesis. The main research questions within the scope of this thesis were:

Where do Love and Rayleigh waves in the ocean microseisms come from? **W**hich regions serve as efficient source areas of these wave types? **H**ow do variations in wavetype proportions link to propagation path, source site and ocean wave parameters? **W**hat constraints do the observations impose on the search for plausible generation theories of Love waves?

For adressing these objectives, the characteristics of Love and Rayleigh waves present in the microseismic noise wave field were systematically studied by means of multiple approaches. Three component beamforming was used in order to obtain directional, spectral and temporal information on the different wave types and to estimate the regional and directional variation of the Love-to-Rayleigh wave energy ratio in the primary and secondary microseismic noise bands in chapter 3. Further, the directional information on the wave-type ratio was linked to ocean surface wave conditions in the source area in order to identify parameters influencing the primary microseismic noise wavetype ratio in chapter 4. Additionally, simulations of point forces, required to describe the observed wavetype ratio, were performed to analyze the nature of potential additional generation mechanisms. Output of a state-of-the-art ocean wave model was used for a first order estimate of vertical component primary microseismic noise in chapter 5. These model results were compared to observations and discrepancies were linked to their likely regional origins. Finally, statistical properties of the instantaneous phase coherence of vertical and horizontal component seismic data were analyzed to

constrain source regions of the microseismic noise field in small ocean basins and further evaluate relevant conditions for efficient noise generation in chapter 6. The main findings are summarized as such:

In chapter 3, Love waves were found to dominate **primary microseisms** on average, with a variation in Love-to-Rayleigh wave energy ratios ranging from 0.6 to 2.0. The clearly directional pattern of the wavetype ratio was found to depend on the activity of different source areas. The temporal stability of this azimuthal ratio pattern indicates that the proportions of generated Love and Rayleigh waves are largely independent of the seasonally varying wave height levels. The significant Love wave portions and a striking directional dependence of the wavetype ratio provides evidence for the presence of a source mechanism involving direct horizontal forces. For **secondary microseisms** clearly lower Love wave contributions were found, corresponding to Love-to-Rayleigh wave energy ratios between 0.4 and 1.2. Wavetype ratios yield little directional dependence, with an exception for locations in Central Europe. A direction dependent influence on wavetype ratios due to the presence of higher modes could not be excluded. Temporal variations of the directionally averaged wavetype ratio were found to correlate with changing contributions from different source areas in varying distances. A significant influence of the Earth's structure along the propagation path on the observed wavetype composition is likely.

Differences between observed Love and Rayleigh wave amplitudes in the **primary microseismic noise band** emitted from the same coastal sections were found in chapter 4 by means of beamforming, correlation of noise amplitudes with ocean wave heights and synthetic tests. Findings hint at a coupled generation of both wave types, which depend equally on ocean-wave heights. Specific parts of the coast appear to be more effective at Love-wave generation than Rayleigh-wave generation and vice versa. Further, a correlation between the wavetype ratio and the peak ocean-wave propagation-direction was found here, hinting towards a dependence of the relative wavetype excitation on swell direction and/or an effective source radiation pattern. The significant Love wave portions, a striking source region imprint on the wavetype ratio and its dependence on ocean wave directions were found as evidence for the presence of a source mechanism involving direct horizontal forces. Spatial variations in the generated wavetype ratio suggest a regionally varying influence of different possible generation mechanisms, with a likely dependence on bathymetric conditions.

Results obtained in chapter 5 demonstrate that average properties of the vertical component **primary microseismic noise field** can be modeled based on average characteristics of ocean-surface waves using a state-of-the-art ocean-wave model and theory of primary microseismic noise generation. The present modeling approach was able

to reproduce several temporal and spectral primary microseismic noise characteristics. However, deviations between the modeled and the observed data remained. They were compensated using a spatially varying effective factor, estimated using an optimization process. The effective factor practically includes a number of parameters, which are not captured by the model approach taken here. These include, among others, the subsurface at the seismometer site, the structural heterogeneity along the propagation path, the accuracy of the ocean-wave model used for calculating the seismic source term and other, possibly neglected, source mechanisms.

In chapter 6, source regions of persistent microseismic noise generation in two small scale ocean basins, the North Sea and the Mediterranean Sea, were estimated by means of a statistical phase coherence analysis and beamforming. Findings agree with a direct and efficient joint generation of Love and Rayleigh waves in the **primary microseismic noise band** due to even moderate wave heights in the shallow southern North Sea, where an undulating topography likely causes the effective excitation of both wave types. The analysis of **secondary microseisms** from the Mediterranean Sea yields, that especially vertical component cross-correlations from seismometers in southern Europe may be influenced by spurious arrivals caused by certain recurring source regions. A broader range of source azimuths observed in transversal component beamformer results could not be explained by modeled coastal sources, pointing to a possible influence of the propagation path.

Findings presented in this thesis highlight the clear difference between characteristics of Love waves in the primary and in the secondary microseismic noise band. The distinction in characteristics between these spectral bands include the wavetype ratio, its azimuthal and temporal variation and the plausibility of a direct generation of Love waves in the source area due to the interaction between ocean waves and the solid Earth, versus an indirect conversion along the propagation path. While a direct coupled generation of both wave types is suggested by results presented here for the primary microseismic noise range, a dominant influence of the Earth structure on the wave-type composition is indicated by findings for the secondary microseismic noise range. Results detailed in this study regarding the primary microseismic noise range were followed up and supported by a recent theoretical investigation [Ardhuin, 2018], which demonstrates how ocean surface waves in shallow water may generate horizontal and vertical forces of comparable magnitudes, allowing for a simultaneous generation of both, Rayleigh waves and Love waves, at the same location. Importantly, the ratio between horizontal and vertical forces was found to vary with water-depth and an amplification of generated Rayleigh wave under shoreward propagating ocean waves was

predicted. This is in agreement with indications of an ocean-wave direction dependent wave-type generation and a spatial dependence of wavetype ratios as detailed here.

The investigation of wavetype ratios and corresponding efficient source regions refines the understanding of the spatial and physical origin of Love waves in microseisms. Since especially Love waves in the primary microseismic noise range were less well studied, findings presented in this thesis provide input for ongoing theoretical considerations regarding additional source mechanisms, capable of describing the generation of both wave types. A simultaneous activity of several generation mechanisms seems likely. Future studies will require more detailed information on small scale bathymetry in shallow water depths in order to focus on quantitative estimations of theoretical wavetype ratios. Such studies will be needed for validating the relative importance of different theoretical source mechanisms proposed to date. Studies with a focus on numerical modeling are further required for evaluating the plausibility of a propagation path influence on observed wavetype ratios, especially in the secondary microseismic noise band. Meanwhile, the consideration of heterogeneous effective wavetype generation factors displays one possible way to represent source and structure dependent variations in wavetype ratios, not yet captured by theoretical models.

On one hand, an improved knowledge and prediction of the microseismic noise field characteristics may be exploited in the context of noise applications. This includes the estimation of dominant source regions, contributing to spurious arrivals in cross-correlation functions, disturbing e.g. seismic tomographies. On the other hand, the accuracy of ocean wave models can be probed, when the physical relation between microseismic noise observations and different ocean wave parameters is known accurately. Finally, understanding the dependence of the Love-to-Rayleigh wave ratio on local small scale bathymetry provides a potential for estimating seafloor properties as long as high resolution bathymetry data remains sparse.

List of Figures

1 Introduction

1.1 Example of a time series of vertical seismic ground displacement, including either two signals or a thousand signals, depending on one's research objectives. 1

1.2 Example of a the mean power spectral density of seismic velocity over the microseismic noise bands observed with a seismic array on the northern hemisphere 4

1.3 Schematic of microseismic noise generation mechanisms 7

2 Theory and methods

2.1 Seismic response to a vertical and horizontal point force 13

2.2 Example of array transfer functions 24

3 A study of Love-to-Rayleigh wave ratios

3.1 Center locations (triangles in map) and geometries of arrays used in this study. 37

3.2 Slowness vs. backazimuth representations of the response functions of the arrays used at a period of 8 s and beamformer performance test . . 40

3.3 (a) Slowness vs. backazimuth representations of beamforming results for Rayleigh and Love waves at NICE, GRF, and THU. (b) Examples of frequency dependent slowness at the corresponding arrays. 42

3.4 Yearly wavetype source direction counts in 2013 at different array sites around the primary and secondary microseism peak 43

3.5 Frequency dependent signal backazimuths of both wavetypes from February to March 2013 46

3.6 Direction dependent average Love/Rayleigh wave kinetic energy density ratios for the primary and the secondary microseism peak 47
3.7 Seasonal variation at GRF of the array averaged vertical component power spectral density 49
3.8 Wavetype ratio histograms from the synthetic test for arrays with varying station configuration 56
3.9 Seasonal variation in 2013 at GRF of source directions for dominant P-wave noise signals 56

4 Linking source region and ocean wave parameters with the observed primary microseismic noise

4.1 Self-normalized mean beampower PSD for vertical (Z), radial (R) and transversal (T) component noise observations in slowness vs. backazimuth representation 64
4.2 Sequence of 4 days in December 2013 showing daily averages of ocean wave height and beampower 66
4.3 Estimate of great circle path deviations using earthquakes 68
4.4 Correlation coefficients between noise and ocean wave heights at different array sites 70
4.5 (a) Map view of the distance range at each location within which the model data has an average CC above 0.8. (b) Average ocean surface displacement PSD at a period of approximately 14 s in 2013. (c) Average seismic source proxy of wave height scaled by water depths. 71
4.6 Map view of number counts of source positions for vertical component and transversal component noise observations from the curved wavefront beamforming localization with the Norsar array 73
4.7 Relation between seismic noise and ocean surface elevation ASD for two locations of high correlation coefficient using Norsar array measurements 75
4.8 Map view of mean relative residuals and corresponding relative values of T from linear function fits 76
4.9 Demeaned transversal/vertical component noise ratio at two arrays vs. ocean gravity wave propagation direction 79
4.10 Relation between transversal/vertical noise ratio vs. ocean gravity wave propagation direction at different locations 80

4.11 Modeled transversal/vertical component RMS displacement amplitude ratios vs. source azimuth observed from the array centers for three different test cases. 82
4.12 Sequence of ocean surface elevation PSD from Feb 24 and 25, 2009 and array based localization of noise sources 88

5 Predicting primary microseimic noise

5.1 Correlation coefficient between theoretical noise source contributions at the array and the observed displacement PSD 94
5.2 Direction dependent back-projection of observed beam PSD at the Norsar array and the Swiss aray 96
5.3 Initial and optimized local slope factor 98
5.4 Difference vector indicating where the modeled data overestimates or underestimates the occurance of observed peak signal directions of arrival 99
5.5 Jackknife test showing the Pearson correlation coefficient between the observed and modeled time series of displacement PSD at three seismic stations 103
5.6 Time series of vertical displacement amplitudes from data and model at station CAN 106
5.7 Rank correlation coefficient τ_b between the time series of the individual modeled noise source contributions and the observation for station CAN 107
5.8 Result of the Jackknife test showing the L1-norm misfit between the modeled and observed time series obtained when disregarding individual theoretical source contributions 109
5.9 (a) Map view of the final $s_{\text{eff}}(A_i)$ (color range) for station CAN and NOUC at $f = 0.5\,\text{Hz}$. (b) Time series of modeled displacement RMS amplitudes for both stations in comparison to observations; with the initial $s_{\text{eff}} = 8$ and the final optimized $s_{\text{eff}}(A_i)$. 112
5.10 (a) Individual modeled time series for 9 seperate areal sections according to the labels and colored regions depicted in the map view inset in comparison to the observed time seris at station CAN. (b) Separate graphs depicting the self normalized time series for sections 1, 4 and 5 in comparison to the observation. 115

6 A phase coherence based analysis of microseisms in marginal seas

6.1 Distribution of pairwise phase-comparisons for a synthetic dataset of random noise . . . 125
6.2 Distribution of pairwise phase-comparisons for a synthetic dataset of random noise with increasing proportions of a perfectly coherent signal . 127
6.3 Distribution of pairwise phase-comparisons, overall coherence and variance for data examples from the European seismic station network . . . 128
6.4 Variance weighted overall coherence . . . 129
6.5 Normalized vertical component beampower at three different arrays . . 132
6.6 Back-projected array beampower for the observed from 3 different array center locations during March 23 and March 25 in 2013 . . . 134
6.7 Map view of the most likely source region of the 23 March microseismic noise outburst . . . 135
6.8 Distribution of pair-wise phase-comparisons using Z-Z, E-E and Z-E correlation function . . . 138
6.9 Map projection of mean beampower for one month of data in 2012 . . . 142
6.10 Difference between ocean surface pressure PSD as source of secondary microseismic noise without (a) and with (b) considering ocean wave reflection at the shore line estimated for February 10 in 2012. . . . 143
6.11 Analysis of data from February 10 and 16 (according to labels) showing vertical component beamforming derived source directions (a) and the modeled seismic source distribution (b). The insets in (a) show transversal component beampower maps. . . . 144
6.12 SRIP derived source localization for February 10 (a) and February 16 (b) at different periods as indicated by labels. . . . 146

References

M. Afanasiev, *D. Peter*, *K. Sager*, *S. Simutė*, *L. Ermert*, *L. Krischer*, and *A. Fichtner*. Foundations for a multiscale collaborative global Earth model. *Geophysical Journal International*, 204(1):39–58 (2016). doi:{10.1093/gji/ggv439}. 66

K. Aki, *P. Richards*, and *U. S. Books*. *Quantitative Seismology*. University Science Books (2002). ISBN 9780935702965. 11

C. Amante and *B. W. Eakins*. *ETOPO1 1 arc-minute global relief model: procedures, data sources and analysis*. US Department of Commerce, National Oceanic and Atmospheric Administration, National Environmental Satellite, Data, and Information Service, National Geophysical Data Center, Marine Geology and Geophysics Division Colorado (2009). 68, 71, 109

F. Ardhuin. Large-Scale Forces Under Surface Gravity Waves at a Wavy Bottom: A Mechanism for the Generation of Primary Microseisms. *Geophysical Research Letters*, 45(16):8173–8181 (2018). doi:https://doi.org/10.1029/2018GL078855. 14, 16, 90, 116, 123, 146, 147, 153

F. Ardhuin, *A. Balanche*, *E. Stutzmann*, and *M. Obrebski*. From seismic noise to ocean wave parameters: General methods and validation. *Journal of Geophysical Research: Oceans*, 117(C5) (2012). doi:https://doi.org/10.1029/2011JC007449. 6

F. Ardhuin, *L. Gualtieri*, and *E. Stutzmann*. How ocean waves rock the Earth: Two mechanisms explain microseisms with periods 3 to 300 s. *Geophysical Research Letters*, 42(3):765–772 (2015). doi:10.1002/2014GL062782. 14, 15, 16, 51, 61, 74, 77, 81, 83, 84, 85, 89, 90, 92, 98, 104, 105, 108, 109, 114

F. Ardhuin and *T. H. Herbers*. Noise generation in the solid Earth, oceans and atmosphere, from nonlinear interacting surface gravity waves in finite depth. *Journal of Fluid Mechanics*, 716:316–348 (2013). doi:10.1017/jfm.2012.548. 8, 17, 18, 19, 48, 51, 53, 131

F. Ardhuin, *A. Rawat*, and *J. Aucan*. A numerical model for free infragravity waves: Definition and validation at regional and global scales. *Ocean Modelling*, 77:20–32 (2014a). doi: doi:10.1016/j.ocemod.2014.02.006. 16, 92

F. Ardhuin, *A. Rawat*, and *J. Aucan*. Numerical ocean wave model output. `ftp://ftp.ifremer.fr/ifremer/ww3/HINDCAST` (2014b). 93

F. Ardhuin, *E. Rogers*, *A. V. Babanin*, *J.-F. Filipot*, *R. Magne*, *A. Roland*, *A. van der Westhuysen*, *P. Queffeulou*, *J.-M. Lefevre*, *L. Aouf*, and *F. Collard*. Semiempirical dissipation source functions for ocean waves. part i: Definition, calibration, and validation. *Journal of Physical Oceanography*, 40(9):1917–1941 (2010). doi:10.1175/2010JPO4324.1. 67

F. Ardhuin, *E. Stutzmann*, *M. Schimmel*, and *A. Mangeney*. Ocean wave sources of seismic noise. *Journal of Geophysical Research: Oceans*, 116(C9) (2011). doi:10.1029/2011JC006952. 18, 35, 36, 43, 67, 77, 133, 141, 143, 145

G. L. . S. E. Ardhuin, F. Physics of Ambient Noise Generation by Ocean Waves, chapter Chap. 3, page 69–108. Cambridge University Press (2019). doi:10.1017/9781108264808.005. 11

Aster R.C., *McNamara D.E.*, and *Bromirski P.D.* Multidecadal climate-induced variability in microseisms. 79(2):194–202 (2008). 61

S. Banerji. Microseisms associated with storms in the Indian seas. *Nature*, 123(3092):163 (1929). 6

S. Banerji. Microseisms associated with disturbed weather in the indian seas. *Philosophical Transactions of the Royal Society of London. Series A, Containing Papers of a Mathematical or Physical Character*, 229:287–328 (1930). ISSN 02643952. 7

G. Barruol, *D. Reymond*, *F. R. Fontaine*, *O. Hyvernaud*, *V. Maurer*, and *K. Maamaatuaiahutapu*. Characterizing swells in the southern Pacific from seismic and infrasonic noise analyses. *Geophysical Journal International*, 164(3):516–542 (2006). 60, 74, 83

D. Becker, *L. Cristiano*, *J. Peikert*, *T. Kruse*, *F. Dethof*, *C. Hadziioannou*, and *T. Meier*. Temporal modulation of the local microseism in the north sea. *Journal of Geophysical Research: Solid Earth*, 125(10):e2020JB019770 (2020). doi:https://doi.org/10.1029/2020JB019770. E2020JB019770 2020JB019770. 140

Y. Behr, *J. Townend*, *M. Bowen*, *L. Carter*, *R. Gorman*, *L. Brooks*, and *S. Bannister*. Source directionality of ambient seismic noise inferred from three-component beamforming. *Journal of Geophysical Research: Solid Earth*, 118(1):240–248 (2013). doi:10.1029/2012JB009382. 9, 36, 51, 61, 63

P. Bernard. Sur certaines proprietes de la boule etudiées a l'aide des enregistrements seismographiques. *Bull. Inst. Oceanogr. Monaco*, 800:1–19 (1941). 7

P. Bernard. Historical sketch of microseisms from past to future. *Physics of the Earth and Planetary Interiors*, 63(3-4):145–150 (1990). doi:10.1016/0031-9201(90)90013-N. 6

Beucler, *A. Mocquet*, *M. Schimmel*, *S. Chevrot*, *O. Quillard*, *J. Vergne*, and *M. Sylvander*. Observation of deep water microseisms in the north atlantic ocean using tide modulations. *Geophysical Research Letters*, 42(2):316–322 (2015). ISSN 1944-8007. doi:10.1002/2014GL062347. 2014GL062347. 60

M. Beyreuther, *R. Barsch*, *L. Krischer*, *T. Megies*, *Y. Behr*, and *J. Wassermann*. ObsPy: A Python toolbox for seismology. *Seismological Research Letters*, 81(3):530–533 (2010). doi:10.1785/gssrl.81.3.530. 38

M. Blaik and *W. L. Donn*. Microseism ground motion at Palisades and Weston. *Bulletin of the Seismological Society of America*, 44(4):597–612 (1954). ISSN 0037-1106. 8

R. N. Bracewell. *The Fourier transform and its applications*, volume 31999. McGraw-Hill New York (1986). 28, 124

F. Brenguier, *M. Campillo*, *C. Hadziioannou*, *N. M. Shapiro*, *R. M. Nadeau*, and *E. Larose*. Postseismic relaxation along the San Andreas fault at Parkfield from continuous seismological observations. *Science (80-.).*, 321(5895):1478–81 (2008). ISSN 1095-9203. doi: 10.1126/science.1160943. 5, 35

P. D. Bromirski. Vibrations from the "Perfect Storm". *Geochemistry, Geophysics, Geosystems*, 2 (2001). doi:10.1029/2000GC000119. 60, 117

Bromirski, Peter D. and Flick, Reinhard E. and Graham, Nicholas. Ocean wave height determined from inland seismometer data: Implications for investigating wave climate changes in the NE Pacific. *Journal of Geophysical Research: Oceans*, 104(C9):20753–20766 (1999). doi:10.1029/1999JC900156. 61, 83

L. A. Brooks, *J. Townend*, *P. Gerstoft*, *S. Bannister*, and *L. Carter*. Fundamental and higher-mode Rayleigh wave characteristics of ambient seismic noise in New Zealand. *Geophysical Research Letters*, 36(23) (2009). doi:10.1029/2009GL040434. 35

J. Capon. High-resolution frequency-wavenumber spectrum analysis. *Proceedings of the IEEE*, 57(8):1408–1418 (1969). ISSN 1558-2256. doi:10.1109/PROC.1969.7278. 25

R. K. Cessaro. Sources of primary and secondary microseisms. *Bulletin of the Seismological Society of America*, 84(1):142–148 (1994). 131

S. Chevrot, *M. Sylvander*, *S. Benahmed*, *C. Ponsolles*, *J. M. Lefèvre*, and *D. Paradis*. Source locations of secondary microseisms in western Europe: Evidence for both coastal and pelagic sources. *Journal of Geophysical Research: Solid Earth*, 112(B11) (2007). doi: 10.1029/2007JB005059. 148

N. Cotte, *H. A. Pedersen*, *M. Campillo*, *V. Farra*, and *Y. Cansi*. Off-great-circle propagation of intermediate-period surface waves observed on a dense array in the French Alps. *Geophysical Journal International*, 142:825–840 (2000). doi:10.1046/j.1365-246X.2000.00187.x. 65

D. Craig, *C. J. Bean*, *I. Lokmer*, and *M. Möllhoff*. Correlation of wavefield-separated ocean-generated microseisms with north atlantic source regions. *Bulletin of the Seismological Society of America* (2016). doi:10.1785/0120150181. 69

J. Darbyshire and *H. Iyer*. Some recent developments in the study of microseisms in Great Britain and the United States. *Geophysical Journal International*, 1(2):180–184 (1958). doi:10.1111/j.1365-246X.1958.tb00049.x. 8, 35

C. Davy, *G. Barruol*, *F. R. Fontaine*, *K. Sigloch*, and *E. Stutzmann*. Tracking major storms from microseismic and hydroacoustic observations on the seafloor. *Geophysical Research Letters*, 41(24):8825–8831 (2014). doi:10.1002/2014GL062319. 6, 34

G. Deacon. Relation between sea waves and microseisms. *Nature*, 160(4065):419–421 (1947). doi:10.1038/160419a0. 6, 7, 34

A. Derode, *E. Larose*, *M. Tanter*, *J. de Rosny*, *A. Tourin*, *M. Campillo*, and *M. Fink*. Recovering the green's function from field-field correlations in an open scattering medium (l). *The Journal of the Acoustical Society of America*, 113(6):2973–2976 (2003). doi:10.1121/1.1570436. 5

C. W. Ebeling. 1 Inferring Ocean Storm Characteristics from Ambient Seismic Noise: A Historical Perspective. *Advances in Geophysics*, 53:1 (2012). 7, 35, 61, 123

C. Esmersoy, *V. Cormier*, and *M. Toksoz*. Three-component array processing. *The VELA Program. A Twenty-Five Year Review of Basic Research* (1985). 23, 26, 38, 62

H.-H. Essen, *F. Krüger*, *T. Dahm*, and *I. Grevemeyer*. On the generation of secondary microseisms observed in northern and central Europe. *Journal of Geophysical Research: Solid Earth*, 108(B10) (2003). doi:10.1029/2002JB002338. 44, 131

G. Ferretti, *A. Zunino*, *D. Scafidi*, *S. Barani*, and *D. Spallarossa*. On microseisms recorded near the ligurian coast (italy) and their relationship with sea wave height. *Geophysical Journal International*, 194(1):524–533 (2013). doi:10.1093/gji/ggt114. 61

A. Friedrich, *F. Krüger*, and *K. Klinge*. Ocean-generated microseismic noise located with the Gräfenberg array. *Journal of Seismology*, 2(1):47–64 (1998). doi:10.1023/A:1009788904007. 9, 36, 42, 44, 50, 51, 53, 61, 65, 77, 78, 81, 83, 84, 131

Y. Fukao, *K. Nishida*, and *N. Kobayashi*. Seafloor topography, ocean infragravity waves, and background Love and Rayleigh waves. *Journal of Geophysical Research: Solid Earth*, 115(B4) (2010). doi:10.1029/2009JB006678. 36, 50, 61, 71, 81, 82, 84, 123, 141

M. Gal, *A. M. Reading*, *S. Ellingsen*, *K. D. Koper*, *R. Burlacu*, and *S. J. Gibbons*. Deconvolution enhanced direction of arrival estimation using one- and three-component seismic arrays applied to ocean induced microseisms. *Geophysical Journal International*, 206(1):345–359 (2016). doi:10.1093/gji/ggw150. 65

I. Gaudot, *Beucler*, *A. Mocquet*, *M. Schimmel*, and *M. Le Feuvre*. Statistical redundancy of instantaneous phases: theory and application to the seismic ambient wavefield. *Geophysical Journal International*, 204(2):1159–1163 (2015). ISSN 0956-540X. doi:10.1093/gji/ggv501. 29, 123, 124, 125, 126, 136

Z. W. Geem, *J. H. Kim*, and *G. Loganathan*. A new heuristic optimization algorithm: Harmony search. *SIMULATION*, 76(2):60–68 (2001). doi:10.1177/003754970107600201. 100

P. Gerstoft, *M. C. Fehler*, and *K. G. Sabra*. When katrina hit california. *Geophysical Research Letters*, 33(17) (2006). doi:10.1029/2006GL027270. 8

P. Gerstoft, *P. M. Shearer*, *N. Harmon*, and *J. Zhang*. Global P, PP, and PKP wave microseisms observed from distant storms. *Geophysical Research Letters*, 35(23) (2008). doi:10.1029/2008GL036111. 8, 35, 48

S. Gregersen. Possible mode conversion between Love and Rayleigh waves at a continental margin. *Geophys. J. R. astr. Soc.*, 54:121–127 (1978). 8, 19, 61, 141

S. Gregersen and *L. E. Alsop*. Mode conversion of Love waves at the continental margin. *Bull*, 66:1855–1872 (1976). 53

I. Grevemeyer, *R. Herber*, and *H.-H. Essen*. Microseismological evidence for a changing wave climate in the northeast atlantic ocean. *Nature*, 408(6810):349–352 (2000). doi:10.1038/35042558. 61

L. Gualtieri, *E. Stutzmann*, *Y. Capdeville*, *F. Ardhuin*, *M. Schimmel*, *A. Mangeney*, and *A. Morelli*. Modelling secondary microseismic noise by normal mode summation. *Geophys. J. Int.*, 193(3):1732–1745 (2013). ISSN 0956-540X. doi:10.1093/gji/ggt090. 14, 35, 82, 141

L. Gualtieri, *E. Stutzmann*, *Y. Capdeville*, *V. Farra*, *A. Mangeney*, and *A. Morelli*. On the shaping factors of the secondary microseismic wavefield. *Journal of Geophysical Research: Solid Earth*, 120(9):6241–6262 (2015). doi:10.1002/2015JB012157. 141

L. Gualtieri, *E. Stutzmann*, *V. Farra*, *Y. Capdeville*, *M. Schimmel*, *F. Ardhuin*, and *A. Morelli*. Modelling the ocean site effect on seismic noise body waves. *Geophys. J. Int.*, 197(2):1096–1106 (2014). ISSN 0956-540X. doi:10.1093/gji/ggu042. 8, 35, 141

L. Gualtieri, *E. Stutzmann*, *C. Juretzek*, *C. Hadziioannou*, and *F. Ardhuin*. Global scale analysis and modelling of primary microseisms. *Geophysical Journal International*, 218(1):560–572 (2019). ISSN 0956-540X. doi:10.1093/gji/ggz161. 10, 16, 91, 104, 105, 106, 107, 108, 113, 114, 117

B. Gutenberg. *Die seismische Bodenunruhe*. Ph.D. thesis, University of Göttingen (1911). 34

B. Gutenberg. Microseisms in North America. *Bulletin of the Seismological Society of America*, 21(1):1–24 (1931). 7

H. Harjes and *M. Henger*. Array-seismologie. *Zeitschrift für Geophysik*, 39:865–905 (1973). 22

D. G. Harkrider and *D. L. Anderson*. Surface wave energy from point sources in plane layered earth models. *Journal of Geophysical Research*, 71(12):2967–2980 (1966). doi:10.1029/JZ071i012p02967. 46

K. Hasselmann. A statistical analysis of the generation of microseisms. *Reviews of Geophysics*, 1(2):177–210 (1963). doi:10.1029/RG001i002p00177. 7, 14, 16, 17, 19, 20, 34, 35, 36, 50, 51, 53, 61, 71, 74, 77, 79, 84, 89, 114, 123, 147

R. A. Haubrich and *K. McCamy*. Microseisms: Coastal and pelagic sources. *Reviews of Geophysics*, 7(3):539–571 (1969). doi:10.1029/RG007i003p00539. 8, 9, 35, 36, 57, 60

R. A. Haubrich, *W. H. Munk*, and *F. E. Snodgrass*. Comparative spectra of microseisms and swell. *Bulletin of the Seismological Society of America*, 53(1):27–37 (1963). ISSN 0037-1106. 5, 7

R. B. Herrmann. Computer programs in seismology: An evolving tool for instruction and research. *Seismological Research Letters*, 84(6):1081–1088 (2013). doi:10.1785/0220110096. 46

H. Iyer. A study on the direction of arrival of microseisms at Kew Observatory. *Geophysical Journal International*, 1(1):32–43 (1958). doi:10.1111/j.1365-246X.1958.tb00032.x. 6, 8, 34

C. Juretzek and *C. Hadziioannou*. Where do ocean microseisms come from? A study of Love-to-Rayleigh wave ratios. *Journal of Geophysical Research: Solid Earth*, 121(9):6741–6756 (2016). doi:10.1002/2016JB013017. 9, 16, 61, 63, 81, 83, 123, 131, 147

C. Juretzek and *C. Hadziioannou*. Linking source region and ocean wave parameters with the observed primary microseismic noise. *Geophysical Journal International*, 211(3):1640–1654 (2017). ISSN 0956-540X. doi:10.1093/gji/ggx388. 10, 17, 123, 131, 147

H. Kanamori and *J. W. Given*. Use of long-period surface waves for rapid determination of earthquake-source parameters. *Physics of the Earth and Planetary Interiors*, 27(1):8 – 31 (1981). ISSN 0031-9201. doi:https://doi.org/10.1016/0031-9201(81)90083-2. 20

S. Kedar, *M. Longuet-Higgins*, *F. Webb*, *N. Graham*, *R. Clayton*, and *C. Jones*. The origin of deep ocean microseisms in the north atlantic ocean. In *Proceedings of the Royal Society of London A: Mathematical, Physical and Engineering Sciences*, volume 464, pages 777–793. The Royal Society (2008). doi:10.1098/rspa.2007.0277. 35, 44, 131

M. G. Kendall. A new measure of rank correlation. *Biometrika*, 30(1/2):81–93 (1938). ISSN 00063444. 69

M. G. Kendall. The treatment of ties in ranking problems . *Biometrika*, 33(3):239–251 (1945). ISSN 0006-3444. doi:10.1093/biomet/33.3.239. 27

B. L. N. Kennett. Seismic wave scattering by obstacles on interfaces. *Geophysical Journal of the Royal Astronomical Society*, 28(3):249–266 (1972). ISSN 1365-246X. doi:10.1111/j.1365-246X.1972.tb06127.x. 8, 19, 61

B. L. N. Kennett and *S. Mykkeltveit*. Guided wave propagation in laterally varying media - ii. lg-waves in north-western europe. *Geophysical Journal of the Royal Astronomical Society*, 79(1):257–267 (1984). ISSN 1365-246X. doi:10.1111/j.1365-246X.1984.tb02854.x. 8, 61

W. Kimman, *X. Campman*, and *J. Trampert*. Characteristics of seismic noise: fundamental and higher mode energy observed in the northeast of the netherlands. *Bulletin of the Seismological Society of America*, 102(4):1388–1399 (2012). doi:10.1785/0120110069. 35, 44, 53, 65

W. P. Kimman and *J. Trampert*. Approximations in seismic interferometry and their effects on surface waves. *Geophysical Journal International*, 182(1):461–476 (2010). doi:https://doi.org/10.1111/j.1365-246X.2010.04632.x. 123

S. Kirkpatrick, *C. D. Gelatt*, and *M. P. Vecchi*. Optimization by Simulated Annealing. *Science*, 220(4598):671–680 (1983). ISSN 0036-8075. doi:10.1126/science.220.4598.671. 109

O. Klotz. Microseisms. *Science*, 32(816):252 (1910). 6

K. D. Koper, *K. Seats*, and *H. Benz*. On the Composition of Earth's Short-Period Seismic Noise Field. *Bull. Seismol. Soc. Am.*, 100(2):606–617 (2010). ISSN 0037-1106. doi:10.1785/0120090120. 8, 35

M. Landès, *F. Hubans*, *N. M. Shapiro*, *A. Paul*, and *M. Campillo*. Origin of deep ocean microseisms by using teleseismic body waves. *Journal of Geophysical Research: Solid Earth*, 115(B5) (2010). doi:10.1029/2009JB006918. 8, 48

G. Laske, *G. Masters.*, *Z. Ma*, and *M. Pasyanos*. Update on CRUST1.0 - A 1-degree Global Model of Earth's Crust. In *Geophys. Res. Abstracts, 15*, pages Abstract EGU2013–2658 (2013). 46

F.-C. Lin, *M. P. Moschetti*, and *M. H. Ritzwoller*. Surface wave tomography of the western United States from ambient seismic noise: Rayleigh and Love wave phase velocity maps. *Geophysical Journal International*, 173:281–298 (2008). doi:10.1111/j.1365-246X.2008.03720.x. 9, 61

O. I. Lobkis and *R. L. Weaver*. On the emergence of the green's function in the correlations of a diffuse field. *The Journal of the Acoustical Society of America*, 110(6):3011–3017 (2001). doi:10.1121/1.1417528. 5

M. S. Longuet-Higgins. A theory of the origin of microseisms. *Philosophical Transactions of the Royal Society of London A: Mathematical, Physical and Engineering Sciences*, 243(857):1–35 (1950). doi:10.1098/rsta.1950.0012. 7, 17, 19, 20, 34, 35, 53, 123, 141, 148

T. Matsuzawa, *K. Obara*, *T. Maeda*, *Y. Asano*, and *T. Saito*. Love-and Rayleigh-Wave Microseisms Excited by Migrating Ocean Swells in the North Atlantic Detected in Japan and Germany. *Bulletin of the Seismological Society of America*, 102(4):1864–1871 (2012). doi:10.1785/0120110269. 51, 63, 73, 123, 131

A. McGarr. Amplitude variations of rayleigh waves—propagation across a continental margin. *Bulletin of the Seismological Society of America*, 59(3):1281–1305 (1969). 84

M. Miche. Mouvements ondulatoires de la mer en profondeur constante ou décroissante. *Annales de Ponts et Chaussées*, (1):26–78 (1944). 7

M. Möllhoff and *C. J. Bean*. Seismic Noise Characterization in Proximity to Strong Microseism Sources in the Northeast Atlantic. *Bulletin of the Seismological Society of America*, 106(2):464—477 (2016). doi:10.1785/0120150204. 65, 83

K. Nishida, *H. Kawakatsu*, *Y. Fukao*, and *K. Obara*. Background Love and Rayleigh waves simultaneously generated at the Pacific Ocean floors. *Geophysical Research Letters*, 35(16) (2008). doi:10.1029/2008GL034753. 9, 36, 50, 51, 53, 61, 123

ObsPy. The ObsPy Development Team (2016). doi:10.5281/ZENODO.46151. 21, 62, 150

J. Oliver. A summary of observed seismic surface wave dispersion. *Bulletin of the Seismological Society of America*, 52(1):81–86 (1962). 65

F. Omori. Horizontal pendulums for the mechanical registration of seismic and other earth movements. *Journal of the College of Science*, 11:121–145 (1899). 6

H. Paulssen, *A. L. Levshin*, *A. V. Lander*, and *R. Snieder*. Time- and frequency-dependent polarization analysis: anomalous surface wave observations in iberia. *Geophysical Journal International*, 103(2):483 (1990). doi:10.1111/j.1365-246X.1990.tb01786.x. 65

V. Poggi and *D. Fäh*. Estimating Rayleigh wave particle motion from three-component array analysis of ambient vibrations. *Geophysical Journal International*, 180(1):251–267 (2010). doi:10.1111/j.1365-246X.2009.04402.x. 39

POLENET/LAPNET data set. Polenet/lapnet data set: continuous seismic data recorded by polenet/lapnet seismic array during the international polar year 2007-2009. Dataset Release Date (2012). doi:10.15778/RESIF.XK2007. 62

P. Poli, *H. Pedersen*, *M. Campillo*, and *the POLENET/LAPNET Working Group*. Noise directivity and group velocity tomography in a region with small velocity contrasts: the northern Baltic shield. *Geophysical Journal International*, 192(1):413–424 (2013). doi: 10.1093/gji/ggs034. 61

L. Retailleau, *P. Boué*, *L. Li*, and *M. Campillo*. Ambient seismic noise imaging of the lowermost mantle beneath the North Atlantic Ocean. *Geophysical Journal International*, 222(2):1339–1351 (2020). ISSN 0956-540X. doi:10.1093/gji/ggaa210. 8

L. Retailleau, *P. Boué*, *L. Stehly*, and *M. Campillo*. Locating microseism sources using spurious arrivals in intercontinental noise correlations. *Journal of Geophysical Research: Solid Earth*, 122(10):8107–8120 (2017). doi:https://doi.org/10.1002/2017JB014593. 123

N. Riahi, *G. Bokelmann*, *P. Sala*, and *E. H. Saenger*. Time-lapse analysis of ambient surface wave anisotropy: A three-component array study above an underground gas storage. *Journal of Geophysical Research: Solid Earth*, 118(10):5339–5351 (2013). doi: 10.1002/jgrb.50375. 26, 38, 62

D. Rind and *W. L. Donn*. Microseisms at Palisades: 2. Rayleigh wave and Love wave characteristics and the geologic control of propagation. *Journal of Geophysical Research: Solid Earth*, 84(B10):5632–5642 (1979). doi:10.1029/JB084iB10p05632. 8, 35, 36, 53

S. Rost and *C. Thomas*. Array seismology: Methods and applications. *Reviews of Geophysics*, 40(3):2–1–2–27 (2002). doi:10.1029/2000RG000100. 21, 22, 24

K. G. Sabra, *P. Gerstoft*, *P. Roux*, *W. a. Kuperman*, and *M. C. Fehler*. Surface wave tomography from microseisms in Southern California. *Geophys. Res. Lett.*, 32(14):n/a–n/a (2005). ISSN 00948276. doi:10.1029/2005GL023155. 5, 35

H. Sadeghisorkhani, *Ó. Gudmundsson*, *R. Roberts*, and *A. Tryggvason*. Mapping the source distribution of microseisms using noise covariogram envelopes. *Geophysical Journal International*, 205(3):1473–1491 (2016). doi:10.1093/gji/ggw092. 63, 65, 83, 131

T. Saito. Love-wave excitation due to the interaction between a propagating ocean wave and the sea-bottom topography. *Geophysical Journal International*, 182(3):1515–1523 (2010). doi:10.1111/j.1365-246X.2010.04695.x. 36, 50, 61, 77, 78, 81, 84, 85, 123

J. C. Samson. Pure states, polarized waves, and principal components in the spectra of multiple, geophysical time-series. *Geophysical Journal of the Royal Astronomical Society*, 72(3):647–664 (1983). doi:10.1111/j.1365-246X.1983.tb02825.x. 26

F. J. Sanchez-Sesma and *M. Campillo*. Retrieval of the Green's Function from Cross Correlation: The Canonical Elastic Problem. *Bull. Seismol. Soc. Am.*, 96(3):1182–1191 (2006). ISSN 0037-1106. doi:10.1785/0120050181. 35

M. Schimmel. Phase cross-correlations: Design, comparisons, and applications. *Bulletin of the Seismological Society of America*, 89(5):1366–1378 (1999). ISSN 0037-1106. 28, 123

M. Schimmel and *H. Paulssen*. Noise reduction and detection of weak, coherent signals through phase-weighted stacks. *Geophysical Journal International*, 130(2):497–505 (1997). doi:10.1111/j.1365-246X.1997.tb05664.x. 28, 123

M. Schimmel, *E. Stutzmann*, *F. Ardhuin*, and *J. Gallart*. Polarized Earth's ambient microseismic noise. *Geochemistry, Geophysics, Geosystems*, 12(7) (2011). doi:10.1029/2011GC003661. 62

C. Sens-Schönfelder and *U. Wegler*. Passive image interferometry and seasonal variations of seismic velocities at Merapi Volcano, Indonesia. *Geophys. Res. Lett.*, 33(21):1–5 (2006). ISSN 0094-8276. doi:10.1029/2006GL027797. 5, 35

A. Sergeant, *E. Stutzmann*, *A. Maggi*, *M. Schimmel*, *F. Ardhuin*, and *M. Obrebski*. Frequency-dependent noise sources in the north atlantic ocean. *Geochemistry, Geophysics, Geosystems*, 14(12):5341–5353 (2013). doi:https://doi.org/10.1002/2013GC004905. 131

N. M. Shapiro and *M. Campillo*. Emergence of broadband rayleigh waves from correlations of the ambient seismic noise. *Geophysical Research Letters*, 31(7) (2004). doi:https://doi.org/10.1029/2004GL019491. 5, 35

N. M. Shapiro, *M. H. Ritzwoller*, and *G. D. Bensen*. Source location of the 26 sec microseism from cross-correlations of ambient seismic noise. *Geophysical Research Letters*, 33(18) (2006). doi:https://doi.org/10.1029/2006GL027010. 123

R. Snieder. Extracting the green's function from the correlation of coda waves: A derivation based on stationary phase. *Phys. Rev. E*, 69:046610 (2004). doi:10.1103/PhysRevE.69.046610. 5

K. Spieker, *I. Wölbern*, *C. Thomas*, *M. Harnafi*, and *L. El Moudnib*. Crustal and upper-mantle structure beneath the western Atlas Mountains in SW Morocco derived from receiver functions. *Geophysical Journal International*, 198(3):1474–1485 (2014). doi:10.1093/gji/ggu216. 37

S. Stein and *M. Wysession*. *Introduction to Seismology, Earthquakes, and Earth Structure*. Blackwell Publishing (2003). 11

E. Stutzmann, *M. Schimmel*, *G. Patau*, and *A. Maggi*. Global climate imprint on seismic noise. *Geochemistry, Geophysics, Geosystems*, 10(11) (2009). doi:https://doi.org/10.1029/2009GC002619. 6, 48, 60, 62, 63

T. Tanimoto. Excitation of microseisms: views from the normal-mode approach. *Geophysical Journal International*, page ggt185 (2013). doi:10.1093/gji/ggt185. 9, 36, 123

T. Tanimoto, *C. Hadziioannou*, *H. Igel*, *J. Wassermann*, *U. Schreiber*, *A. Gebauer*, and *B. Chow*. Seasonal variations in the rayleigh-to-love wave ratio in the secondary microseism from colocated ring laser and seismograph. *Journal of Geophysical Research: Solid Earth*, 121(4):2447–2459 (2016). doi:https://doi.org/10.1002/2016JB012885. 131

T. Tanimoto, *S. Ishimaru*, and *C. Alvizuri*. Seasonality in particle motion of microseisms. *Geophysical Journal International*, 166(1):253–266 (2006). doi:10.1111/j.1365-246X.2006.02931.x. 48

M. N. Toksöz and *R. T. Lacoss*. Microseisms: Mode structure and sources. *Science*, 159(3817):872–873 (1968). doi:10.1126/science.159.3817.872. 8, 35

H. L. Tolman. A third-generation model for wind waves on slowly varying, unsteady, and inhomogeneous depths and currents. *Journal of Physical Oceanography*, 21(6):782–797 (1991). doi:10.1175/1520-0485(1991)021⟨0782:ATGMFW⟩2.0.CO;2. 67

V. C. Tsai. On establishing the accuracy of noise tomography travel-time measurements in a realistic medium. *Geophys. J. Int.*, 178(3):1555–1564 (2009). ISSN 0956540X. doi:10.1111/j.1365-246X.2009.04239.x. 6, 35, 123

M. van Driel, *L. Krischer*, *S. C. Stähler*, *K. Hosseini*, and *T. Nissen-Meyer*. Instaseis: instant global seismograms based on a broadband waveform database. *Solid Earth Discussions*, 7:957–1005 (2015). doi:10.5194/sed-7-957-2015. 13, 81

M. Wathelet. An improved neighborhood algorithm: parameter conditions and dynamic scaling. *Geophysical Research Letters*, 35(9) (2008). doi:10.1029/2008GL033256. 46

R. L. Weaver, *B. Froment*, and *M. Campillo*. On the correlation of non-isotropically distributed ballistic scalar diffuse waves. *J. Acoust. Soc. Am.*, 126(4):1817–26 (2009). ISSN 1520-8524. doi:10.1121/1.3203359. 6, 35, 123

E. Wiechert. Discussion, verhandlung der zweiten internationalen seismologischen konferenz. *Beitrage zur Geophysik*, 2:41–43 (1904). 6, 34

Y. Yang and *M. H. Ritzwoller.* Characteristics of ambient seismic noise as a source for surface wave tomography. *Geochemistry, Geophysics, Geosystems*, 9(2):n/a–n/a (2008). ISSN 1525-2027. doi:10.1029/2007GC001814. Q02008. 63

Y. Ying, *C. J. Bean*, and *P. D. Bromirski.* Propagation of microseisms from the deep ocean to land. *Geophysical Research Letters*, 41(18):6374–6379 (2014). doi:https://doi.org/10.1002/2014GL060979. 141

A. P. Young, *R. T. Guza*, *P. N. Adams*, *W. C. O'Reilly*, and *R. E. Flick.* Cross-shore decay of cliff top ground motions driven by local ocean swell and infragravity waves. *Journal of Geophysical Research: Oceans*, 117(C6):n/a–n/a (2012). ISSN 2156-2202. doi:10.1029/2012JC007908. C06029. 74

A. P. Young, *R. T. Guza*, *M. E. Dickson*, *W. C. O'Reilly*, and *R. E. Flick.* Ground motions on rocky, cliffed, and sandy shorelines generated by ocean waves. *Journal of Geophysical Research: Oceans*, 118(12):6590–6602 (2013). ISSN 2169-9291. doi:10.1002/2013JC008883. 60

Z. Zhan, *V. C. Tsai*, and *R. W. Clayton.* Spurious velocity changes caused by temporal variations in ambient noise frequency content. *Geophys. J. Int.*, 194(3):1574–1581 (2013). ISSN 0956-540X. doi:10.1093/gji/ggt170. 6

J. Zhang, *P. Gerstoft*, and *P. D. Bromirski.* Pelagic and coastal sources of P-wave microseisms: Generation under tropical cyclones. *Geophysical Research Letters*, 37(15) (2010). doi:10.1029/2010GL044288. 8, 48

D. Ziane and *C. Hadziioannou.* The contribution of multiple scattering to love wave generation in the secondary microseism. *Geophysical Journal International*, 217(2):1108–1122 (2019). 141

K. Zoeppritz. Seismische Registrierungen in Göttingen im Jahre 1906. *Nachrichten von der Königlichen Gesellschaft der Wissenschaften zu Göttingen*, Mathematisch-Physikalische Klasse:129–200 (1908). 6